Triplet-Pair States in Exciton Fission and Fusion

David Bossanyi

Department of Physics and Astronomy

Faculty of Science

The University of Sheffield

A thesis submitted in partial fulfilment of the requirements for the degree of Doctor of Philosophy

February 2022

Declaration

The work within this thesis was completed by the author, unless explicitly stated in the text where the work involves collaboration. Throughout, we use the first person plural for readability. This work has never been submitted for the awarding of a degree at any other institution and is within the 80,000 word limit.

— David Bossanyi
February 2022

Abstract

In this thesis, we present our investigations into the intermediate triplet-pair states that mediate the twin photophysical processes of singlet fission and triplet fusion. Unique to certain conjugated organic materials, singlet fission and triplet fusion refer to the splitting of bright, spin-0 singlet excitons into pairs of dark, spin-1 triplet excitons, and vice versa. First invoked more than 50 years ago, the triplet-pair states that mediate these processes have recently enjoyed a resurgence of interest, largely due to the realisation that exciton fission and fusion could be harnessed in photovoltaic devices to exceed the theoretical power conversion efficiency limit. Despite great progress in our understanding of these intriguing states, many aspects of their nature and behaviour remain unclear.

We begin by probing the photoluminescence signatures of the strongly exchange-coupled spin-0 triplet-pair state, ^{1}(TT), in polycrystalline films of diF-TES-ADT and single crystals of pentacene, demonstrating that it is a real, observable intermediate state. We then present brief investigations of ^{1}(TT) photoluminescence, or lack thereof, and ^{1}(TT) formation in rubrene single crystals. Our results here cast doubt on the vibronic coherent mechanism of singlet fission and highlight the role of defect sites and disorder.

Next, we turn to the spin statistical factor governing the probability of obtaining a spin-0 state from the annihilation of two spin-1 triplets and explain why it has been incorrectly described in much of the recent literature. Using rubrene as a model system, we investigate the key parameters affecting this important quantity and uncover previously overlooked strategies for engineering materials with favourable spin statistics.

Finally, we investigate the photophysics of rubrene nanoparticles for photon upconversion. We show that the addition of a singlet energy collector, used to improve the upconversion quantum yield, does not suppress singlet fission as previously assumed but instead competes with triplet-pair separation.

Acknowledgements

This thesis and the work presented within it would not have been possible without the help and support of many people, whose contributions I would like to acknowledge here.

First and foremost, I would like to thank my supervisor, Dr. Jenny Clark. Her infectious enthusiasm and energy has been invaluable over the past few years. I am very grateful for the trust she has shown in me, from letting me loose in the lab from day one to encouraging me to talk at conferences and for giving me the freedom to develop and pursue research projects. Her support has gone well beyond the academic and for her role as friend as well as supervisor, I cannot thank her enough.

I would also like to thank the members of the Fast Spectroscopy Group and Laser Facility, past and present, alongside whom it has been a pleasure to work. Andrew, for his frequent help in the lab in the early days and for sharing his extensive knowledge and experience with me; Daniel for getting me started with the iCCD; James for showing me around the Helios; Sandra, for many a good laugh; Jozra, for all those coffees and chats in the office; Sayantan for the walks and talks; Simon, for bringing his expertise to the lab and for setting up the electromagnet; Rahul, James, Daniel, Kirsty, Ravi and everybody else I've worked with for making the last few years such an enjoyable experience. A special mention also goes to Dimitri and Matt, who kept the Chemistry and Physics labs running smoothly throughout.

I want to acknowledge my collaborators, without whom these projects would not have taken place. I want to thank Jana and the NMOE group for hosting me in Heidelberg and especially Maik, whose patience and skill enabled us to grow such high quality pentacene crystals. Thanks to Yoichi, with whom it has been a real delight to work, both during his visit to Sheffield and throughout the fruitful collaboration that we have enjoyed since. Thanks also to Nobu for the many interesting upconversion discussions.

My PhD was funded by the Centre for Doctoral Training in New and Sustainable Photovoltaics, a programme that would not have existed but for the dedication of Ken, Alison and Asim and now Alan as well. Thanks also to my fellow members of the C4 family: Alan, Emma, Kilian, Laurie, Leo, Lewis, Liam, Sam and Tomi, for some very memorable times together during our tour of the restaurants, pubs and occasionally labs of the UK.

I am very grateful to everybody else who has made my time in Sheffield so

enjoyable. In particular, to Steph, Tara and Earl for many hikes and cherished memories in the beginning; to James for the music and happy evenings spent scraping away in the double bass section of the SPO and to Judy, whose friendship and company was invaluable during the pandemic. Finally, I would like to thank my family for their constant love, support and encouragement.

‘*The science of today is the technology of tomorrow.*’

— Edward Teller

Contents

List of Figures

List of Tables

List of Abbreviations

Molecules

DBP	tetraphenyldibenzoperiflanthene
diF-TES-ADT	2,8-difluoro-5,11-bis(triethylsilylethynyl)anthradithiophene
DPA	9,10-diphenylanthracene
DPH	diphenyl-1,3,5-hexatriene
DPP	diketopyrrolopyrrole
DPT	5,12-diphenyltetracene
PDI	perylene diimide
PVA	poly(vinyl alcohol)
TDI	terrylene diimide
TIPS	triisopropylsilylethynyl

Others

CT	charge transfer
DFT	density functional theory
FRET	Förster resonance energy transfer
HL-RISC	high-level reverse intersystem crossing
HOMO	highest occupied molecular orbital
ISC	intersystem crossing
IVR	intramolecular vibrational energy redistribution
LUMO	lowest unoccupied molecular orbital
MFE	magnetic field effect
NIR	near infrared
NP	nanoparticle
OLED	organic light-emitting diode
PL	photoluminescence
PLQY	photoluminescence quantum yield
RISC	reverse intersystem crossing

SSA	singlet-singlet annihilation
TA	transient absorption
TET	triplet energy transfer
trEPR	time-resolved electron paramagnetic resonance
TRPL	time-resolved photoluminescence
TTA	triplet-triplet annihilation
TTA-UC	triplet-triplet annihilation upconversion
UCQY	upconversion quantum yield
UV	ultraviolet

List of Publications

David G. Bossanyi, Maik Matthiesen, Shuangqing Wang, Joel A. Smith, Rachel C. Kilbride, James D. Shipp, Dimitri Chekulaev, Emma Holland, John E. Anthony, Jana Zaumseil, Andrew J. Musser and Jenny Clark. Emissive spin-0 triplet-pairs are a direct product of triplet-triplet annihilation in pentacene single crystals and anthradithiophene films. *Nature Chemistry*, **13**, 2, 163-171 (2021)

David G. Bossanyi, Yoichi Sasaki, Shuangqing Wang, Dimitri Chekulaev, Nobuo Kimizuka, Nobuhiro Yanai and Jenny Clark. Spin statistics for triplet-triplet annihilation upconversion: exchange coupling, intermolecular orientation and reverse intersystem crossing. *JACS Au*, **1**, 12, 2188-2201 (2021)

David G. Bossanyi, Yoichi Sasaki, Shuangqing Wang, Dimitri Chekulaev, Nobuo Kimizuka, Nobuhiro Yanai and Jenny Clark. In optimized rubrene-based nanoparticle blends for photon upconversion, singlet energy collection outcompetes triplet-pair separation, not singlet fission. *J. Mat. Chem. C* (2022)

Kezia Sasitharan, David G. Bossanyi, Naoum Vaenas, Andrew J. Parnell, Jenny Clark, Ahmed Iraqi, David G. Lidzey and Jonathan A. Foster. Metal-organic framework nanosheets for enhanced performance of organic photovoltaic cells. *J. Mat. Chem. A*, **8**, 12, 6067-6075 (2020)

Daniel Polak, Rahul Jayaprakash, Thomas P. Lyons, Luis Á. Martínez-Martínez, Anastasia Leventis, Kealan J. Fallon, Harriet Coulthard, David G. Bossanyi, Kyriacos Georgiou, Anthony J. Petty II, John Anthony, Hugo Bronstein, Joel Yuen-Zhou, Alexander I. Tartakovskii, Jenny Clark and Andrew J. Musser. Manipulating molecules with strong coupling: harvesting triplet excitons in organic exciton microcavities. *Chemical Science*, **11**, 2, 343-354 (2020)

George A. Sutherland, Daniel Polak, David J. K. Swainsbury, Shuangqing Wang, Frank C. Spano, Dirk B. Auman, David G. Bossanyi, James P. Pidgeon, Andrew Hitchcock, Andrew J. Musser, John E. Anthony, P. Leslie Dutton, Jenny Clark, and C. Neil Hunter. A Thermostable Protein Matrix for Spectroscopic Analysis of Organic Semiconductors. *J. Am. Chem. Soc.*, **142**, 32, 13898-13907 (2020)

Chapter 1

Introduction

Climate change is one of the gravest threats to the future of sustainable life on Earth. Addressing it is the most important challenge that we face in the coming decades, during which time we must reach 'net zero' anthropogenic greenhouse gas emissions[1–3]. Potential pathways for achieving this goal have been, and continue to be, developed by the Intergovernmental Panel on Climate Change[2]. Among many technological and behavioural factors that contribute to the net zero pathways, solar photovoltaics (PV), whereby electricity is generated directly from sunlight, will play a critical role in the transition to a renewable energy system[4,5].

Deployment of solar PV has increased exponentially in recent years, driven by a dramatic reduction in manufacturing costs and improvements to the technology, the vast majority of which is crystalline silicon[5]. Indeed the levelised cost of energy from large-scale solar PV is already well below that of combined-cycle gas turbines, the cheapest fossil fuel source[5]. The cost of PV modules (solar panels) has fallen particularly precipitously over the last few decades[6] with the result that the modules themselves now represent only around one quarter of the total cost of a PV installation[7]. Further technological innovations should therefore focus on increasing the power conversion efficiency of PV modules in order to have the biggest impact on levelised energy costs.

Crystalline silicon solar cells are already approaching their maximum theoretical efficiency limit of around 30%[8,9]. This has inspired research into ways to circumvent this limit, which for silicon arises principally due to thermalisation losses for above-bandgap photons. In the case of higher-bandgap solar cell materials such as cadmium telluride[10] or the recently developed lead-halide perovskites[11], such thermalisation losses are less detrimental, but a reduced proportion of the solar spectrum is absorbed to begin with.

One potential strategy to exceed conventional efficiency limits is to construct

tandem devices, in which two (or more) solar cells with differing bandgaps are stacked together, thus enabling wider coverage of the solar spectrum and reducing thermalisation losses. Perovskite-silicon tandems show particular promise[12] although it remains to be seen whether the increase in efficiency can offset the significantly higher costs[5].

An alternative strategy is spectral conversion. Here the spectral content of the incident sunlight is manipulated to enhance the power conversion efficiencies of existing solar cell technologies[13]. Spectral downconversion, whereby high energy photons are split into pairs of low energy photons, is suited to materials such as silicon for which thermalisation is the dominant loss mechanism. The reverse process, spectral upconversion, involves combining pairs of low energy photons into higher energy ones and would benefit higher-bandgap solar absorbers such as cadmium telluride and lead-halide perovskites.

To be technologically relevant, spectral conversion must be efficient and occur in solid materials under weak, incoherent illumination such as sunlight. Certain molecular materials offer a unique platform to realise this through the twin photophysical processes of singlet fission and triplet-triplet annihilation, both of which could push power conversion efficiencies to above 45%[14].

During singlet fission[15,16], a photo-excited spin-0 singlet exciton can split into a pair of spin-1 triplet excitons, each of approximately half the original photon energy. This can be extremely efficient[17]. The challenge is to extract the energy from the triplet excitons, hence the recent excitement generated by reports of energy transfer from singlet fission borne triplets directly into silicon[18].

Triplet-triplet annihilation is the inverse process, whereby two low-energy spin-1 triplet excitons are generated and combined to yield a single spin-0 singlet, which subsequently emits a higher energy photon[19]. Here the challenge is to obtain high efficiencies in solid materials under weak illumination[20]. Additional motivation for pursuing triplet-triplet annihilation upconversion comes from the biomedical sciences. Human tissue is transparent to near-infrared light, which could be upconverted inside the body to the blue light needed for processes such as drug release[21], photodynamic therapy[22] or optogenetics[23].

Singlet fission and triplet-triplet annihilation were first studied in the late 1960s[24,25], before the connection to solar energy harvesting was made[26,27]. At the time, these photophysical processes were presented from the perspective of fundamental physics: understanding radiationless transitions and interactions between excitonic species.

The realisation that singlet fission and triplet-triplet annihilation could en-

able a step change in PV efficiency[26,27] has precipitated a great resurgence of research interest over the last decade. This has coincided with the widespread availability of ultrafast (femtosecond) laser systems[28] that have allowed the photophysical mechanisms, particularly of singlet fission, to be unravelled in great detail and with unprecedented time resolution. As a result, the critical importance of intermediate triplet-pair states, first postulated in the 1960s, has come to the fore[29,30]. In addition to mediating spectral conversion processes, these triplet-pair states are fascinating objects from a fundamental point of view. For example they can exist as spin-0, spin-1 or even spin-2 states, and the constituent triplets may be quantum-entangled at room temperature[31].

Despite extensive investigation in recent years, many unanswered questions remain regarding the photophysical mechanisms of singlet fission and triplet-triplet annihilation. In particular, the role, character and behaviour of the intermediate triplet-pair states is still subject to controversy and debate[29,30], particularly in the context of triplet-triplet annihilation[32]. This thesis helps to answer some of the outstanding questions and uncertainties surrounding triplet-pair states and is organised as follows.

In Chapter 2 we present the theoretical background needed to understand the research in later chapters. We start by discussing the electronic structure of conjugated organic molecules. We introduce the concept of spin and explain how it gives rise to singlet and triplet excitons possessing remarkably different characteristics. Next, we study the interactions of such molecules with light and discuss the different electronic transitions that can occur between excited states. Since we are primarily interested in the solid state, we describe the effects of neighbouring molecules in close proximity to each other. This leads us to the photophysical processes of singlet fission and triplet-triplet annihilation, which we describe in detail, finishing with an extensive review of the recent literature.

Chapter 3 introduces the molecular systems that we study in subsequent chapters as well as the techniques used to prepare and characterise samples. We explore the principles behind time-resolved photoluminescence spectroscopy and transient absorption spectroscopy, which we used to collect the majority of the data presented in this thesis, and give details of the experimental setups.

Our first experimental investigation, Chapter 4, studies a particular triplet-pair state, called ^{1}(TT), in two contrasting singlet fission materials. The ^{1}(TT) state is crucial to the singlet fission process since it acts as the gateway between spin-0 singlets (hence the 'one') and pairs of triplets (hence the 'TT'). Recent controversy has arisen over whether ^{1}(TT) could be observed by its photoluminescence signature during triplet-triplet annihilation, with one study casting

doubt on the role of ^{1}(TT) as a real, observable intermediate state[32]. In this chapter, we demonstrate that emissive ^{1}(TT) states are real intermediates both in singlet fission and triplet-triplet annihilation.

Having observed photoluminescence from the ^{1}(TT) state in Chapter 4, we hypothesised that ^{1}(TT) might be particularly emissive in rubrene single crystals and could explain curious photoluminescence behaviour reported previously[33,34]. In Chapter 5, we investigate this hypothesis but find no evidence of emissive ^{1}(TT) states, instead highlighting the role of defects in anomalous photoluminescence behaviour. In Chapter 6, we find that the defects present in polycrystalline rubrene films enable ultrafast formation of ^{1}(TT) states that we do not observe in bulk crystals, in contrast to previous reports[35–37].

Having established the role of the spin-0 ^{1}(TT) as a key intermediate during triplet-triplet annihilation, in Chapter 7 we continue with rubrene as a model system and investigate the spin statistical factor that governs the probability of obtaining a spin-0 singlet exciton from the annihilation of two spin-1 triplet excitons. This factor is critical in determining the efficiency of devices such as blue-emitting OLEDs and photon upconverters that employ triplet-triplet annihilation and we demonstrate that it has been incorrectly described in much of the recent literature[22,38–42]. We explore the factors that affect the spin statistics of triplet-triplet annihilation and identify previously overlooked strategies for engineering materials with favourable spin statistics.

Whilst high values of the spin statistical factor are important for efficient OLEDs and photon upconverters, the singlet energy must be emitted as light to make useful devices. In Chapter 8, we seek to understand how adding a dopant molecule to solid rubrene can greatly increase the proportion of singlet energy emitted as light, following triplet-triplet annihilation. We find that the role of the dopant is not to suppress singlet fission as previously assumed[43–46], but instead to compete with the separation of triplet-pair states.

Finally in Chapter 9 we summarise the main conclusions of the experimental studies and identify the most pressing areas for future research.

Chapter 2

Theory and Background

In this chapter we develop the theoretical concepts needed to understand the experimental results presented in subsequent chapters. Starting from, "what is an organic molecule?" we work our way to the interactions of such molecules with light and their resulting excited states. We see how different excited states can interconvert, leading to a rich variety of photophysical behaviour. Finally, we describe the twin processes of singlet fission and triplet-triplet annihilation and their application to spectral energy conversion.

2.1 Photophysics of conjugated organic molecules: a brief introduction

What is an organic molecule? In everyday language, 'organic' is often synonymous with 'natural' and indeed the natural world contains a bewildering array of molecules ranging from simple sugars and lipids all the way to the staggering complexity of proteins and DNA. Yet chemists too have synthesised a huge range of molecules that are also 'organic', from pharmaceutical drugs to the dyes found in display technologies. What all of these molecules have in common is a framework consisting largely of carbon and hydrogen. Each carbon atom can form up to four bonds with neighbouring atoms, which may include 'heteroatoms' such as nitrogen, oxygen and sulphur, leading to an almost infinite playground of possible structures.

As we shall see below, if organic molecules contain alternating double and single bonds, the resulting 'conjugated' electronic structure allows them to absorb photons of light, forming *excited states* that can have a very different character to the molecular ground state.

In some situations, the formation of these photo-excited states kick-starts a chemical reaction and leads to the creation of new products. This is termed

photochemistry. The conversion of carbon dioxide and water into carbohydrates (photosynthesis) that occurs in green plants[47] and the production of vitamin D from 7-dehydrocholesterol in skin cells[48] are examples of photochemical reactions.

In other cases, absorption of light may not result in a chemical change. Instead, the energy is transferred between different types of excited states and the molecule eventually returns to its original ground state. This is termed photophysics. For example, the absorption and emission of light by fluorescent dyes[49] and the conversion of sunlight into electricity by solar cells[50] are both photophysical processes.

The same conjugation that allows certain molecules to absorb light also allows them to conduct electrical charge and so conjugated organic molecules are also known as organic semiconductors when in the solid state. During the 1990s and 2000s, the field of molecular (and polymer) opto-electronics was rapidly advanced and has led to the development of organic light-emitting diodes[51], lasers[52], transistors[53] and photovoltaics[54], all devices that were traditionally made of inorganic semiconductors such as crystalline silicon.

However, with the notable exception of organic light-emitting diodes (OLEDs), conjugated organic molecules have so far not displaced inorganic semiconductors in commercial applications. What, then, is the motivation for continuing to study their photophysics? What can organic molecules do well that inorganic semiconductors cannot?

One example is the efficient conversion of low energy photons into high energy photons and vice versa. Certain organic semiconductor systems can enable this through the photophysical processes of singlet fission and triplet-triplet annihilation. Efficient spectral conversion is hugely desirable, not only as a mechanism for boosting the efficiency of conventional photovoltaics[14,17], but also for biomedical purposes: the conversion of tissue-penetrating near infrared light to reaction-starting blue light is highly sought after for targeted drug delivery, photodynamic therapy and opto-genetics[21–23,55].

2.2 Electronic properties of conjugated organic molecules

We can obtain an exact description of the electronic properties of an organic molecule by solving the time-independent Schrödinger equation,

$$H\left|\Psi\right\rangle = E\left|\Psi\right\rangle, \tag{2.1}$$

for the many-body Hamiltonian,

$$H = H_{el-el} + H_{nuc-nuc} + H_{el-nuc}, \tag{2.2}$$

where

$$H_{el-el} = \sum_i \frac{\mathbf{p}_i^2}{2m_i} + \frac{1}{2}\sum_{i\neq j} \frac{e^2}{|\mathbf{r}_i - \mathbf{r}_j|} \tag{2.3}$$

describes the kinetic energy of the electrons and their mutual Coulomb repulsion,

$$H_{nuc-nuc} = \sum_\alpha \frac{\mathbf{P}_\alpha^2}{2M_\alpha} + \frac{1}{2}\sum_{\alpha\neq\beta} \frac{Z_\alpha Z_\beta e^2}{|\mathbf{R}_\alpha - \mathbf{R}_\beta|} \tag{2.4}$$

represents the analogous description for the nuclei and

$$H_{el-nuc} = -\frac{1}{2}\sum_{\alpha,i} \frac{Z_\alpha e^2}{|\mathbf{R}_\alpha - \mathbf{r}_i|} \tag{2.5}$$

describes the Coulomb attraction between the nuclei and electrons. Here $\{\mathbf{R}\}$ and $\{\mathbf{r}\}$ are the set of nuclear and electronic coordinates respectively, M and m are the nuclear and electronic masses and Z_α is the atomic number of the α^{th} nucleus. Note that the momentum operators take the general form $\mathbf{p} = -i\hbar\nabla$.

In practice of course, an exact solution is impossible for anything more complex than a single hydrogen atom. Fortunately, in the case of conjugated organic molecules, there are a number of simplifying assumptions that we can make that allow us to obtain an excellent description of their optical and electronic properties. During the course of this chapter, we will introduce these simplifications mathematically whilst at the same time building up a more intuitive and pictorial description of the electronic states. For the full quantitative analysis, readers are directed to Barford's textbook[56] whilst Turro[49] provides an excellent and complementary qualitative approach.

2.2.1 π-conjugation

Carbon is the sixth element in the periodic table. Thus the electronic structure of carbon atoms, according to Hund's rules, is $(1s)^2(2s)^2(2p)^2$. There are pairs of electrons in the inner $1s$ orbital and the outer $2s$ orbital; the remaining two electrons reside in the $2p$ orbitals. Carbon therefore has four valence electrons in its outer shell.

In order to understand the nature of bonding in carbon-based molecules, we employ the well-known approximation of sp^n hybridisation. Rather than considering atomic orbitals, we construct new hybrid orbitals consisting of linear

combinations of s and p. For example the central carbon atom of methane (CH_4) is sp^3 hybridised — the $2s$ and three $2p$ atomic orbitals are mixed to form four degenerate hybrid sp^3 orbitals, arranged tetrahedrally.

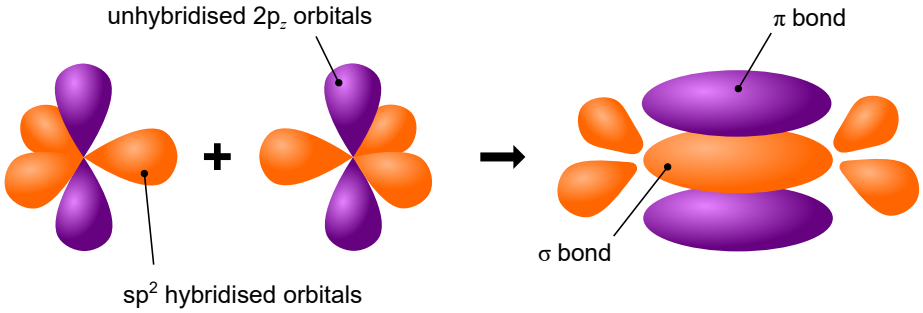

Figure 2.1 | sp^2 hybridisation and π-bonding. sp^2 hybrid orbitals (orange) are oriented at an angle of 120° in the xy plane, leaving unhybridised out-of-plane $2p_z$ orbitals (purple). The sp^2 orbitals form tightly bound σ-bonds that determine the (planar) molecular structure. The $2p_z$ orbitals overlap to form weakly bound π-bonds in which electrons are delocalised above and below the molecular plane.

Of particular interest here is sp^2 hybridisation. In this case, as shown in Figure 2.1, the $2s$, $2p_x$ and $2p_y$ orbitals are hybridised, forming three sp^2 orbitals oriented in the xy plane at an angle of 120°. Each of the sp^2 orbitals contains one electron. The remaining electron occupies the unhybridised $2p_z$ orbital which is oriented perpendicular to the sp^2 plane.

The simplest molecule exhibiting sp^2 hybridisation is ethylene (C_2H_4). Figure 2.1 illustrates the carbon-carbon bonding in ethylene. The sp^2 orbitals between the two carbon atoms form a σ-bond (the bonds to the four hydrogen atoms, not shown, are also σ-bonds). The σ-bonds dictate the molecular structure but importantly, since the electrons within them are so tightly bound ($\sim 10\,\text{eV}$)[56], they do not influence the optical or electronic properties that we are concerned with here. The $2p_z$ orbitals on the other hand overlap, forming a π-bond which consists of electron density that is *delocalised* above and below the molecular plane. This overlap of $2p_z$ orbitals to form π-bonds is known as conjugation.

The π-bond has the effect of restricting rotation about the σ-bond. As a result, conjugated molecules tend to be rigid and planar. The more sp^2 carbon atoms contributing to the conjugation, the more delocalised, and hence less tightly bound, the π-electrons. As a result, the π-electrons are not associated with a particular atom, instead they are delocalised across the whole molecule and are best described as occupying molecular orbitals.

2.2.2 Molecular orbitals

The delocalisation of the π-electrons in conjugated organic molecules means that they are well separated in energy from the σ-electrons[56]. This allows us to decouple the molecular wavefunction into distinct σ and π contributions,

$$|\Psi\rangle = |\Psi\rangle_\sigma |\Psi\rangle_\pi . \tag{2.6}$$

The tightly bound σ and core electrons act to screen the coulomb interactions among the nuclei and π-electrons. These electrons can therefore be included simply through a static dielectric constant which is typically in the range of 2-4[56] and is discussed further in Section 2.2.3. We can therefore consider only the π-electrons in Equations 2.3-2.5 provided that the Coulomb interaction terms are replaced by pseudopotentials. We introduce $V^{\text{eff}}_{el-el}(\mathbf{r}-\mathbf{r}')$ to represent the effective interaction between π-electrons, $V_p(\mathbf{r},\mathbf{R})$ which describes the effective interactions between the nuclei and π-electrons and $V_{nuc-nuc}$ for the screened nuclear-nuclear potential. It is the π-electrons, moving in these effective potentials, that govern the low-energy (optical) photophysics.

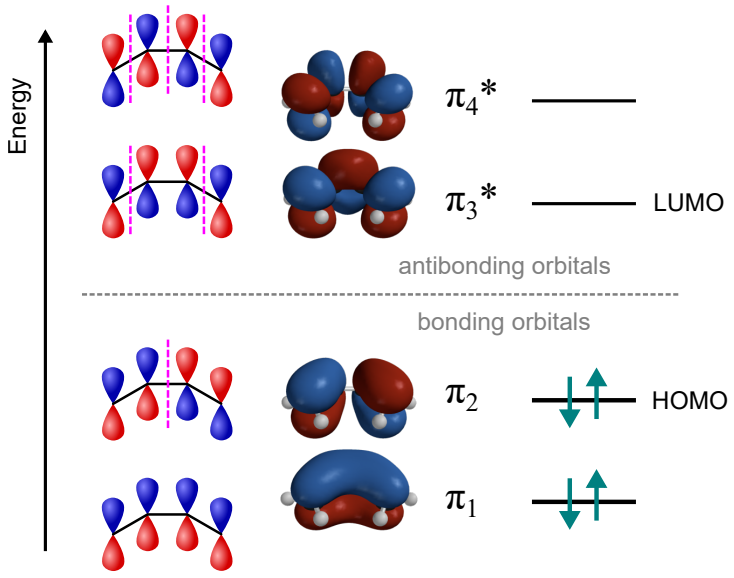

Figure 2.2 | Molecular orbitals. The molecular orbitals of *cis*-butadiene can be constructed from the $2p_z$ orbitals of the four carbon atoms. The energy of the molecular orbitals increases with the number of nodes (pink dashed lines). The energy of the original $2p_z$ orbitals is indicated by the dashed grey line.

We can therefore build molecular orbitals by considering only the π-electrons. Figure 2.2 illustrates this process for the archetypal example of *cis*-butadiene. From the four $2p_z$ orbitals, we can construct four linearly

independent molecular orbitals that span the entire molecule. Schrödinger's equation (2.1) tells us that the energy of each orbital is proportional to the curvature of its wavefunction, which increases with the number of nodes (points at which the wavefunction changes sign), shown by pink dashed lines in Figure 2.2. Adding the four available electrons pairwise results in the two lowest energy orbitals being fully occupied. These are termed bonding (π) orbitals since they lower the overall energy of the molecule. The two highest energy orbitals are empty and are known as antibonding (π^*) orbitals, since their occupation raises the energy of the molecule. The highest occupied molecular orbital (HOMO) and lowest unoccupied molecular orbital (LUMO) are therefore somewhat analogous to the valence and conduction bands of inorganic semiconductors.

The molecular orbital picture provides an intuitive visual understanding of the symmetry of the different electronic states of molecules. Symmetry in this context refers to the behaviour of wavefunctions under spatial operations such as reflection and inversion. As we discover in Section 2.3.2, symmetry has important consequences for the optical properties of molecules by placing requirements on the symmetries of wavefunctions participating in electronic transitions.

The lowest energy electronic transition is that which moves an electron from the HOMO to the LUMO which, as is the case for *cis*-butadiene, is often a $\pi \rightarrow \pi^*$ transition. By undergoing such a transition, a molecule changes from being in its ground state to being in a higher energy excited state. A mathematical treatment of such transitions is developed in Section 2.3, but first we take an important excursion to consider the types of excited state that are formed.

2.2.3 Excitons

The promotion of an electron to the conduction band, or LUMO, leaves behind a positively charged hole, or absence of an electron, in the valence band, or HOMO. There exists a Coulomb interaction between the electron and hole that causes them to be bound together in an electrically neutral quasiparticle known as an exciton. For 3-dimensional inorganic semiconductors such as silicon and gallium arsenide the dielectric constant is high and so the electron-hole interaction is very effectively screened. As a result, the exciton binding energy is typically less than 10 meV and the distance between the electron and hole can be very great, even extending across thousands of unit cells[57]. As a result, the electron can often move freely throughout the crystal at room temperature. These excitations are termed Wannier-Mott excitons (Figure 2.3).

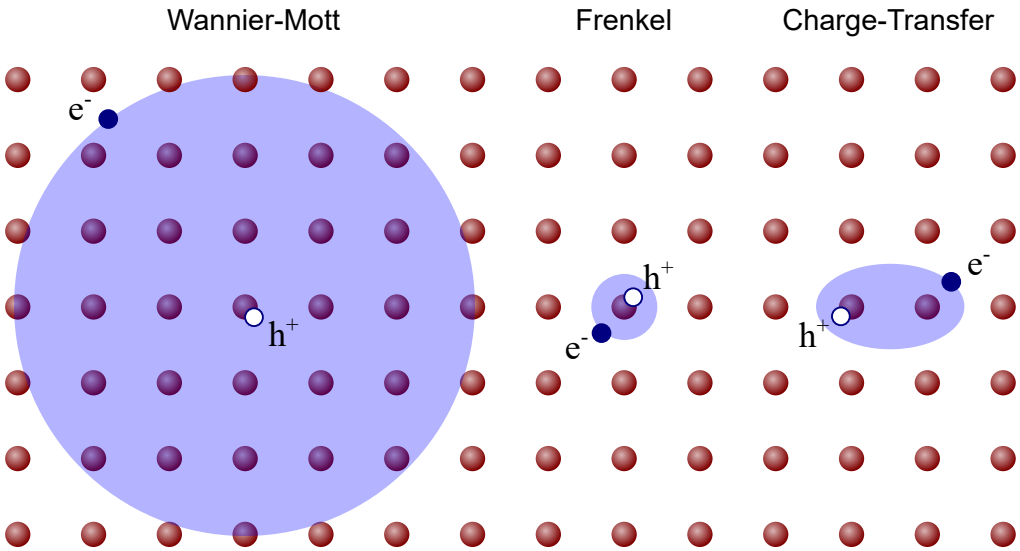

Figure 2.3 | Types of exciton. Wannier-Mott excitons are very weakly bound and so have a large spatial extent. Frenkel excitons are strongly bound and localised. Charge-transfer excitons are also localised, but the electron and hole are spatially separate.

Organic molecules on the other hand typically exhibit relatively poor dielectric screening. As a result, there is a strong Coulomb binding of 0.5–1 eV between the electron and hole, which localises the exciton, often to around a single molecule. These are molecular, or Frenkel excitons[56]. For highly ordered crystalline organic semiconductors, Frenkel excitons can delocalise over several molecules, particularly at low temperature[58]. Frenkel exciton delocalisation is distinct from Wannier-Mott excitons in that the electron-hole separation remains small. Instead, the localised Frenkel exciton can be thought of as situated on several molecules at once in a quantum mechanical superposition.

A third type of exciton, common in organic semiconductors, is the charge-transfer (CT) exciton. It is still localised, but the electron and hole reside either on spatially separated parts of one molecule or on neighbouring molecules. As a result, CT excitons possess a static dipole moment.

From here on in, 'exciton' will generally refer to a Frenkel exciton unless explicitly stated otherwise. Within the one-electron approximation, excitons are inherently two-electron excited states and since electrons are spin-$\frac{1}{2}$ particles, spin plays a critical role in exciton photophysics.

2.2.4 Spin

In the ground state, two electrons occupy the HOMO, $|\phi_a\rangle$. The Pauli exclusion principle therefore requires them to have different spins. Accordingly, one

electron is 'spin up', $|\uparrow\rangle_1$, and the other is 'spin down', $|\downarrow\rangle_2$.

In the excited state, one of the electrons has transitioned to the LUMO, $|\phi_b\rangle$. Thus the two electrons that comprise the exciton now reside in different orbitals and the requirement that they have opposite spins is relaxed. Two electrons, each with two spin states, gives a total of four possible spin wavefunctions for the exciton. These two-electron spin wavefunctions can be constructed from products of the one-electron spins, for example $|\uparrow\rangle_1 |\downarrow\rangle_2$.

The spin wavefunctions are the eigenstates of both the total spin operator $\mathbf{S}^2 = (\mathbf{S}_1 + \mathbf{S}_2)^2$, with eigenvalue S, and its projection S_z onto the z-axis, with eigenvalue m_S. The eigenstates are thus denoted $|S, m_S\rangle$ and are given by

$$|0,0\rangle = \frac{1}{\sqrt{2}} \left(|\uparrow\rangle_1 |\downarrow\rangle_2 - |\downarrow\rangle_1 |\uparrow\rangle_2\right) \tag{2.7}$$

$$|1,1\rangle = |\uparrow\rangle_1 |\uparrow\rangle_2 \tag{2.8}$$

$$|1,0\rangle = \frac{1}{\sqrt{2}} \left(|\downarrow\rangle_1 |\uparrow\rangle_2 + |\uparrow\rangle_1 |\downarrow\rangle_2\right) \tag{2.9}$$

$$|1,-1\rangle = |\downarrow\rangle_1 |\downarrow\rangle_2 \tag{2.10}$$

Figure 2.4a is a vector diagram of these four spin states. We immediately notice two things. Firstly, there is one spin state with a total spin of 0 and three with a total spin of 1. There are therefore two 'flavours' of exciton: those with a spin of 0 are known as singlet excitons, whilst those with a spin of 1 are called triplet excitons.

The second observation we can make is that the symmetry of the spin wavefunctions with respect to particle exchange is opposite for singlets and triplets. To see this, we can investigate the effect of switching the two electrons using the particle exchange operator, $P_{1\leftrightarrow 2}$. For the singlet, the wavefunction changes sign under this operation:

$$P_{1\leftrightarrow 2} |0,0\rangle = \frac{1}{\sqrt{2}} \left(|\uparrow\rangle_2 |\downarrow\rangle_1 - |\downarrow\rangle_2 |\uparrow\rangle_1\right) = -|0,0\rangle . \tag{2.11}$$

The singlet spin wavefunction is therefore antisymmetric. In contrast, particle exchange does not change the sign of the triplet spin wavefunctions, for example

$$P_{1\leftrightarrow 2} |1,1\rangle = |\uparrow\rangle_2 |\uparrow\rangle_1 = |1,1\rangle . \tag{2.12}$$

This symmetry has vital consequences for the relative energies of singlet and triplet excitons. In the absence of electron-electron interactions, singlet and triplet excitons would be degenerate. We have seen above however that there

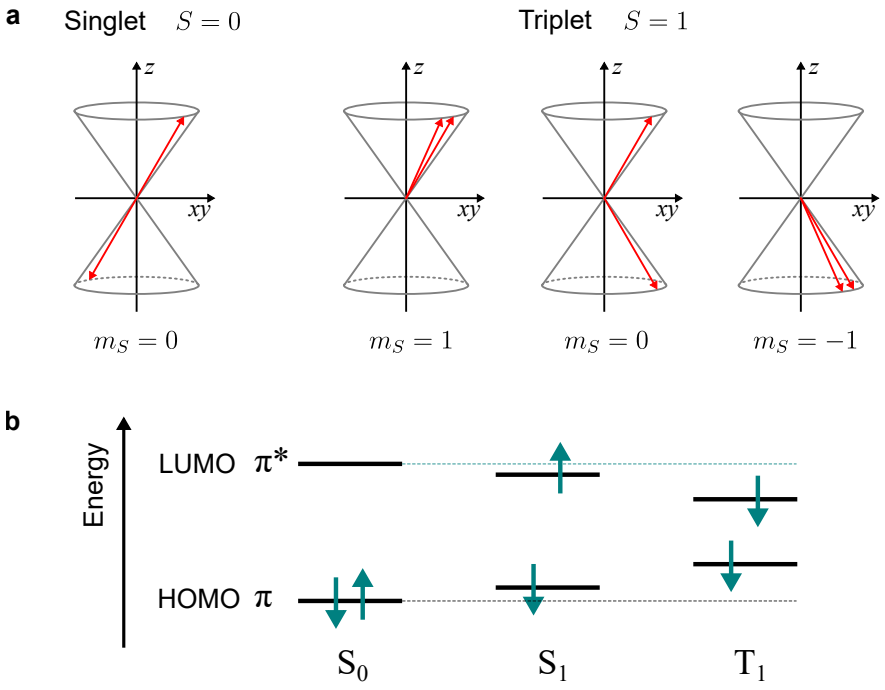

Figure 2.4 | Singlet and triplet excitons. a, Vector representation of the singlet (antiparallel spins) and triplet (parallel spins) spin states. **b**, The HOMO and LUMO levels of the singlet exciton S_1 and the triplet exciton T_1 are shifted from those of the ground state S_0 by the exciton binding energy (Coulomb interaction) and the exchange interaction.

exists a (screened) Coulomb repulsion V_{el-el}^{eff} between the electrons. Classically, this electrostatic repulsion would raise the energies of both the singlet and triplet excitons by the same amount, which we will call C.

We must also consider the quantum mechanical aspect. The Pauli exclusion principle forbids electrons with the same spin from occupying the same space. Thus the electrons in the triplet state are forced slightly further apart by the Pauli exclusion, thereby reducing the Coulomb repulsion between them and lowering the overall energy. The singlet electrons on the other hand have anti-parallel spins and so have a tendency to be in close proximity. This increases the Coulomb interaction and raises the overall energy.

This extra change in energy is known as the exchange energy, J, which can be described as the quantum mechanical correction to the classical Coulomb repulsion. The energy splitting between singlet and triplet excitons is therefore equal to $2J$, and triplet excitons are usually lower in energy than singlets (Figure 2.4b).

What determines the value of J and hence the singlet-triplet gap? In order to answer this question, we can derive simple mathematical expressions for C

and J. The spin wavefunctions defined in Equations 2.7-2.10 are only parts of the total electron wavefunctions $|\Psi_k\rangle$. We must also consider the spatial wavefunctions $|\psi_k\rangle$. The Pauli exclusion principle requires the *total* wavefunction to be antisymmetric under the exchange of two electrons. We have seen that the spin wavefunction of singlet excitons is antisymmetric, and so the spatial wavefunction must be symmetric. Likewise, for triplet excitons, the spatial wavefunction must be antisymmetric[59]. We can therefore write down the spatial wavefunctions for electrons 1 and 2 in orbitals $|\phi_a\rangle$ and $|\phi_b\rangle$ as

$$|\psi^{singlet}\rangle = \frac{1}{\sqrt{2}}\left(|\phi_a^1\rangle\,|\phi_b^2\rangle + |\phi_b^1\rangle\,|\phi_a^2\rangle\right) \tag{2.13}$$

$$|\psi^{triplet}\rangle = \frac{1}{\sqrt{2}}\left(|\phi_a^1\rangle\,|\phi_b^2\rangle - |\phi_b^1\rangle\,|\phi_a^2\rangle\right) \tag{2.14}$$

where $|\phi_a^1\rangle$ refers to electron 1 in orbital $|\phi_a\rangle$. Since V_{el-el}^{eff} has no spin dependence, the expected potential energies of the singlet and triplet excitons are given by

$$E^{singlet} = \langle\psi^{singlet}|\, V_{el-el}^{\text{eff}}\, |\psi^{singlet}\rangle = C + J \tag{2.15}$$

and

$$E^{triplet} = \langle\psi^{triplet}|\, V_{el-el}^{\text{eff}}\, |\psi^{triplet}\rangle = C - J \tag{2.16}$$

where

$$C = \iint \phi_a^*(\mathbf{r}_1)\phi_b^*(\mathbf{r}_2)V_{el-el}^{\text{eff}}(\mathbf{r}_1 - \mathbf{r}_2)\phi_a(\mathbf{r}_1)\phi_b(\mathbf{r}_2)d^3\mathbf{r}_1 d^3\mathbf{r}_2 \tag{2.17}$$

represents the classical electrostatic Coulomb integral and

$$J = \iint \phi_a^*(\mathbf{r}_1)\phi_b^*(\mathbf{r}_2)V_{el-el}^{\text{eff}}(\mathbf{r}_1 - \mathbf{r}_2)\phi_b(\mathbf{r}_1)\phi_a(\mathbf{r}_2)d^3\mathbf{r}_1 d^3\mathbf{r}_2 \tag{2.18}$$

is the exchange integral[56].

From Equation 2.18, we can see that J depends strongly on the overlap between $|\phi_a\rangle$ and $|\phi_b\rangle$. In other words, molecules for which the HOMO and LUMO are considerably overlapped will have a large energetic separation between the singlet and triplet excitons and vice versa. It is therefore possible to tune the singlet-triplet gap through careful molecular design[60].

The existence of distinct singlet and triplet exciton species gives rise to a rich variety of photophysical processes which we describe in Section 2.4. In particular, the variable singlet-triplet energy gap has important implications for singlet fission and triplet-triplet annihilation, discussed in Section 2.6.

2.3 Interaction of organic molecules with light

The interaction of conjugated organic molecules with light is of central importance. An understanding of the absorption and emission of photons, together with the photophysical or photochemical processes that follow, is fundamental for technologically relevant applications such as solar energy harvesting. Furthermore, the principal experimental probes that we use in this thesis to study conjugated molecules are all in some way measures of photon absorption or emission. In this section we therefore describe in detail the interaction between π-electrons and light.

Light, comprising photons of energy $\hbar\omega$, can be described as an electromagnetic wave with a time-varying electric field component $\mathbf{E}(t) = \hat{\epsilon}E_0e^{i\omega t}$, where $\hat{\epsilon}$ is a unit vector in the direction of the electric field. This electric field will interact with the negatively charged electrons of the molecule, giving a contribution to the total Hamiltonian of

$$H_1(t) = \mathbf{p} \cdot \hat{\epsilon}E_0e^{i\omega t} \tag{2.19}$$

where we have defined the dipole operator $\mathbf{p}$ as

$$\mathbf{p} = -e\sum_j \mathbf{r}_j \tag{2.20}$$

and the sum runs over the π-electrons. Treating $H_1(t)$ as a perturbation and following the derivation in Appendix A, we find that the rate of radiative transitions k_r from an initial state $|\psi_i\rangle$ to a final state $|\psi_f\rangle$ is given by Fermi's Golden Rule as

$$k_r = \Gamma_{i\to f} = \frac{2\pi}{\hbar}E_0^2|\mu_{if}|^2\rho(E_f)\delta(E_f - E_i \pm \hbar\omega) \tag{2.21}$$

where $\rho(E_f)$ is the density of (final) states and the delta function ensures that energy is conserved. The transition dipole moment μ_{if} is defined as

$$\mu_{if} = \langle\Psi_f|\,\mathbf{p}\cdot\hat{\epsilon}\,|\Psi_i\rangle\,. \tag{2.22}$$

When $|\Psi_i\rangle$ is the ground state, Equations 2.21 and 2.22 describe the absorption of a photon of energy $\hbar\omega$ to produce an excited state $|\Psi_f\rangle$. Conversely, if $|\Psi_i\rangle$ is an excited state, the process described is the stimulated emission of a photon of energy $\hbar\omega$ as the molecule returns to the ground state.

The likelihood of a radiative transition occuring between two states is termed the oscillator strength, f, which is proportional to the square of the transition

dipole moment μ_{if}. In principle, to evaluate μ_{if} we would need to solve Equations 2.1-2.4 for the electronic states of the molecule which, even considering only the π-electrons as described in Section 2.2.2, is impossibly complex. In practice, transition dipole moments are typically evaluated numerically using quantum-chemical calculations. Fortunately however, there is another key simplification that we can make in order to gain useful physical insight.

2.3.1 The Born-Oppenheimer approximation

The assumption that we make is that the total molecular wavefunction $|\Psi\rangle$ can be factored into separate electronic and nuclear parts. In fact, this was implicit in much of the discussion above which dealt solely with the electronic and spin parts of the wavefunction. In the following, we justify this assumption and formalise it into the adiabatic Born-Oppenheimer approximation.

Nuclei are more than three orders of magnitude heavier than electrons and their dynamics are therefore very 'slow' by comparison. The electrons experience a potential that depends on the *static* positions of the nuclei and so we introduce electronic states $|\psi_k(\mathbf{r};\mathbf{R})\rangle$ that depend only *parametrically* on the nuclear coordinates $\mathbf{R} = \{\mathbf{R}\}$. Thus the electronic states are each defined for a given set of nuclear coordinates and transitions between them cannot occur through the action of nuclear motion alone. We write the total wavefunction as

$$|\Psi_{k,\nu}(\mathbf{r},\mathbf{R})\rangle = |\psi_k(\mathbf{r};\mathbf{R})\rangle\,|\chi_{k,\nu}(\mathbf{R})\rangle\,, \tag{2.23}$$

where $|\chi_{k,\nu}(\mathbf{R})\rangle$ are nuclear wavefunctions associated with the electronic state k, labelled by a vibrational quantum number ν. $|\psi_k(\mathbf{r};\mathbf{R})\rangle$ are not eigenstates of the total molecular Hamiltonian defined in Equation 2.2, but rather of the electronic Born-Oppenheimer Hamiltonian H_{BO} that also has a parametric dependence on $\mathbf{R}$:

$$\begin{aligned} H_{BO}(\mathbf{r};\mathbf{R})\,|\psi_k(\mathbf{r};\mathbf{R})\rangle &= (H_{el-el} + H_{el-nuc} + V_{nuc-nuc})\,|\psi_k(\mathbf{r};\mathbf{R})\rangle \\ &= E_k(\mathbf{R})\,|\psi_k(\mathbf{r};\mathbf{R})\rangle\,. \end{aligned} \tag{2.24}$$

The variation of eigenvalue $E_k(\mathbf{R})$ with nuclear coordinates $\mathbf{R}$ defines the adiabatic *potential energy surface* of the electronic state k. As we demonstrate in Appendix B, combining Equations 2.1-2.5 with 2.23 and 2.24, we obtain

$$H\,|\psi_k(\mathbf{r};\mathbf{R})\rangle\,|\chi_{k,\nu}(\mathbf{R})\rangle \approx (E_k(\mathbf{R}) + T_{nuc})\,|\psi_k(\mathbf{r};\mathbf{R})\rangle\,|\chi_{k,\nu}(\mathbf{R})\rangle\,, \tag{2.25}$$

provided that certain nonadiabatic coupling terms are neglected. Here T_{nuc}

represents the nuclear kinetic energy operator and we immediately see that the potential energy surfaces $E_k(\mathbf{R})$ represent the effective potential in which the nuclei move.

We show in Appendix B that the Born-Oppenheimer approximation is valid provided that the potential energy surfaces are well separated in energy and the electronic states do not vary rapidly as a function of the nuclear coordinates. In such cases the aforementioned nonadiabatic coupling can become very large leading to a breakdown of the Born-Oppenheimer picture. Common examples of nonadiabatic behaviour are explored further in Section 2.4.

For the present discussion, the Born-Oppenheimer approximation holds and allows us to separate out the pure electronic and vibrational (nuclear) contributions to the total wavefunction[49]. When considering interactions with light we can also factor out the spin component $|\xi_{k,\sigma}\rangle$ because the oscillating electric field does not affect electron spin, and the magnetic field is so weak as to be negligible. Finally, we note that the energies associated with molecular rotations are orders of magnitude smaller than the electronic, vibrational and spin contributions and so we write the total molecular wavefunction as

$$|\Psi_{k,\nu,\sigma}\rangle = |\psi_k\rangle\,|\chi_{k,\nu}\rangle\,|\xi_{k,\sigma}\rangle\,. \tag{2.26}$$

Inserting this wavefunction into the expression for the transition dipole moment (Equation 2.22) gives

$$\mu_{if} = \langle\psi_f|\,\mathbf{p}\cdot\hat{\epsilon}\,|\psi_i\rangle\,\langle\chi_{f,\nu'}|\chi_{i,\nu}\rangle\,\langle\xi_{f,\sigma'}|\xi_{i,\sigma}\rangle\,. \tag{2.27}$$

Writing the transition dipole moment in this form allows us to identify various selection rules associated with photon absorption and emission.

Firstly, since $\langle\xi_{f,\sigma'}|\xi_{i,\sigma}\rangle = \delta_{\sigma'\sigma}$, radiative transitions are forbidden (on this level of approximation) between states of different multiplicities (differing total spin). This has critical consequences for the photophysics of organic molecules. The ground state is almost always a singlet so triplet excitons cannot be populated through photon absorption, nor can they emit light — they are 'dark' states. In contrast singlet excitons can absorb and emit photons and are therefore 'bright' states. In practice however the triplet transition dipole moment is not completely suppressed and transitions between singlet and triplet states do occur, albeit slowly. We explore this further in Section 2.4.2.

The remaining two factors in Equation 2.27 relate to the spatial symmetry of electronic wavefunctions and the overlap between the nuclear coordinates of different electronic states. Both of these are critical to the interpretation of

optical absorption and emission spectra of organic molecules.

2.3.2 Symmetry

In addition to the spin selection rules, the overall intensity of a radiative transition is proportional to the square of the electronic dipole matrix element μ^e_{if}:

$$I \propto |\mu^e_{if}|^2 = |\langle\psi_f|\,\mathbf{p}\cdot\hat{\epsilon}\,|\psi_i\rangle\,|^2. \tag{2.28}$$

If μ^e_{if} vanishes, the transition is said to be dipole-forbidden. For the transition to be dipole-allowed, μ^e_{if} must be non-zero which introduces constraints on the symmetries of $|\psi_i\rangle$ and $|\psi_f\rangle$. In Section 2.2.2, we saw that molecular wavefunctions can be assembled from combinations of atomic orbitals and that the symmetry of these wavefunctions is dictated by the geometry of the molecule itself.

In order to understand the effects of wavefunction symmetry on radiative transitions, we choose as an example the C_{2h} point group*, characterised by a two-fold rotation axis normal to a mirror plane. This is equivalent to invariance under spatial inversion $\mathbf{r} \to -\mathbf{r}$ so molecules exhibiting such symmetry are said to be centrosymmetric. We choose C_{2h} since it nicely illustrates the role of symmetry and is the point group of one of the molecules studied in this thesis.

The wavefunctions of molecules with C_{2h} symmetry can be labelled using the irreducible representation of that group: A or B denote symmetry or antisymmetry with respect to a 180° rotation and the subscripts g (*gerade*) or u (*ungerade*) indicate symmetry or antisymmetry under spatial inversion. There are thus four possible wavefunction symmetries, written A_g, A_u, B_g and B_u. Given the above approximations, the ground state of C_{2h} molecules possesses A_g symmetry[56]. The dipole selection rules therefore depend on the behaviour of the dipole operator under these same rotation and inversion operations.

Referring to Equation 2.20, we see that the dipole operator $\mathbf{p}$ is antisymmetric with respect to spatial inversion. Thus only transitions between states of opposite inversion symmetry ($g \leftrightarrow u$) are dipole allowed. To see this, consider the action of the spatial inversion operator $\hat{I}$ on $\mathbf{p}$[56],

$$\begin{aligned}\langle\psi_f|\,\mathbf{p}\,|\psi_i\rangle &\equiv \langle\psi_f|\,\hat{I}^\dagger\hat{I}\mathbf{p}\hat{I}^\dagger\hat{I}\,|\psi_i\rangle \\ &= -\langle\psi_f|\,\hat{I}^\dagger\mathbf{p}\hat{I}\,|\psi_i\rangle \\ &= -i_i i_f\,\langle\psi_f|\,\mathbf{p}\,|\psi_i\rangle\,,\end{aligned} \tag{2.29}$$

*Note that *cis*-butadiene (Figure 2.2) belongs to the C_{2v} point group.

where $\hat{I}\left|\psi_k\right\rangle = i_k\left|\psi_k\right\rangle, i_k = \pm 1$ and $\hat{I}\mathbf{p}\hat{I}^\dagger = -\mathbf{p}$. Hence, the transition dipole moment is non-zero only if $i_i i_f = -1$, i.e. when the two states have opposite inversion symmetry.

A similar argument can be made for other types of symmetry and so additional selection rules may arise that depend on the orientation of $\mathbf{p}$ with respect to the molecular symmetry axes. For example, if the dipole moment is oriented parallel to the two-fold rotation axis it possesses A_u symmetry. In this case only $A_g \leftrightarrow A_u$ transitions are dipole-allowed. Conversely, transitions such as $A_g \leftrightarrow B_u$ would require a dipole moment with B_u symmetry oriented perpendicular to the rotation axis.

Just as for the spin selection rules described above, transitions are never truly dipole-forbidden. Molecular geometries do not in practice precisely obey the rules of group theory and so wavefunctions do not possess perfect symmetries. Furthermore, as we shall see in Section 2.4.3, 'dark' electronic states can couple to symmetry-breaking vibrational modes. The resulting wavefunction distortion means that radiative transitions can become weakly-allowed. Nevertheless, the symmetry- and spin-based selection rules outlined above provide an important starting point for understanding the likelihood of different radiative transitions.

2.3.3 Vibrations

Whilst the electronic dipole term μ_{if}^e is principally responsible for the energy and overall strength of spin-allowed radiative transitions, it is the vibrational component $\langle\chi_{i,\nu}|\chi_{f,\nu'}\rangle$ that modifies the shape of the resulting absorption and emission spectra. To describe this effect, we turn to the Franck-Condon principle which is based around the Born-Oppenheimer approximation.

Before we continue however, it will be useful to recast nuclear motion into a new coordinate system. Thus far, we have described the electronic and nuclear wavefunctions in terms of $\mathbf{R}$, the positions of the nuclei. A much more convenient coordinate system is that of *normal coordinates*, $\mathbf{Q}_k$ (recall that k labels the electronic state). For each vibrational mode α of the molecule, all the nuclei oscillate at the same frequency ω_α, though with amplitudes weighted by their masses. The normal vibrational mode description is useful because at allows us to transform the nuclear Hamiltonian (see for example Equation 2.25) from

$$H_k(\mathbf{R}) = \sum_\alpha \frac{\mathbf{P}_\alpha^2}{2M_\alpha} + E_k(\mathbf{R}), \tag{2.30}$$

where $E_k(\mathbf{R})$ is the nuclear potential, or adiabatic potential energy surface, into

$$H_k(\mathbf{Q}_k) = \frac{1}{2}\sum_{\alpha}\left(\mathbf{P}_{\alpha}^2 + \omega_{k,\alpha}^2\mathbf{Q}_{k,\alpha}^2\right). \tag{2.31}$$

provided that the nuclear motions are small (see Appendix C). We recognise Equation 2.31 as the Hamiltonian of a quantum harmonic oscillator, allowing us to use the well known vibrational energy levels

$$E_{k,\alpha}^{\nu} = \left(\nu + \frac{1}{2}\right)\hbar\omega_{k,\alpha} \tag{2.32}$$

and wavefunctions (given in Appendix C) in our analysis. We will make one final simplification, which is to consider only a single 'effective' vibrational mode Q, assumed to be the same for the ground and excited states. Of course in reality the potential energy surfaces are complicated multidimensional functions of many different vibrational modes. Fortunately, for most π-conjugated molecules radiative transitions are dominantly coupled to the symmetric vinyl stretching mode of energy $\hbar\omega_0 \sim 0.18\,\mathrm{eV}$[61], so this is usually a good approximation.

Figure 2.5 shows harmonic potential energy surfaces and associated vibrational wavefunctions for the ground and excited states. In general, the equilibrium geometry of the excited state will be displaced from that of the ground state by some ΔQ. We now consider the processes of photon absorption and emission within this picture, remembering that under the Born-Oppenheimer approximation, electron dynamics are much faster than nuclear motion.

Since $\hbar\omega_0 \gg k_B T$, the molecule begins in the $\nu = 0$ vibrational level of the ground state. Absorption of a photon causes a 'vertical' transition whereby the electrons rearrange into the new excited state configuration whilst the nuclei remain stationary. The offset between the ground and excited state minima means that transitions occur into the various vibrational levels $\nu' = 0, 1, 2, 3, \ldots$ of the excited state. The lifetime of the excited state is typically on the order of nanoseconds, much greater than the femtosecond timescale of nuclear motion and so the molecule relaxes rapidly to the $\nu' = 0$ vibrational level of the excited state. This relaxation is known is intramolecular vibrational energy redistribution (IVR): the excess energy is quickly distributed among various vibrational modes and dissipated as heat[62]. Subsequent vertical transitions to the vibrational levels of the ground state result in fluorescence emission. Finally, further IVR returns the molecule to its equilibrium ground state configuration.

From this description, we see that the energies of the vibronic (vibrational

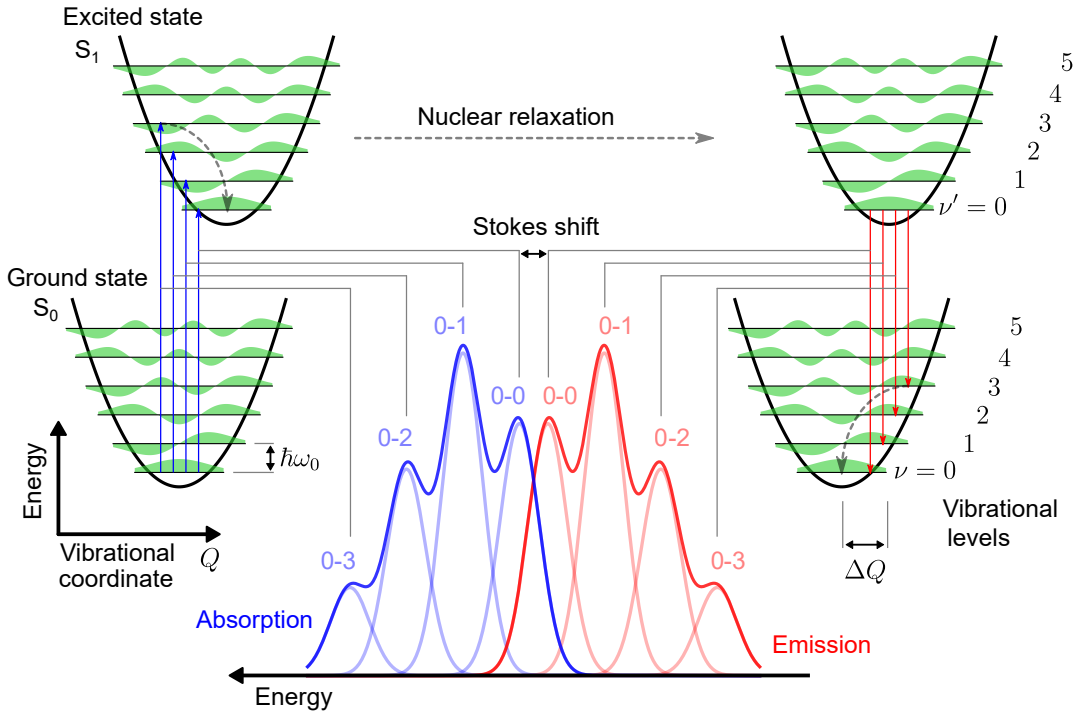

Figure 2.5 | Franck-Condon principle. Photon absorption (blue arrows) causes a vertical vibronic transition from the ground state to excited vibrational levels of the excited state. Rapid vibrational cooling occurs (grey dashed arrow) before the molecule returns to the ground state by fluorescence emission (red arrows). The intensities of the transitions are related to the overlap between the vibrational wavefunctions involved, giving rise to the characteristic vibronic progression of peaks observed in absorption spectra and mirrored in fluorescence spectra. Though not predicted by the Franck-Condon principle, the fluorescence spectrum is generally redshifted from the absorption spectrum by the Stokes shift, which we discuss below.

and electronic) transitions involved in absorption and fluorescence are given by

$$\begin{aligned} E^{abs}_{0-\nu'} &= E_{0-0} + \nu'\hbar\omega_0 \\ E^{fl}_{0-\nu} &= E_{0-0} - \nu\hbar\omega_0, \end{aligned} \tag{2.33}$$

where E_{0-0} is the energy of the vibrationless 0-0 transition, while their intensities are proportional to the so-called Franck-Condon factors, given by the square of the overlap between the vibrational wavefunctions. We are assuming the same harmonic potential for both the ground and excited state, in which case the Franck-Condon factors can be evaluated as[56]

$$|\langle\chi_{i,0}|\chi_{f,\nu}\rangle|^2 = \left|\int \phi_0(Q)\phi_\nu(Q-\Delta Q)dQ\right|^2 = \frac{S^\nu e^{-S}}{\nu!}, \tag{2.34}$$

where $\phi_\nu(Q)$ represent quantum harmonic oscillator wavefunctions and the

Huang-Rhys parameter S is given by

$$S = \frac{M\omega_0}{2\hbar}|\Delta Q|^2. \tag{2.35}$$

In summary, the Franck-Condon principle predicts that molecular absorption spectra consist of a vibronic progression of peaks, separated by the energy $\hbar\omega_0$ of the coupled effective vibrational mode and with relative intensities that follow a Poisson distribution. The Huang-Rhys parameter is related to the number of vibrational quanta associated with the dominant peak in the progression. The fluorescence spectrum is predicted to be a mirror image of the absorption spectrum, reflected about the 0-0 transition energy.

Before concluding this section, we discuss the predictions of the Franck-Condon principle in the context of absorption and emission spectra of real molecules. Firstly, the above description suggests that we should observe discrete sharp lines at the energies of the vibronic transitions. Experimentally however, we measure spectra much more like those depicted in Figure 2.5 where the peaks are significantly broadened in energy. Spectral broadening has a variety of causes which we discuss in the following.

Lifetime broadening reflects the range in energy associated with a short excited state lifetime and gives rise to a Lorentzian lineshape (the Fourier transform of an exponential decay is Lorentzian). In molecular systems however, Lorentzian lineshapes are typically observed only in the absence of other types of broadening, for example at very low temperature[63].

Spectra are further broadened by dynamic disorder, which arises because the electronic transition couples to low-energy vibrational modes which typically have high Huang-Rhys parameters[64]. The Poisson distribution (Equation 2.34) tends towards a Gaussian in this limit, with the peak of the Gaussian offset from the true 0-0 energy. Dynamic disorder therefore gives rise to Gaussian broadening of the vibronic transitions and also results in a Stokes shift, since the apparent peaks of the absorption and emission 0-0 lineshapes are oppositely offset from true 0-0 energy.

Dynamic disorder can also be thought of as a kind of time-dependent static disorder. At each snapshot in time, low energy vibrational modes are active that result in a distribution of instantaneously static site energies across an ensemble of molecules[65]. These site energies change with time, but the distribution is retained. True static disorder, which also gives rise to Gaussian lineshapes, can arise when different molecules in a sample experience different environments and hence different site energies. For example, molecules in solution can have

slightly differing solvent interactions[49] while in solid materials, local disordering causes static variation in site energies[59].

Finally, we note that the mirror symmetry between absorption and emission predicted by Franck-Condon theory is often distorted in reality. For isolated molecules in solution, one common cause is differences in the shapes of the ground and excited state potential energy surfaces and corresponding changes in vibrational mode energies between the ground and excited states[66]. Differences can also arise if the emissive excited state is not the same one populated by absorption from the ground state. In the solid state (Section 2.5), intermolecular interactions, such as exciton migration (Section 2.5.4), aggregate formation (Section 2.5.1) and excimer formation (Section 2.5.2) can all result in asymmetric absorption and emission spectra.

We conclude our discussion of absorption and fluorescence by incorporating the Franck-Condon factors (Equation 2.34), vibronic transition energies (Equation 2.33) and the spectral broadening discussed above into expressions that approximate the experimentally measured shapes of absorption and fluorescence spectra. These can be expressed as

$$\alpha(\hbar\omega) \propto (n\hbar\omega) \sum_{\nu} \frac{S^{\nu} e^{-S}}{\nu!} \Gamma[\hbar\omega - (E_{0-0} + \nu\hbar\omega_0)] \tag{2.36}$$

for the absorption and

$$I(\hbar\omega) \propto (n\hbar\omega)^3 \sum_{\nu} \frac{S^{\nu} e^{-S}}{\nu!} \Gamma[\hbar\omega - (E_{0-0} - \nu\hbar\omega_0)] \tag{2.37}$$

for fluorescence, where Γ describes the spectral broadening and is, in the most general case, a convolution of Lorentzian and Gaussian lineshapes. The preceding factors $(n\hbar\omega)$ and $(n\hbar\omega)^3$, where n denotes the refractive index, describe the influence of the photon density of states of the surrounding environment on the absorbing or emitting molecule[67].

2.4 Transitions between electronic states

We have seen how the Born-Oppenheimer approximation allows us to describe the intensity of radiative transitions and predict the shapes of the resulting optical spectra. Yet this represents only a small part of the photophysics of organic molecules. In the following we introduce several additional kinds of transition involving behaviour that goes beyond the Born-Oppenheimer approximation.

2.4.1 Non-radiative transitions

We discussed the Franck-Condon principle in terms of absorption and emission of photons between the ground state S_0 and first excited state S_1. For excitation of a sufficiently short wavelength, photon absorption into higher-lying singlet states, S_n, also occurs . Despite being allowed, radiative $S_n \rightarrow S_0$ transitions are generally outcompeted by extremely rapid, non-radiative decay to the lowest-energy excited state of the singlet manifold, S_1, from which fluorescence occurs (provided that it is dipole-allowed). This is embodied in the semi-empirical Kasha-Vavilov rule, which states that "the emitting level of a given multiplicity is the lowest excited level of that multiplicity" [68] and that "the quantum yield of luminescence is independent of the wavelength of exciting radiation" [69].

Non-radiative transitions between the initially excited state and other states of the same multiplicity are called internal conversions. Figure 2.6 illustrates the processes involved. Following IVR, the molecule occupies the $\nu' = 0$ vibrational level of the higher-lying potential energy surface. Next, a horizontal transition into the upper vibrational levels of the lower-lying potential energy surface occurs, followed by rapid IVR and relaxation to lower potential energy minimum.

IVR is extremely rapid because high up on the potential energy surface, the vibrational levels are very closely spaced. As a result vibrational energy is rapidly and efficiently distributed among many different modes. Instead, the rate determining step of an internal conversion is usually the horizontal transition[59], during which nuclear motion alone causes a change in the electronic state. This is nonadiabatic behaviour representing a breakdown of the Born-Oppenheimer approximation and is driven by the nuclear kinetic energy terms that we neglected in Equation 2.25. The transition rate is given by a modified version of the Fermi Golden Rule[59,70],

$$k_{nr} = \frac{2\pi}{\hbar}\rho J^2 F, \tag{2.38}$$

where the energy of interaction J between the initial and final states is related to the nonadiabatic coupling defined in Appendix B. The Franck-Condon factor F describing the overlap between the vibrational wavefunctions is given by

$$F = \sum_P \hat{P}\left(\prod_\alpha |\,\langle \chi^{\nu}_{1,\alpha} | \chi^{0}_{2,\alpha}\rangle\,|^2\right). \tag{2.39}$$

The operator $\sum_P \hat{P}$ permutes the vibrational quanta among the different modes

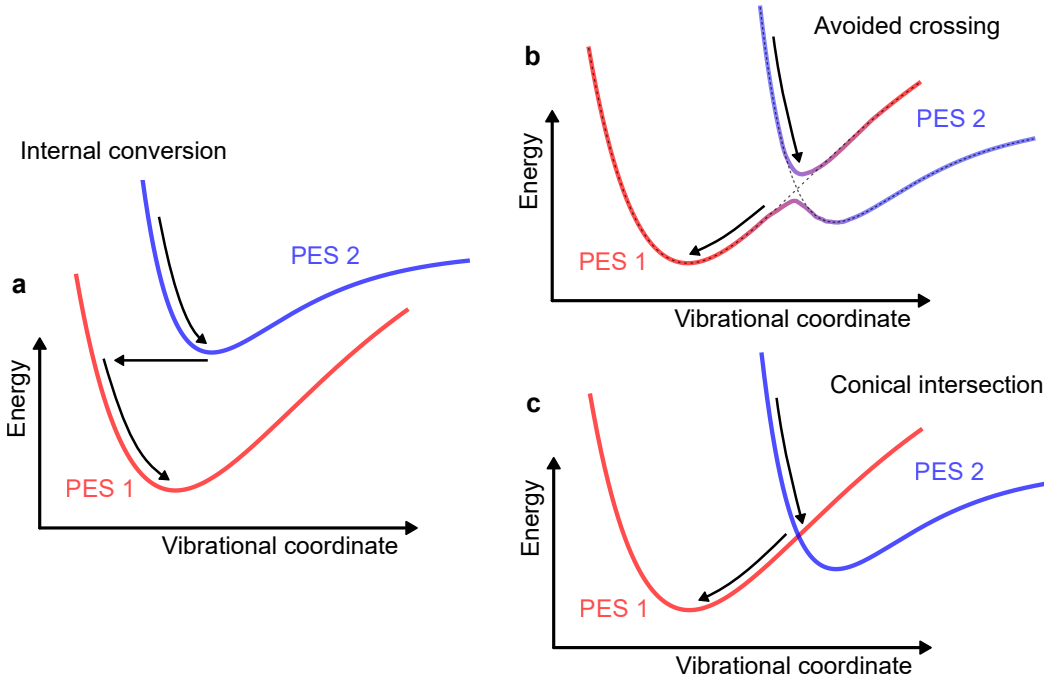

Figure 2.6 | Non-radiative transitions. **a**, Internal conversion between potential energy surfaces. Vibrational relaxation to the bottom of the upper potential energy surface is followed by a non-adiabatic transition into the continuum of closely spaced vibrational levels of the lower potential energy surface. Further vibrational relaxation occurs as the molecule reaches the new equilibrium geometry. **b**, When two potential energy surfaces are very close in energy, mixing can occur leading to an avoided crossing. **c**, Conical intersection between potential energy surfaces. When two potential energy surfaces intersect, electronic energy can be funnelled extremely efficiently from one to the other on the timescales of vibrational relaxation.

α and $|\chi_{i,\alpha}^{\nu}\rangle$ are vibrational wavefunctions on the i^{th} potential energy surface possessing ν quanta of vibrational energy in the α^{th} mode. Again, the higher-lying vibrational levels populated by the horizontal transition are very closely spaced, leading to rapid distribution of the energy across all of the different vibrational states. This causes an exponential energy dependence of the Franck-Condon factor[70] and results in the well-known energy gap law for non-radiative decay[59]:

$$k_{nr} \propto \exp\left(-\frac{\gamma \Delta E}{\hbar \omega_0}\right). \tag{2.40}$$

Here γ is a constant determined by molecular parameters, in particular the force constants and displacements of the vibrational modes, ΔE is the energy gap between the electronic states and ω_0 is the highest available vibrational frequency that couples to the electronic states which, as we have noted before, is usually the symmetric vinyl stretching mode at around 0.18 eV[61].

We have discussed internal conversions in terms of rapid relaxation to the

equilibrium geometry of the lowest excited state of a given multiplicity. Such internal conversion among excited states typically occurs on timescales of femtoseconds to picoseconds[49], owing to the large density of available vibrational states and small energy gaps. Internal conversions can also occur from the lowest excited state to the ground state. In the case of singlet states with energies in the visible spectral range, fluorescence usually outcompetes non-radiative decay. The radiative decay channel is dipole-allowed with fluorescence rates on the order of nanoseconds, whilst the non-radiative rate is suppressed by the large energy gap to the ground state.

Avoided crossings and conical intersections

Recalling that the Born-Oppenheimer approximation is only valid for potential energy surfaces that are well-separated in energy, we might wonder what happens when two surfaces meet. When two potential energy surfaces become very close in energy, the two states can mix, leading to an avoided crossing as shown in Figure 2.6b. The Born-Oppenheimer approximation can break down in the vicinity of an avoided crossing, allowing electronic energy to move from the upper to the lower potential energy surface.

The situation when the two surfaces truly intersect is depicted in Figure 2.6c. In the immediate vicinity of the intersection the potential energy varies linearly with vibrational coordinate, hence the name conical intersection[71]. At the specific geometry of the intersection point, the two surfaces are non-adiabatically coupled. Thus conical intersections can be considered as a special case of internal conversion, where the final state is a single degenerate electronic state rather than a continuum of vibrational ones. Since no nuclear motion is needed to change the electronic state, transitions through conical intersections occur on the timescale of vibrational relaxation, typically tens of femtoseconds. Conical intersections are therefore extremely efficient at funnelling electronic energy between potential energy surfaces.

2.4.2 Spin-orbit coupling

In Section 2.3.1 we saw that within the Born-Oppenheimer approximation transitions between singlet and triplet states are forbidden by spin selection rules. In the following, we describe how a perturbation known as spin-orbit coupling can enable transitions from excited singlet states into the triplet manifold, as well as allowing radiative decay of the first excited triplet state.

Spin is a form of intrinsic angular momentum. Thus the spin selection rule that forbids interconversion between singlets and triplets is a consequence of the

conservation of angular momentum. If the orbital and spin angular momenta are coupled however, the change in angular momentum caused by the change in spin can be balanced by a change in orbital angular momentum. This is termed spin-orbit coupling, and is governed by the spin-orbit Hamiltonian[59,72]

$$H_{SO} = \alpha_{fs}^2 \sum_{\alpha,i} \frac{Z_\alpha}{|\mathbf{r}_\alpha - \mathbf{r}_i|^3} \mathbf{L}_i \cdot \mathbf{S}_i \propto \frac{Z^4}{n^3(l+1)(l+\frac{1}{2})l}, \tag{2.41}$$

where α_{fs} is the fine structure constant, Z_α is effective charge of the α^{th} nucleus, $\mathbf{L}_i$ and $\mathbf{S}_i$ are the angular momentum and spin operators of the i^{th} electron and $|\mathbf{r}_\alpha - \mathbf{r}_i|$ is the distance between the α^{th} nucleus and i^{th} electron. On the right hand side, n and l are quantum numbers. From Equation 2.41, we see that the spin-orbit coupling becomes very large in the presence of heavy atoms, and when electrons become close to the nucleus (small n and l).

The matrix element governing spin-orbit mediated transitions between singlets and triplets can be determined by treating H_{SO} as a perturbation and expanding to first order in vibrational coordinate[73]:

$$\begin{aligned} \langle \Psi_{i,\nu} | \, H_{SO} \, | \Psi_{f,\nu'} \rangle = & \langle \psi_i | \, H_{SO} \, | \psi_f \rangle \\ & + \sum_\alpha \left(\frac{\partial \langle \psi_i | \, H_{SO} \, | \psi_f \rangle}{\partial Q_\alpha} \right)_{Q_0} \langle \chi_{i,\nu} | \, Q_\alpha \, | \chi_{f,\nu'} \rangle \, . \end{aligned} \tag{2.42}$$

The first (zero-order) term on the right hand side corresponds to direct spin-orbit coupling whilst the second (first-order) is called vibronic spin-orbit coupling. Thus molecules that do not possess heavy atoms can still undergo singlet-triplet transitions provided that vibrational modes capable of perturbing the direct spin-orbit term exist.

Intersystem crossing

The transition from S_1 to T_1 is called intersystem crossing. Treating the spin-orbit Hamiltonian as a perturbation, and using Equation A.21, we can write the intersystem crossing rate as a modified Fermi Golden Rule:

$$k_{isc} = \frac{2\pi}{\hbar} | \langle \phi_T | \, H_{SO} \, | \phi_S \rangle |^2 [FCWD]. \tag{2.43}$$

In this expression, ϕ_S and ϕ_T are the spatial wavefunctions of the singlet and triplet state respectively and $[FCWD]$ is the Franck-Condon weighted density of states, i.e. the density of vibrational states in the triplet manifold multiplied by the Franck-Condon overlap factor (Equation 2.39).

In Section 2.4.1, we showed that the Franck-Condon factor depends exponentially on the energy gap between the initial and final states. Thus intersystem crossing between S_1 to T_1 is slow in most organic molecules owing to the significant exchange energy.

On the other hand, intersystem crossing into approximately degenerate higher-lying triplet states, followed by rapid internal conversion to T_1, can be very efficient. This will be an important consideration when we investigate the spin statistics of triplet-triplet annihilation upconversion in Chapter 7. For most hydrocarbons, the spin-orbit coupling is sufficiently weak, and the energy gaps large enough, that intersystem crossing is still fairly slow, and doesn't outcompete radiative decay[59]. For molecules containing heavy atoms however, such as transition metal complexes, intersystem crossing can be extremely rapid and efficient, occurring on a picosecond timescale[59].

Phosphorescence

Spin-orbit coupling also governs the oscillator strength of the radiative $T_1 \rightarrow S_0$ transition known as phosphorescence. To see this, we again treat the spin-orbit Hamiltonian as a perturbation, allowing us to write the perturbed triplet wavefunction as[59]

$$|T_1'\rangle = |T_1\rangle + \sum_k \frac{\langle S_k| H_{SO} |T_1\rangle}{E(T_1) - E(S_k)} |S_k\rangle \,, \tag{2.44}$$

where $|S_k\rangle$ are the singlet wavefunctions. The $T_1 \rightarrow S_0$ transition therefore obtains oscillator strength from the allowed transitions between the ground state and excited singlet states that are mixed into the triplet wavefunction. Just as for intersystem crossing, the rate of phosphorescence can become significant when the exchange energy is small and spin-orbit coupling is strong. In most cases however, emission through phosphorescence is weak since it is outcompeted by non-radiative decay, especially for low-energy triplet states.

2.4.3 Herzberg-Teller intensity borrowing

Spin-orbit coupling provides a mechanism for spin-forbidden transitions to acquire oscillator strength. Analogously, mechanisms exist that enable dipole-forbidden transitions to do the same. In this section, we discuss one such mechanism, Herzberg-Teller intensity borrowing. This mechanism is of particular interest since it is thought to enable the nominally dark triplet-pair state ^{1}(TT), studied in detail in Chapter 4, to emit light[74].

In Section 2.3.2 we saw that an electronic transition is dipole-forbidden when the electronic dipole matrix element is equal to zero and that this depends on the respective symmetry of the initial and final wavefunctions. Consider a molecule in an adiabatic Born-Oppenheimer excited state

$$|\Psi_{n,\nu'}\rangle = |\psi_n\rangle\,|\chi_{n,\nu'}\rangle \tag{2.45}$$

that is forbidden from transitioning to the ground state by its symmetry and suppose that the electronic wavefunction $|\psi_n\rangle$ is coupled to some vibrational mode Q_α. As the molecule vibrates, the shape and therefore the symmetry of the electronic wavefunction changes. If the mode Q_α has appropriate symmetry, the electronic wavefunction can change in such a way as to break the symmetry barrier for radiative transitions to the ground state. The mathematical treatment is exactly analogous to that for vibronic spin-orbit coupling (Equation 2.42). Treating the vibration as a perturbation, we can expand the dipole matrix element given by

$$\mu_{mn,\nu\nu'} = \langle\Psi_{m,\nu}|\,\mathbf{p}\cdot\hat{\epsilon}\,|\Psi_{n,\nu'}\rangle = \langle\chi_{m,\nu}|\,\mu^e_{mn}\,|\chi_{n,\nu'}\rangle\,, \tag{2.46}$$

where μ^e_{mn} is the electronic dipole matrix element defined in Equation 2.28, about some equilibrium geometry Q_0 to give:

$$\mu_{mn,\nu\nu'} = \mu^e_{mn}(Q_0)\,\langle\chi_{m,\nu}|\chi_{n,\nu'}\rangle + \sum_\alpha \left(\frac{\partial\mu^e_{mn}}{\partial Q_\alpha}\right)_{Q_0} \langle\chi_{m,\nu}|\,Q_\alpha\,|\chi_{n,\nu'}\rangle + \ldots \tag{2.47}$$

The transition from $|\Psi_{n,\nu'}\rangle$ to the ground state $|\Psi_{m,\nu}\rangle$ is formally dipole-forbidden if $\mu^e_{mn}(Q_0) = 0$. Using results from perturbation theory, we can write the dipole matrix element to first order (see Appendix D) as[75,76]

$$\mu_{mn,\nu\nu'} = \sum_\alpha \sum_{i\neq n} \mu^e_{mi}(Q_0) \left(\frac{\langle\psi_i|\,\frac{\partial H_{el-nuc}}{\partial Q_\alpha}\,|\psi_n\rangle}{E_i - E_n}\right)_{Q_0} \langle\chi_{m,\nu}|\,Q_\alpha\,|\chi_{n,\nu'}\rangle\,. \tag{2.48}$$

From Equation 2.48 we find that in order for the dipole-forbidden excited state to decay radiatively through this vibronic coupling mechanism, there must exist another excited electronic state $|\psi_i\rangle$ that is dipole-allowed i.e. $\mu^e_{mi}(Q_0) \neq 0$ and energetically close by. The dark state effectively borrows oscillator strength from this nearby bright state through a symmetry-breaking vibrational mode, hence this mechanism is termed Herzberg-Teller intensity borrowing.

Finally, we note that for harmonic displacements and low temperature ($k_BT \ll \hbar\omega_\alpha$), the factor $\langle\chi_{m,\nu}|\,Q_\alpha\,|\chi_{n,\nu'}\rangle$ vanishes for $\nu = \nu' = 0$[75,76]. Thus we

expect the vibrationless 0-0 band to be suppressed for states that emit light through Herzberg-Teller intensity borrowing.

To conclude this section on transitions between electronic states, we summarise the basic photophysics of organic molecules in Figure 2.7.

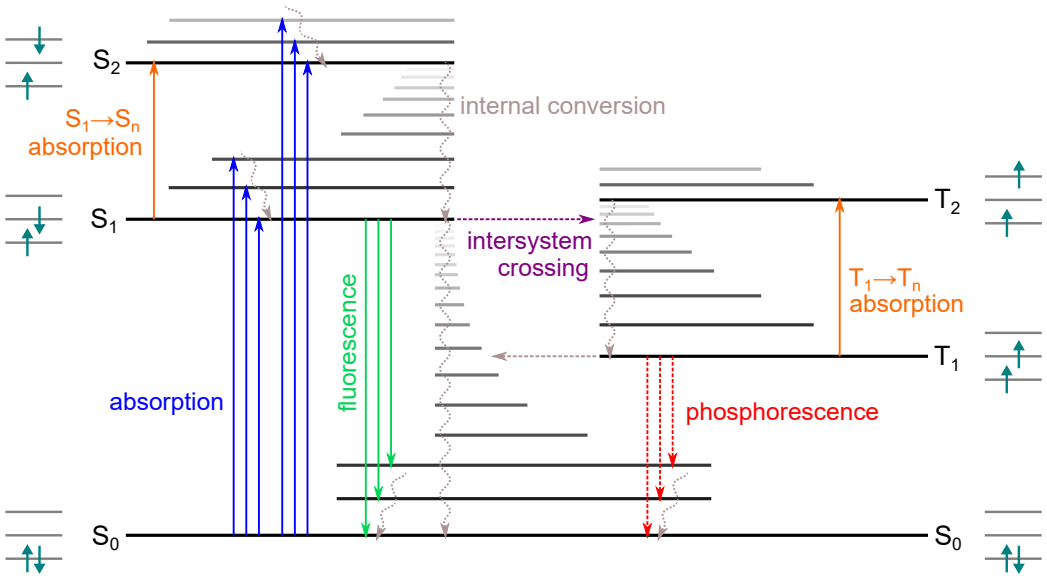

Figure 2.7 | Basic photophysics of organic molecules. Absorption (blue arrows) can occur into any state in the singlet manifold. Direct absorption into the triplet manifold is weakly allowed through spin-orbit coupling but is generally insignificant. Absorption into higher-lying singlet states results in rapid internal conversion (grey wavy arrows) back to S_1. S_1 can decay back to the ground state radiatively (fluorescence, green arrows) or non-radiatively through internal conversion. Alternatively, spin-orbit coupling may facilitate a transition into vibrational states of the triplet manifold (intersystem crossing, purple arrow). T_1 states may decay radiatively to the ground state (phosphorescence, red arrows), though this weakly allowed process is typically outcompeted by non-radiative decay. Once S_1 and T_1 states become populated, further absorption into higher lying states within the same manifold is possible (orange arrows); these excited state absorption transitions are probed in transient absorption spectroscopy.

2.5 Organic molecules in the solid state

Our discussion so far has been limited to the photophysics of isolated molecules such a those found in dilute solution. In the solid state however, where molecules pack tightly together, phenomena such as charge and energy transport can occur, turning organic molecules into organic semiconductors that can be used in practical optoelectronic devices such as OLEDs and solar cells. This thesis explores singlet fission, a photophysical process which requires pairs of closely-spaced chromophores. An understanding of the interactions between nearby

molecules, and how these manifest themselves in optical spectra, is therefore needed before introducing singlet fission.

2.5.1 Molecular aggregates

The simplest description of the changes in optical spectra due to a pair of interacting molecules (a dimer) was developed by Kasha in the 1960s[77]. If a molecule is in an excited state $|\psi^*\rangle$, and is next to an identical molecule in the ground state $|\psi\rangle$, the overall wavefunction of the dimer is given by[77]

$$|\psi_d^{\pm}\rangle = \frac{1}{\sqrt{2}} \left(|\psi_m^*\rangle \, |\psi_n\rangle \pm |\psi_m\rangle \, |\psi_n^*\rangle \right), \tag{2.49}$$

where m and n label the two molecules. The Hamiltonian of the dimer can be expressed as

$$H_d = H_m + H_n + V_{mn}, \tag{2.50}$$

where H_m and H_n are the Hamiltonians for isolated molecules and V_{mn} describes the interaction between them. V_{mn} contains both exchange interactions and Coulomb interactions, though we will assume here that the intermolecular distance is sufficiently great that the exchange terms are negligible. Inserting 2.49 and 2.50 into Schrödinger's equation and treating the molecules as point dipoles, we find that the energies of the excited states of the dimer, relative to the ground state, are given by[77]

$$E_d^{\pm} = E^* + \Delta D \pm \kappa_{mn} J, \tag{2.51}$$

where E^* is the excited state energy of an isolated molecule, ΔD is the difference in the Van-der-Waals interaction between the ground state and excited state dimer, J is related to the strength of the transition dipole moment μ of an isolated molecule and the intermolecular distance R by

$$J = \frac{\mu^2}{R^3} \tag{2.52}$$

and κ_{mn} is an orientational factor that depends on the relative alignment of the two molecular dipoles (unit vectors $\hat{\mathbf{r}}_m$ and $\hat{\mathbf{r}}_n$):

$$\kappa_{mn} = \hat{\mathbf{r}}_m \cdot \hat{\mathbf{r}}_n - 3(\hat{\mathbf{r}}_m \cdot \hat{\mathbf{R}})(\hat{\mathbf{r}}_n \cdot \hat{\mathbf{R}}). \tag{2.53}$$

We see from Equation 2.51 that the resonant Coulomb interaction stabilises the excited state, though the amount of oscillator strength in that stabilised

state depends strongly on the relative orientation of the molecules in the dimer. Figure 2.8 illustrates the dramatic effect of this orientational factor on the radiative transitions of molecular dimers for three different cases.

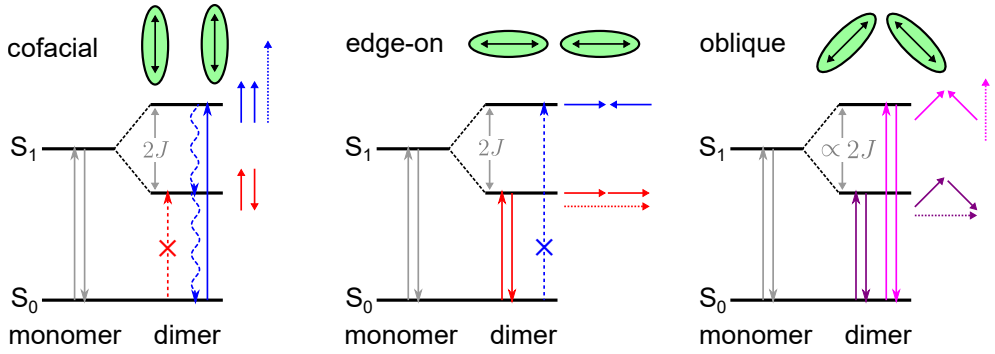

Figure 2.8 | Molecular aggregates. The effect of intermolecular dipole-dipole interactions on the optical properties of aggregates within the framework of the Kasha model. Three cases are shown: cofacial molecules (H-aggregates) characterised by blueshifted spectra and weak emission, edge-on molecules (J-aggregates) that exhibit redshifted spectra and strong emission and the more general case of oblique orientation, which have mixed H and J character.

For a pair of cofacial molecules, the lower of the excited states occurs when the dipole moments of the constituent molecules are antiparallel. Thus the net dipole moment is zero and radiative transitions to this state are forbidden. In contrast, the dipoles are parallel for the higher lying state, giving it significant oscillator strength. Such a cofacial arrangement is known as an H-aggregate, and is characterised by a blueshift in the optical spectra relative to the monomer, though this is often counteracted by redshifts associated with Van-der-Waals interactions among neighbouring molecules. Furthermore, H-aggregates typically show weak fluorescence, since radiative decay from the bright higher-lying state is outcompeted by rapid internal conversion to the dark lower-lying state. If the non-radiative rates are also low however, appreciable emission can be observed.

The situation is reversed in the case of edge-on or head-to-tail molecules. Now the lower-energy state has parallel dipoles and so is bright, whilst the higher-energy state is dark. J-aggregates are therefore characterised by strong redshifted absorption and fluorescence. These two extreme cases are rarely encountered in reality; more often molecules will have some oblique orientation to one another, meaning that oscillator strength is shared to some degree between the two excited states.

Intermolecular interactions beyond this simple model have been extensively studied by Spano and colleagues, including the effects of aggregate size, intramolecular and intermolecular vibrations, temperature and charge transfer

states[61,78–85]. Within this framework, analysis of the absorption and emission spectra of molecular aggregates can yield a wealth of information, for example the interaction strength, extent of exciton delocalisation[82] and charge-transfer character of excited states[86]. Though the details are beyond the scope of this thesis, this work highlights the profound influence that intermolecular interactions have on the optical properties of molecular aggregates.

2.5.2 Excimer formation

In addition to altering the absorption and fluorescence spectra of the monomer, the presence of neighbouring molecules can lead to new types of excited states with distinct spectral signatures. One important example of this is the excited state dimer, or excimer.

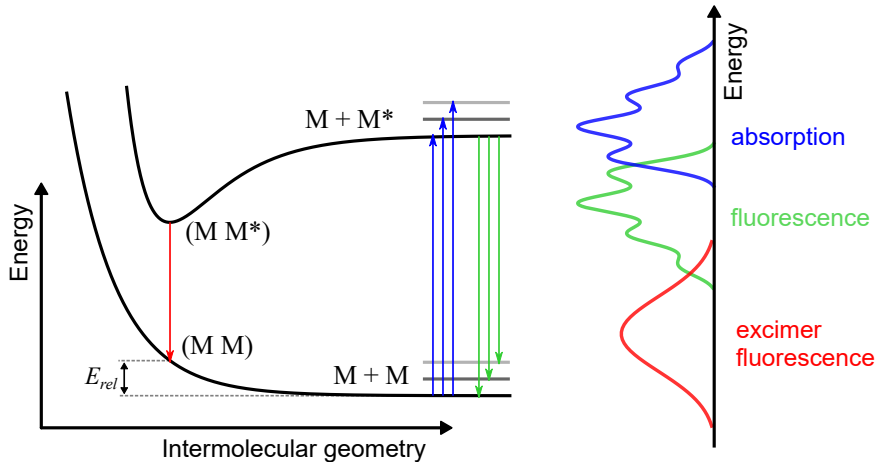

Figure 2.9 | Excimer formation. The ground and excited state adiabatic potential energy surfaces of a dimer are shown as a function of intermolecular geometry (distance along some intermolecular coordinate). Stabilisation of the excited state can occur at some geometry for which the ground state is repulsive, leading to an excimer that can exist only in the excited state. It has no absorption signature, but has a characteristic redshifted emission spectrum that is broad and unstructured.

Figure 2.9 illustrates the process of excimer formation by considering the adiabatic potential energy surfaces of the ground and excited states of a dimer. Once one of the molecules in the dimer has absorbed a photon (blue arrows), the resulting excited state may be able to stabilise further by physically changing the intermolecular geometry. This additional stabilisation may come from the resonant Coulomb interaction described above; a further contribution can come from charge-transfer character, which results in a Coulomb attraction between an electron on one molecule and a hole on the other. At this new, stabilised intermolecular geometry the ground state is now repulsive. As a result, excimers

are characterised by a redshifted, broad and featureless emission, but have no signature in absorption.

The distinction between excimers and charge-transfer (CT) excitons is not always clear. For example, both types of excited state typically exhibit redshifted, broad, featureless photoluminescence. Both are stabilisations of the excited state and as discussed above, excimers often possess CT character and could be considered a special case of the CT state. We suggest that the distinguishing feature of an excimer is the repulsive ground state at the stabilised geometry and hence the lack of absorption signature. In general, CT exciton signatures can be present in both absorption and fluorescence spectra.

2.5.3 Excitation energy transfer

Interactions between nearby molecules can also allow energy to be transferred from one molecule to another. In the solid state for example, this excitation energy transfer enables excitons to diffuse through materials by hopping from site to site. We have seen how radiative and non-radiative transitions between electronic states can be described through Fermi's Golden Rule (Sections 2.3 and 2.4, Appendix A). In much the same way, we can write the rate of exciton transfer from an excited donor molecule D and a ground state acceptor molecule A as

$$k_{DA} = \frac{2\pi}{\hbar} |\langle \Psi_{A,f}| H_{DA} |\Psi_{D,i}\rangle|^2 \rho_A(E_f)\delta(E_f - E_i), \tag{2.54}$$

where $|\Psi_{D,i}\rangle$ denotes the wavefunction of the donor (initial state), $|\Psi_{A,f}\rangle$ is that of the acceptor (final state), $\rho_A(E_f)$ is the density of states of the acceptor and the delta function ensures energy conservation. The Hamiltonian describing the interactions between the two molecules, H_{DA}, generally comprises two parts: a Coulomb interaction (Equation 2.17) and an exchange interaction (Equation 2.18). These two types of interaction give rise to two different mechanisms of energy transfer.

Förster transfer

We begin by considering the Coulomb interaction, first considered by Förster in 1948[87]. In the simplest case, we can again treat the donor and acceptor molecules as point dipoles, allowing us to write the transfer rate as[56]

$$k_{DA} = \frac{2\pi}{\hbar} \frac{\kappa_{DA}^2 |\mu_D|^2 |\mu_A|^2}{R_{DA}^6} \int_{-\infty}^{\infty} \delta(E - \hbar\omega)\delta(\hbar\omega - E) d(\hbar\omega), \tag{2.55}$$

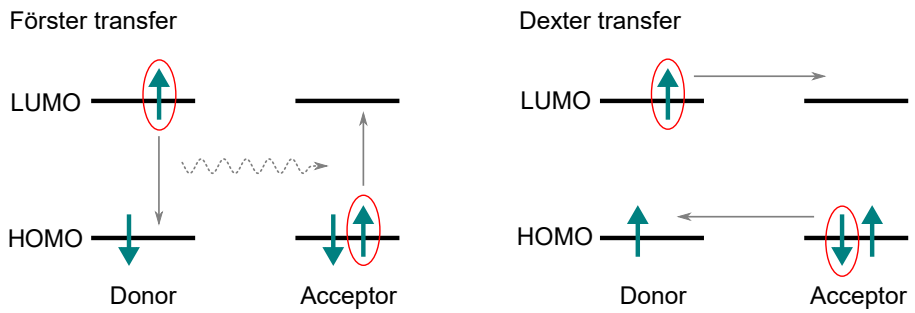

Figure 2.10 | Energy transfer mechanisms. Förster transfer is a resonant dipole interaction involving the simultaneous emission and absorption of energy by the donor and acceptor respectively. It can also be thought of as the exchange of a virtual photon. In contrast Dexter transfer involves the direct exchange of electrons between donor and acceptor.

where $E = E_f = E_i$ and we have used equations 2.52 and 2.53 and a delta function identity. Writing the rate in this form highlights several key elements of Förster transfer.

Firstly, the rate is proportional to the squares of the electronic dipole matrix elements of the donor and acceptor. Thus Förster transfer can only occur if the excited states involved have allowed radiative transitions to the ground state, or in other words, can absorb and emit photons. Secondly, the delta functions provide a simple interpretation of the underlying mechanism. The first delta function corresponds to the absorption of a photon by the acceptor and the second to emission of a photon by the donor. Förster transfer can therefore be thought of as a dipole resonance between donor and acceptor, in which energy is simultaneously emitted by the donor and absorbed by the acceptor. As such, this transfer mechanism is often called Förster resonance energy transfer, or FRET. It is important to note that no physical photon is involved; instead FRET can be thought of as the exchange of a *virtual* photon. This is illustrated in Figure 2.10.

Since FRET involves the simultaneous absorption and emission of energy through a dipole interaction, it is convenient to express the rate in terms of the emission spectrum of the donor $I_D(\omega)$ and the absorption spectra of the acceptor $\alpha_A(\omega)$[56,59]

$$k_{DA} \propto \frac{\kappa_{DA}^2}{R_{DA}^6} \int_0^\infty \frac{I_D(\omega)\alpha_A(\omega)}{\omega^4} d\omega = \frac{\kappa_{DA}^2 f_D f_A}{\omega^2 R_{DA}^6} J_{DA}, \tag{2.56}$$

where f denotes oscillator strength and J_{DA} is the spectral overlap between the normalised absorption and emission spectra. Note that J_{DA} is independent of

oscillator strength. From Equation 2.56, we see that efficient FRET requires good spectral overlap between donor and acceptor, strongly allowed radiative transitions and suitable orientation of the participating molecules. Thus singlet excitons can undergo FRET, but triplet excitons, for which the oscillator strength is very low, cannot. We also find that the FRET rate decays like R_{DA}^{-6}, where R_{DA} is the distance between donor and acceptor. It is therefore conventional to define the Förster radius R_F as the distance below which FRET is more probable than radiative decay:[49,56,87–89]

$$k_{DA} = \frac{1}{\tau_r}\left(\frac{R_F}{R_{DA}}\right)^6 \tag{2.57}$$

where τ_r is the radiative lifetime.

Dexter transfer

In contrast to singlet excitons, triplets cannot undergo FRET owing to their low oscillator strength. Instead, triplets transfer their energy through the exchange-mediated pathway, first described by Dexter in 1953[90]. Inserting the exchange interaction in place of the Coulomb interaction, we arrive at the following expression for the Dexter rate[59,88]

$$k_{DA} \propto J_{DA} \exp\left(-\frac{2R_{DA}}{L}\right), \tag{2.58}$$

where L is the effective average Bohr radius (electron-hole separation) of the donor and acceptor states, typically 0.1–0.2 nm[49,88]. Being exchange-mediated, Dexter transfer involves the simultaneous transfer of electrons between donor and acceptor (Figure 2.10) and so can only occur with an appreciable rate when there is significant wavefunction overlap. This requirement gives rise to the exponential dependence of the Dexter rate with intermolecular distance, making Dexter transfer a more short-range interaction than FRET. Whilst there is no dependence on oscillator strength, the requirement for spectral overlap is still present.

For typical molecular solids, the intermolecular distances are such that Dexter transfer is several orders of magnitude slower than FRET[91]. As a result, triplet energy transfer is much slower than singlet energy transfer.

2.5.4 Exciton diffusion and annihilation

The rate at which excitons can hop from molecule to molecule in an organic semiconductor is directly related to the macroscopic diffusivity D, which describes how fast excitation energy can be transported in a material. The diffusivity of a particular excitonic species is given by

$$D = \frac{kR^2}{2z}, \tag{2.59}$$

where k is the exciton hopping rate, $z = 1, 2, 3$ gives the dimensionality of the diffusion and since we will consider a material made up of only one type of molecule, we have dropped the donor and acceptor subscripts.

A key question when considering materials for optoelectronic devices such as solar cells is how far an exciton can migrate during its lifetime τ. This distance, known as the exciton diffusion length L_D, is related to both the diffusivity and lifetime of excitons through

$$L_D = \sqrt{2zD\tau}. \tag{2.60}$$

Singlet excitons diffuse rapidly through FRET. However, we saw in section 2.3.1 that the same oscillator strength that enables rapid energy transfer also results in fast radiative decay, giving singlet excitons a relatively short lifetime on the order of a nanosecond[49,89,91]. As a result, singlet excitons diffuse only around 10 nm in typical organic solids[89,91,92]. Triplet excitons on the other hand do not undergo radiative decay and can have lifetimes approaching 1 ms. So although they are limited to much slower Dexter transfer, triplets can migrate several microns in molecular crystals[33,91,93,94].

Excitons diffusing through a material in this way can encounter and interact with other excitons. This typically results in the loss of one or both excitons and is therefore termed exciton-exciton annihilation. In the case of singlet-singlet annihilation, such an interaction results in an overall loss of excitation energy[89,92,95,96]. In certain materials however, the annihilation of a pair of triplet excitons can lead to the formation of higher energy singlet states with little or no loss of energy[19,39,97,98]. This triplet-triplet annihilation process is one of the major themes of this thesis and will be discussed in detail in the following section and chapters.

For both singlet and triplet excitons the dynamics of diffusion and annihilation are governed by an equation of the general form[92]

$$\frac{\partial N(\mathbf{r},t)}{\partial t} = D\nabla^2 N(\mathbf{r},t) - \frac{N(\mathbf{r},t)}{\tau} - f\gamma(t)N^2(\mathbf{r},t) + G(\mathbf{r},t), \tag{2.61}$$

where $N(\mathbf{r},t)$ describes the distribution of excitons, $G(\mathbf{r},t)$ is the exciton generation rate, f reflects the number of excitons lost in an annihilation event and $\gamma(t)$ is the annihilation rate constant. $\gamma(t)$ is itself related to the diffusivity of the excitons, but takes different forms depending on the dimensionality of the exciton diffusion[95]. In the case of strongly anisotropic, one-dimensional diffusion, $\gamma(t)$ takes the form[95,99]

$$\gamma_{1D}(t) = 4\pi D R_a \frac{R_a}{\sqrt{2\pi D t}} \tag{2.62}$$

where R_a is an interaction radius within which annihilation will occur[100], typically $\sim 1\,\mathrm{nm}$[89,96,101]. For isotropic, three-dimensional diffusion, the annihilation rate can be found from the solution of the Smoluchowski equation[100]:

$$\gamma_{3D}(t) = 8\pi D R_a \left(1 + \frac{R_a}{\sqrt{2\pi D t}}\right). \tag{2.63}$$

In the limit $t \to \infty$, Equation 2.63 reduces to the more familiar expression

$$\gamma = 8\pi D R_a. \tag{2.64}$$

We have described the photophysics of singlet and triplet excited states in organic molecules and introduced the concepts of exciton diffusion and annihilation that can occur when molecules pack together in the solid state. Next, we consider the intriguing case where the annihilation of a pair of triplet excitons leads to the formation of a singlet excited state.

2.6 Singlet fission and triplet-triplet annihilation

The first observation that annihilating triplets could produce singlet excitons came from measurements of the 'delayed' fluorescence of anthracene crystals in 1963[97]. The fluorescence was found to persist far longer than the intrinsic radiative lifetime, and its behaviour as a function of time and laser intensity showed that it must arise from the bimolecular annihilation of long-lived triplet excitons. Merrifield and co-workers subsequently showed that the photoluminescence of anthracene crystals depends sensitively on weak applied magnetic fields[25]. This observation was particularly striking since the Zeeman energy of such fields (tens of mT) is only a few µeV, orders of magnitude less than the energies of the excited states involved. This pointed towards a mechanism where weak interactions between annihilating triplets modulate the rate of singlet exciton formation. Merrifield and co-workers developed a kinetic scheme to

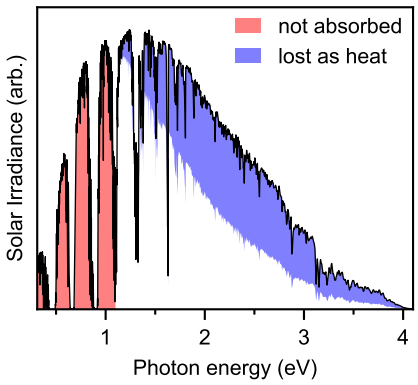

Figure 2.11 | Spectral conversion for photovoltaics. The power conversion efficiency of conventional single-junction solar cells is limited by two principal factors. Photons below the bandgap E_g are not absorbed, whilst higher energy photons produce charge carriers that thermalise rapidly to the band edge, dissipating their excess energy as heat. The balance between these two loss mechanisms depends on the bandgap energy E_g and together they limit the power conversion efficiency to 33.7%[8]. Singlet fission could enable high-energy photons to be downconverted to pairs of low energy photons, thereby avoiding thermalisation losses and raising the maximum efficiency to around 45%[14]. Alternatively, triplet-triplet annihilation could be employed to harvest sub-bandgap photons and upconvert them to higher energy photons that can be absorbed by the cell, resulting in similar efficiency gains[14].

describe triplet-triplet annihilation, which they formulated as[102]

$$T_1 + T_1 \underset{k_{-1}}{\overset{k_1}{\rightleftharpoons}} (TT) \xrightarrow{k_2} S_1. \tag{2.65}$$

The intermediate '(TT)' was dubbed a triplet-pair state, in which the triplets are close enough to interact[102]. The nature of these triplet-pair states was[102] and remains[15,16,29,30,103,104] the subject of considerable uncertainty and debate.

The inverse process to TTA is singlet exciton fission, whereby a singlet exciton splits into a pair of triplets via a spin-0 triplet-pair state[15,16]. This rapid, spin-allowed production of dark triplet states from photo-excited singlets was first discovered in tetracene crystals[24,105]. Based on similar measurements of magnetic field effects on fluorescence[24], Merrifield and co-workers modified their kinetic scheme to include singlet fission with a rate k_{-2}:

$$T_1 + T_1 \underset{k_{-1}}{\overset{k_1}{\rightleftharpoons}} (TT) \underset{k_{-2}}{\overset{k_2}{\rightleftharpoons}} S_1. \tag{2.66}$$

Research into singlet fission and triplet-triplet annihilation entered something of a hiatus following the initial work in the late 1960s and early 1970s. Interest was rekindled in 2006 following work by Hanna and Nozik[27] who demonstrated that using singlet fission materials to efficiently convert high energy

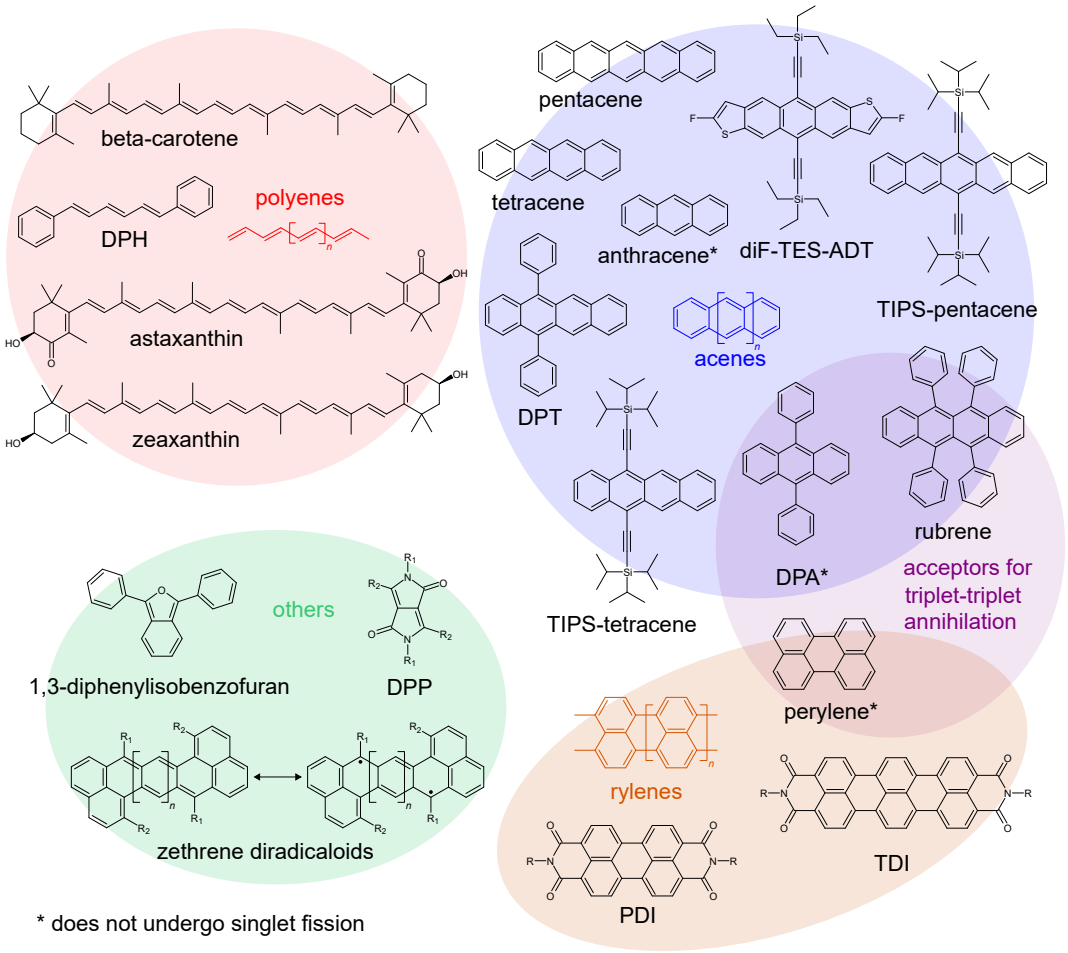

Figure 2.12 | Molecules for singlet fission and triplet-triplet annihilation. Singlet fission has been reported to occur in carotenoid aggregates, acenes, rylenes, zethrenes and others[15,16]. Molecules for TTA-UC are typically chosen from a much smaller range[107], most commonly rubrene, perylene or DPA. This thesis presents research on pentacene, diF-TES-ADT and rubrene and we therefore focus our discussion of singlet fission and triplet-triplet annihilation on the acene family. Acronyms are defined in the List of Abbreviations.

photons into pairs of low energy photons could enable solar cells to exceed the Shockley-Queisser limit of 33.7%[8], and potentially reach power conversion efficiencies of around 45%. Triplet-triplet annihilation could result in similar efficiency boosts for higher-bandgap solar cells by upconverting sub-bandgap photons[14,106]. Figure 2.11 illustrates the potential for overcoming losses in photovoltaics using such spectral conversion.

The new motivation provided by potential photovoltaic applications, together with rapid developments in ultrafast spectroscopy techniques, have fuelled a boom in singlet fission and triplet-triplet annihilation research in recent years. Triplet-triplet annihilation has received additional interest from the biomedical sciences owing to its potential to convert tissue-penetrating

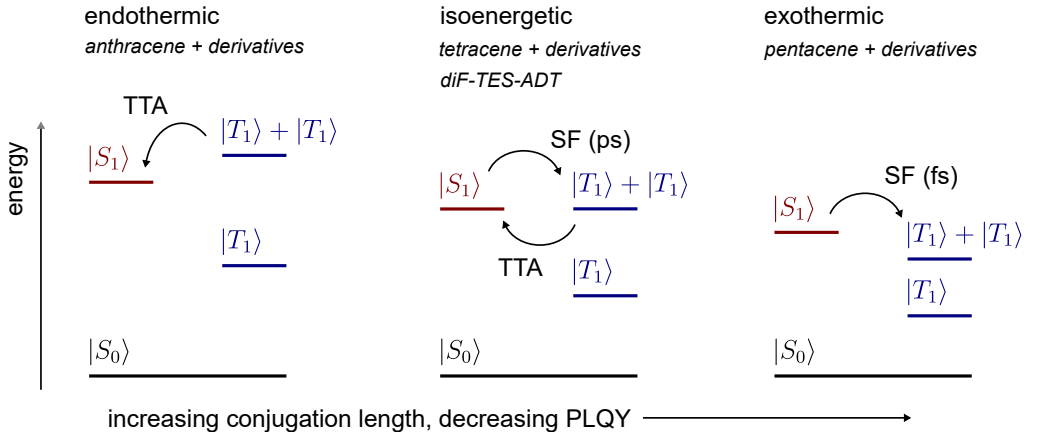

Figure 2.13 | Singlet fission and triplet-triplet annihilation in acenes. The singlet fission and triplet-triplet annihilation characteristics of acenes can be roughly divided into three categories based on the relative singlet and triplet energy levels. Molecules like anthracene for which singlet fission is impossible are described as endothermic. Pentacene is exothermic and undergoes rapid singlet fission. Singlets and triplet-pairs are approximately equal in energy for tetracene and similar molecules, leading to complex photophysics.

near-infrared light into the high-energy photons required to kick-start chemical processes, thereby opening up a new approach to photodynamic therapy, optogenetics and targeted drug delivery[21]. The recent resurgence in interest has led to the identification of a wide range of molecules that undergo singlet fission, a selection of which are shown in Figure 2.12. Later chapters in this thesis specifically investigate singlet fission and triplet-triplet annihilation in diF-TES-ADT, pentacene and rubrene. We will therefore largely constrain our discussion of triplet-pair states and their photophysics to the acene family.

Figure 2.13 summarises the most basic features of singlet fission and triplet-triplet annihilation in acenes. In particular, we highlight that as the conjugation length increases, the S_1 and T_1 states become lower in energy, such that the energy of a pair of triplets can lie above, at, or below, the energy of the S_1 state. As a result, the acenes can be divided into three broad categories with distinct singlet fission and TTA properties.

For short acenes such as anthracene, the energy of two triplets lies well above that of the singlet, making singlet fission energetically unfeasible and resulting in a high photoluminescence quantum yield[24,105]. Triplet-triplet annihilation on the other hand does occur, and results in the formation of singlet states[25].

For long acenes such as pentacene, twice the triplet energy is well below the singlet level[108,109]. As a result, singlet fission occurs extremely rapidly in under 100 fs, producing triplets with nearly 200% yield[108]. As a result, the pho-

toluminescence quantum yield is extremely small, particularly since the bright singlet state cannot be formed through triplet-triplet annihilation.

In between, we find materials like tetracene, diF-TES-ADT and rubrene, in which the singlet and triplet-pair energies are roughly isoenergetic. Singlet fission is slower than in pentacene, typically on the order of picoseconds[74,110], but it occurs alongside triplet-triplet annihilation leading to rich photophysical behaviour. We explore such behaviour in Chapter 8.

Despite these differences, triplet-pair intermediates play a key role in the photophysics of all the molecules depicted in Figure 2.12. In the next section, we explore their spin physics.

2.6.1 Triplet-pair states

We recall from Section 2.2.4 that a triplet exciton has three possible spin wavefunctions. We obtained expressions for these wavefunctions by diagonalising the total spin operator for two electrons. Alternatively, we can think of these two-electron spin wavefunctions, given by equations 2.8-2.10 in terms of the eigenstates of the two-electron spin Hamiltonian,

$$\begin{aligned}\hat{H} &= \hat{H}_{Zeeman} + \hat{H}_{Zero-Field} \\ &= g\mu_B \boldsymbol{B}\cdot\hat{\boldsymbol{S}} - X\hat{S}_x^2 - Y\hat{S}_y^2 - Z\hat{S}_z^2 \\ &= g\mu_B \boldsymbol{B}\cdot\hat{\boldsymbol{S}} + D\left(\hat{S}_z^2 - \frac{1}{3}\hat{\boldsymbol{S}}^2\right) + E\left(\hat{S}_x^2 - \hat{S}_y^2\right),\end{aligned} \tag{2.67}$$

where $\boldsymbol{B}$ is an external magnetic field. The zero-field term reflects the intramolecular dipole-dipole coupling and is usually parametrised by the so-called zero-field splitting parameters D and E. The zero-field splitting is typically anisotropic, hence the Hamiltonian is written in terms of a molecular coordinate system (x, y, z). We define this coordinate system in the context of acene molecules such that x is parallel to the long axis of the acene backbone and y is parallel to the short axis[111], as shown in Figure 2.14.

In the limit of strong magnetic fields, such that the Zeeman term dominates the spin Hamiltonian, the eigenstates are those presented in Section 2.2.4. This is therefore called the high-field basis. In the zero-field limit however, the triplet

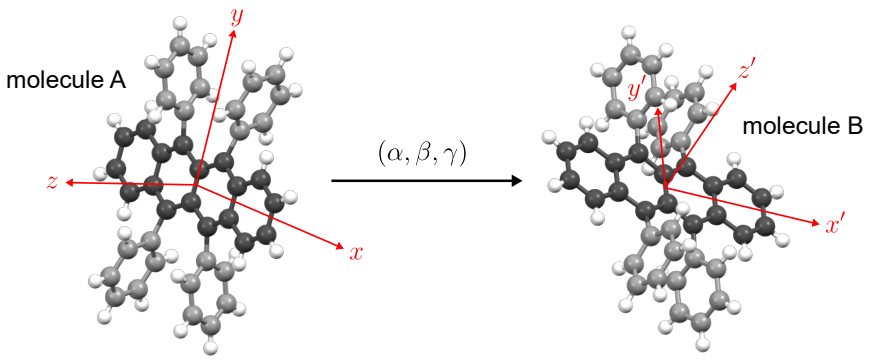

Figure 2.14 | Molecular coordinate systems. We define our coordinate system such that x is parallel to the long axis of the acene backbone (shown here for rubrene), y is parallel to the short axis and z is perpendicular to the molecular plane. In general the coordinate system of the second molecule in the triplet-pair will not coincide; instead a rotation operation must be applied. Here we use the Euler angles (α, β, γ) to parametrise the rotation from A onto B using the $zx'z''$ convention.

eigenstates become

$$\begin{aligned} |x\rangle &= \frac{1}{\sqrt{2}}(|\downarrow\downarrow\rangle - |\uparrow\uparrow\rangle) \\ |y\rangle &= \frac{i}{\sqrt{2}}(|\downarrow\downarrow\rangle + |\uparrow\uparrow\rangle) \\ |z\rangle &= \frac{1}{\sqrt{2}}(|\uparrow\downarrow\rangle + |\downarrow\uparrow\rangle), \end{aligned} \tag{2.68}$$

which is known as the zero-field basis. We will use this basis to describe the spin states of triplet-pair states.

The interactions between two triplet excitons A and B in a triplet-pair state are once again described by a spin Hamiltonian, this time for four electrons:

$$\hat{H} = \hat{H}_{Exchange} + \hat{H}_{Dipole-Dipole} + \sum_{i=A,B} \left(\hat{H}_{Zeeman,i} + \hat{H}_{Zero-Field,i} \right). \tag{2.69}$$

In addition to the 2-electron spin Hamiltonians (Equation 2.67) for individual triplets on molecules A and B, there are two additional intertriplet terms. Firstly, there is an intertriplet exchange interaction, analogous to that given by Equation 2.18, which depends on the degree of wavefunction overlap between the two triplets in the pair. Second, we have an intertriplet dipole-dipole coupling term. Writing the triplet-pair spin Hamiltonian in terms of the spin operators

$\hat{\boldsymbol{S}}_i$ gives

$$\begin{aligned}\hat{H} = J\hat{\boldsymbol{S}}_A \cdot \hat{\boldsymbol{S}}_B + X\left[\hat{\boldsymbol{S}}_A \cdot \hat{\boldsymbol{S}}_B - 3\left(\hat{\boldsymbol{S}}_A \cdot \hat{\boldsymbol{r}}\right)\left(\hat{\boldsymbol{S}}_B \cdot \hat{\boldsymbol{r}}\right)\right] \\ + \sum_{i=A,B}\left[g\mu_B \boldsymbol{B} \cdot \hat{\boldsymbol{S}}_i + D\left(\hat{S}_{i,z}^2 - \frac{1}{3}\hat{\boldsymbol{S}}_i^2\right) + E\left(\hat{S}_{i,x}^2 - \hat{S}_{i,y}^2\right)\right],\end{aligned} \tag{2.70}$$

where J is the intertriplet exchange energy, X gives the magnitude of intertriplet dipole coupling, $\hat{\boldsymbol{r}}$ is the unit vector between the two molecules, $\boldsymbol{B}$ is the applied magnetic field strength and D and E ($\gg X$) are the intratriplet zero-field splitting parameters.

This spin Hamiltonian is valid in the absence of other terms with magnitude similar or greater to the D and E parameters. For example, spin-orbit interactions (Section 2.4.2) are assumed to be very weak. We note that the intertriplet dipolar term acts as a weak perturbation in Equation 2.70 and therefore its precise form is unimportant[111,112]. Other hyperfine terms, such as the interactions between unpaired electrons and nuclei, are not included[113].

We obtain the nine eigenstates $|\psi_l\rangle$ of the spin Hamiltonian by diagonalising it in the zero-field basis of product pair states, i.e. $|xx\rangle, |xy\rangle, \ldots, |zz\rangle$ where we have dropped the A, B subscripts for clarity. As highlighted by Tapping and Huang[111], the coordinate system of molecule B does not in general coincide with that of A (Figure 2.14). A rotation operation must therefore be applied to $\hat{H}_{Zero-Field,B}$. As a result, $\hat{H}_{Zero-Field,B}$ contains off-diagonal elements in the zero-field basis, hence even when there is no applied magnetic field, the triplet-pair spin wavefunctions $|\psi_l\rangle$ carry a dependence on relative molecular orientation[111]. In this context, we define a 'parallel' triplet-pair orientation as one for which molecule A can be mapped onto molecule B by means of a translation operation alone.

In the limit of strong intertriplet exchange coupling, where $J \gg D$, such effects are negligible and the nine eigenstates of the spin Hamiltonian in the

zero-field basis are pure singlet, triplet and quintet spin states, given by[114]:

$$\begin{aligned}
|S\rangle &= \frac{1}{\sqrt{3}}(|xx\rangle + |yy\rangle + |zz\rangle) \\
|T_x\rangle &= \frac{1}{\sqrt{2}}(|yz\rangle - |zy\rangle) \\
|T_y\rangle &= \frac{1}{\sqrt{2}}(|zx\rangle - |xz\rangle) \\
|T_z\rangle &= \frac{1}{\sqrt{2}}(|xy\rangle - |yx\rangle) \\
|Q_a\rangle &= \frac{1}{\sqrt{2}}(|xx\rangle - |yy\rangle) \\
|Q_b\rangle &= \frac{1}{\sqrt{6}}(|xx\rangle + |yy\rangle - 2\,|zz\rangle) \\
|Q_x\rangle &= \frac{1}{\sqrt{2}}(|yz\rangle + |zy\rangle) \\
|Q_y\rangle &= \frac{1}{\sqrt{2}}(|zx\rangle + |xz\rangle) \\
|Q_z\rangle &= \frac{1}{\sqrt{2}}(|xy\rangle + |yx\rangle).
\end{aligned} \tag{2.71}$$

In this case, spin and energy eigenstates coincide and spin is a good quantum number. The triplet and quintet states are separated in energy from the singlet by J and $3J$ respectively[115,116].

These pure spin states also represent the nine lowest-energy eigenstates of the total four-electron spin operator[†]

$$\hat{\boldsymbol{S}}^2 = \left(\hat{\boldsymbol{S}}_A + \hat{\boldsymbol{S}}_B\right)^2. \tag{2.72}$$

Similarly to the procedure in Section 2.2.4, we can diagonalise $\hat{\boldsymbol{S}}^2$ in the 4-electron product basis $|\uparrow\uparrow\uparrow\uparrow\rangle, |\uparrow\uparrow\uparrow\downarrow\rangle, \ldots, |\downarrow\downarrow\downarrow\downarrow\rangle$ to obtain the 16 eigenstates[29,118]. Of particular importance to singlet fission and triplet-triplet annihilation is the lowest-energy singlet:

$$\begin{aligned}
|S\rangle &= \frac{1}{\sqrt{12}}\left(|\uparrow\downarrow\uparrow\downarrow\rangle + |\downarrow\uparrow\uparrow\downarrow\rangle + |\uparrow\downarrow\downarrow\uparrow\rangle + |\downarrow\uparrow\downarrow\uparrow\rangle - 2\,|\uparrow\uparrow\downarrow\downarrow\rangle - 2\,|\downarrow\downarrow\uparrow\uparrow\rangle\right) \\
&\approx \frac{1}{\sqrt{3}}\left(|xx\rangle + |yy\rangle + |zz\rangle\right).
\end{aligned} \tag{2.73}$$

[†]Recent calculations by Scholes[117] put the triplet states $|T_1\rangle = \{|T_x\rangle, |T_y\rangle, |T_z\rangle\}$ higher in energy than the singlets and quintets by $\frac{2}{3}J_0$, where $J_0 \sim 1\,\text{eV}$ is the intramolecular exchange interaction. This contrasts with earlier work by Kollmar[118] for reasons discussed in a recent review[29]. Kollmar's description of the 4-electron states is consistent with recent interpretations of magnetic field effects on fluorescence[114,119–121] and so we use it throughout this thesis.

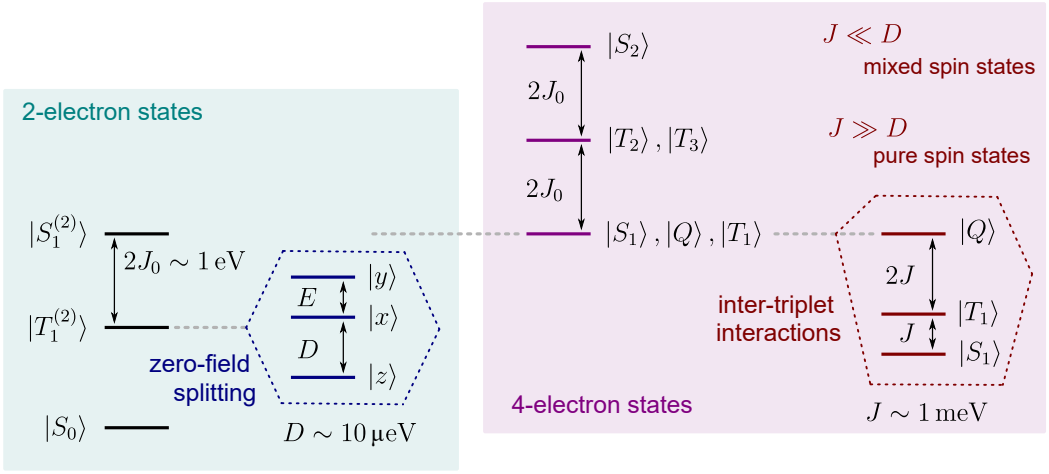

Figure 2.15 | Triplet-pair states. The familiar 2-electron excited states consist of a singlet and three triplets which are lower in energy by J_0, the intramolecular exchange energy. Intramolecular dipole-dipole interactions break the degeneracy of the three triplets, resulting in a small zero-field splitting. There are 16 possible four-electron states: two singlets (2×1), three triplets (3×3) and one quintet (1×5). The lowest energy of these 16 states are a singlet, triplet and quintet that can each be written as a correlated pair of triplets and are therefore also denoted ^{1}(TT), ^{3}(TT) and ^{5}(TT). These nine states are eigenstates of the spin Hamiltonian for a pair of interacting triplet excitons, provided that the intertriplet exchange coupling J is greater than the intramolecular dipole-dipole interactions D. If $J \ll D$, spin is no longer a good quantum number, the nine eigenstates become almost degenerate and mixing can occur.

Equation 2.73 shows that there is a combination of four electrons that has an overall spin of zero (a singlet) that can nonetheless be written as a linear combination of pairs of triplet states. This state is therefore described as a correlated pair of triplets and is denoted ^{1}(TT). It is this ^{1}(TT) that makes singlet fission possible: pairs of triplets can be formed from a singlet state without flipping any spins, a process that we describe in more detail in Section 2.6.3. Similarly, the lowest energy four-electron triplet and quintet states can be written as correlated triplet-pairs, denoted ^{3}(TT) and ^{5}(TT).

The ^{1}(TT) state is also described as a strongly exchange-coupled triplet-pair because, as shown above, it is an eigenstate of the spin Hamiltonian for a pair of triplet excitons provided that the exchange interaction is large ($J \gg D$). Following ^{1}(TT) formation, dynamic fluctuations or spatial separation of triplets can occur, processes which we discuss in Section 2.6.3. Either way, the exchange interaction is dramatically reduced and weakly exchange-coupled triplet-pairs (T...T)^l are formed, which are the eigenstates of the spin Hamiltonian in the limit $J \ll D$. These states are not spin eigenstates: spin is no longer a good quantum number and so the (T...T)^l states have mixed character. We see from

Equation 2.71 that the singlet and quintet states are symmetric with respect to triplet exchange, whilst the triplets are antisymmetric. For parallel molecules, the zero-field Hamiltonian is symmetric under triplet exchange and thus can only mix singlet and quintet states. In this case the (T...T) states comprise triplets $|T\rangle$, quintets $|Q\rangle$ and singlet-quintet mixtures $|SQ\rangle$. For randomly oriented molecules however, this symmetry is broken allowing singlet-triplet mixing[115]. Figure 2.15 summarises the multiplicities and energies of the different triplet-pair states.

2.6.2 Experimental evidence of triplet-pair states

Having introduced the different kinds of triplet-pair states, we can re-write Merrifield's original description of the singlet fission process as

$$\mathrm{S_1} \xrightarrow[\text{fission}]{\text{singlet}} {}^1(\mathrm{TT}) \xrightarrow[\text{separation}]{\text{triplet}} (\mathrm{T...T}) \xrightarrow[\text{decoherence}]{\text{spin}} \mathrm{T_1} + \mathrm{T_1}, \tag{2.74}$$

where (T...T) are weakly interacting triplet-pairs. There are nine such possible $(\mathrm{T...T})^l$ states, but importantly only those with some singlet character will be initially formed via singlet fission. Since the Zeeman term in the spin Hamiltonian alters the spin mixing of triplet-pair states, the photophysics of singlet fission materials depends sensitively on applied magnetic fields. Indeed, measurements of changes in the fluorescence of acene crystals under applied magnetic fields provided the first experimental evidence of triplet-pair states. In this section we describe these and other magnetic field effects in more detail along with more recent experimental probes of triplet-pair states.

Magnetic field effects

In the late 1960s, several reports of magnetic field effects on the photoluminescence (PL) of anthracene[25,102] and tetracene[24,122] single crystals emerged. In the case of anthracene, measured PL intensity increased for applied magnetic fields of a few tens of mT but reduced at higher fields[25]. The opposite effect was observed for tetracene[122]. In both cases, the magnetic field effects were highly dependent on the orientation of the magnetic field with respect to the crystal symmetry axes[24,102,122].

Merrifield and co-workers explained these phenomena by invoking singlet fission and triplet-triplet annihilation processes that occur via intermediate triplet-pair states. In their model, these intermediates are the eigenstates $|\psi_l\rangle$ of the spin Hamiltonian given in Equation 2.70 with $J = 0$ which we would

now describe as weakly exchange-coupled or weakly-interacting $(\mathrm{T...T})^l$ states. Merrifield realised that the coupling between the triplet-pairs and the singlets depended on the singlet character $|C_S^l|^2$ of the triplet-pair wavefunctions where[123,124]

$$\begin{aligned} C_S^l &= \langle S|\psi_l\rangle \\ &\approx \frac{1}{\sqrt{3}}\left(\langle xx| + \langle yy| + \langle zz|\right)|\psi_l\rangle \end{aligned} \tag{2.75}$$

and we have used the definition of the spin-0 correlated triplet pair from Equation 2.73. Merrifield therefore wrote the kinetic scheme for singlet fission and triplet-triplet annihilation as

$$\mathrm{S}_1 \underset{k_2|C_S^l|^2}{\overset{k_{-2}|C_S^l|^2}{\rightleftharpoons}} (\mathrm{TT})^l \underset{k_1}{\overset{k_{-1}}{\rightleftharpoons}} \mathrm{T}_1 + \mathrm{T}_1, \tag{2.76}$$

where we now interpret $(\mathrm{TT})^l$ to mean $(\mathrm{T...T})^l$.

The fluorescence from S_1 is thus dependent on magnetic field through the $|C_S^l|^2$ factors, which in turn are governed by the spin Hamiltonian. For identically oriented molecules (the typical case for acene crystals), the number of $(\mathrm{T...T})^l$ states possessing singlet character is 3. At intermediate fields where $g\mu_B B \sim D$ this increases to five before dropping to two at higher fields[123], as shown in Figure 2.16a. For materials such as tetracene, singlet fission (rate k_{-2}) is energetically feasible. The overall rate of singlet fission, which competes with 'prompt' fluorescence, depends on the number of (T...T) states that have singlet character. This leads to the characteristic magnetic field effect observed in tetracene crystals[122] and shown in Figure 2.16b. In the case of anthracene, where triplet fusion (rate k_2) causes delayed fluorescence, increased coupling of the $(\mathrm{T...T})^l$ states to S_1 will give increased fluorescence, hence the magnetic field effect has the opposite sign[25].

This simple kinetic model provides the basic framework for understanding magnetic field effects but there are several additional factors that influence the measured lineshapes. A much more complicated quantum-mechanical theory developed concurrently by Suna[98] included the effects of exciton diffusion and spin relaxation and provided a more quantitative fit to the experimental data. More recent measurements of magnetic field effects on polycrystalline and amorphous rubrene films showed significantly different lineshapes which were explained by magnetic field dependent spin-lattice relaxation[125].

Even within Merrifield's original framework, sample morphology can affect magnetic field effects because the zero-field splitting terms in the spin Hamilto-

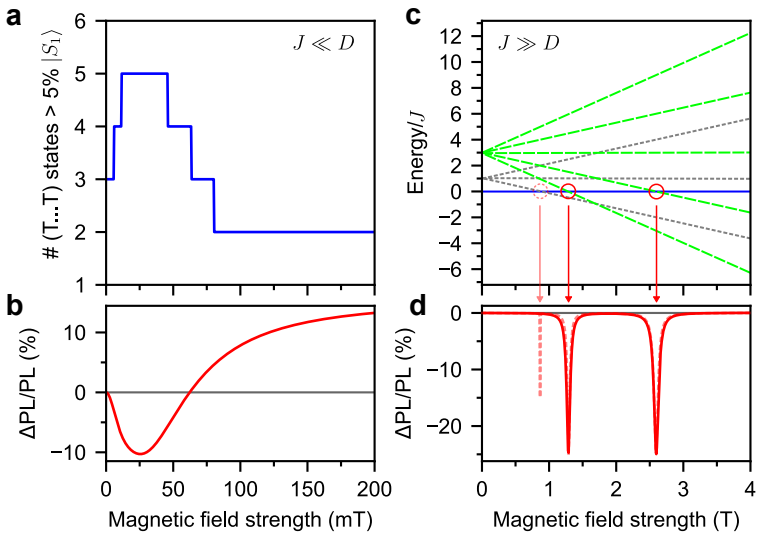

Figure 2.16 | Magnetic field effects. **a**, Simulation of the number of $(\mathrm{T...T})^l$ states with more than 5% singlet character as a function of magnetic field, for $J = 0$. For a material that undergoes singlet fission, this causes a characteristic variation in the measured fluorescence as shown in (**b**). This effect would be inverted in the case of triplet fusion. **c**, Triplet-pair energies as a function of magnetic field for strong exchange coupling ($J = 0.1\,\mathrm{meV}$). Singlet-quintet mixing at level crossings gives rise to dips in the observed emission as shown in (**d**). For non-parallel molecules, singlet-triplet mixing can occur, causing an additional dip. For the simulations, we took $D = 5\,\mu\mathrm{eV}$, $E = D/3$ and $X = D/10000$, and assumed an angle $\theta = \pi/4$ between the magnetic field and the molecular z axis.

nian are dependent on relative molecular orientation. These effects have been investigated in nominally amorphous rubrene films[111,112]. Molecular orientation can also play a role in the spin physics of strongly exchange-coupled triplet pairs, which give rise to markedly different magnetic field effects at much higher magnetic fields[115].

When $J \gg D$, we have seen that the triplet-pairs are the pure spin states given by Equation 2.71. Spin is a good quantum number, the singlet projections do not change with magnetic field and hence there is no change in the measured PL. Exceptions occur at the so-called level crossings, where the Zeeman splitting causes degeneracies between the singlet, triplet and quintet states, as shown in Figure 2.16c. At these level crossings, the degenerate states are mixed by the zero-field Hamiltonian, which acts as a perturbation. As a result, singlet character is shared across more than one eigenstate resulting in a dip (for a singlet fission material) in the observed emission in the vicinity of the level crossing[115]. For parallel molecules, only singlet-quintet mixing is possible, leading to dips in emission at $g\mu_B B \simeq 3J$ and $g\mu_B B \simeq \frac{3}{2}J$ as shown in Figure 2.16d. If the molecules are not parallel singlet-triplet mixing can occur, causing a third dip in the observed emission at $g\mu_B B \simeq J$[115].

Dips in fluorescence at high magnetic fields have been measured at 1.4 K[119] for a single crystal of the singlet fission material TIPS-tetracene. In addition to providing clear evidence of strongly-exchange coupled triplet-pairs, detailed analysis of the various dips allowed the authors to identify three types of triplet-pair site in the material with differing exchange interactions.

Similar high-field effects on the room temperature fluorescence of single crystal diphenylhexatriene (DPH) have also been recently reported[114,120,121]. By analysing the lineshapes and positions of the dips in fluorescence at different magnetic field orientations[‡] the authors were able to determine the intermolecular geometry of the strongly exchange-coupled triplet-pair[114,120,121]. Rather than using the standard Merrifield formulation, the authors modelled their data using the Stochastic Liouville equation[114,120] which had previously been applied to magnetic field effects of radical pairs[126,127].

This highlights an important point: singlet fission and triplet-triplet annihilation are by no means the only photophysical processes that can give rise to magnetic field effects[113,128]. The formation and subsequent recombination of radical pairs (anions and cations) also gives rise to a magnetic field effect because the unpaired electrons are affected by nuclear spins through a hyperfine interaction[113]. This effect has been studied in light-harvesting complexes[129] and is even thought to allow migratory birds to sense the Earth's magnetic field[130]. The quenching of triplet excitons by charges also caries a magnetic field dependence[131] and this has been shown to complicate the interpretation of measured magnetic field effects during triplet-triplet annihilation[132]. Fortunately, there are many other experimental probes of triplet-pair states beyond static magnetic field effects.

Quantum beating

We have seen that the correlated triplet-pair ^{1}(TT) is overall a singlet state, but that its spin wavefunction $|S\rangle$ is a linear combination of the $|xx\rangle$, $|yy\rangle$ and $|zz\rangle$ triplet-pairs, as shown in Equation 2.73. Thus $|S\rangle$ itself is not an eigenstate of the spin Hamiltonian in the case of weak exchange coupling, instead it is a superposition of eigenstates, each of which evolves in time with a phase proportional to its energy. Thus the initial state formed by singlet fission carries a time dependence:

$$|S(t)\rangle = \frac{1}{\sqrt{3}}\left(e^{-iE_{xx}t/\hbar}|xx\rangle + e^{-iE_{yy}t/\hbar}|yy\rangle + e^{-iE_{zz}t/\hbar}|zz\rangle\right) \tag{2.77}$$

[‡]Interestingly, the fluorescence dips measured in Refs. 114,120,121. were assigned to different level crossings than those in Ref. 119. The reasons for this are unclear.

Strictly speaking, Equation 2.77 holds if the spin wavefunction $|S(t)\rangle$ is that of a weakly exchange coupled spin-zero triplet-pair, which we will write as ^{1}(T...T)[133]. Since E_{xx}, E_{yy} and E_{zz} differ, the coupling $|\langle S_1|^1(T...T)\rangle|^2$ will vary periodically with time, resulting in oscillations in the delayed fluorescence. We expect three oscillation frequencies at zero applied magnetic field which are determined by the D and E zero-field splitting parameters[134]. These oscillations are known as quantum beats.

Quantum beating in delayed fluorescence was first observed in tetracene crystals in 1981[135]. Bardeen and co-workers expanded this early work by measuring the fluorescence decay of crystalline tetracene at room temperature. They again saw oscillations on a timescale of a few ns[134]. The oscillatory signal was superimposed on the population decay; subtraction of a multi-exponential background followed by a Fourier transform yielded three clearly distinguishable beat frequencies consistent with reported zero-field splitting parameters[134]. The authors were able to simulate their experimental data using a Merrifield-style[102] density matrix model[134]. In order to reproduce the observed damping of the oscillations with time, they included spin dephasing of the ^{1}(T...T) state on a timescale of 10 ns. More recently, similar quantum beating has been observed for crystalline diF-TES-ADT films[74], zethrene diradicaloids[136] and rubrene single crystals[137]. Observation of quantum beating is considered unambiguous evidence for a weakly exchange coupled correlated triplet-pair intermediate in singlet fission[124,133,134].

Magnetic resonance

Further evidence of strongly exchange-coupled triplet-pairs has recently been provided by time-resolved electron paramagnetic resonance spectroscopy (trEPR). In a trEPR experiment, paramagnetic excited states generated by an optical pulse are probed with a continuous microwave source as a function of time and external magnetic field, B. At certain B values, the Zeeman splitting between sublevels (for example $|Q\rangle_{m_S=0} \rightarrow |Q\rangle_{m_S=1}$) becomes resonant with the continuous microwave field causing absorptive or emissive features in the trEPR signal. This technique is sensitive to long-lived (> 50 ns) pure spin states with non-zero spin such as ^{5}(TT) and T_1 but blind to spin-0 states like ^{1}(TT)[104].

Signals from singlet fission generated T_1 states had previously been observed by trEPR in tetracene crystals[138]. A breakthrough came in 2016 when clear signatures of the strongly exchange coupled quintet state ^{5}(TT) were observed for the first time in trEPR spectra of TIPS-tetracene thin films[139] and pentacene-

bridge-pentacene dimers[140]. Since then, ^{5}(TT) has been measured by trEPR in dilute pentacene films[141], TDI derivatives[142,143] and a variety of pentacene dimers[144–148]. To date, ^{3}(TT) has not been observed directly in trEPR experiments[104].

In addition to the strongly exchange coupled ^{5}(TT) states observed in TIPS-tetracene films by trEPR, weakly exchange coupled triplet-pairs comprising singlet-quintet mixtures have also been observed in the same material by optically-detected magnetic resonance spectroscopy[149].

Direct photon emission

None of the experimental probes discussed so far can provide direct evidence for the strongly exchange-coupled ^{1}(TT) state. Its existence is implied by the resonances at high magnetic field[114,119–121] but this is not a direct spectroscopic signature. Recently however, features in photoluminescence spectra have been attributed to direct photon emission from the ^{1}(TT) state[74,136,150,151], although these assignments have proven to be controversial[32].

The first hints of a (weakly) emissive ^{1}(TT) state came from studies of the photoluminescence properties of polycrystalline tetracene thin films[152,153]. Following prompt emission characteristic of the S_1 state, a longer-lived redshifted spectral feature was observed and tentatively assigned as a 'dull' multiexcitonic intermediate state. A few years later red-shifted excimer-like emission in concentrated solutions of TIPS-tetracene was directly correlated with the dynamics of the triplet-pair state determined through transient absorption measurements and explicitly assigned as ^{1}(TT) emission[150]. Further similar studies of zethrene diradicaloids[136], solid TIPS-tetracene[151] and diF-TES-ADT, rubrene and tetracene[74] all came to a similar conclusion: the ^{1}(TT) state is emissive. The observation via 2D electronic spectroscopy of acene crystals of an $S_0 \rightarrow {}^1$(TT) absorption peak[154] supports the idea that ^{1}(TT) possesses oscillator strength.

This is a surprising finding since the symmetry of the ^{1}(TT) wavefunction is such that a radiative transition to the ground state is forbidden[103]. It is thought that instead, the ^{1}(TT) state is able to acquire oscillator strength from the nearby bright S_1 state via Herzberg-Teller intensity borrowing[29,74,103,136], as described in Section 2.4.3. This mechanism is analogous to the Herzberg-Teller coupling that enables the formally dark $2A_g$ state in polyenes to emit light[155,156].

Several authors have since assigned long-lived redshifted photoluminscence spectral features to ^{1}(TT)[157–159]. Recently however, Dover et al. called these assignments into question by demonstrating that the excimer-like emission in

concentrated TIPS-tetracene solutions could not arise from an intermediate to singlet fission, but instead was a signature of a trap state that hinders singlet fission[32]. These controversies provided some of the motivation for our work in Chapter 4, in which we investigate ^{1}(TT) emission in diF-TES-ADT in detail and show for the first time that the ^{1}(TT) state in pentacene has a similar photoluminescence signature.

Transient absorption signatures

By far the most common experimental probe of singlet fission materials is transient absorption spectroscopy, a technique that we describe in detail in Section 3.4.2. We might expect the excited state absorption spectrum of triplet-pair states such as ^{m}(TT) and (T...T) to be identical to that of free triplets, T_1. In fact, a variety of calculations[160–165] have shown that small admixtures of singlet and charge-transfer character to the ^{1}(TT) state do result in lineshape differences with T_1. This is particularly pronounced in the near infrared spectral region, where charge-transfer character of ^{1}(TT) results in an excited state absorption not present for T_1[163–165]. This has been verified experimentally for pentacene dimers[166–168].

Such lineshape differences between triplet-pair excited state absorption spectra even allowed Pensack and co-workers to distinguish between strongly interacting ^{1}(TT) and weakly interacting (T...T) states in TIPS-pentacene, and therefore track these sub-populations in time[169,170]. More recently still, Jones and co-workers were able to correlate spatially-resolved changes in the transient absorption lineshape of TIPS-pentacene crystals with regions of different molecular packing[171].

We note that the transient absorption signatures of S_1, T_1 and triplet-pair excited state absorptions are usually broad and significantly overlapped, particularly in the visible spectral region. This, coupled with the relatively small changes in lineshape between different triplet species, makes the extraction of the different triplet-pair species from transient absorption data by spectral deconvolution algorithms such as global or target analysis challenging and artefact-prone.

Nevertheless, transient absorption spectroscopy has been a vital tool in developing our understanding of singlet fission. Tracking the various excited state populations in time provides us with a wealth of information about the underlying mechanisms of singlet fission.

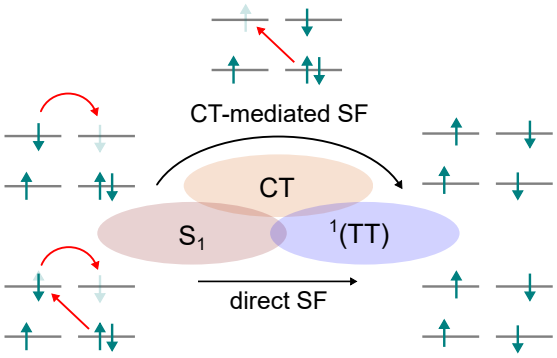

Figure 2.17 | Singlet fission pathways. The formation of ^{1}(TT) from S_1 can proceed directly via a two-electron transfer, or in a two-step process via a charge-transfer intermediate, which may be a virtual state.

2.6.3 Mechanisms of singlet fission

In Equation 2.74 we described the mechanism of singlet fission in three steps. Firstly, photo-excited singlets S_1 transition into strongly-exchange coupled spin-0 triplet-pair states ^{1}(TT). Next, triplet separation results in weakly exchange coupled mixed-spin (T...T) states, though only those with some singlet character are formed. Finally, the spin coherence is lost, leaving a pair of independent triplet excitons. However, this simple picture hides a wealth of underlying complexity and as we shall see, the mechanisms of singlet fission are highly material-dependent, even within the polyacene family.

Initial triplet-pair formation

The first step in singlet fission is the formation of a (nominally) four-electron singlet state, ^{1}(TT), from a two-electron singlet state and ground state chromophore, S_1S_0. As shown in Figure 2.17, there are two basic ways for this to occur[15,16]. The so-called 'direct' mechanism involves a concerted two-electron transfer. *Ab initio* calculations by Zimmerman and co-workers[172–174] on dimers and clusters of pentacene and tetracene found that singlet fission in these materials could be entirely explained by direct coupling between S_1S_0 and ^{1}(TT). They concluded that this coupling was driven by a conical intersection (Section 2.4.1) between the S_1S_0 and ^{1}(TT) potential energy surfaces. DFT calculations of PDI derivatives similarly concluded that singlet fission yields could only be explained by this direct mechanism[175].

Alternatively, the 2-electron transfer can be broken into two distinct steps. In this case, singlet fission occurs via an intermediate state with charge-transfer (CT) character. Berkelbach and others have shown that in fact this mediated pathway should dominate[176–179]. Even in cases where the charge-transfer

state is energetically inaccessible, singlet fission can be mediated by a 'virtual' charge-transfer state via a superexchange mechanism[177]. This virtual pathway is expected to be spectroscopically indistinguishable from the direct pathway, although indirect experimental evidence suggests otherwise[180]. There are even reports of an experimentally observable charge-transfer intermediate in the singlet fission of 1,3-diphenylisobenzofuran dimers[181].

Subsequent calculations of the singlet fission rate for a range of acenes suggest that both the direct and mediated mechanisms may be operational and that the importance of the CT-mediated pathway is determined by the charge-transfer character of the optical singlet[182]. This hypothesis is supported by studies of the S_1 state in single crystal pentacene: around 45% charge transfer character needed to be included in the lower Davydov component of the S_1 state in order to quantitatively fit the measured absorption spectrum[86].

It is worth noting at this juncture the distinction between diabatic and adiabatic states. Strictly speaking, states of pure character such as S_1S_0, ^{1}(TT) and CT are diabatic states. The real excited states measured in experiments rarely have such pure character and instead are mixed adiabatic states, for example S_1S_0 can mix with both CT and ^{1}(TT). Such mixing can become especially pronounced at avoided crossings between the potential energy surfaces (Section 2.4.1). In calculations, adiabatic states are usually obtained by through the configuration interaction which mixes in proportions of computed diabatic states[182].

Using time-resolved two-photon photoemission spectroscopy, Chan et al., provided evidence of a third 'quantum coherent' mechanism, in which strong electronic coupling between S_1S_0 and ^{1}(TT) means that they are formed simultaneously in superposition[183–185]. More recently, several studies have developed the idea of vibrationally coherent singlet fission dynamics, mediated by a conical intersection, in thin films of pentacene[186], TIPS-pentacene[187], TIPS-tetracene[151] and in rubrene single crystals[35]. Here the S_1S_0 and ^{1}(TT) potential energy surfaces are degenerate at a conical intersection which is accessed via movement along certain vibrational coordinates.

The vibrationally coherent singlet fission mechanism is thought to be particularly important in the case of rubrene single crystals. The lowest energy crystal structure of rubrene is orthorhombic with C_{2h} symmetry[34]. As a result, the coupling between S_1 and ^{1}(TT) vanishes[188] and symmetry breaking vibrations are required to enable singlet fission. This was believed to be a thermally-activated, incoherent process resulting in relatively slow singlet fission[189,190] compared to pentacene. Recently however, several studies have re-

ported femtosecond ^{1}(TT) formation in rubrene single crystals[35–37] and this has been attributed to vibrational coherence by some authors[35], though not by others[36]. This particular debate is discussed in a recent review[191] and we explore it further in Chapter 6.

This leads us to discuss another area of considerable uncertainty regarding the formation of triplet-pair states through singlet fission, namely the character of the initial triplet-pair state. We have seen that quantum beating is an unambiguous experimental signature of the weakly exchange coupled ^{1}(T...T) state. Recently, Wang et al. performed a detailed analysis of the quantum beats in tetracene and suggested that in addition to the commonly assumed $S_1 \rightarrow {}^1$(TT) $\rightarrow {}^1$(T...T) mechanism, there may be an additional parallel pathway $S_1 \rightarrow {}^1$(T...T) that directly forms weakly-exchange coupled triplet pairs[133]. This conclusion is supported by a recent kinetic study of tetracene, which found that several parallel pathways for singlet fission may coexist, with different mechanisms more pronounced at different temperatures[192].

Triplet-pair dynamics

Having discussed the formation mechanisms of the ^{1}(TT) state, we turn now to the processes that lead to separation of the two triplets. After all, for singlet fission to be useful in photon downconversion for photovoltaics, triplet-pairs must dissociate into independent triplets whose energy can be harvested individually. Furthermore, Scholes has shown theoretically that the spin coherence between fission-borne triplets can in principle remain intact even as the triplets become spatially separated[117]. This has lead to recent interest in the potential of singlet fission materials as sources of entangled quantum states[31]. An understanding of how triplet-pairs separate is therefore of great interest.

A series of transient absorption-based studies of pentacene and TIPS-pentacene have provided evidence that ^{1}(TT) dissociates into ^{1}(T...T) via triplet energy transfer on a timescale of a few picoseconds[193–198]. This Dexter-like process was found to be driven by thermally-activated hopping at room temperature but thought to be disorder driven below around 200 K[194,196]. Since the Dexter rate for triplet transfer is dependent on orbital overlap (Section 2.5.3) the rate of triplet-pair separation is highly dependent on morphology[193]. For example, ^{1}(TT) separates rapidly into free triplets in amorphous TIPS-tetracene but can remain bound for tens of microseconds in a polycrystalline sample[151].

If triplet-pair separation requires one triplet to hop away from the other, a third chromophore must be present in the system. This has been verified

experimentally: Korovina et al. synthesised a range of oligomers with different numbers of perylene chromophores in a linear arrangement[199]. Strikingly, they found that singlet fission occurred only when at least three coupled chromophores were present. With only two, rapid triplet fusion simply repopulated S_1. They concluded that triplet-pair separation drives the singlet fission process for (slightly) endothermic singlet fission materials. For exothermic pentacene however, careful design of the dimer energy landscape can enable triplet-pair separation with only two coupled chromophores[144].

Since there is no direct coupling between the pure spin singlet ^{1}(TT) and the pure spin quintet ^{5}(TT), the observation of ^{5}(TT) in trEPR experiments (Section 2.6.2) means that weakly-exchange coupled triplet-pairs consisting of singlet-quintet mixtures must act as intermediates[139]. In addition to individual triplet hopping, several other mechanisms have been suggested for the interconversion of strongly and weakly exchange-coupled triplet-pairs. These are all based on a time-varying intertriplet exchange interaction J[200], and include polaronic (exciton-lattice) distortion, molecular relaxation or hopping to sites with different J[139]. The latter mechanism has been used to explain the changes in fluorescence of DPH crystals under strong magnetic fields[114] and is supported by the identification of several distinct triplet-pair sites in TIPS-tetracene with differing exchange interactions[119].

The distinction between strongly and weakly exchange-coupled triplet-pairs has only been made in recent years. Merrifield's description of singlet fission considered only vaguely-defined '(TT)' states. Based on the spin Hamiltonian and observed magnetic field effects, we know that these must be weakly-exchanged coupled states. Nevertheless, kinetic schemes containing only a single triplet-pair intermediate have persisted well into the 2010s[15,16,74,142,150,151,184,201], leading to considerable confusion over the nature and interplay of the different triplet-pair states[30]. For example, the role of strongly exchanged-coupled quintets is decidedly unclear. Several reports propose that ^{5}(TT) states can be formed directly from ^{1}(TT) via 'spin evolution' and even that they act as the intermediates between ^{1}(TT) and free triplets $T_1 + T_1$[141–143,147]. In reality, both these processes must be mediated by weakly exchange-coupled triplet-pair states that allow singlet-quintet mixing. We conclude this section by attempting to crystallise our current understanding of the interplay between the various different triplet-pair states in singlet fission in Figure 2.18.

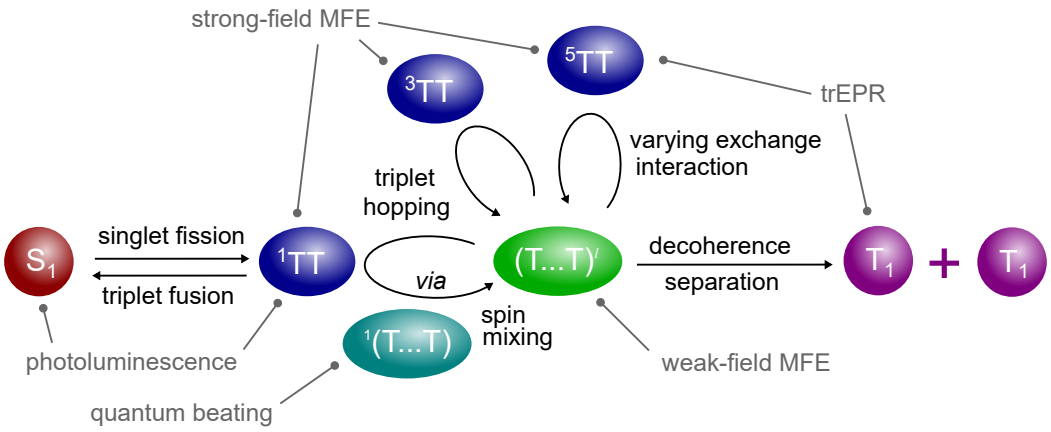

Figure 2.18 | Triplet-pair dynamics following singlet fission. The first step of singlet fission involves the formation of the strongly exchange-coupled spin-0 triplet-pair ^{1}(TT) from the singlet S_1. Both of these states, in principle, possess photoluminescence signatures. Changes to fluorescence under weak applied magnetic fields tell us that weakly exchange-coupled triplet-pairs are formed and the phenomenon of quantum beating shows that this occurs via a singlet superposition state ^{1}(T...T). A time-dependent intertriplet exchange interaction, likely arising through triplet hopping, permits interconversion between the weakly and strongly exchange-coupled pair states, giving rise to the pure spin quintet states observed in trEPR experiments. These have also been inferred through measurements of changes to fluorescence under strong applied magnetic fields. Eventually, weakly exchange-coupled triplet-pairs separate even further and lose their spin interaction resulting in independent triplet excitons T_1, though this last step is rather vaguely defined.

2.6.4 Triplet-triplet annihilation upconversion

We have seen how the intricate triplet-pair dynamics following singlet fission have been investigated in considerable detail in recent years. Much less focus has been given to the role of triplet-pair states during triplet-triplet annihilation yet, as we shall see, they have an important influence on the overall efficiency of the process.

Triplet-triplet annihilation upconversion (TTA-UC) is typically described according to the simple scheme in Figure 2.19. A donor species is photo-excited and produces triplet states, which are transferred to acceptor molecules. Subsequent annihilation of two triplets results in an acceptor singlet state which decays radiatively[40,107,202]. TTA-UC is particularly attractive for solar photon upconversion since excitation energy is stored in long-lived triplet states, potentially allowing efficient upconversion under weak, incoherent illumination.

Donor species for TTA-UC are often metallo-porphyrins or phthalocyanines, in which a heavy metal atom such as platinum or palladium results in large spin-orbit coupling and hence rapid and efficient intersystem crossing (Section 2.4.2)[19]. Osmium-based donor molecules with a direct $S_0 \rightarrow T_1$ absorption allow

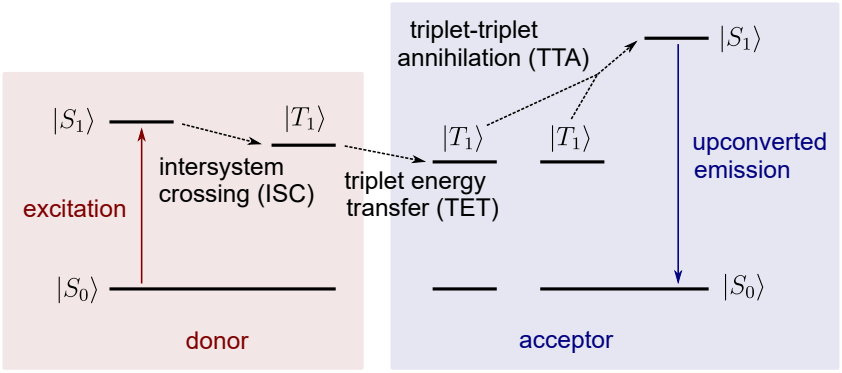

Figure 2.19 | Triplet-triplet annihilation upconversion. Triplet states created on a donor species, for example via intersystem crossing, are transferred to acceptor molecules. Following triplet exciton diffusion, annihilation events can occur between pairs of triplets, resulting in singlet excited states which then decay radiatively.

the energy losses associated with ISC to be circumvented, thereby pushing the incident photon energy further into the near infrared (NIR) and giving a larger anti-Stokes shift[45,203,204]. In this spectral region the low triplet energies result in relatively short lifetimes due to the energy gap law (Equation 2.40) which can limit the efficiency of triplet energy transfer (TET) to the acceptor. To overcome this, inorganic semiconductor nanocrystals such as CdSe, PbSe or PbS can be used as NIR triplet sensitisers, offering tunable bandgaps extending into the infrared[43,205,206].

Upconverting from the NIR to the visible is the most useful type of TTA-UC for photovoltaic applications due to the low bandgaps of common solar absorbers such as silicon[20]. Whilst there has been a concerted effort to develop a variety of new and improved NIR triplet donors, the acceptor molecule is typically selected from only a handful of candidates[107]. Indeed, the vast majority of NIR-visible upconversion systems are based on rubrene[38,42,44–46,203,207,208]. TTA-UC must take place efficiently in solid state devices to be useful for solar energy harvesting. In rubrene, the singlet (2.3 eV) and triplet (1.14 eV) energy level alignment[19] mean that it undergoes efficient singlet fission in the solid state[189], thereby reducing the probability that singlet states emit radiatively. As a result, rubrene is often doped with a small quantity of tetraphenyldibenzoperiflanthene (DBP), which harvests singlet energy from rubrene via FRET[43–46] (Section 2.5.3). The resulting interplay between triplet-triplet annihilation, singlet fission and FRET leads to complex photophysics which we explore in detail in Chapter 8.

An alternative strategy for avoiding singlet fission during rubrene-based TTA-UC is to introduce bulky side groups that force the molecules further apart

and hence reduce the intermolecular interactions required for singlet fission[44]. The limited success of such strategies highlights another important consideration for solid-state TTA-UC: triplet diffusion. In order for upconversion to be efficient under low excitation densities, triplets must be able to diffuse rapidly through the material[20] which requires significant orbital overlap between neighbouring molecules (Section 2.5.3).

As a result of these various challenges, NIR-visible TTA-UC in the solid state has an efficiency of only a few percent or less[45,202]. This overall TTA-UC efficiency Φ_{UC} is typically expressed as the product of the efficiencies of the individual steps:[42,202]

$$\Phi_{UC} = \frac{1}{2}\eta\Phi_{PL}\Phi_{TTA}\Phi_{TET}\Phi_{ISC}. \tag{2.78}$$

Here Φ_{ISC} and Φ_{TET} represent the efficiency of triplet generation on the donor and triplet transfer to the acceptor respectively, Φ_{TTA} describes the competition between decay and annihilation for the fate of acceptor triplets and Φ_{PL} is the photoluminescence quantum yield (PLQY) of the acceptor, in other words the probability that singlet excitons decay radiatively. The spin-statistical factor η gives the probability that a pair of annihilating triplets produces a singlet exciton and it is heavily dependent on the nature and energy levels of the intermediate triplet-pair states.

Spin statistics of annihilation

Magnetic field effects on the delayed fluorescence of anthracene crystals are explained by a model in which annihilating triplet excitons formed mixed-spin triplet-pair states governed by a spin Hamiltonian comprising Zeeman and dipolar terms. In today's language we would call these weakly exchange-coupled triplet-pair states. It is perhaps surprising then that the spin statistics of TTA-UC are discussed solely in terms of strongly exchange-coupled annihilation products[40,202]: ^{1}(TT), ^{3}(TT) and ^{5}(TT). We address this discrepancy in detail in Chapter 7; here we review the conventional treatment of spin statistics.

We have seen that the nine possible strongly exchange-coupled triplet-pair states comprise five quintets, three triplets and one singlet (Equation 2.71). In the simplest terms therefore, we might expect the probability of obtaining a singlet ^{1}(TT) from a pair of triplets to be $\frac{1}{9}$. However, molecular quintet states are energetically inaccessible[209]. ^{5}(TT) states must therefore break apart again into independent triplets[40,202], thus there is a $\frac{5}{9}$ probability that the energy will be recycled. The triplet states ^{3}(TT) on the other hand can undergo rapid

internal conversion (Section 2.4.1) to an energetically nearby triplet state T_N. If this channel is efficient, then half the triplets are lost for $\frac{3}{9}$ of triplet encounters. Putting this together results in a 40% probability that a pair of triplets will annihilate to produce a singlet state, though this could rise to 100% if the $^3(TT) \rightarrow T_N$ channel is inefficient[40].

For rubrene in solution, the spin statistical factor has been measured to be over 60%[38,208], and in Chapter 7 we provide new insight into the reasons for this. Hoseinkhani et al. have claimed near unity spin statistical conversion for perylene-based TTA-UC in solution[41]. The authors suggest that this occurs because the T_2 state is energetically inaccessible in perylene, i.e. $E_{T_2} > 2E_{T_1} + k_BT$. As a result, the $^3(TT)$ states cannot undergo internal conversion and must relax back into a pair of triplets[41]. The dynamics of triplet-pair states thus impacts TTA-UC both via the spin statistical factor and, in NIR-visible systems, through the interplay between singlet fission and triplet fusion.

Chapter 3

Materials and Methods

In this chapter we present the molecules and materials used to make the samples studied in subsequent chapters. We describe in general terms how such samples were prepared and characterised. Finally, we introduce the experimental techniques used to obtain the majority of the data presented in this thesis: time-resolved photoluminescence spectroscopy and transient absorption spectroscopy.

3.1 Materials

Materials and solvents were purchased from commercial suppliers and used as received, with the exception of diF-TES-ADT which was synthesized and purified by collaborators. Unless stated otherwise, solid materials were stored in powder form in a nitrogen-filled glovebox with minimal exposure to ambient light.

3.1.1 diF-TES-ADT

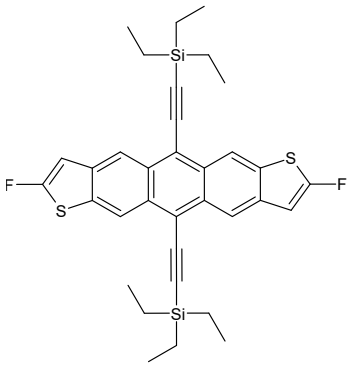

2,8-difluoro-5,11-bis(triethylsilylethynyl)anthradithiophene (diF-TES-ADT) was synthesized and purified by Emma Holland at the University of Kentucky,

following previously reported procedures[210]. diF-TES-ADT is an example of a heteroacene since it contains thiophene as well as benzene rings. It was originally developed as a high-mobility organic semiconductor for solution-processable organic field effect transistors[210–213]. More recently it has been investigated as a singlet fission chromophore that possesses remarkably similar characteristics to tetracene[74].

3.1.2 Palladium (II) octabutoxyphthalocyanine

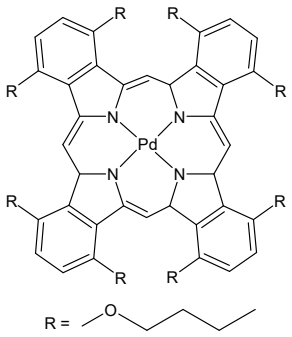

Palladium (II) octabutoxyphthalocyanine (PdPc) was purchased from Frontier Scientific. This molecule acts as a triplet sensitizer: the heavy metal centre enables rapid and efficient intersystem crossing (Section 2.4.2) to form triplets which can then transfer by a Dexter process (Section 2.5.3) to the molecule of interest. PdPc has been used to sensitize triplets on rubrene for triplet-triplet annihilation upconversion[207]; here it was used to sensitize triplets in solid films of diF-TES-ADT.

3.1.3 Pentacene

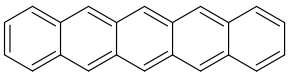

Like diF-TES-ADT, crystalline pentacene was initially of interest as a high-mobility organic semiconductor for organic field effect transistors[214]. Pentacene also exhibits extremely rapid and efficient singlet fission[108] and is the archetypal exothermic singlet fission material. Triple-sublimed grade pentacene was purchased from Merck and used to grow single crystals.

3.1.4 Rubrene

Rubrene is best known as the organic semiconductor with the highest reported charge carrier mobility: $15\,\mathrm{cm}^2/(\mathrm{Vs})$ in single crystal form[215]. It exhibits

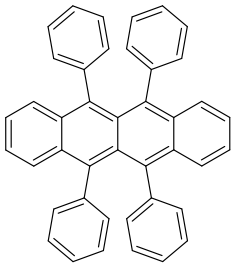

singlet fission[189] and, since its triplet energy is almost exactly half of its singlet energy, concurrent triplet fusion[216]. Rubrene is by far the most common acceptor molecule for near-infrared-to-visible triplet-triplet annihilation upconversion[107]. Rubrene, purified by sublimation, was purchased from TCI and used to make nanoparticle samples and solution procssed polycrystalline films. Rubrene for single crystal growth was purchased from Merck, and rubrene for thermal evaporation was purchased from Ossila.

3.1.5 DBP

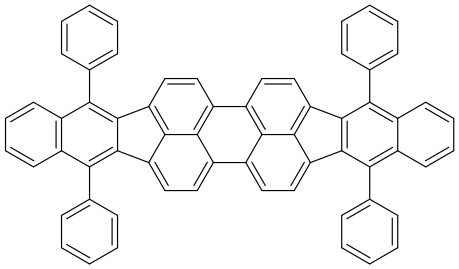

Tetraphenyldibenzoperiflanthene (DBP) is a red-emitting fluorescent dye. It is used in solid rubrene-based triplet-triplet annihilation upconversion systems as an emissive singlet energy sink[43]. DBP was purchased from Merck.

3.1.6 Poly(vinyl alcohol)

Poly(vinyl alcohol) (PVA) is a water-soluble polymer. Here, PVA was used as an oxygen-blocking solid matrix in which to disperse rubrene-based nanoparticles. PVA (99+% hydrolyzed, average molecular weight 130,000) was purchased from Merck.

3.2 Sample preparation

Various kinds of solid-state samples of the above materials were prepared. Where possible, sample preparation was carried out inside a nitrogen-filled glovebox to minimise exposure to oxygen. Some exposure of the solid starting materials was unavoidable during weighing procedures.

3.2.1 Solutions

Solutions were prepared using anhydrous solvents stored inside the glovebox. The general procedure used for preparing solutions was as follows. Solid starting materials were weighed out into amber glass vials on a mass balance located in ambient conditions. Following transfer of the vials back inside the glovebox, anhydrous solvent was added using a graduated pipette and the solution shaken until no solids remained. Solutions were then passed through a polytetrafluoroethylene filter (pore size 0.2 µm) and stored, if necessary, inside the glovebox. In order to study the photophysics of isolated diF-TES-ADT and rubrene molecules, 1×10^{-4} M toluene solutions were obtained by dilution of the more concentrated solutions needed to prepare thin solid films; this minimised errors associated with weighing out small masses of solids.

3.2.2 Thin film fabrication

All solid samples were prepared on clean quartz-coated glass substrates. The substrate cleaning protocol was as follows: 10 minutes sonication in hot deionised water containing a small quantity of Hellmanex III, rinsing under cold deionised water, 10 minutes sonication in pure hot deionised water followed by more rinsing, 10 minutes sonication in acetone and 10 minutes sonication in isopropyl alcohol followed by drying under a continuous stream of nitrogen gas. For solution processed samples, a 10 minute UV-ozone treatment was applied immediately prior to film deposition.

diF-TES-ADT

In Chapter 4, we investigate the ^{1}(TT) state in crystalline diF-TES-ADT. Polycrystalline films were prepared by spin-coating from a 15 mg mL^{-1} solution of diF-TES-ADT in toluene. The spin speed used was 1200 rpm for 40 s, which resulted in thin films with a thickness of $\sim$ 60 nm, evaluated using stylus profilometry (Dektak, Bruker). Additionally, thin films of diF-TES-ADT doped with a small mole fraction of the triplet sensitizer palladium (II) octabutoxyph-

thalocyanine (PdPc) were fabricated. This was achieved by mixing individual solutions of appropriate concentrations in such a ratio as to obtain a final solution of 15 mg mL^{-1} diF-TES-ADT in toluene with PdPc at a ratio of 250:1. This was then spin-coated using exactly the same method as for pure films.

A diF-TES-ADT film comprising large (mm) crystalline grains, used for magnetic field dependent measurements, was prepared by drop-casting. diF-TES-ADT was dissolved at a concentration of 5 mg mL^{-1} in toluene. A substrate was placed in a small petri dish situated inside a larger petri dish containing 1 mL of toluene. 80 µL of the diF-TES-ADT solution was drop-cast quickly onto the substrate and the whole system covered with another glass dish. The solvent was allowed to slowly evaporate overnight. This procedure yielded large single crystalline domains many hundreds of microns in size.

Rubrene

In Chapters 6 and 7 we present data recorded on a polycrystalline rubrene film deposited by thermal evaporation. Rubrene powder was placed in a ceramic crucible inside an evaporation chamber evacuated to 2×10^{-6} mbar or lower. The powder was heated to around 180 °C, causing the rubrene to sublime and deposit itself on substrates held at the top of the chamber. The evaporation rate was continuously measured by a quartz crystal microbalance and maintained at 0.3 Å s^{-1} during deposition by PID feedback control. 125 nm of rubrene was deposited in this way. The films were then annealed at 185 °C for 17 minutes, resulting in visible spherulite formation.

In Chapter 8, we present data on the photophysics of polycrystalline rubrene and DBP-doped rubrene thin films. A 10 mg mL^{-1} solution of rubrene in toluene was spin-coated onto substrates at 1000 rpm for 60 s. The resulting film thickness was $\sim$ 50 nm. For DBP-containing samples, solutions of rubrene (11.3 mg mL^{-1}) and DBP (0.83 mg mL^{-1}) in toluene were combined in a 10:1 ratio, producing a 10 mg mL^{-1} solution of rubrene containing 0.5 mol% DBP. Samples containing 0.1 mol% DBP were also prepared by diluting the DBP solution five-fold before mixing. Films were prepared in the same way as for pure rubrene samples.

3.2.3 Single crystal growth

Single crystals of organic semiconductors can be readily grown by physical vapour transport (PVT)[217,218]. A small quantity of starting material is placed in the hottest part of a horizontal tube furnace, along which a slow, steady flow of carrier gas is flowing. The starting material sublimes and molecules are

transported by the carrier gas down the tube furnace, along which a negative temperature gradient is applied. Once molecules reach a cooler region of the furnace, they can attach themselves to the crystals forming there. Impurities generally crystallise at a different temperature to the target molecule, thus they are spatially separated out by the physical vapour transport method. To obtain highly pure crystals, the sublimation is repeated a second time, using crystals grown during the first growth run as the starting material.

Pentacene single crystals

Single crystals of pentacene were grown by Maik Matthiesen and myself at the University of Heidelberg. A horizontal PVT furnace (Trans Temp, Thermcraft) was used for the growth, and the apparatus was enclosed to prevent possible photo-degradation.

Quartz tubes used inside the PVT furnace were first cleaned with soap and a succession of solvents before being baked at 325 °C for 16 h and allowed to cool fully. 79 mg of starting material was placed at the end of the furnace and the whole assembly was purged under flowing ultra high purity argon gas (99.999%, 50 $cm^3\,min^{-1}$) for 21 h. This gas flow was then maintained for the entirety of the first sublimation. The temperature of the starting material was next raised to 137 °C for 2.5 h and finally set at 289 °C and left for 3 d before being allowed to cool to room temperature. During the first sublimation, pentacene crystals were observed in the hottest part of the crystallization zone ∼220–260 °C, with orange, green and yellow impurities forming in the cooler parts as shown in Figure 3.1.

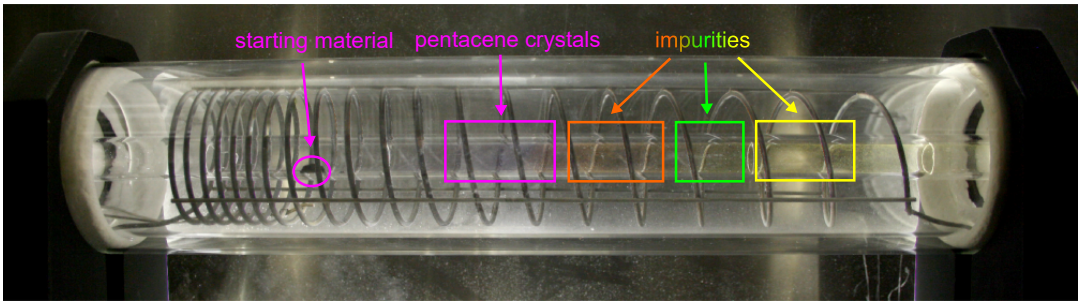

Figure 3.1 | Pentacene single crystal growth. Photograph of the PVT furnace taken during the first sublimation of pentacene. Purple pentacene crystals were observed in the leftmost (hottest) part of the crystallization zone, with orange, green and yellow impurities in the cooler regions.

The purple pentacene crystals grown in the first sublimation were used as the starting material for the second sublimation. The remaining quartz tubes were cleaned and baked as before, and again the whole assembly was purged

with argon for 17 h, this time at a flow rate of 30 $cm^3\,min^{-1}$. The temperature was next held at 137 °C for 2 h, then set to 289 °C for sublimation. After 1 d of sublimation, pentacene crystals were observed in the crystallization zone within a temperature range of ∼220–260 °C. No impurities were observed during the second sublimation.

Rubrene single crystals

The single crystals of rubrene studied in Chapters 5 and 6 were grown by Maik Matthiesen at the University of Heidelberg, using the same PVT furnace. The tube cleaning and purging protocol was similar to that used for the pentacene growth. Rubrene crystals were grown following the procedures in Ref. 219.

Figure 3.2 shows the spatial separation of impurities following the first sublimation run in the PVT furnace. Figure 3.3 shows which of the rubrene crystals obtained from the first run were used as starting materials for the second run, and indicates the crystals used for lamination.

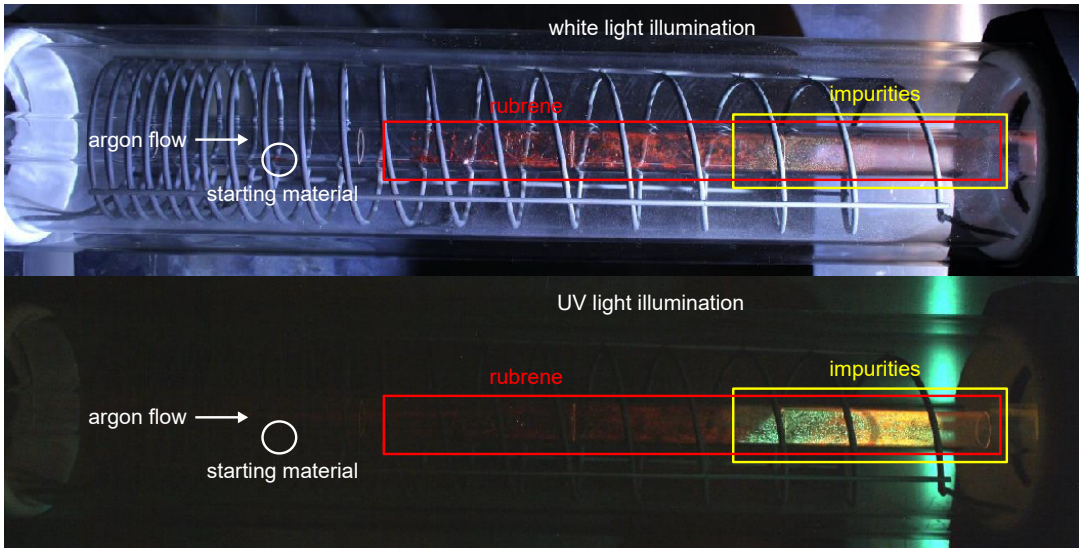

Figure 3.2 | Rubrene single crystal growth I. Photographs of the PVT furnace after the first sublimation run of rubrene. Lateral separation of impurities in the commercial starting material can be clearly observed, allowing high purity crystals to be grown in a second run.

3.2.4 Rubrene-based nanoparticles

In Chapters 7 and 8, we study the photophysical properties of rubrene, focussing on nanoparticles in a PVA matrix as the model system. The rubrene nanoparticle films were prepared by Yoichi Sasaki during his visit to The University of Sheffield. Films of rubrene-based nanoparticles (NPs) dispersed in

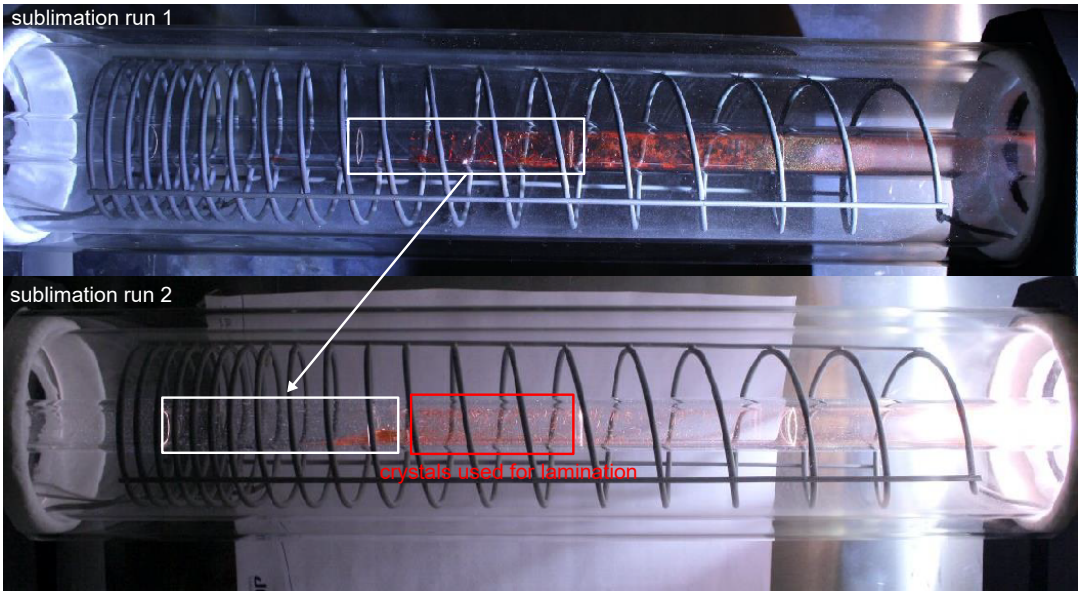

Figure 3.3 | Rubrene single crystal growth II. Photographs of the PVT furnace after the first and second sublimation runs, indicating the crystals from the first run that were used as starting material for the second. The crystals used for lamination are also highlighted.

poly(vinyl alcohol) (PVA) were prepared following previously reported procedures[45,203]. Briefly, a tetrahydrofuran solution of rubrene and DBP ([rubrene] = 5 mM, [DBP] = 0 or 0.5 mol%, 3 mL) was injected into an aqueous solution of sodium dodecyl sulfate (10 mM, 15 mL). The NPs formed were collected by centrifugation and dispersed into an aqueous solution of PVA (8 wt%). The solution was cast onto quartz-coated glass substrates and dried overnight to form films.

3.2.5 Encapsulation

In order to minimise oxygen-induced photo-degradation and/or triplet quenching, all samples measured in ambient conditions were first encapsulated inside a nitrogen-filled glovebox. Films deposited onto substrates were placed face down onto a thin, cleaned glass coverslip. A quick drying two-component epoxy resin was liberally applied around all four edges, resulting a complete seal.

3.3 Sample characterisation techniques

We used a variety of techniques for basic characterisation of both optical and morphological sample properties. These techniques are outlined below.

3.3.1 Optical microscopy

Optical microscopy was used to obtain images of large scale features of certain samples. Microscope images can be collected either using bright-field or dark-field illumination. Bright-field images collect all the reflected and scattered light from the sample and substrate, whilst dark-field illumination excludes the reflected portion and therefore better highlights features of interest on the sample. Images can also be collected by placing the sample between crossed polarisers to provide contrast between differently oriented crystalline domains, each of which has its fast axis in a different direction. In this thesis, we used optical microscopy to qualitatively determine the morphology and quality of samples since the sizes and relative orientations of crystalline domains can be obtained and surface defects can be observed.

For example, Figure 3.4a-i shows bright-field, dark-field and crossed polariser microscope images of the three pentacene single crystals studied in Chapter 4. From these images we can conclude (i) that crystal **1** comprises a single crystalline domain approximately 80 µm × 120 µm that has cracked at one side; (ii) that crystal **2** is approximately 110 µm × 150 µm in size, varies in thickness and has defects on its surface and (iii) that crystal **3** is free of micron-scale defects but is smaller at only around 70 µm × 30 µm.

3.3.2 Atomic force microscopy

Atomic force microscopy (AFM) is a scanning probe technique that enables the topology of a sample surface to be imaged with sub-µm spatial resolution. A cantilever ending in a fine tip is scanned across the sample surface while the position of a laser beam reflected from it is monitored by a photodiode. This allows the deflection of the tip to be monitored as a function of position on the sample surface. A feedback mechanism is employed to maintain a constant height between sample and tip.

The AFM data presented in this thesis were obtained in tapping mode, whereby the cantilever is driven near its resonant frequency. Changes to the oscillation amplitude as the tip is scanned across the surface are related to changes in topology. AFM images of the pentacene single crystals were measured by Maik Matthiesen at the University of Heidelberg using a Bruker Dimension Icon AFM fitted with Scanasyst-Air tips. For example, the thicknesses of the pentacene single crystals were measured by imaging their edges using AFM, as shown in Figure 3.4j-l. AFM images of thin film samples were measured by Rachel Kilbride (University of Sheffield) using a Veeco Dimension 3100

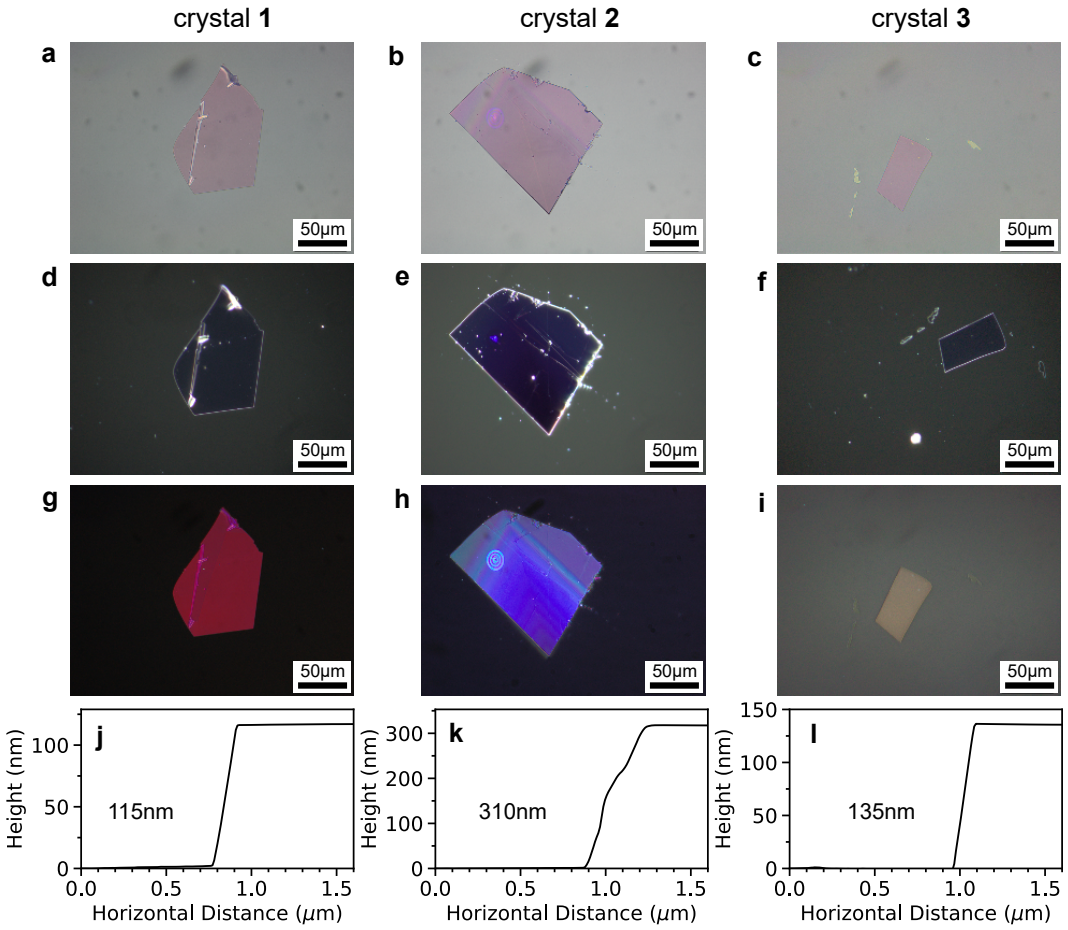

Figure 3.4 | Pentacene single crystal characterisation. **a-i**, Microscope images of pentacene single crystals **1-3**. Bright-field (**a-c**), dark-field (**d-f**) and cross-polarised (**g-i**). **j-l**, Atomic force microscopy was used to measure the thicknesses of the single crystals.

AFM with a nanoscope 3 A feedback controller. The AFM tips were TESPA-V2 probes (Bruker) with a resonance of around 320 kHz and spring constant of 42 N m^{-1}. Gwyddion 2.54 software was used to process the AFM images (levelling by mean plane subtraction, row alignment, horizontal scar correction, zero correction for the height scale).

3.3.3 Grazing incidence wide angle X-ray scattering

The scattering of X-rays from materials can give structural information on atomic length scales. Bragg's law states that constructive interference between scattered X-rays occurs at an angle 2θ when

$$n\lambda = 2d \sin\theta. \tag{3.1}$$

In this equation, λ is the wavelength of the X-rays, $n = 1$ is the refractive index at that wavelength and d is the spacing between planes of atoms. Thus monitoring scattered X-ray intensity as a function of angle gives information, via peaks associated with particular values of d, about the crystal structure of the sample.

In grazing incidence wide angle X-ray scattering (GIWAXS) measurements, the incident X-ray beam is almost parallel to the sample plane; incidence angles are typically around 0.2° and can be tuned in order to selectively probe bulk or, via total external reflection, surface properties of the sample. Scattered X-rays are detected by a two-dimensional detector thus, in addition to crystallographic data, information regarding the orientation(s) of crystallites with respect to the substrate is also obtained. GIWAXS data is typically presented in terms of the reciprocal space scattering vector $\boldsymbol{q}$, where

$$|\boldsymbol{q}| = \frac{4\pi}{\lambda} \sin\theta = \frac{2\pi}{d} \tag{3.2}$$

For this thesis, GIWAXS measurements were performed by Joel Smith and Rachel Kilbride, both at the University of Sheffield, using a Xenocs Xeuss 2.0 system with a liquid Ga MetalJet X-ray source (Excillum). The 9.243 keV X-ray beam was collimated with two sets of slits and the sample chamber, flight tube and detector were held under vacuum to minimise additional scatter. Scattered X-rays from the sample surface were collected with a Pilatus3R 1M hybrid photon counting detector (Dectris) at a distance of 330 mm and a grazing incidence angle of 0.18°. Geometry was refined with a AgBe calibrant after which azimuthal integrations of the data were performed with a full pixel-splitting algorithm to account for issues with detector resolution and binning at small angles[220]. The 2D data was corrected and processed with the GIXSGUI MATLAB toolbox[221].

3.3.4 Absorption and photoluminescence spectroscopy

Ground state absorption spectroscopy, sometimes called UV-vis absorption spectroscopy, is one of the simplest techniques for the optical characterisation of samples. Nevertheless, in addition to providing the energy levels of optically bright states, the lineshape of the measured absorption spectrum can provide useful information regarding vibronic coupling and intermolecular interactions, as described in Sections 2.3.3 and 2.5.1.

In a typical UV-vis absorption experiment, the transmission of light through a sample is monitored as a function of wavelength, λ. The UV-vis spectra

presented in this thesis were measured using a Cary 60 spectrophotometer (Agilent), for which this is achieved by passing light from a broadband Xenon lamp through a scanning monochromator. Transmitted intensity $I(\lambda)$ is recorded by a photomultiplier tube. The transmission $T(\lambda)$ is described by the Beer-Lambert law

$$T(\lambda) = \frac{I(\lambda)}{I_0(\lambda)} = e^{-\alpha(\lambda)d} \tag{3.3}$$

where $\alpha(\lambda)$ is the absorption coefficient, d is the sample thickness and $I_0(\lambda)$ is the incident light intensity, measured internally in the Cary 60 by a second detector. Absorption spectra are presented in (dimensionless) units of absorbance, or optical density, A, where

$$A(\lambda) = -\log_{10} T(\lambda) = \alpha(\lambda) d \log_{10} e. \tag{3.4}$$

We saw in Section 2.3.3 that the absorption spectra of conjugated organic molecules typically comprise progressions of vibronic peaks associated with each optically-allowed electronic transition. For the molecules studied in this thesis, the lowest lying allowed electronic transition, $S_0 \rightarrow S_1$ is in the visible spectral region, with higher energy transitions appearing in the UV.

Photoluminescence spectroscopy is a sensitive probe of light-emitting excited states, in which the intensity of light emitted by a photo-excited sample is collected as a function of wavelength. In Section 2.3.3 we described the simplest case, whereby photoluminescence occurs only from the lowest excited state possessing oscillator strength and is approximately a mirror image of the absorption spectrum associated with that transition. Just as for absorption, intermolecular interactions can alter the photoluminescence lineshape, as discussed in Section 2.5.1.

Other excited states besides S_1 may also have a signature in photoluminescence spectroscopy. For example, we saw in Section 2.5.2 how the formation of excimers can lead to additional broad features in photoluminescence spectra. In Chapter 4, we show that the strongly exchange-coupled spin-0 triplet-pair state ^{1}(TT) can also be detected directly using photoluminescence spectroscopy. The steady-state photoluminescence spectra presented in this thesis were measured on a variety of different experimental setups, described individually in the relevant experimental chapters.

3.4 Time-resolved optical spectroscopy

The absorption and photoluminescence spectroscopies described above provide information regarding the energies and character of optically bright excited states. However, they do not tell us anything about the *dynamics* of these excited states. To truly investigate the photophysics of conjugated organic molecules, we must use time-resolved spectroscopies, in which the absorption or photoluminescence spectra are monitored as a function of time after photo-excitation. In this way, we can build up a 'movie' that shows how excitation energy is transferred between different excited states and how it is lost as molecules return to the ground state.

Time-resolved optical spectroscopy relies on pulsed lasers for excitation. Photons from a 'pump' laser pulse are absorbed, creating a population of excited states and initiating photophysical processes, which we can probe as a function of time delay after excitation. Eventually, the molecules return to the ground state in time to receive the next laser pulse, and the process is repeated. In this thesis, we use two main types of time-resolved optical spectroscopy: time-resolved photoluminescence spectroscopy and transient absorption spectroscopy. These are described in detail below.

3.4.1 Time-resolved photoluminescence spectroscopy

Time-resolved photoluminescence (TRPL) spectroscopy tracks the emitted light intensity as a function of time delay after photo-excitation. This allows us to track the dynamics of emissive excited states in time. If the measurement is spectrally resolved as well, we can also monitor changes to photoluminescence spectra as a function of time. In the data presented in this thesis, such changes typically occur when more than one emissive excited state is present. The detectors in TRPL experiments measure the arrival of individual photons and therefore TRPL can be an extremely sensitive technique. However, it is not selective: photons from any light-emitting state (or indeed other background light sources) will be detected.

Electronically-gated intensified CCD

The majority of the TRPL data presented in this thesis was recorded using an electronically-gated intensified CCD, or iCCD (iStar DH334T-18U-73, Andor) connected to a spectrograph (Shamrock 303i, Andor) that disperses the light onto the iCCD pixel array. Inside the iCCD camera, the dispersed photons are incident on a photocathode, producing photoelectrons. The photoelectrons are

drawn towards a thin plate comprising a honeycomb network of small glass tubes with a resistive coating. A high potential difference is applied across this plate, which causes the photoelectrons to accelerate and dislodge secondary electrons from the tube walls, resulting in a gain (or intensification) that depends on the applied voltage. The cloud of electrons exiting the plate next hits a phosphor screen, producing photons that are detected by a CCD array cooled to −30 °C by a Peltier element.

In addition to the extremely high sensitivity of the iCCD, the image intensifier can also act as a fast optical switch. Application of a high negative voltage between the photocathode and honeycomb plate causes the photoelectrons to be swept across the gap and subsequently detected: the iCCD is gated 'on'. If a positive voltage is applied instead, the photoelectrons are unable to cross the gap and the iCCD is gated 'off'.

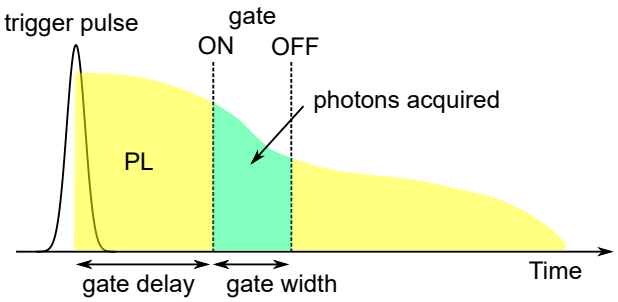

Figure 3.5 | iCCD gating. A camera read cycle is triggered for each laser shot. The gate is opened after an adjustable gate delay, remains open for an adjustable gate width and then closes. Photons are acquired by the camera during this time. Typically thousands of laser shots are averaged for each PL spectrum acquired in this way.

The timing of the electronic gating is controlled by a digital delay generator (DDG). A read cycle is initiated by an electronic trigger pulse corresponding to a pump laser shot. The DDG introduces a time delay (the 'gate delay') following receipt of the trigger, after which the iCCD is gated 'on' for a period of time called the 'gate width'. During this interval, photons are accumulated by the camera. Both the gate delay and gate width, as well as the gain voltage, can be controlled externally by computer software. In this way, photoluminescence spectra can be recorded at different time delays relative to optical excitation. This is illustrated in Figure 3.5. The repetition rate of the pump lasers used was either 1 kHz or 5 kHz and each spectrum is an average of many hundreds of laser shots. The shortest possible gate width is principally determined by the photocathode and gating electronics and is around 2 ns for our system. The longest gate delay depends on the repetition rate of the laser; for example it is

1 ms for a 1 kHz repetition rate.

In order to measure the dynamics of the PL as a function of time, the gate delay is incremented by a gate step for each data point. Since the PL signal decreases with time as the excited states decay, the signal to noise ratio gets progressively worse at later time delays. To overcome this and take advantage of the excellent sensitivity of the iCCD over the full range of timescales that we can measure (ns to ms), the PL dynamics were recorded in short sections, using a constant gate step and gate width for each section (Figure 3.6a). The gate width was always less than or equal to the gate step. The gate delay, width and step were increased for each subsequent section. The gain and exposure (number of shots accumulated) could also be increased. A temporal overlap was ensured between the end of each section and the start of the following one. Background spectra were also collected for each section.

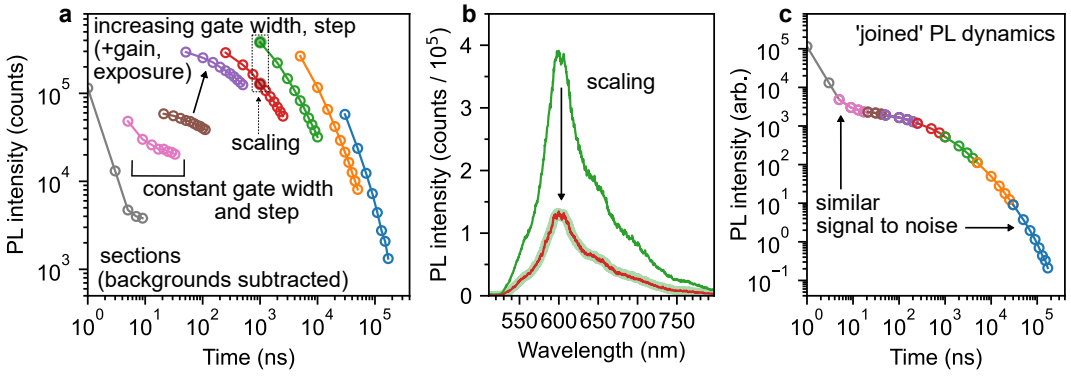

Figure 3.6 | iCCD data processing. **a**, PL dynamics are collected in sections during which the gate width and step are kept constant (shown here for $\lambda = 600$ nm). For sections starting at later time delays, the gate width and step are increased (gain and exposure can also be increased). **b**, At the overlapping time point between sections, the second PL spectrum is scaled by a constant factor such that it coincides with the first. **c**, This procedure results in a complete TRPL dataset (plotted here for $\lambda = 600$ nm).

To obtain the full TRPL dynamics, the sections were joined together. First, the background was subtracted from every spectrum in each section. Next, at each overlapping time point between sections, the second section was scaled by a constant factor until the spectra at the overlapping time point exactly match in shape and intensity. In this way, the true PL kinetics can be obtained over many orders of magnitude in time and intensity whilst maintaining a good signal to noise ratio. This procedure for obtaining complete TRPL dynamics using the iCCD is illustrated in Figure 3.6.

The spectral sensitivity of our iCCD is governed principally by the photocathode (third generation 'VIH') and spectrograph grating (blazed at 500 nm,

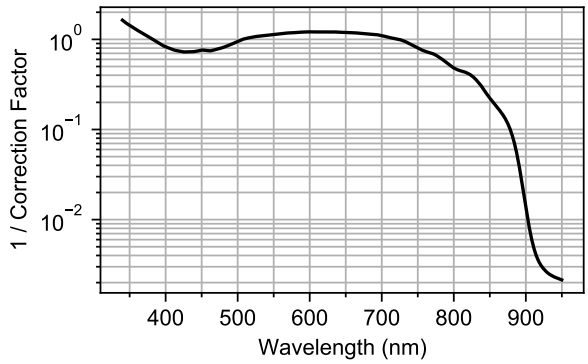

Figure 3.7 | iCCD spectral sensitivity. Spectral sensitivity of our iCCD measured by Andrew Musser using a calibrated light source. The sensitivity is flat in the visible spectral region but drops off significantly in the near-infrared.

150 lines per mm). Figure 3.7 shows the spectral sensitivity of our iCCD, measured by Andrew Musser using a calibrated broadband light source. The sensitivity is almost constant across the visible spectral region, but decreases significantly in the near-infrared. All PL spectra recorded using the iCCD and presented in this thesis have been corrected for spectral sensitivity.

The optical setup surrounding our iCCD is highly configurable and was adjusted and optimised based on the sample and type of measurement. Figure 3.8 shows the most common configurations. Figure 3.8a shows the standard configuration used for most room temperature measurements. Figure 3.8b illustrates how the setup was modified to allow a magnetic field to be applied across the sample. Figure 3.8c shows how the sample can be placed inside a nitrogen bath cryostat, allowing TRPL data to be collected at temperatures down to 77 K.

Signals that are often weak, coupled with the relatively low kHz repetition rates of the pump lasers, mean that the density of excited states generated by each pulse must be fairly high in order to obtain a good signal to noise ratio. For a given pump fluence F (energy per pulse per unit area), the density of generated excited states n is given by approximately by

$$n = \frac{F\lambda}{hcd}(1 - 10^{-A}) \tag{3.5}$$

where h and c are Planck's constant and the speed of light respectively, d is the sample thickness and A is the sample absorbance at the excitation wavelength λ. The pump fluences used throughout this thesis are typically on the order of 1–100 µJ cm^{-2}. For a 'typical' organic thin film 100 nm thick, with an absorbance of 0.2 at 532 nm, such fluences result in initial excited state densities of approximately 10^{17}cm^{-3} to 10^{19}cm^{-3}.

At such densities, photo-excited singlet excitons may interact with each

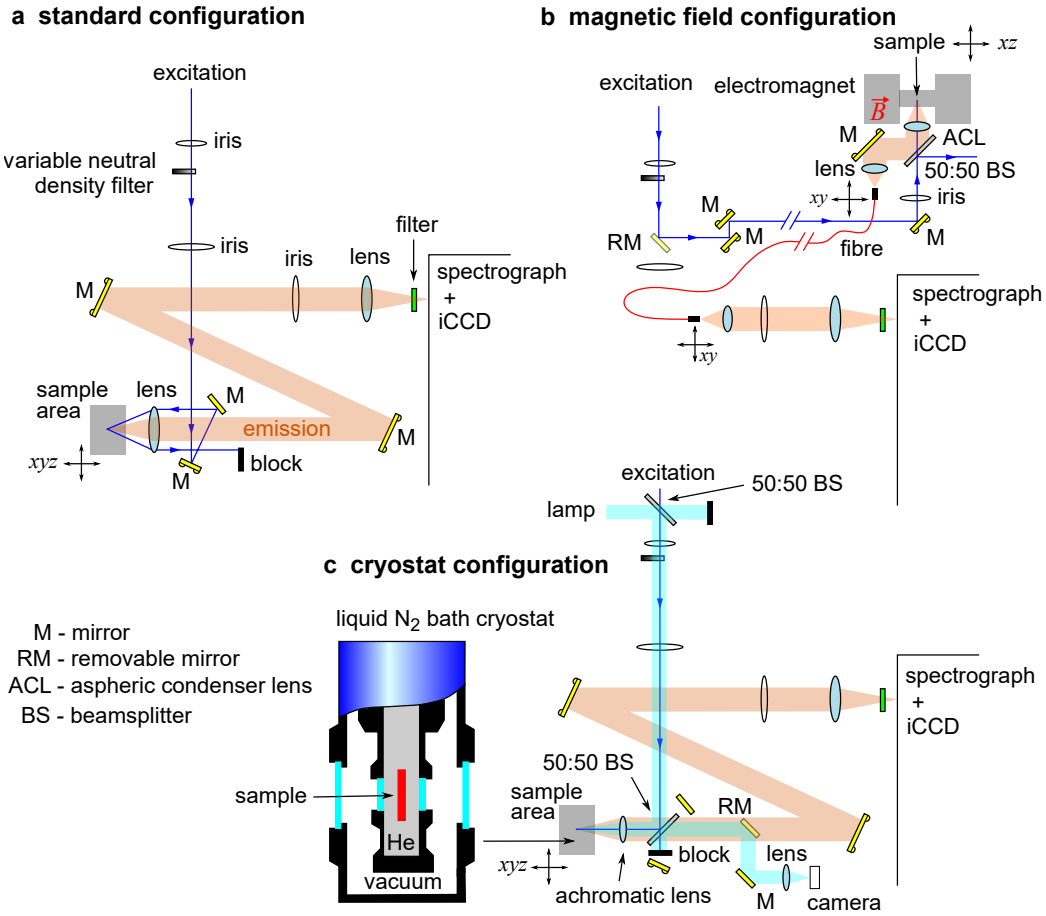

Figure 3.8 | iCCD setups. **a**, Pulsed excitation (various sources) is focussed onto the sample, usually using an aspherical condensing lens. The photoluminescence is collimated by the same lens and directed onto the entrance slit of the spectrograph. A filter is placed before the slit to remove scattered pump light. **b**, The setup can be modified to allow measurements of TRPL under applied magnetic field. Here, the PL is sent via optical fibre back to the spectrograph. **c**, The setup can also be modified to include a sample-in-exchange-gas nitrogen bath cryostat. Excitation is changed to normal incidence, which allows the sample to be simultaneously imaged using a broadband lamp and camera. This imaging capability was used to locate the pentacene single crystals inside the cryostat.

other and undergo singlet-singlet annihilation, which can complicate the measured time-resolved population dynamics. To test for such effects, we repeated our time resolved experiments at several pump fluences. When these data are normalised and overlayed, any differences in the initial population dynamics indicate the presence of singlet exciton annihilation. For example, singlet-singlet annihilation is absent from the data in Figure 4.8 but present in that of Figure J.11.

Time-correlated single photon counting

A small amount of TRPL data presented in this thesis was instead collected by time-correlated single photon counting (TCSPC). Here the laser repetition rates are typically much greater ($\sim$ MHz). Following each laser pulse, an electronic timer is started. The timer is stopped once a photon emitted from the sample arrives at the detector and the time delay recorded. Once enough photons have been accumulated the histogram of arrival times reflects the photoluminescence dynamics of the sample. The data is not spectrally resolved; instead the emitted light can be passed through a monochromator before detection, allowing the PL dynamics to be monitored separately at different wavelengths. TCSPC data has better time resolution than the iCCD, typically $\sim$ 100 ps, and measurements are performed at much lower pump pulse energies. The iCCD on the other hand can access a far greater range of time delays, with excellent sensitivity.

The TCSPC measurements in Chapter 8 were carried out by Yoichi Sasaki at Kyushu University using a lifetime spectroscopy system (Quantaurus-Tau C11367-02, Hamamatsu). The excitation wavelength was 470 nm.

3.4.2 Transient absorption

TRPL measurements can only directly probe the photophysics of emissive states. The dynamics of dark excited states, such as triplet excitons can at best be indirectly inferred. Transient absorption (TA) spectroscopy is able to probe the dynamics of, in principal, all excited state species.

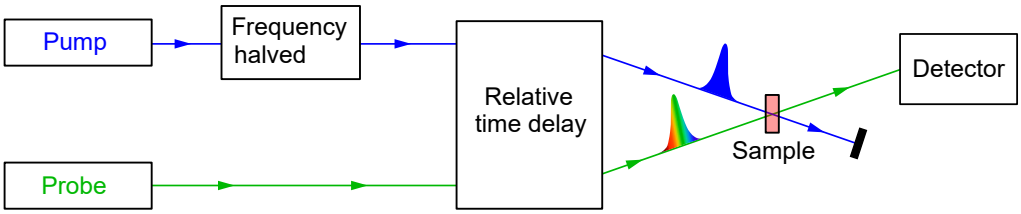

Figure 3.9 | Transient absorption spectroscopy. Pump and broadband probe beams are focussed and overlapped at the sample. The frequency of the pump pulses is modulated to be half that of the probe pulses. A tuneable time delay is also introduced between them. The probe pulses are dispersed onto a detector that repeatedly records their spectrum for each laser shot.

TA spectroscopy is a pump-probe technique, of which the most basic components are shown in Figure 3.9. The sample is photo-excited with a pump pulse. After a controllable time delay, a second, spectrally broad probe pulse arrives, focussed onto the sample at the same location as the pump. The frequency

of the pump is halved relative to the probe, such that the spectrally-resolved absorbance of the probe pulses is recorded both in the presence and absence of photo-excitation. The transient absorption signal ΔA is the difference between these two absorption spectra

$$\Delta A = A_{on} - A_{off}, \tag{3.6}$$

and is averaged over many laser shots at each time delay. Transient absorption data is sometimes recorded or presented as changes in transmission, $\Delta T/T$, which we can easily relate to ΔA using equation 3.4:

$$\frac{\Delta T}{T} = \frac{T_{on} - T_{off}}{T_{off}} = 10^{-\Delta A} - 1. \tag{3.7}$$

Three types of spectral feature contribute to the total TA signal. Figure 3.10 illustrates how these different features arise and how they manifest themselves in TA spectra. Figure 3.10a shows the effect of the probe pulse when the pump is absent. The sample absorbs some of the probe light as molecules undergo transitions from the ground state to optically-allowed excited states, for example S_1. A_{off} is therefore the ground state UV-vis absorption spectrum of the sample, as demonstrated in Figure 3.10b. In Figure 3.10c, we show the situation when the probe pulse follows a pump pulse. The pump promotes some molecules to excited states, for example S_1. Subsequent photophysical processes may additionally populate other excited states: for example triplet states could be populated by intersystem crossing or singlet fission. When the probe pulse arrives, there are new optically allowed transitions available to absorb some of the light, for example $S_1 \rightarrow S_N$ or $T_1 \rightarrow T_N$, that were not possible when the sample was in the ground state. These are known as photo-induced absorptions (PIAs). Since the pump pulse has depleted the ground state population, fewer ground state molecules are able to absorb probe photons, and the absorbance of the probe is decreased. This is known as the ground state bleach (GSB). Finally, molecules may decay radiatively back to the ground state. These emitted photons manifest themselves as a negative absorption, known as stimulated emission (SE). These three types of signal combine to give an A_{on} spectrum, drawn in Figure 3.10d, that is different to A_{off}. Figure 3.10e shows the resulting TA spectrum, with the negative GSB and SE features and positive PIA features highlighted.

In addition to these 'real' signals that truly arise due to excited state species, TA data can also contain artefacts. There are two main types. The first is the so-called thermal artefact[222]. This can arise when the ground-state ab-

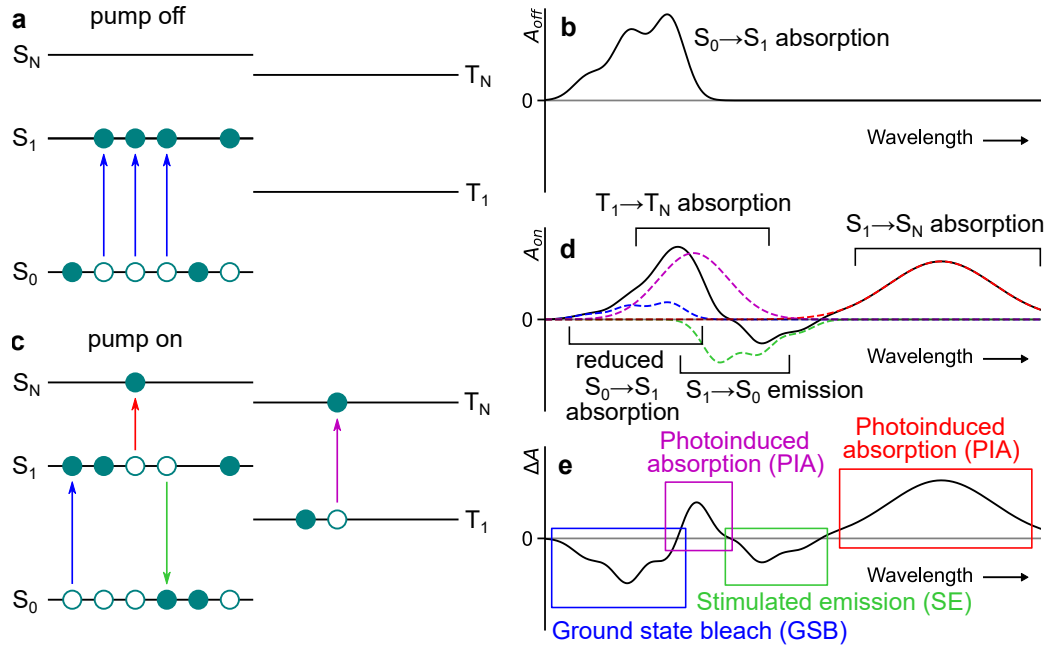

Figure 3.10 | Transient absorption features. **a**, When the pump is off, the probe simply excites molecules from the ground state to optically allowed excited states, such as S_1. As a result the probe absorbance is simply the ground state UV-vis absorption spectrum, as shown in (**b**). **c**, When the probe is preceded by a pump pulse, some molecules exist in excited states such as S_1 and T_1. This changes the probe absorption. **d**, There is a reduction of the ground state absorption, the possibility of radiative emission which adds light to the probe, and new excited state absorptions in, for example, the singlet and triplet manifolds. **e**, The resulting transient absorption signal can contain all of these features: negative GSB and SE signals and positive PIA signals.

sorption spectrum shifts with temperature. The intense pump pulses can cause localised heating of the sample, causing a shift in the ground-state absorption spectrum that is picked up by the probe. Thermal artefacts therefore often resemble a derivative-like feature in the GSB spectral region. Measuring the dynamics of samples deposited on substrates of different thermal conductivities (such as quartz and sapphire) can distinguish between real signals and thermal artefacts: heating-induced signals decay faster in substrates of higher thermal conductivity[223].

The second category of artfact occurs when the pump and probe pulses are temporally overlapped (around the so-called 'time zero'). These 'coherent artefacts' arise from non-sequential light interactions involving pump and probe simultaneously[224] and can complicate TA spectra in the immediate vicinity of time zero.

Transient absorption data is also affected by chirp, whereby the temporal overlap between pump and probe is wavelength-dependent. This occurs because

the broadband white light probe has an intrinsic group velocity dispersion, i.e. redder wavelengths are generated at a slightly different time to bluer ones. If the probe passes through any dense materials such as quartz or glass before hitting the sample, the group velocity dispersion can increase to picoseconds[224]. In our transient absorption setups, this is minimised by using reflective optics where possible. All transient absorption data presented in this thesis has been corrected for chirp.

Finally, we note that the relative polarisation of the linearly polarised pump and probe beams is an important consideration in TA spectroscopy. The pump will preferentially excite molecules whose dipole moment is parallel to the pump polarisation. Similarly, the probe will preferentially interact with molecules whose dipole moments are parallel to the probe polarisation. This could in principal lead to artefacts, for example in solution molecules may rotate away from their initial orientation with time, giving spurious dynamics. To eliminate such polarisation and photo-selection effects, the pump and probe polarisations are usually set to the so-called magic angle of $\theta = 54.7°$, at which the dipole orientation factor $3\cos^2\theta - 1$ (see, for example, equation 2.53) vanishes[224].

In some cases we may wish to explicitly monitor the changes in excited state polarisation with time, for example to learn about the timescales of exciton migration by site-to-site hopping[224]. In such cases, we can measure the time-dependent anisotropy $r(t)$, defined as

$$r(t) = \frac{\Delta A_{\parallel}(t) - \Delta A_{\perp}(t)}{\Delta A_{\parallel}(t) + 2\Delta A_{\perp}(t)} \tag{3.8}$$

where $\Delta A_{\parallel}(t)$ and $\Delta A_{\perp}(t)$ are measured with pump and probe polarisations parallel and perpendicular respectively. In this thesis, transient absorption data were recorded with the pump and probe polarisations set to the magic angle unless stated otherwise.

We used two different transient absorption setups to obtain data ranging from < 1 ps to 1 ms. These two systems are described below. As described above for the case of time-resolved photoluminescence, transient absorption measurements were repeated at several pump fluences in order to test for exciton-exciton annihilation effects.

Picosecond transient absorption setup

Our picosecond TA setup, a modified version of a commercial instrument (Helios Fire, Ultrafast Systems), is depicted in Figure 3.11. It allows transient absorption data to be collected from < 1 ps to around 7 ns in time, with a time

resolution of around 100 fs.

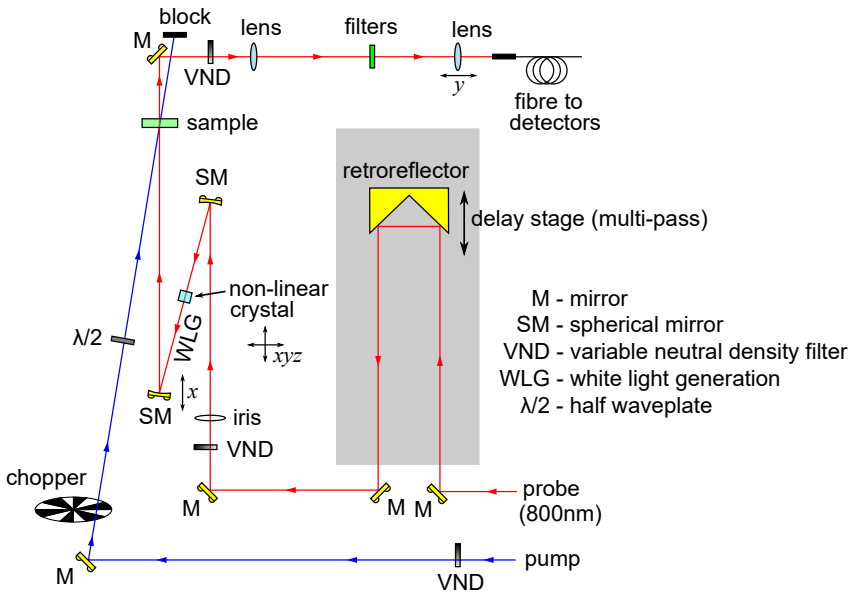

Figure 3.11 | Picosecond transient absorption setup. The probe pulses are generated by focussing the 800 nm beam through a non-linear crystal (continuously translating calcium fluoride for UV-visible or sapphire for near-infrared). The probe is focussed and overlapped with the pump (chopped to half the probe frequency) at the sample. The pump is focussed by a long focal length spherical mirror not shown in the diagram. Pump-probe delay is controlled using a motorised linear stage. Pump-probe polarisation is set using a half waveplate in the pump line.

A Ti:sapphire regenerative amplifier (Spitfire ACE PA-40, Spectra-Physics) providing 800 nm pulses (40 fs FWHM, 10 kHz, 1.2 mJ) is used to generate both the pump and probe beams. A portion of the amplifier output is passed into an optical parametric amplifier (TOPAS Prime, Light Conversion), generating tuneable narrowband pump pulses. Probe pulses spanning the ranges 350–700 nm and 850–1300 nm are generated by focussing another portion of the 800 nm beam through a continuously translating calcium fluoride or sapphire crystal, respectively. The delay between pump and probe is controlled using a multi-pass motorized linear stage. Detection of the probe is carried out using a commercial instrument (Helios, Ultrafast Systems) equipped with CMOS and InGaAs detectors for the UV-visible and NIR spectral regions respectively.

Nanosecond transient absorption setup

Our nanosecond TA setup is depicted in Figure 3.12. It allows transient absorption data to be collected from $\sim$ 1 ns to 1 ms in time, with a time resolution of around 1 ns.

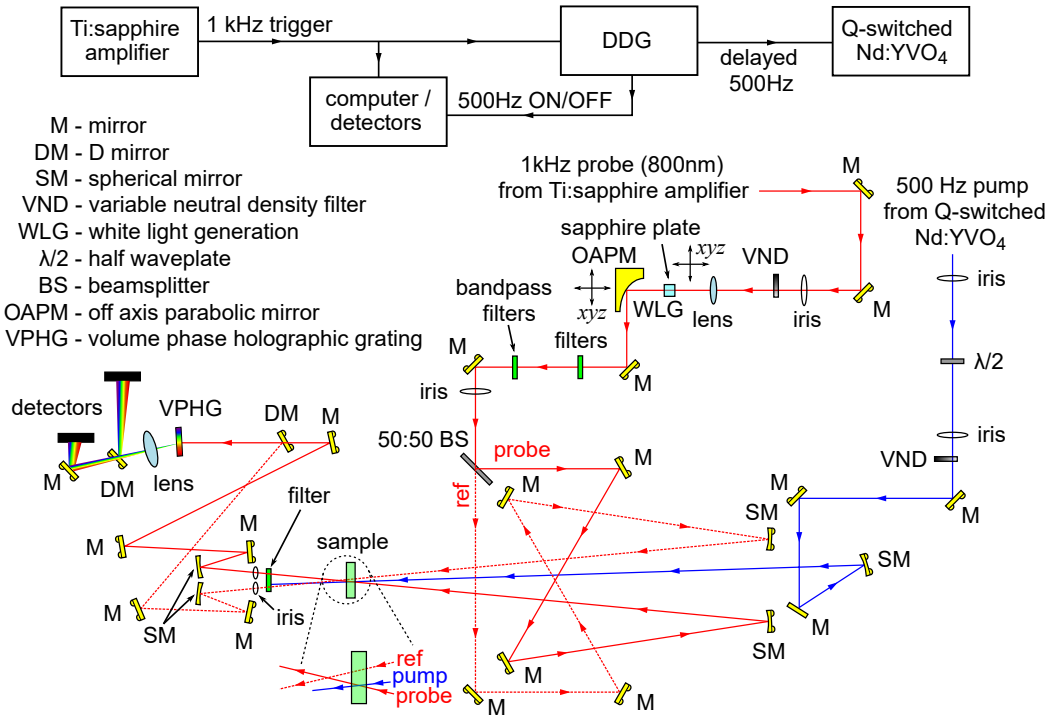

Figure 3.12 | Nanosecond transient absorption setup. In order to measure transient absorption signals with long time delays, pump and probe beams are generated from different laser systems, with the relative relay and frequency modulation provided electronically by a digital delay generator (DDG).

A different Ti:sapphire regenerative amplifier (Solstice, Spectra-Physics) providing 800 nm pulses (90 fs FWHM, 1 kHz, 4 mJ) is used to generate the probe beam. Probe pulses spanning the range 450–700 nm are generated by focusing a portion of the 800 nm beam through a sapphire crystal. 532 nm or 355 nm pump pulses (temporal width < 500 ps, 500 Hz) were provided by the frequency-doubled or -tripled output of a Q-switched Nd:YVO_4 laser (Picolo-AOT, Innolas). Pump–probe delay is controlled electronically using a digital delay generator (DG645, Stanford). The pump and probe beams are overlapped at the sample adjacent to a reference beam obtained by passing the probe through a 50:50 beamsplitter. The reference is used to correct for shot-to-shot variation in the probe spectrum, thereby improving the signal to noise ratio. The probe and reference beams are dispersed by a volume phase holographic grating (Wasastch) and detected by a pair of linear image sensors (S7030, Hamamatsu) driven and read out at the full laser repetition rate by a custom-built board from Entwicklungsbüro Stresing. The TA data is acquired using home-built software.

Pump-push-probe spectroscopy

The pump-push-probe TA setup is depicted in Figure 3.13. When the push path is blocked, the setup can be used for ordinary picosecond TA experiments. The probe path is shared with the nanosecond transient absorption setup and is shown in Figure 3.12.

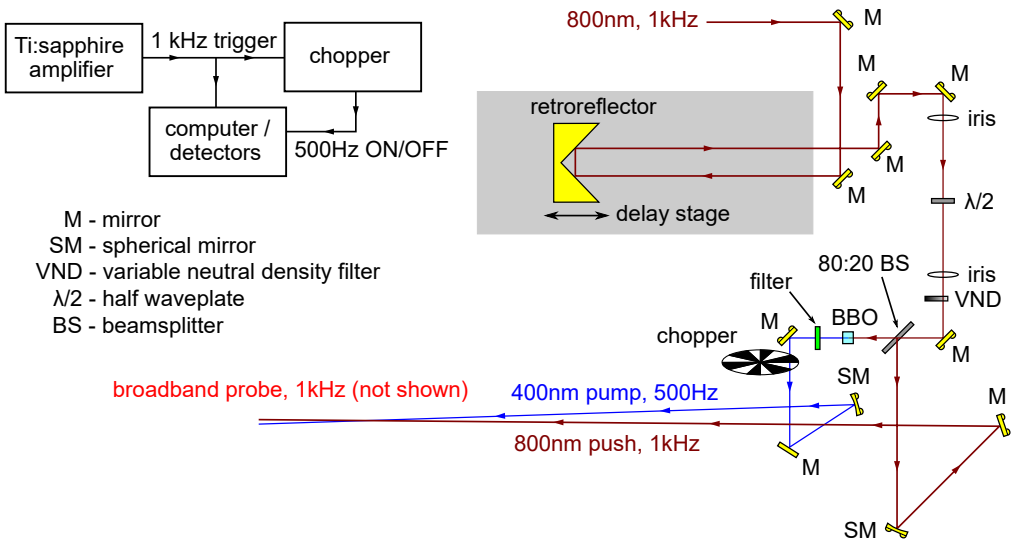

Figure 3.13 | Pump-push-probe setup. The nanosecond transient absorption setup (Figure 3.12) can be adapted to enable pump-push-probe experiments with picosecond time resolution. Only the pump and push beams are shown here for clarity. There is a fixed 1070 ps delay between pump and push.

Pump and push pulses are generated from another portion of the Ti:sapphire regenerative amplifier output. An 800 nm beam is sent along a computer controlled optical delay line. Following the delay, the beam is split into two parts. Pump pulses at 400 nm are obtained by passing the 80% transmitted portion through a BBO crystal. A Schott BG39 filter is used to remove residual 800 nm light and the pump pulses are chopped to 500 Hz using an optical chopper. The remaining 20% reflected portion is used as the push. Both the pump and push are focussed and overlapped at the sample position. The differing path lengths result in a fixed 1070 ps delay between the pump and push pulses. The probe optics and data acquisition are identical to those described above for the nanosecond transient absorption setup.

3.4.3 Spectral deconvolution

Both TRPL and TA data can contain spectrally overlapping contributions from different excited state species. In such cases, we cannot obtain the dynamics of the different excited states without first disentangling the different components.

Various algorithms exist for this purpose but in this thesis we use only one: Multivariate Curve Resolution Alternating Least Squares (MCR-ALS)[225,226].

The central, and only, assumption of MCR-ALS is that the time- and wavelength-resolved dataset comprises a fixed number of spectrally invariant components. This is not always a valid assumption: for example vibrational relaxation can cause spectra to shift as a function of time[224]. If the assumption does hold, then a dataset $\boldsymbol{D}$ represented as a matrix of p time points (rows) and q wavelength values (columns) can be decomposed into the product of two matrices $\boldsymbol{C}$ ($p \times n$) and $\boldsymbol{S}$ ($q \times n$) that contain the concentrations and associated spectra respectively of the n components:

$$\boldsymbol{D} = \boldsymbol{C}\boldsymbol{S}^T + \boldsymbol{E} \tag{3.9}$$

where $\boldsymbol{E}$ is the matrix of residuals[225,226]. The MCR-ALS algorithm, implemented as a MATLAB toolbox, finds the spectral profiles and their associated concentrations that minimise these residuals, for a given number of components and an appropriate initial guess. In this thesis, we use MCR-ALS solely to extract the spectra and dynamics of known excited states and never to determine the number of components in the dataset.

Chapter 4

Emissive spin-0 triplet-pairs via triplet-triplet annihilation*

As discussed in Chapter 2, singlet fission and triplet-triplet annihilation represent two highly promising ways of increasing the efficiency of photovoltaic devices. Both processes are believed to be mediated by a biexcitonic triplet-pair state, $^1(TT)$. Recently however, controversy has arisen over the role of $^1(TT)$ in triplet-triplet annihilation. In this chapter, we use intensity-dependent, low-temperature photoluminescence measurements, combined with kinetic modelling, to show that distinct $^1(TT)$ emission arises directly from triplet-triplet annihilation in high-quality pentacene single crystals and anthradithiophene (diF-TES-ADT) thin films. These results demonstrate that a real, emissive triplet-pair state acts as an intermediate in both singlet fission and triplet-triplet annihilation and that this is true for both endo- and exo-thermic singlet fission materials.

4.1 Introduction

The conversion from singlet to triplets through singlet fission is widely accepted to proceed via a correlated triplet-pair state usually denoted ^{1}(TT) in a process which we wrote in Section 2.6 as[134,169,228]

$$S_1 \rightarrow {}^1(TT) \rightarrow (T...T) \rightarrow T_1 + T_1. \tag{4.1}$$

^{1}(TT) is a multiexcitonic triplet-pair state with overall spin-0 (a singlet), yet as described in Section 2.6.1, its spin wavefunction can be approximated as a superposition of pairs of individual triplet excitons[29,30,117,124]. As discussed in

*This chapter has been adapted with permission from Springer Nature from the following publication[227]: Bossanyi et al., *Nature Chemistry* **13**, 2, 163-171 (2021). The majority of the work was performed by myself; contributions from collaborators are explicitly noted.

Section 2.6.2, spectral signatures of this state are widely debated in part because the main method used to study it, transient absorption spectroscopy (Section 3.4.2), provides very similar signatures for ^{1}(TT), (T...T) and free triplets. Calculations[163–165] suggest that this is particularly true in the visible spectral region where most experiments are performed. In addition, paramagnetic resonance techniques[139,140,149], which we introduced in Section 2.6.2, are blind to spin-zero states such as ^{1}(TT).

Instead, the simplest and most explicit probes of the ^{1}(TT) state are direct ground state absorption or photon emission. While many authors have assigned features from emission spectra to ^{1}(TT) with varying degrees of conviction[74,136,150,151,153,157–159,229,230], recent work by Dover et al.[32] calls these assignments into question. In particular, they argue that the redshifted spectral features are not direct intermediates to singlet fission, i.e. ^{1}(TT), but emission from trap states which instead hinder singlet fission, as previously reported[231–234]. This is important because a lack of spectral signature of ^{1}(TT) implicitly questions the existence of ^{1}(TT) as a real, bound intermediate state[74].

Dover et al. pointed out that an intermediate to singlet fission must also be present in the reverse process, triplet-triplet annihilation. They showed that this was not the case in concentrated TIPS-tetracene solutions[32]. This raises two related questions: what (if any) is the photoluminescence signature of the ^{1}(TT) state and do we observe it during triplet-triplet annihilation as well as singlet fission?

In this chapter, we study both high-quality pentacene single crystals and thin films of 2,8-difluoro-5,11-bis(triethylsilylethynyl)anthradithiophene (diF-TES-ADT) and observe clear ^{1}(TT) emission via triplet-triplet annihilation. This demonstrates conclusively that in the solid state, which is most relevant to device applications, ^{1}(TT) plays the role of a bound intermediate state in *both* singlet fission and triplet-triplet annihilation (TTA). We show that ^{1}(TT) emission signatures are consistent with Herzberg-Teller intensity borrowing, and are distinct from the broad, featureless excimer spectra (Section 2.5.2) sometimes attributed to ^{1}(TT)[150,157].

4.2 Model systems

In order to study ^{1}(TT) produced via singlet fission or TTA, we focussed on two materials as model systems: diF-TES-ADT (Section 3.1.1) and pentacene (Section 3.1.3). We chose to focus on diF-TES-ADT (Figure 4.1a) as our endothermic model system for several reasons.

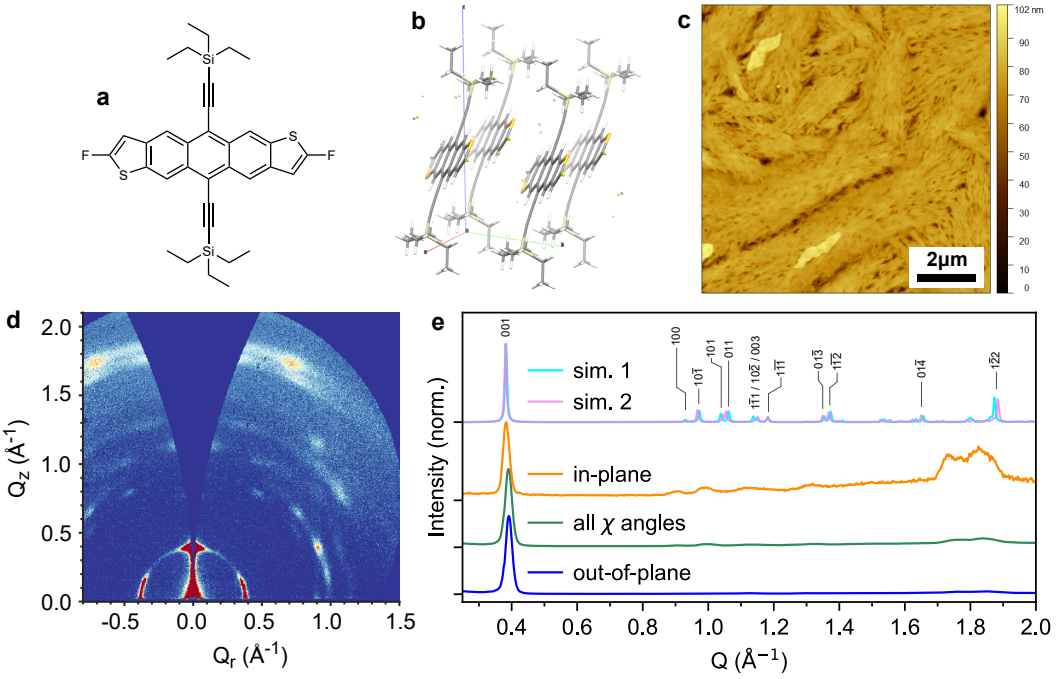

Figure 4.1 | Morphological characterisation of diF-TES-ADT films. **a**, Structure of the diF-TES-ADT molecule. **b**, Brickwork crystal packing of diF-TES-ADT[213]. **c**, AFM scan of the film surface showing micron-scale crystalline texture similar to previous reports of diF-TES-ADT crystal growth with the edge-on motif[235]. **d**, GIWAXS pattern of a diF-TES-ADT thin film indicating polycrystalline structure with primarily lamellar stacking. **e**, Simulated and experimental diffraction patterns for diF-TES-ADT. GIWAXS data was integrated through various χ angles normal to the beam incidence at the detector; out-of-plane (in the Q_z direction, $\chi = 90° \pm 20°$), in-plane (which includes all other angles, $0° \leq \chi \leq 70°$), and the full χ range. The out-of-plane scatter is dominated by a feature corresponding to the (001) plane, indicating a predominantly lamellar textured film (edge-on motif[235]). Simulated patterns were generated from Ref. 210 (light blue line, sim. 1) and Ref. 213 (purple line, sim. 2) with the latter acquired from a single crystal of the pure anti diF-TES-ADT isomer at 180 K. Slight peak shifts between the measured and simulated data could be explained by thermal expansion and modified crystal packing at room temperature.

Firstly, compared with tetracene, it has a simple brickwork crystal structure[210], illustrated in Figure 4.1b and confirmed by our grazing incidence wide-angle X-ray scattering (GIWAXS) measurements from a polycrystalline film in Figure 4.1d. In addition, there is no known polymorphism or other phase transition between 100 K and room temperature[74,236]. We note that both the GIWAXS (Figure 4.1d,e) and AFM (Figure 4.1c) characterisation[†] are consistent with previous reports of polycrystalline diF-TES-ADT with predominantly lamellar stacking (the edge-on motif)[235].

Secondly, we found diF-TES-ADT to be air- and photo-stable and we were

[†]Joel Smith performed the GIWAXS measurement and data analysis. Rachel Kilbride measured the AFM data.

able to reliably make thin films with highly reproducible optical behaviour. Finally, distinct emission signatures have previously been attributed to the ^{1}(TT) state[74].

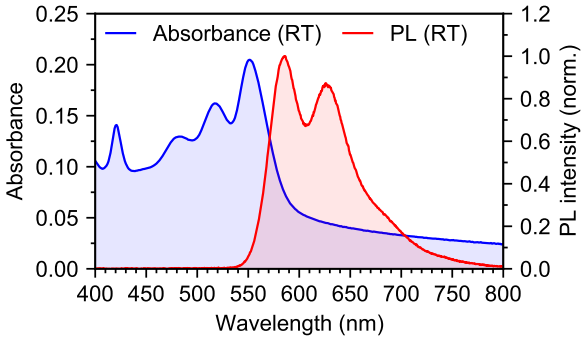

Figure 4.2 | Absorption and emission of diF-TES-ADT. Room temperature (RT) absorption and steady-state PL of a diF-TES-ADT thin film. The emission comes predominantly from the S_1 state.

Figure 4.2 shows the absorption and emission spectra of a diF-TES-ADT thin film at room temperature. The spectra arise from the vibronic progression of the $S_0 \leftrightarrow S_1$ transition, and the spacing between the peaks corresponds to a vibrational energy of 0.17 eV.

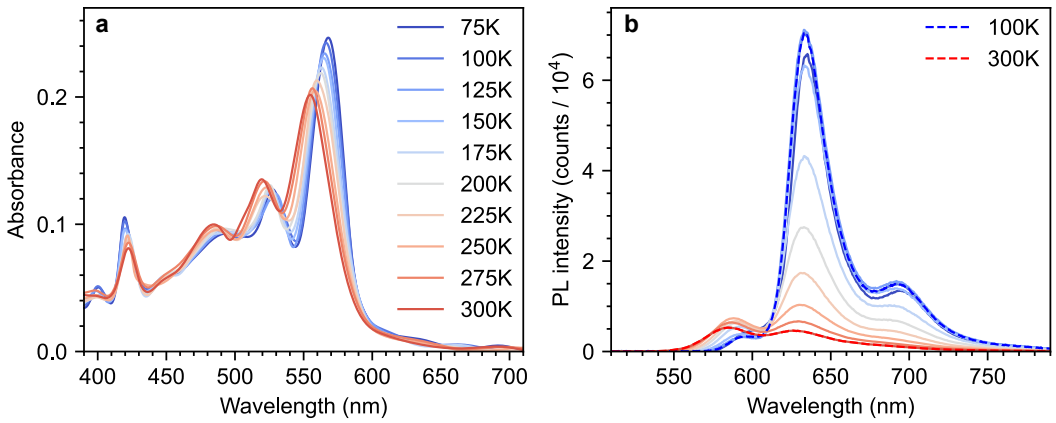

Figure 4.3 | Temperature dependent absorption and emission of diF-TES-ADT. a, Temperature-dependent absorbance of the thin film sample. No significant changes with temperature are observed. **b**, Temperature-dependent steady-state PL of the thin film, showing the growth of the ^{1}(TT) emission at low temperature. Spectra at room temperature and 100 K are highlighted.

At low temperature however, the emission spectrum is dominated by a feature previously assigned to ^{1}(TT)[74]. Figure 4.3b demonstrates the increasing brightness of ^{1}(TT) emission with decreasing temperature, as well as the reduction in singlet contribution. In contrast, the ground state absorption spectrum

(Figure 4.3a) does not change significantly with temperature: the small red-shift of S_1 and accompanying linewidth narrowing with decreasing temperature are consistent with molecular crystals possessing some J-aggregate character[83]. The absorption spectrum evolves smoothly: there is no obvious phase transition, consistent with previously reported temperature-dependent X-ray diffraction[74].

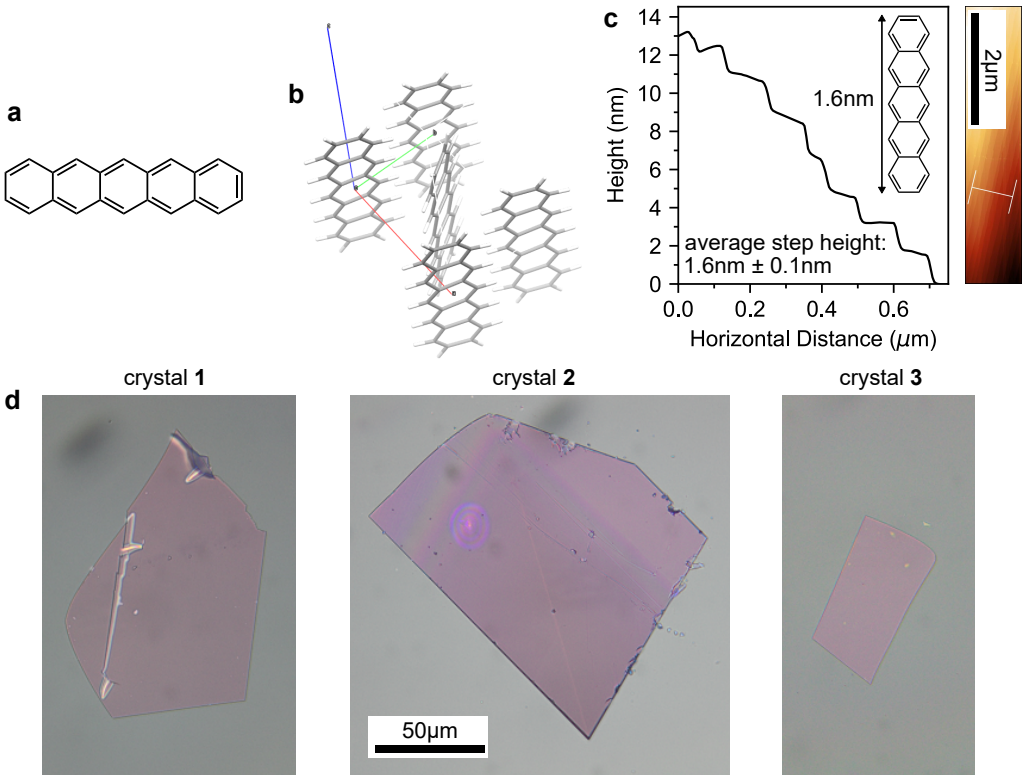

Figure 4.4 | Pentacene single crystals. **a**, Structure of the pentacene molecule. **b**, Crystal structure of pentacene[237], showing the herringbone packing in the a-b plane. **c**, AFM-measured profile of the surface of pentacene single crystal **2** showing terraces of average step height 1.6 nm, corresponding to the c-axis of the pentacene crystal. **d**, Bright-field microscope images of pentacene single crystals **1**-**3**.

We also chose to study pentacene (Figure 4.4a) because of the energetic separation between S_1 and $2 \times T_1$[238], which ensures that annihilation of triplets cannot produce S_1[239]. Any signature of ^{1}(TT) due to TTA must therefore indicate that it is a real intermediate state. In addition, to minimise contributions from impurities and disorder, we grew high-quality optically thin single crystals by physical vapour transport[‡] (Figure 4.4c,d, see also Section 3.2.3). Pentacene crystallises in the herringbone arrangement[237], illustrated in Figure 4.4b, allowing us to compare results with those from brickwork diF-TES-ADT. Polarised

[‡]Pentacene single crystals were grown and characterised by Maik Mattheisen and myself at the University of Heidelberg.

ground state absorption measurements[§] in Figure 4.5 reveal strong Davydov splitting of the 0-0 transition, consistent with previous reports[86]. This demonstrates that the crystals grew in the ab plane, further confirmed by the heights of the terraces on the surface of crystal **2** (Figure 4.4c).

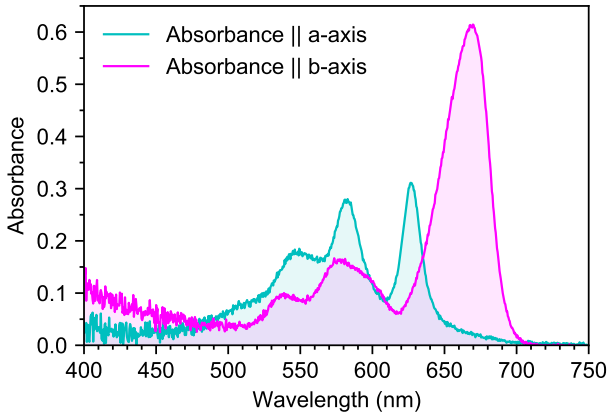

Figure 4.5 | Polarised absorption of a pentacene single crystal. Polarised absorption spectra of pentacene single crystal **1** showing clear Davydov splitting of the 0-0 band.

4.3 Bimolecular TTA populates ^{1}(TT) in diF-TES-ADT

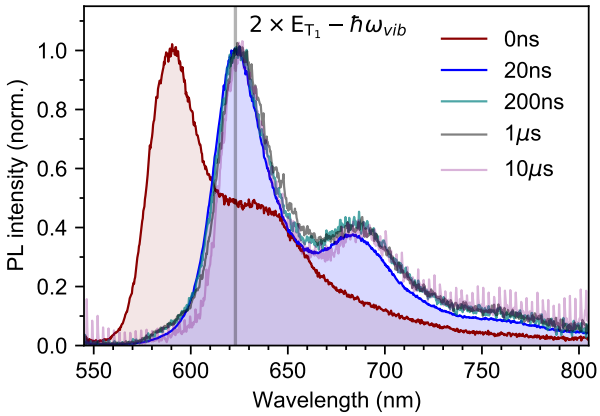

Figure 4.6 | Emissive ^{1}(TT) states in diF-TES-ADT at 100 K. Time-gated emission spectra of a diF-TES-ADT thin film at 100 K. Immediately after excitation S_1 fluorescence is observed; structured ^{1}(TT) emission then persists, spectrally unchanged, for tens of microseconds. The highest energy band of the ^{1}(TT) emission coincides with twice the diF-TES-ADT triplet energy minus one vibrational quantum (0.17 eV), consistent with a Herzberg-Teller intensity borrowing mechanism[74].

Time-resolved photoluminescence measurements of diF-TES-ADT thin films at 100 K in Figure 4.6 reveal an instrument limited evolution from the S_1 fluores-

[§]The absorption spectra of the pentacene crystals were measured by Rahul Jayaprakash.

cence (red trace) to a redshifted, vibronically structured emission that persists, unchanged, for tens of microseconds. A previous study of diF-TES-ADT demonstrated that the delayed PL arises from the ^{1}(TT) state[74]. At first glance this assignment may seem surprising since the transition dipole moment of ^{1}(TT) at its equilibrium nuclear geometry is zero due to the symmetry of its wavefunction. In fact, this is a zero-order approximation: ^{1}(TT) can couple to a symmetry-breaking vibrational mode, allowing it to mix with the nearby S_1 state. Since S_1 is a bright state, the transition dipole moment of ^{1}(TT) becomes non-zero to first order. This is the Herzberg-Teller intensity borrowing[75] mechanism (or equivalently the Albrecht B-term in Raman spectroscopy[76]) that we described in detail in Section 2.4.3 and Appendix D. Since coupling to a vibration is required, the 0-0 peak of ^{1}(TT) emission is expected to be suppressed. Thus the luminescence spectrum of ^{1}(TT) is expected to form a vibronic progression, with the first visible peak (the 0-1 phonon replica) lying at approximately $2 \times E_{T_1} - \hbar\omega_{vib}$, i.e. twice the triplet energy minus one vibrational quantum[29,74,103]. In the case of diF-TES-ADT, twice the triplet energy of 1.08 eV (Ref. 74) minus one vibrational quantum (0.17 eV) exactly matches the first peak of the delayed fluorescence (vertical line in Figure 4.6), entirely consistent with Herzberg-Teller emission from the ^{1}(TT) state.

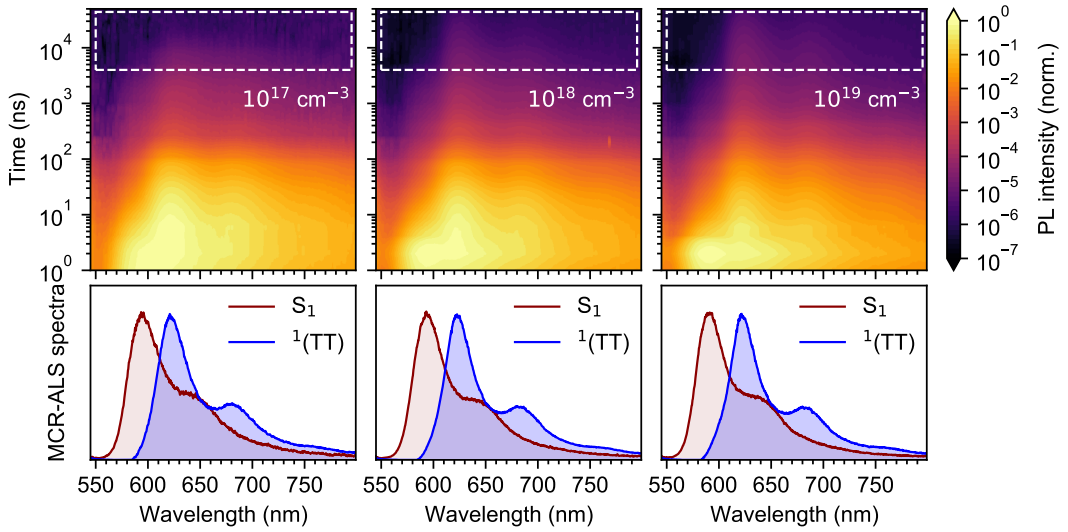

Figure 4.7 | Time-resolved PL dynamics of diF-TES-ADT at 100 K. False-colour maps of the TRPL measured at 100 K and normalised at 4 ns. Laser intensities corresponding to excitation densities of 10^{17}cm^{-3} (left), 10^{18}cm^{-3} (middle) and 10^{19}cm^{-3} (right) were used. Dashed boxes highlight the regime of TTA, for which a relative increase in PL intensity is observed at higher excitation densities. No S_1 signatures are observed on these timescales. Spectral components extracted using MCR-ALS[225,226] are shown below each map.

To determine whether ^{1}(TT) is formed from bimolecular TTA as well as

through singlet fission[74], we turn to the PL dynamics. Figure 4.7 shows false-colour maps of time-resolved PL (TRPL) measured at three different excitation densities at 100 K. We extracted the S_1 and ^{1}(TT) spectral components using the Multivariate Curve Resolution Alternating Least Squares (MCR-ALS) algorithm[32,225,226], as described in Sections 3.4.3 and 4.7.4. The extracted spectra are shown below the PL maps.

The TRPL maps demonstrate an increase in relative emission intensity beyond 10 µs as the excitation density increases. On these timescales triplet excitons are the dominant excited states[74] and delayed emission can be reasonably attributed to bimolecular triplet-triplet annihilation (TTA)[94,240]. If TTA populates ^{1}(TT) by first forming S_1[32], we would expect to see a small S_1 contribution to the PL spectrum on these timescales. Importantly, we do not observe any such contribution, suggesting that the initial products of TTA are triplet-pair states rather than S_1 states. To confirm this, we examine the emission dynamics in more detail.

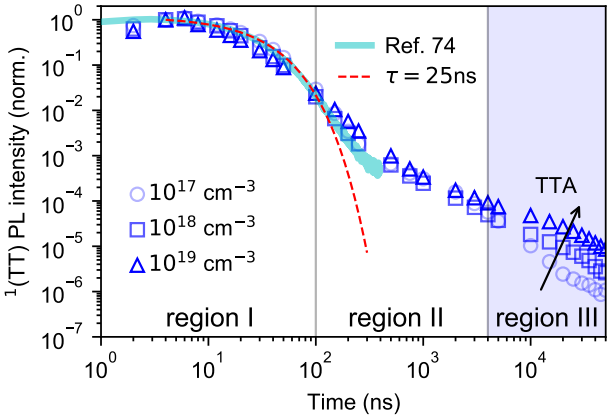

Figure 4.8 | ^{1}(TT) from bimolecular TTA in diF-TES-ADT at 100 K. Excitation density dependent dynamics of the ^{1}(TT) component extracted via MCR-ALS (markers). Three regions are apparent: a mono-exponential decay with time constant ∼25 ns (region I) which has been previously measured (light-blue line)[74], followed by delayed emission in region II that becomes excitation density dependent (region III) after several microseconds. These three regions correspond to the initial decay of ^{1}(TT) (I), followed by geminate (T...T) recombination (II) and bimolecular TTA (III). Data corresponding to the light blue line was obtained from Ref. 74, licensed under a Creative Commons Attribution 4.0 International License.

Figure 4.8 shows the excitation density dependent dynamics extracted via MCR-ALS, for which three distinct regions are apparent. During region I, the PL intensity decays exponentially with a single time constant of ∼ 25 ns (dashed red line). In region II, the decay becomes non-exponential but shows no dependence on excitation density. Region III marks the onset of the excitation density dependence, with higher densities leading to more intense emission.

This behaviour can be qualitatively explained as follows. We know from transient absorption spectroscopy (Figure E.1) that singlet fission occurs with a time constant of 100 ps. During region I therefore, emissive ^{1}(TT) states formed via singlet fission either decay to the ground state or form long-lived 'dark' triplets, as described previously[74] (light blue line). Region III shows the expected intensity dependence for bimolecular TTA. We assign the intermediate region II to geminate (T...T) recombination.

This qualitative description is backed up by kinetic modelling (Figure 4.9). We find that we need to explicitly include two distinct triplet-pair populations in our rate model to reproduce our emission dynamics (Figure 4.9a). This is only slightly different to the original Merrifield model[102]. We separate out the S_1 and ^{1}(TT) states (strongly exchange-coupled triplet-pairs) and take Merrifield's '(TT)' to be $(T...T)^l$ (weakly exchange-coupled triplet-pairs), see Figure 4.9a. As described in Section 2.6.1, there are nine $(T...T)^l$ states ($l = 1, 2, ..., 9$) whose singlet character is given by the coefficients $|C_S^l|^2$ which give their degree of overlap with the singlet.

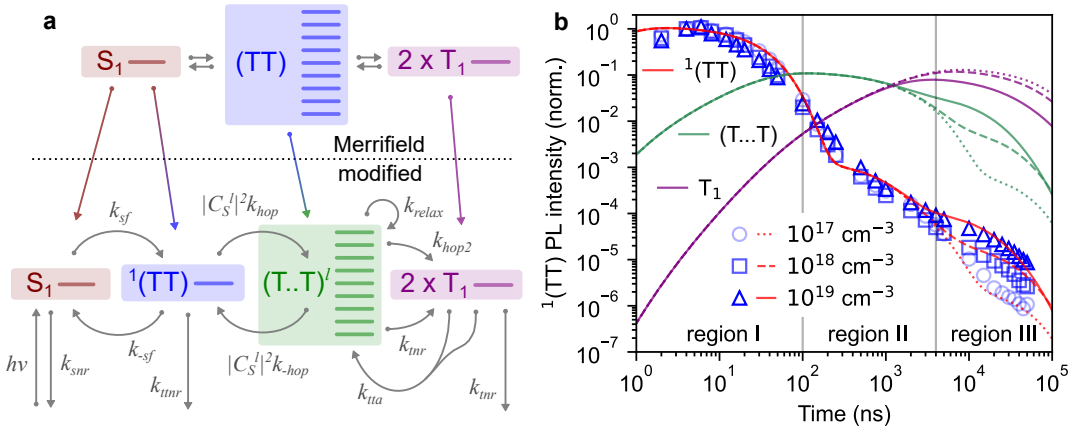

Figure 4.9 | Kinetic modelling of diF-TES-ADT TRPL dynamics at 100 K. **a**, Our kinetic scheme (below dotted line) involves only a slight modification of the Merrifield model, with the explicit inclusion of the strongly exchange-coupled ^{1}(TT) state. **b**, Measured (blue markers) and simulated (red lines) ^{1}(TT) dynamics in diF-TES-ADT at 100 K normalised at 4 ns. The behaviour of (T...T) and T_1 are also shown. The scheme in panel (**a**) accurately captures the measured dynamics at all three excitation densities measured; this is replicated for five other temperatures (Figure 4.11).

This is equivalent to the currently accepted description of singlet fission, usually written as a variation of

$$S_1 \leftrightarrow {}^1(TT) \leftrightarrow (T...T)^l \leftrightarrow T_1 + T_1. \tag{4.2}$$

We note that, as pointed out in a recent review[30], the nomenclature used in the literature can be confusing. Merrifield assumed that triplet-pairs have no electronic interaction (orbital overlap). In other words, the triplet-pair '(TT)' state described by Merrifield is identical to what we describe as (T...T). Others write ^{1}(TT) and implicitly include both the electronically coupled ^{1}(TT) and weakly-interacting (T...T)[16,74]. The different kinds of triplet-pair states are discussed in Section 2.6.1 and we note that these distinctions become especially important when we discuss the spin statistics of TTA-UC in Chapter 7.

We use this scheme (Figure 4.9a) to model our data with additional inclusion of spin-lattice relaxation[124] and non-radiative triplet decay from $(\mathrm{T...T})^l$ (i.e. $(\mathrm{T...T})^l \rightarrow \mathrm{T_1}$). Both of these additions are found to have little effect (Figure E.10). The governing rate equations are below and the resulting kinetics are shown in Figure 4.9b.

$$\frac{d[\mathrm{S_1}]}{dt} = -\left(k_{sf} + k_{snr}\right)[\mathrm{S_1}] + k_{-sf}[^1(\mathrm{TT})] \tag{4.3}$$

$$\begin{aligned}\frac{d[^1(\mathrm{TT})]}{dt} &= k_{sf}[\mathrm{S_1}] - \left(k_{-sf} + k_{hop}\sum_{l=1}^{9}|C_S^l|^2 + k_{ttnr}\right)[^1(\mathrm{TT})] \\ &\quad + k_{-hop}\sum_{l=1}^{9}|C_S^l|^2[(\mathrm{T...T})^l]\end{aligned} \tag{4.4}$$

$$\begin{aligned}\frac{d[(\mathrm{T...T})^l]}{dt} &= k_{hop}|C_S^l|^2[^1(\mathrm{TT})] + \frac{1}{8}k_{relax}\sum_{j\neq l}[(\mathrm{T...T})^j] + \frac{1}{9}k_{tta}[\mathrm{T_1}]^2 \\ &\quad - \left(k_{-hop}|C_S^l|^2 + k_{hop2} + k_{tnr} + k_{relax}\right)[(\mathrm{T...T})^l]\end{aligned} \tag{4.5}$$

$$\frac{d[\mathrm{T_1}]}{dt} = \left(k_{tnr} + 2k_{hop2}\right)\sum_{l=1}^{9}[(\mathrm{T...T})^l] - 2k_{tta}[\mathrm{T_1}]^2 - k_{tnr}[\mathrm{T_1}] \tag{4.6}$$

In these equations square brackets denote concentrations of species in units of $\mathrm{cm^{-3}}$. Rate constant definitions are shown in Figure 4.9a. The $|C_S^l|^2$ coefficients are calculated from the spin Hamiltonian in Ref. 111, using zero-field splitting (D and E) parameters from Ref. 74 and molecular orientation calculated from the published crystal structure[210].

Before proceeding with this kinetic model, we confirm that ^{1}(TT) is a direct product of bimolecular TTA and is not formed via the $\mathrm{S_1}$ state and subsequent singlet fission. We have already provided experimental evidence that this is the case; recall that we observe no contribution from $\mathrm{S_1}$ emission in the delayed PL at 100 K (Figures 4.6 and 4.7). Using kinetic modelling, we can predict the expected $\mathrm{S_1}$ contribution if it, rather than ^{1}(TT), were the direct product of

TTA, as proposed for concentrated TIPS-tetracene[32].

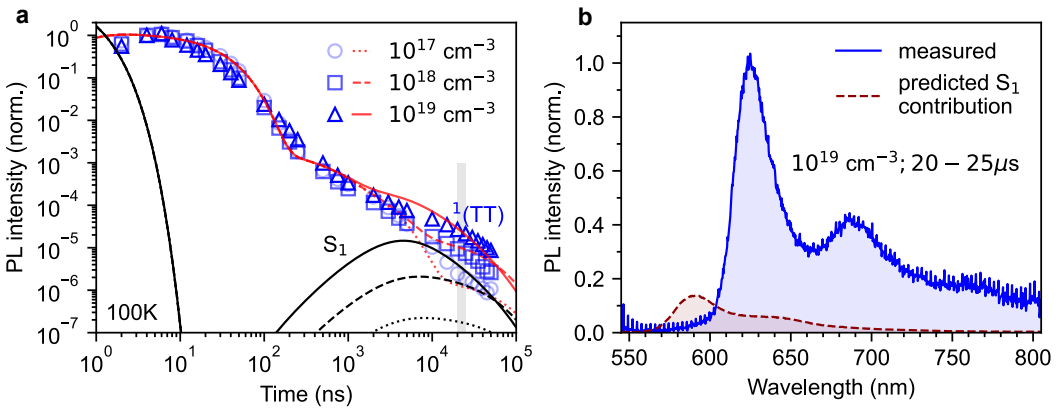

Figure 4.10 | TTA does not populate ^{1}(TT) via S_1. **a**, ^{1}(TT) dynamics can be reproduced using a kinetic model in which TTA populates S_1 directly rather than triplet-pairs. However, this would lead to an appreciable contribution to the total PL from S_1 (black lines) on long timescales which we do not observe. **b**, The measured PL spectrum (100 K) on a timescale of tens of microseconds. The PL arises entirely from ^{1}(TT); the predicted contribution from S_1 (red dashed line) is not observed.

If we modify the kinetic model of Figure 4.9a such that TTA populates S_1 rather than (T...T)^l, we find that we can still obtain a good fit to the experimentally measured ^{1}(TT) dynamics (Figure 4.10a). However, we would expect from the balance of rates that a small fraction (1/120) of S_1 excitons formed from TTA should decay radiatively, rather than undergoing fission. Yet since the radiative rate of S_1 is approximately 40 times greater than that of ^{1}(TT) in diF-TES-ADT[74], this would still lead to an appreciable S_1 contribution to the total PL of around 14% (Figure 4.10a, black lines) on timescales of tens of microseconds, which we do not observe (Figure 4.10b). We therefore conclude that TTA populates the triplet-pair states directly and not via S_1.

Figure 4.9b shows the simulated ^{1}(TT) population dynamics, fitted globally to the measured excitation density-dependent ^{1}(TT) population using the kinetic model illustrated in Figure 4.9a. Where possible, rate constants were calculated or taken from the transient absorption data in Figure E.1 (k_{sf}, k_{-sf}, k_{snr}). The remaining seven were optimised to globally fit the full excitation density dependent dataset at each temperature and our uncertainty analysis (Figures E.11-E.16) shows that they are tightly constrained. For full details of the kinetic modelling, see Sections 4.7.5 and E.3. At every temperature, we find excellent agreement between simulation and data across all measured timescales and excitation densities, as shown in Figure 4.11.

Many of the time-resolved photoluminescence measurements that have been performed on singlet fission materials and combined with kinetic or density

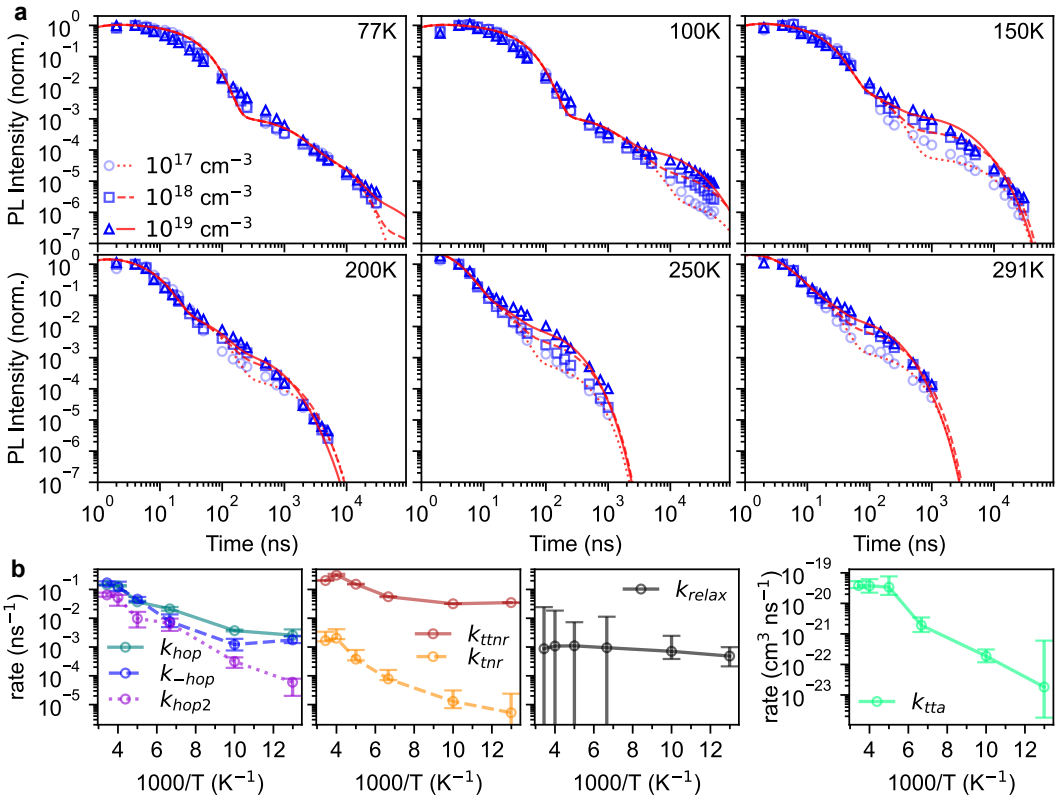

Figure 4.11 | Kinetic modelling of all diF-TES-ADT TRPL dynamics. **a**, Measured ^{1}(TT) population dynamics as function of exciton density and temperature (blue markers) together with the simulated population (red lines) using the kinetic scheme illustrated in Figure 4.9a. The kinetic scheme accurately reproduces the excitation density-dependent dynamics across all six temperatures. **b**, Rate constants extracted from the kinetic modelling as a function of temperature. All the rate constants display plausible temperature dependencies. Uncertainty in the rate constants, reflected here by the error bars, is discussed in Appendix E.

matrix modelling have tracked the population of the S_1 state[102,112,114,120,121,134]. ^{1}(TT) population dynamics are typically extracted from transient absorption data through global or target analysis[74,151,169] but as noted above, this becomes difficult when, for example, ^{1}(TT), (T...T) and T_1 all have very similar excited-state absorption spectra[241]. Furthermore, signal-to-noise limitations of transient absorption spectroscopy mean that, at best, only the first three orders of magnitude of population decay can be measured. While this may be sufficient to capture the dominant 'forward' dynamics, the finer details of the interactions and equilibria between triplet-pair species are obscured.

We have demonstrated that, at low temperature, diF-TES-ADT thin films exhibit remarkably bright photoluminescence from the ^{1}(TT) state which can be tracked over many orders of magnitude using highly sensitive time-resolved photoluminescence techniques. By applying our kinetic model, we can examine

the behaviour of the various rate constants that govern the intricate triplet-pair dynamics as a function of temperature (Figure 4.11b). Firstly, we note that the large error bars for k_{hop2} and k_{tta} at 77 K reflect the fact that complete triplet-pair dissociation is largely suppressed at this temperature. We find that the forwards and backwards rates for triplet-pair separation, k_{hop} and k_{-hop}, are approximately equal at every temperature. According to the principle of detailed balance, this implies a near-zero difference in free energy between ^{1}(TT) and (T...T). If, as widely claimed[184], there is an entropic gain for free triplet formation, then the electronic energy of the ^{1}(TT) state must be lower than $2 \times E_{T_1}$. As expected, we find that the rate constant associated with processes thought to be governed by triplet hopping (k_{hop}, k_{-hop}, k_{hop2}, k_{tta}) all follow a qualitatively similar temperature dependence.

Merrifield's model was originally developed to describe magnetic field dependent fluorescence. Our kinetic scheme should, therefore, also be able to describe these effects, which arise as the $|C_S^l|^2$ coefficients vary with magnetic field according to the spin Hamiltonian[111] (Equation 2.70). Figure 4.12b therefore shows a plot of ΔPL/PL as a function of magnetic field at two different delay times, measured at room temperature on a drop-cast sample[¶] (Figure 4.12a). We then used our kinetic model to simulate the expected magnetic field dependence. The model (Figure 4.12b), reproduces the shape, magnitude and zero-crossing at both delay times. We adjusted the values of the rate constants slightly from those used to describe the ^{1}(TT) dynamics in the thin film sample (Figure 4.11) and adjusted the D and E parameters within the experimental errors given in Ref. 74 to fine tune the zero crossing point of the simulation. As shown in Figure 4.12b-d, the modified rate constants allowed us to simulate both the PL kinetics and magnetic field effect of the drop-cast sample.

We note that in our model, the magnetic field dependence arises specifically from ^{1}(TT) $\leftrightarrow$ (T...T), which occurs on longer timescales than ultrafast singlet fission $S_1 \leftrightarrow {}^1$(TT). Thus kinetic schemes, such as the original Merrifield model[102], that do not explicitly include both of these steps cannot correctly simulate the time dependence of the magnetic field effect. We illustrate this in Figure 4.13. Whilst a good description of the magnetic field effect is obtained at 20–30 ns delay (blue), at 100–200 ns (orange) the Merrifield model predicts almost no effect at all. Steady-state magnetic field effects are likely to be well described by Merrifield's model, highlighting the importance of performing time-resolved measurements.

[¶]Shuangqing Wang prepared the drop-cast sample and measured the magnetic field effect. I performed the data analysis and simulations.

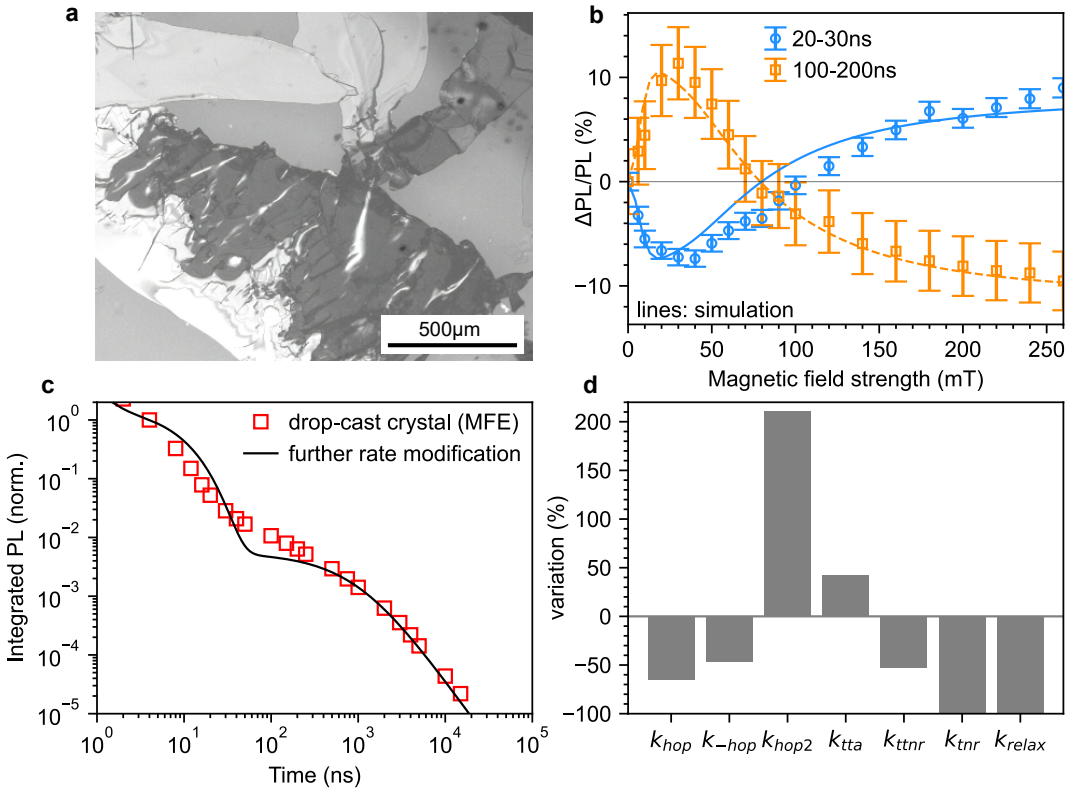

Figure 4.12 | Magnetic field effect on a diF-TES-ADT crystal at room temperature. **a**, Polarised microscope image of the drop-cast diF-TES-ADT sample. Rather than forming a thin film, diF-TES-ADT crystallised into large domains scattered over the substrate. Viewed through crossed polarisers, we see that these crystalline domains are single-orientation and many hundreds of micrometers in size. Thus we conclude that our laser spot (50 µm diameter) sampled a single crystalline domain during the measurement. Note that medium grey areas (such as the bottom left corner) are bare substrate. **b**, Measured (markers) and simulated (lines) effect of magnetic field on the room temperature PL of a single crystalline domain of diF-TES-ADT. Error bars were calculated from the small differences in measured PL intensity between spectra obtained while sweeping up in magnetic field and those obtained while sweeping back down. The differences arise principally from small fluctuations in laser intensity. The kinetic scheme from Figure 4.9a reproduces all features of the measured effect at both time delays. **c**, The same kinetic model provides a reasonable description of the PL dynamics, provided that the rate constants are adjusted from those used for the thin film sample as shown in (**d**).

The kinetic scheme proposed by Dover et al.[32] includes an emissive excimer-like state (Section 2.5.2) that acts as a singlet trap rather than an intermediate to singlet fission, but does not include any intermediates between S_1 and $2 \times T_1$. This model is not applicable here: the magnetic field-dependent PL requires the presence of ^{1}(TT) and (T...T) intermediates. Since ^{1}(TT) is a singlet state and thus expected to be emissive[29,74,103], we find no reason to assume that trap states are responsible for the emission we observe.

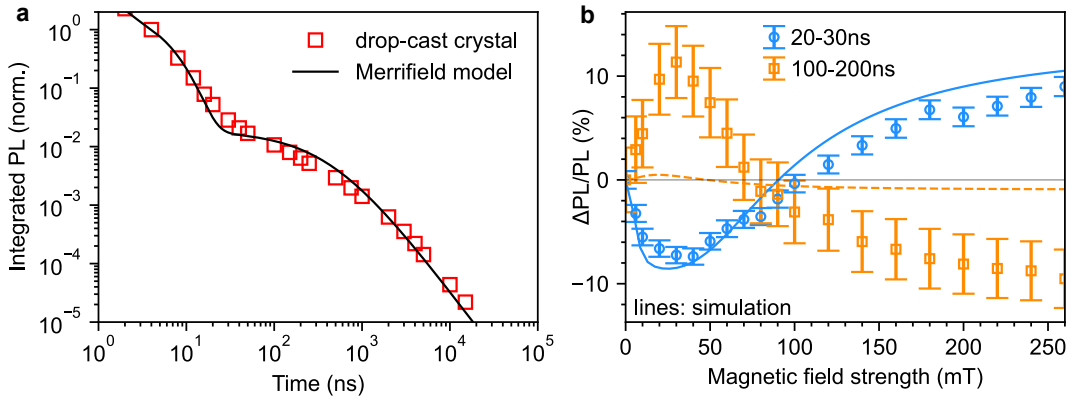

Figure 4.13 | Merrifield's model does not describe both kinetics and magnetic field effect. **a**, The singlet emission dynamics of the diF-TES-ADT crystal (red markers) can be well described by Merrifield's scheme. **b**, The magnetic field effect can be very well described at 20–30 ns delay (blue), however the model predicts almost no effect at 100–200 ns (orange), in contrast to our measurement.

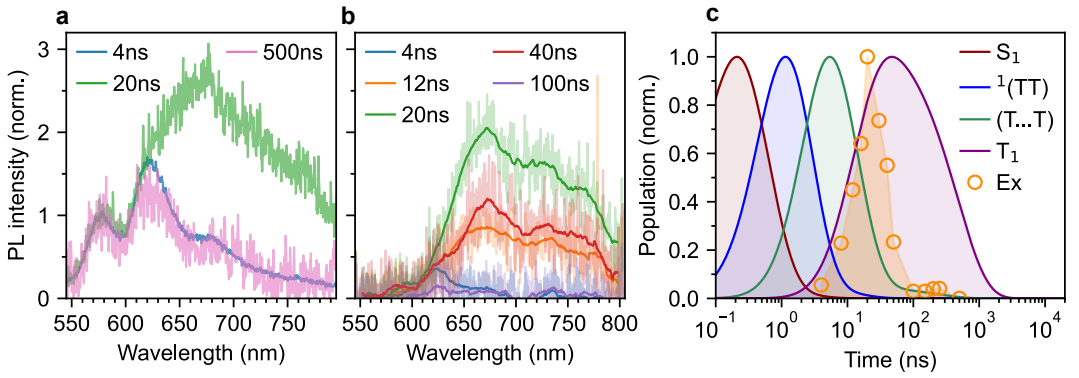

Figure 4.14 | Excimers in diF-TES-ADT are distinct from ^{1}(TT). **a**, Time-gated spectra of a diF-TES-ADT thin film at 250 K, 4, 20 and 500 ns after excitation with an initial excitation density of 10^{17}cm^{-3}. **b**, Subtraction of the 500 ns spectra (S_1 and ^{1}(TT) only) from the early-time data yields the excimer spectrum as a function of time. The integrated PL dynamics of the excimer are shown in (**c**). **c**, Simulated population dynamics for diF-TES-ADT at 250 K and an initial excitation density of 10^{17}cm^{-3} using the kinetic model described in the text. The rise of the excimer PL (orange markers) coincides with the rise of free triplets.

In fact, at a temperature of 250 K, we do observe distinct excimer-like emission *in addition to ^{1}(TT) and S_1 emission.* Figure 4.14a shows time-gated spectra of a diF-TES-ADT thin film at 4, 20 and 500 ns after excitation with an initial excitation density of 10^{17}cm^{-3}. Over the first 20 ns, a broad excimeric feature grows in which disappears by 100 ns, leaving only the S_1 and ^{1}(TT) spectra. To isolate the excimer component, we subtract the unchanging S_1 and ^{1}(TT) spectra at 500 ns from the early-time data. The excimer spectrum as a function of time delay is shown in Figure 4.14b and its dynamics are shown by the markers in Figure 4.14c, alongside excited state populations simulated

using the kinetic model from Figure 4.9a. Interestingly, the rise of the excimer emission appears to match the growth of the free triplet population.

It is perhaps surprising that the rise in the excimer population appears to occur so late, well after the decay of the singlet exciton. It could be that the excimers are indeed forming from singlet excitons at sites in the film more suited to excimer relaxation. Such a parallel pathway has been proposed for crystalline tetracene[242]. Alternatively, excimers may be forming from triplets, as has recently been shown in perylene[243].

We do not wish to speculate further on the behaviour of the excimers, since we observe them only at this particular temperature and low excitation density (and not at all at 100 K, which is the focus of this chapter). However, we reiterate that the excimers are distinct from ^{1}(TT) in this system. This suggests that, while excimers may be present in singlet fission systems[32,231–234,243], they are not by themselves direct evidence of ^{1}(TT).

Having demonstrated that emissive triplet-pairs are populated through bimolecular TTA in a polycrystalline endothermic singlet fission material, we now turn to our highly ordered, exothermic model system: single crystals of pentacene. Previous reports of pentacene photoluminescence are scarce, and the spectral assignments[244,245] were made before the recent boom in singlet fission research. We therefore start by revisiting this literature and find evidence that the observed emission is consistent with ^{1}(TT). We further show, using fluence- and time-dependent measurements, that the ^{1}(TT) emission arises from bimolecular TTA.

4.4 Redshifted emission in pentacene single crystals is from ^{1}(TT)

Figure 4.15a shows delayed emission from single crystals of pentacene. Despite the sub-100 fs, near-200% conversion of singlets to triplets in crystalline pentacene[108,238], we were able to measure weak photoluminescence from the crystals at 77 K. Just as for diF-TES-ADT, we found an instrument limited conversion from the S_1 fluorescence at around 690 nm to a redshifted feature that includes a peak at around 740 nm. Due to poor spectral sensitivity beyond around 820 nm (Figure 3.7), we cannot resolve the spectral shape at longer wavelengths and can only say that some emission is present in this region. This poor sensitivity, coupled with the weakness of the PL signal make the assignment of the redshifted feature considerably more challenging than for diF-TES-ADT.

We therefore begin by comparing our emission spectra to those previously

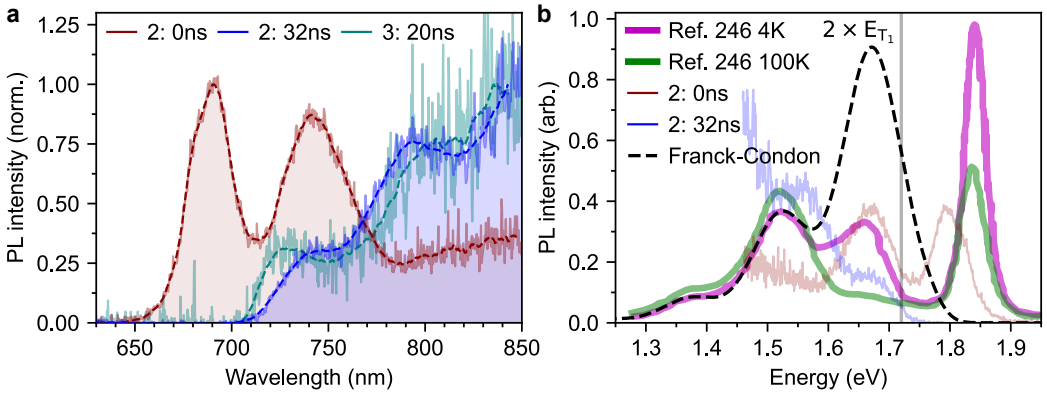

Figure 4.15 | Delayed emission from pentacene single crystals at 77 K. **a**, Time-gated emission spectra of pentacene single crystals **2** and **3**; both the raw and smoothed spectra are shown. As for diF-TES-ADT, initial S_1 fluorescence is replaced by redshifted emission on longer timescales. **b**, Delayed emission from (**a**) overlayed with luminescence spectra from Ref. 246. All the features in our time-resolved data are present in the previously measured spectra. The literature data is well described by a Franck-Condon progression (dashed black line) provided that the 0-0 band is suppressed. This type of emission is predicted for ^{1}(TT) states that emit via Herzberg-Teller intensity borrowing. Panel **b** adapted from Ref. 246, with the permission of AIP Publishing.

measured[244–246] (Figures 4.15b and E.17). The features that we observe are consistent with previously reported emission spectra of pentacene single crystals[244,245] and high-quality 20 nm thin layers[246], all of which report bands at around 1.85 eV, 1.65 eV, 1.5 eV and 1.35 eV. In Figure 4.15b we plot the delayed emission measured in this work alongside that reported at 4 K and 100 K in Ref. 246 which we judge to be the least affected by artefacts, particularly self-absorption. A comparison with other reported spectra is presented in Figure E.17.

The three redshifted bands in the PL spectrum at 4 K (purple line in Figure 4.15b) appear to form a vibronic progression. If all these bands arise from the same electronic state, the 0-1 and 0-2 peaks should follow a standard Franck-Condon progression whilst the 0-0 may be either enhanced or suppressed, depending on symmetry constraints[85]. We therefore fitted the two lowest energy peaks of the 4 K spectrum to the 0-2 and 0-1 bands of a Franck-Condon progression. We used the in-plane C-H bending mode at 1180 cm^{-1} as the main vibrational mode coupled to the electronic transition. Resonance Raman experiments have shown that this mode is resonant with both the S_1 fluorescence and the peak at 1.65 eV[247]. It also matches the separation between the 0-1 and 0-2 vibronic replicas in our polarised absorption measurement (Figure 4.5). Strikingly, the emission band at 1.65 eV coincides with the 0-0 peak of the resulting

progression (dashed line in Figure 4.15b), provided that its intensity is partially suppressed, as expected for emission enabled by Herzberg-Teller intensity borrowing (Section 2.4.3). Within this context, intensity borrowing from S_1, which is expected to become superradiant below $\sim$ 10 K (Refs. 29,58,86,152), may explain the observed temperature dependence of the 0-0 peak[244,246]. The 0-0 energy is slightly below that of two triplets in pentacene[109] (vertical line, Figure 4.15b). The energy and spectral shape are therefore consistent with emission from ^{1}(TT).

Historically however, various alternative sources for the redshifted emission in pentacene have been proposed, namely defects[245] and self-trapped excitons[244–246]. It is also possible that excimers contribute to the redshifted emission. While difficult to rule out, we highlight that excimeric emission has been reported in several polyacenes and other singlet fission materials[32,150,231,232,234,248], yet in every case the spectrum is broad, featureless and quite unlike the narrower, well resolved progression of peaks under consideration here.

Defects in single crystals may include extrinsic impurities or intrinsic vacancies or edge states. In the case of pentacene single crystals, extrinsic defects are reported to give rise to dominant emission at 1.5 eV (Ref. 245), overlapping with the 0-1 vibronic feature described above. While we cannot rule out extrinsic defect emission in this spectral region, we expect it to be minimised in our crystals, grown using a two-stage sublimation of triple-sublimed starting material (see Section 3.2.3). We focus instead on the 1.65 eV emission, which He et al.[245] demonstrated to be intrinsic. They showed resonant Raman enhancement of the 42 cm^{-1} phonon mode across the 1.65 eV band at 8 K. This phonon mode is a sensitive indicator of intermolecular structure and is often used to distinguish between different polymorphs[249–251]. Such resonant enhancement of this pure mode suggests that the 1.65 eV emission arises from an intrinsic exciton species[245], rather than a vacancy or extrinsic impurity. Following previous literature[244], He et al. assigned it to a self-trapped exciton[245]. However, we argue in the following that self-trapped excitons are highly unlikely to be present in pentacene.

Exciton self-trapping occurs when low-energy intermolecular phonon modes, in other words lattice vibrations, act to localise the exciton wavefunction. The stability of self-trapped excitons in organic crystals is thus dependent on the exciton-lattice coupling.

The assignment of the 1.65 eV emission band in pentacene to self-trapped excitons[244] rests on a similar assignment in tetracene[252,253] and the lack of non-

S_1 emission in anthracene[254,255]. To explain this trend, Matsui et al. extracted the exciton-lattice coupling for tetracene and anthracene from single exponential fits to the temperature-dependent low-energy absorption edge[244,252–257] – the so-called Urbach tail[258]. This procedure can be problematic due to the large error in fitting a single exponential to the Urbach tail[259–262], for example in rubrene single crystals three exponentials are required[262]. However, the main issue with their analysis is the assumption that the excitons in anthracene and tetracene are 3D[252,255].

The dimensionality of the exciton is important because it determines the relationship between the slope extracted from Urbach tails and the exciton-lattice coupling, which in turn governs self-trapped exciton stability[263]. For a given slope, a 2D lattice gives weaker exciton-lattice coupling than a 3D one. In order to assign the non-S_1 emission in tetracene to self-trapped excitons, Matsui et al. were forced to invoke a 3D lattice, despite the evidence that excitons are 2D in tetracene[237,252,264]. Thus the *assumption* that self-trapped excitons are the source of the emission is built into their *assignment* (of the emission to self-trapped excitons), which we find to be a somewhat circular argument.

Taking the more physically realistic 2D lattice, self-trapped excitons should be unstable in both anthracene and tetracene[252], and the predicted trend in exciton-lattice coupling[265] would match widely accepted calculations of electron-lattice coupling by Brédas et al.[266,267]. Following this trend, exciton-lattice coupling should be even weaker in pentacene than in tetracene[266], although to our knowledge it has never been determined experimentally[268,269]. Such weak exciton-lattice coupling means that self-trapped excitons should be unstable in pentacene. There is therefore no clear basis for the assignment of redshifted emission in crystalline pentacene to self-trapped excitons[244–246].

Self-trapped excitons cannot explain the trend in non-S_1 emission in acenes: none in anthracene to redshifted in pentacene. The emission instead tracks the energy gap between S_1 and $2 \times T_1$[29]. Given this trend, together with the evidence that ^{1}(TT) is responsible for the non-S_1 emission in diF-TES-ADT[74], tetracene[153,229] and TIPS-tetracene[151], as well as the spectral shape with suppressed 0-0 (Figure 4.15b), we conclude that the 1.65 eV emission band in pentacene arises from ^{1}(TT).

4.5 Bimolecular TTA populates ^{1}(TT) in pentacene single crystals

We demonstrated above that ^{1}(TT) is formed from bimolecular TTA in diF-TES-ADT. To see if this is also the case in exothermic pentacene, we investigate the behaviour of the ^{1}(TT) 1.65 eV emission band as a function of time and excitation density.

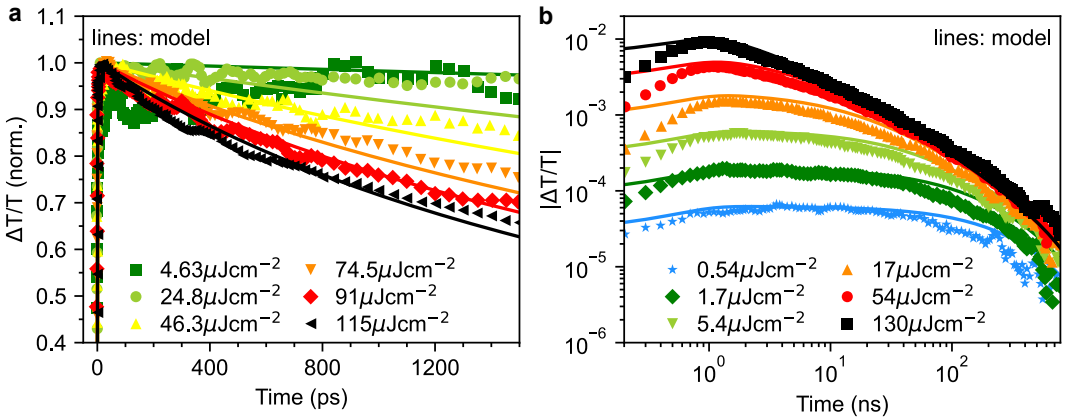

Figure 4.16 | Modelling triplet dynamics in pentacene single crystals. Fluence-dependent photo-induced absorption (PIA) of triplets in a pentacene single crystal at room temperature (markers), reproduced from Ref. 239. The solid lines represent the bimolecular TTA model described in the text and methods. Panels **a** and **b** adapted with permission from Reference 239; copyright 2013 WILEY-VCH Verlag GmbH & Co. KGaA, Weinheim.

Figure 4.16 shows previously reported room temperature transient absorption data of pentacene single crystals[239]. The data show the fluence dependence of the triplet photoinduced absorption (PIA) on ps (a) and ns (b) timescales. In Ref. 239, the authors fitted the triplet dynamics to a simple bimolecular annihilation model given by:

$$\frac{d[\mathrm{T_1}]}{dt} = -k_{tta}[\mathrm{T_1}]^2 - k_{tnr}[\mathrm{T_1}] \tag{4.7}$$

where, $k_{tta} = 1.2 \times 10^{-10}\,\mathrm{cm^3\,s^{-1}}$ and $k_{tnr} = 1/500\,\mathrm{ns}$. Ref. 239 was published before the role of ^{1}(TT) was well-established in pentacene. We therefore re-modelled their data using a more complete description of the singlet fission dynamics, in which $\mathrm{S_1} \rightarrow {}^1$(TT) occurs with a rate of $k_{sf} = 1/100\,\mathrm{fs}$ (Refs. 108,238) and ^{1}(TT) $\rightarrow \mathrm{T_1} + \mathrm{T_1}$ occurs with a rate of $k_{sep} = 1/1\,\mathrm{ps}$ (Refs. 169,194,197). The $\mathrm{T_1}$ decay is governed by the rate constants established in Ref. 239. One of the conclusions of Ref. 239 is that not all triplet-triplet annihilation events in pentacene represent a loss of excited state population. Indeed we find

here that a fraction f of TTA events form ^{1}(TT) instead. The exact value of this fraction turned out to be unimportant and we take a value of 10% here. For the two-dimensional pentacene lattice, triplet excitons have infinite probability to collide[98], suggesting that both elastic and inelastic scattering events may be taking place. Furthermore, the spin-statistics of triplet-triplet annihilation (Chapter 7) mean that we expect only a fraction of TTA events to yield a spin-0 exciton. The rate equations are as follows

$$\frac{d[\mathrm{S_1}]}{dt} = -\left(k_{sf} + k_{snr}\right)[\mathrm{S_1}] \tag{4.8}$$

$$\frac{d[^1(\mathrm{TT})]}{dt} = k_{sf}[\mathrm{S_1}] - k_{sep}[^1(\mathrm{TT})] + f k_{tta}[\mathrm{T_1}]^2 \tag{4.9}$$

$$\frac{d[\mathrm{T_1}]}{dt} = 2k_{sep}[^1(\mathrm{TT})] - 2k_{tta}[\mathrm{T_1}]^2 - k_{tnr}[\mathrm{T_1}], \tag{4.10}$$

and we take the triplet PIA to be proportional to the sum of the ^{1}(TT) and $\mathrm{T_1}$ populations.

In order to apply this model to the experimental data, the measured laser pulse energies (units of $\mu\mathrm{J\,cm^{-2}}$) had to be converted to units of $\mathrm{cm^{-3}}$. Ref. 239 did not report their calculation for this conversion. We therefore obtained a constant conversion factor simply by applying the model to their fluence-dependent TA data and varying its value until the data was well reproduced by eye and the simulation matched that reported in Ref. 239. The value obtained was $8 \times 10^{15}\,\mathrm{cm^{-1}\,\mu J^{-1}}$. Taking a typical crystal thickness of around 300 nm[239], this number implies that roughly 10% of photons in each pulse result in an excitation in the crystal. This is reasonable, firstly since the crystals in our measurement (and those in Ref. 239) are of a size similar to our laser spot itself, so not all of the light is incident on the crystal and secondly because we observed significant scattering of the laser from the crystal surface. Using no other free parameters, the modelled triplet dynamics match those of Ref. 239, as shown by the solid lines in Figure 4.16.

We next investigate whether the ^{1}(TT) behaviour predicted by this model is consistent with our measurements of the time and fluence dependence of the 1.65 eV emission band. Figure 4.17a shows a false-colour map of the pentacene TRPL and the kinetics of the 1.65 eV (750 nm) band are plotted in Figure 4.17b. On a timescale of tens of nanoseconds, the decay is a power law with a slope of -2. Figure 4.17c shows the fluence dependence of the 1.65 eV emission at four different time delays. The intensity varies linearly with fluence within the first few nanoseconds and becomes increasingly sub-linear at later times. Both the power-law decay with a slope of -2, and the increasingly sub-linear intensity

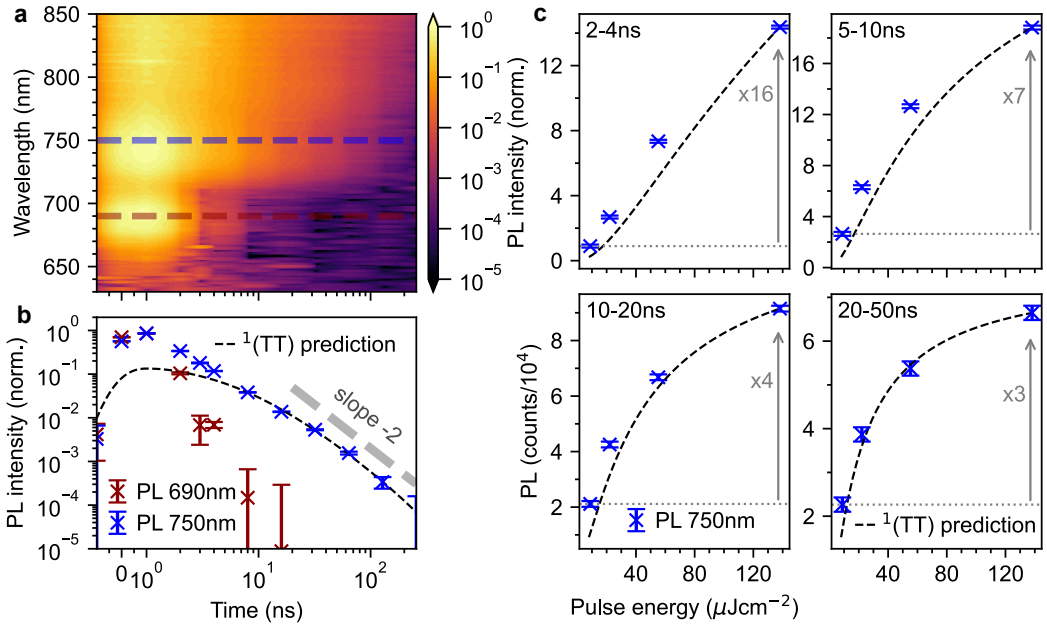

Figure 4.17 | Bimolecular TTA directly populates ^{1}(TT) in pentacene single crystals. **a**, False-colour map of the TRPL of pentacene single crystal **2**. Distinct bands at 690 nm (corresponding to S_1 emission) and 750 nm are observed. **b,c**, The kinetics (**b**) and fluence dependence (**c**) of the 750 nm (1.65 eV) emission band (blue markers) match the behaviour of ^{1}(TT) predicted by the modelling of the TA data in Figure 4.16 (dashed lines), demonstrating that this emission arises from bimolecular TTA. The error bars in **b,c** represent the standard deviation of the noise across a 10 nm spectral window around 750 nm.

dependence are characteristic of bimolecular TTA[97,270–272].

The dashed lines of Figure 4.17b,c show the *non-fitted*, normalised ^{1}(TT) behaviour predicted by the model used to describe the transient absorption data. All parameters, including the fluence scaling, remained the same as for Figure 4.16. The match to our time-gated fluence dependence is remarkable and as expected the slope of -2 in Figure 4.17b is also reproduced. It is perhaps surprising that this independent model prediction and our data are so similar, given the difference in measurement temperature between Figure 4.16 and Figure 4.17 (the crystal dimensions and excitation source are comparable). For polycrystalline organic semiconductors, triplet transfer becomes slower at low temperature[194,273], as we observed for our diF-TES-ADT films (Figure 4.11). However, charge carrier mobility, and therefore expected triplet transfer rate[273], is independent of temperature for single crystal pentacene[214,274,275]. The room temperature model is therefore valid for our low-temperature PL data, and the excellent match confirms that ^{1}(TT) is populated directly through bimolecular TTA. S_1 cannot be involved in this process since it lies too high in energy.

We have shown that a weakly emissive ^{1}(TT) state is formed directly

from bimolecular TTA in pentacene single crystals. Considerably brighter ^{1}(TT) emission is found in a range of acenes including diF-TES-ADT[74], tetracene[153,229], and TIPS-tetracene[151]. The increase in ^{1}(TT) brightness between pentacene and diF-TES-ADT is explained by the reduced energy gap between ^{1}(TT) and S_1, which increases the Herzberg-Teller mixing. A consistent picture thus emerges of biexcitonic ^{1}(TT) intermediates that emit light through a Herzberg-Teller mechanism. Crucially for spectral upconversion, we have demonstrated here that such states are directly formed through bimolecular TTA.

4.6 Conclusions

We have shown here that ^{1}(TT) is an emissive, and real, intermediate state in both singlet fission and TTA, resolving a recent controversy in the literature. We find that ^{1}(TT) emission in our systems is distinct from excimer-like features. These results provide the first direct spectroscopic evidence that the strongly exchange-coupled ^{1}(TT) triplet-pair state can be directly formed from bimolecular triplet-triplet annihilation in both nominally endothermic and single crystal exothermic systems. In addition, we have shown that emission previously assigned to self-trapped excitons instead arises from ^{1}(TT).

Magnetic resonance techniques are blind to spin-zero states. Yet these states, including the strongly exchange-coupled ^{1}(TT), can be easily detected using photoluminescence spectroscopy. We find that we can track the population of ^{1}(TT) over the same timescales as transient electron paramagnetic resonance experiments[14,139]. We suggest that a combination of trEPR and TRPL measurements may provide a more complete picture of the spin physics of singlet fission and triplet-triplet annihilation and, in particular, may help to elucidate the role of strongly exchange-coupled quintet states.

In order to describe the emission dynamics and magnetic field effect, we used a modified Merrifield model which includes distinct (TT) and (T...T) populations. We find that to accurately describe our kinetic data, free triplets undergoing bimolecular TTA first recombine to form (T...T). (T...T) is rarely considered in studies of TTA upconversion and yet its inclusion has profound implications for the overall efficiency. In Chapter 7, we explore the ramifications of considering weak and strong intertriplet exchange coupling on the spin statistical limit of TTA upconversion.

More speculatively, if the ^{1}(TT) $\rightarrow S_0$ transition implied by our observations of ^{1}(TT) photoluminescence signatures is a direct, 2-electron transition, a direct,

2-electron $S_1 \rightarrow {}^1(TT)$ transition may also be possible. This could support the idea of the direct singlet fission mechanism, as opposed to the indirect, charge transfer mediated mechanism that is generally favoured by the singlet fission community (see Section 2.6.3).

4.7 Methods

4.7.1 Sample preparation and characterisation

The preparation of diF-TES-ADT thin films is described in Section 3.2.2 and details of the pentacene single crystal growth are provided in Section 3.2.3. A description of the optical microscopy, GIWAXS and AFM measurements is also given in Section 3.3.

4.7.2 Steady-state absorption and PL measurements

Room temperature ground state absorption of thin film samples was performed using a UV-visible spectrophotometer (Cary60, Agilent). For temperature-dependent absorption and PL, the sample was mounted in a closed-cycle helium cryostat (OptistatDry BLV, Oxford Instruments). White light for absorption measurements was provided by a deuterium-halogen lamp (DH2000-BAL, Ocean Optics) and excitation for PL measurements was provided by a 405 nm CW laser diode (Thorlabs). Spectra were recorded using a fibre-coupled spectrometer (HR2000+ES, Ocean Optics). A 435 nm longpass filter (GG435, Schott) was placed before the detector for PL measurements.

The polarised absorption of the pentacene single crystals was measured by focussing light from a tungsten lamp through a variable linear polariser and onto the crystal using a 100 mm focal length lens. Transmitted light was collected with a 50× Mitutoyo Plan Apo SL infinity-corrected objective and delivered to a spectrometer (Andor).

4.7.3 Time-resolved PL measurements

For time-resolved measurements, samples were situated in the helium exchange gas of a nitrogen bath cryostat (Optistat DN, Oxford Instruments). The temperature of the exchange gas was controlled using an inbuilt heater and thermocouple connected to an external PID controller (Mercury iTC, Oxford Instruments). The sample temperature was assumed to have stabilised at that of the exchange gas once repeated fluorescence measurements yielded exactly the same

spectrum and intensity. Excitation was provided by the frequency-doubled output of a Q-switched Nd:YVO_4 laser (Picolo-AOT, Innolas). The laser produces pulses at 5 kHz with temporal width < 500 ps and a wavelength of 532 nm. The photoluminescence was detected by a spectrograph (Shamrock 303i, Andor) and time-gated intensified CCD (iStar DH334T-18U-73, Andor). A combination of a 532 nm notch filter and 550 nm longpass filter (OG550, Schott) were used to cut out pump scatter. The TRPL setup and data processing procedures are described in detail in Section 3.4.1.

Measurements of average laser power P were carefully converted into values of average exciton density N using the following expression:

$$N = F_A \left(1 - F_S\right) R_P \frac{P}{f \pi r_x r_y d} \frac{\lambda}{hc} \tag{4.11}$$

Here, F_S and F_A represent the fraction of incident light scattered and absorbed by the sample respectively, evaluated from the UV-visible transmission spectrum (0.44 and 0.18 respectively for diF-TES-ADT), R_P is the ratio of measured power between the sample position and power meter position (0.58 for our setup), f is the repetition rate of the laser (1 kHz for internally triggered power measurements), r_x and r_y are the radii of the excitation beam spot, measured as 130 nm and 100 nm respectively with a CCD beam profiler (Thorlabs), d is the sample thickness, λ is the excitation wavelength and h and c are Planck's constant and the speed of light respectively.

4.7.4 Transient absorption spectroscopy

Transient absorption measurements were carried out using the picosecond TA setup described in Section 3.4.2. The pump and probe polarizations were set to magic angle. Pump beam spot size was measured at the sample position using a CCD beam profiler (Thorlabs).

Multivariate curve resolution alternating least squares

The extraction of spectral components was achieved using Multivariate Curve Resolution Alternating Least Squares (MCR-ALS)[225,226]. A description of the basic principles of MCR-ALS is given in Section 3.4.3. Here, two components only were used in each case and pure spectra were used as the initial point. Both the spectra and concentrations were forced to be non-negative using fast non-negative least squares. The spectral matrix was normalised and the algorithm run until convergence was achieved.

In general, the separation of S_1 and ^{1}(TT) components is only relevant during the first few nanoseconds, where singlet fission is 'smeared out' in our instrument response. Beyond a few nanoseconds, the spectrum does not change with time, and consists only of ^{1}(TT) at low temperatures or a mixture of ^{1}(TT) and S_1 at higher temperatures, which are in any case in equilibrium. Thus after the first few nanoseconds, the extracted dynamics are essentially identical to the wavelength-integrated PL.

Figures E.2-E.7 in Appendix E show the TRPL data sets alongside spectra and dynamics of S_1 and ^{1}(TT) extracted via MCR-ALS. At 200 K (Figure E.5) for example, the algorithm very successfully separated the ^{1}(TT) and S_1 spectra and we can see the equilibrium maintained between the two populations. However, at 250 K and 291 K, the algorithm did an imperfect job of fully separating the spectra; this is because the S_1 contribution starts to dominate leading to very little spectral change at all with time, even over the first few nanoseconds.

Despite the presence of a third component, the excimer, at an exciton density of 10^{17}cm^{-3} at 250 K, the MCR-ALS algorithm could not successfully extract it. This makes little difference to the extracted dynamics, since the excimer was only observed at this particular temperature and low excitation density and over a limited range of delay times. As such, we do not include excimers in our kinetic scheme.

4.7.5 Kinetic modelling for diF-TES-ADT

Algorithms

All simulations and fitting were performed using custom-made python code[‖]. The systems of rate equations were solved using an ordinary differential equation solving algorithm that switches automatically between stiff and non-stiff problems. A least squares procedure was used to globally fit the kinetic models to the exciton density-dependent data through variation of certain rate constants. The logarithm of data and simulation were taken when calculating residuals in order to treat all timescales equally. Rate constants were manually adjusted prior to fitting to ensure convergence to the global minimum.

Spin Hamiltonian

Spin wavefunction overlap factors $|C_S^l|^2$ were computed by diagonalaising the spin Hamiltonian in Equation 2.70 using custom-made python code. The orientation of the molecules was determined from the published crystal structure

[‖] The code is freely available at https://github.com/davidbossanyi/sfmodelling

of diF-TES-ADT[210]. We took the zero-field splitting parameters D and E from PL quantum beating experiments reported previously ($D = 1 \times 10^{-6}$eV, $E = 3 \times 10^{-6}$eV)[74]. The strength of the triplet-triplet dipole-dipole interaction was taken as 60 neV[149].

Instrument response

We took the instrument response of our iCCD into account in a somewhat crude fashion by assuming an exponentially rising population of photoexcited singlet excitons. Mathematically, this involved introducing an additional rate equation to the kinetic models for the pre-excitation ground state as follows:

$$\frac{d[\mathrm{GS}]}{dt} = -k_{gen}[\mathrm{GS}] \tag{4.12}$$

$$\frac{d[\mathrm{S_1}]}{dt} = k_{gen}[\mathrm{GS}] + ... \tag{4.13}$$

We calculated the initial value of [GS] according to equation 4.11. We then determined the value of k_{gen} by modelling the decay of the S_1 state in pentacene single crystal **2**. Since singlet fission is known to occur within 100 fs in pentacene[108], the PL decay of S_1 is instrument-limited. We found a value of 1.8 ns^{-1} using this method. We note that this is a reasonable number, given the laser pulse width of < 500 ps. The precise shape of the instrument response function (IRF) is immaterial since all the dynamics of interest occur on longer timescales. The decay of the pentacene S_1 fluorescence gives a very reasonable idea of the IRF, since the decay constant is known to be ≤ 100 fs (Ref. 108). This is equivalent to (for example) measuring the decay of pump scatter.

Fixed rate constants

We determined the value of the singlet fission rate constant k_{sf} from TA measurements as 10 ns^{-1} (Figure E.1). Since this rate is thought to be independent of temperature[110], we fixed it for all the modelling presented here.

We set the rate constant for conversion of ^{1}(TT) back to S_1 (k_{-sf}) to zero for temperatures of 100 K and below since little or no singlet contribution was observed in the delayed photoluminescence. From 150 K upwards, we estimated the rate using the following relation, which assumes a thermal equilibrium between ^{1}(TT) and S_1:

$$\frac{k_{-sf}}{k_{sf}} = \frac{\mathrm{P}_S}{\mathrm{P}_{TT}} \frac{k_{ttr}}{k_{sr}} \tag{4.14}$$

Here $\mathrm{P}_S/\mathrm{P}_{TT}$ is the ratio of S_1 PL to ^{1}(TT) PL in the delayed photolumines-

cence and we took the ratio of radiative rates k_{ttr}/k_{sr} to be 1/40 as previously reported[74].

Finally, we took the intrinsic lifetime of the singlet to be 12 ns, as measured using TA for dilute solutions of diF-TES-ADT (Figure E.1). We note however, that the precise values of all these fixed rate constants have a negligible effect on the ^{1}(TT) population dynamics (Section E.3.4).

4.7.6 Magnetic field effect measurements

The PL dynamics at 0 mT were measured first in order to check rate constant values for magnetic field effect modelling. The effects of magnetic field on PL were measured by recording PL spectra at a series of magnetic field strengths at two different gate delays: 20–30 ns and 100–200 ns. The measured spectra were identical in shape and magnitude both while sweeping upwards and subsequently downwards in magnetic field strength, allowing us to rule out any effects from photo-degradation or laser power fluctuations and giving us high confidence in the reproducibility of the observed magnetic field effect. Spectra were integrated along the wavelength axis and the magnetic field effect evaluated as

$$\frac{\Delta PL}{PL}(B) = \frac{PL(B) - PL(0)}{PL(0)} \tag{4.15}$$

Chapter 5

Searching for triplet-pair emission in crystalline rubrene

Rubrene single crystals exhibit curious polarisation-dependent photoluminescence somewhat reminiscent of Herzberg-Teller emission from the ^{1}(TT) state that we measured in the previous chapter. Here, we use time-resolved photoluminescence to investigate the possibility that ^{1}(TT) is responsible for the ab-polarised component in the absorption and emission spectra of orthorhombic rubrene single crystals. We find that this is not the case: different behaviours of the two components are found only at specific sites on the crystals and likely arise from surface defects.

5.1 Introduction

In Chapter 4, we showed that ^{1}(TT) states formed through both singlet fission and triplet-triplet annihilation give rise to photoluminescence signatures consistent with Herzberg-Teller intensity borrowing from the nearby S_1 state. We postulated that diF-TES-ADT thin films gave brighter ^{1}(TT) emission compared to pentacene single crystals in part because the energy gap between S_1 and ^{1}(TT) is smaller. In fact, this can be seen by examining the expression for the first-order ^{1}(TT) dipole moment, which we can obtain from Herzberg-Teller theory (Section 2.4.3 and Equation 2.48) as:

$$\mu_{S_0-TT} = \sum_\alpha \mu^e_{S_1}(Q_0) \left(\frac{\langle \psi_{S_1} | \frac{\partial H}{\partial Q_\alpha} | \psi_{TT} \rangle}{E_{S_1} - E_{TT}} \right)_{Q_0} \langle \chi_{S_0,\nu} | Q_\alpha | \chi_{TT,\nu'} \rangle \,. \tag{5.1}$$

Here Q_α are symmetry-breaking vibrational modes, $|\psi_i\rangle$ are electronic wavefunctions, $|\chi_{i,\nu}\rangle$ are vibrational wavefunctions (ν is a vibrational quantum number)

and H is the Hamiltonian governing Coulomb repulsion between electrons and nuclei. From equation 5.1, we see that the brightest ^{1}(TT) emission should be observed for (i) small S_1-^{1}(TT) energy gaps and (ii) large vibronic coupling between S_1 and ^{1}(TT) through appropriate vibrational modes that break the symmetry forbidding ^{1}(TT) from emitting at the equilibrium geometry Q_0.

Crystalline rubrene (Figure 5.1) is a singlet fission material[189] for which S_1 and ^{1}(TT) are almost isoenergetic[74,276–278]. We therefore hypothesised that ^{1}(TT) states in crystalline rubrene might be particularly emissive.

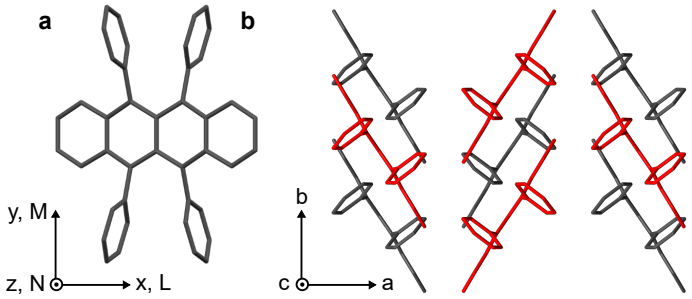

Figure 5.1 | Crystal structure of rubrene. **a**, Molecular structure of rubrene, indicating the molecular coordinate system. **b**, Orthorhombic crystal structure of rubrene obtained from Ref. 279. Molecules coloured red are displaced along the c-axis.

Furthermore, there is recent experimental evidence of significant vibronic coupling between S_1 and ^{1}(TT) in rubrene single crystals[35]. At the equilibrium geometry (Q_0), the C_{2h} π-stacking symmetry of crystalline rubrene (Figure 5.1b) means that electronic couplings between ^{1}(TT) and S_1 (and indeed ^{1}(TT) and charge-transfer states) vanish[35,188]. Singlet fission is therefore enabled by symmetry-breaking vibrational modes. The observation of coherent, instantaneous excitation of both S_1 and ^{1}(TT) in impulsive transient absorption, followed by coherent oscillations at the frequency of a candidate symmetry-breaking mode, suggests that the vibronic coupling between S_1 and ^{1}(TT) can be significant[35]. Similar instantaneous co-formation of S_1 and ^{1}(TT)[35] has been observed in other time-resolved studies[36,37], and could even be due to direct $S_0 \rightarrow {}^1$(TT) absorption, a transition that has been observed in pentacene derivatives by coherent 2D electronic spectroscopy[154].

Further hints of a strong ^{1}(TT) dipole matrix element can be found in studies of the photoluminescence and absorption of rubrene single crystals[33,34]. The strong S_0-S_1 transition dipole moment is polarised along the M-axis of the rubrene molecule, and hence the c-axis of the rubrene crystal[34] (Figure 5.1). The c-polarised absorption (emission) spectrum of rubrene single crystals consists of a vibronic progression, with the 0-0 transition at 2.32 eV (2.22 eV)[34]. Inter-

estingly, rubrene crystals also possess pronounced ab-polarised absorption and emission. The ab absorption (emission) spectra appear as vibronic progressions with the same vibrational and 0-0 energy as the c-polarised spectra, yet with the 0-0 transition suppressed, giving the first apparent peak at 2.49 eV (2.04 eV)[34].

Strikingly, experiments have shown that the rubrene single crystal photoluminescence spectrum at around 565 nm (c-polarised only[34]) and around 607 nm (both c- and ab-polarised) exhibit different behaviour[33]. In particular, it was shown that only the redder part of the emission spectrum was quenched by an exciton splitter deposited at the surface of a rubrene crystal, and that the yellow-green part (c-polarised only[34]) was short-lived with a lifetime of approximately 15 ns[33]. As a result of these observations, the authors proposed a singlet exciton origin for the yellow-green part and a triplet exciton origin for the redder part.

These results are highly suggestive. One possible interpretation of the spectral components is that the S_1 state is responsible for the c-polarised absorption/emission and the ∼isoenergetic ^{1}(TT) state, which borrows intensity from S_1 through Herzberg-Teller coupling, gives rise to the ab-polarised absorption/emission. This intepretation is consistent with the results of Ref. 33. However, we might expect the ^{1}(TT) dipole moment to retain the polarisation of the state from which it borrows intensity, in this case the M- and hence c-polarised S_1.

An alternative explanation is that the ab-polarised absorption/emission arises from Herzberg-Teller coupling between S_1 and a higher-lying singlet state that has its dipole moment along the L-axis. A similar mechanism has been proposed to be active in other polyacenes[280,281] and the effect would be especially pronounced in rubrene due to its unique crystal structure. However, this explanation cannot account for the different quenching and dynamical behaviour of the two components[33].

In order to test the hypothesis that an emissive ^{1}(TT) state is the source of ab-polarised absorption and emission in rubrene crystals, we began by attempting to reproduce the results of Ref. 33, in which the emission at around 565 nm was initially found to decay much faster than that at 607 nm. We find that whilst we can indeed observe this effect, it occurs only at specific sites on the crystal surface and is therefore likely a result of morphological or surface inhomogeneities.

5.2 Rubrene single crystals

Figure 5.2 shows microscope images of the two vapour-grown rubrene crystals (see Section 3.2.3) used in this work. Crystal 1 (Figure 5.2a) is a 0.7 µm thick platelet, 120 µm wide and several mm long, with few visible imperfections. Crystal 2 (Figure 5.2b) is much larger, thicker, less uniform and more damaged. Optical experiments were confined to the region indicated by the red box in Figure 5.2b. This region is approximately 2 µm thick.

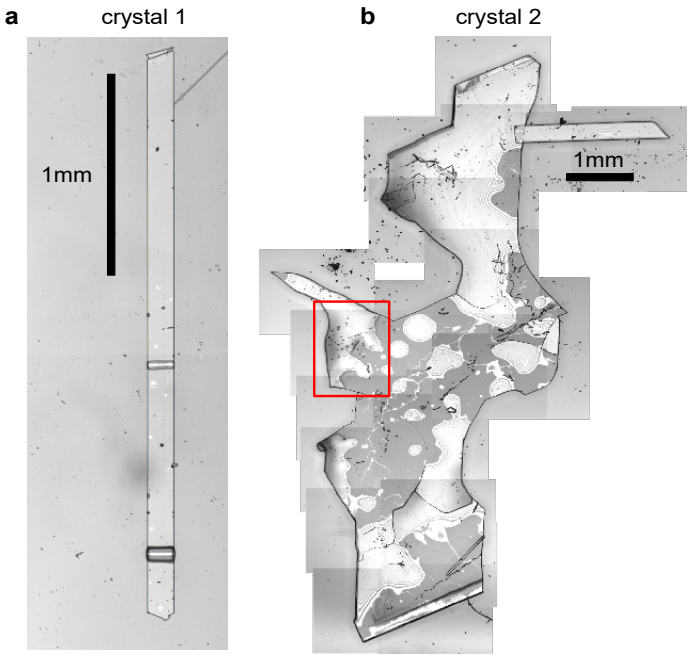

Figure 5.2 | Rubrene single crystals. **a,b**, Microscope images of crystals 1 and 2 respectively, grown by physical vapour transport. All spectroscopic measurements of crystal 2 were conducted within the region indicated by the red box.

The absorption spectra of crystals 1 and 2 are shown in Figures 5.3a and 5.3b respectively for incidence angles of 0° and 30°. The 0° spectra are consistent with the ab-polarised absorption of orthorhombic rubrene single crystals[34]. The increased absorption and appearance of a peak at 532 nm upon rotation of the crystal to 30° incidence reflect the contribution of the c-polarised component. This demonstrates that the M-axes of the rubrene molecules, and hence the c-axis of the crystals, is normal to the substrate plane. Crystals 1 and 2 therefore have their largest dimensions in the ab plane, as expected for vapour grown rubrene crystals[34]. Excitation at 532 nm therefore selectively excites the c-polarised transition, whilst excitation at around 500 nm excites both the c- and ab-polarised transitions, with the ratio of absorptions dependent on incidence angle.

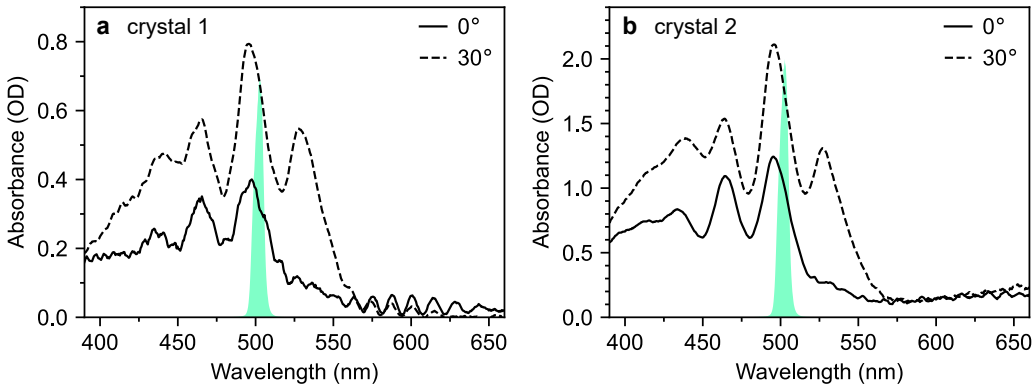

Figure 5.3 | Absorption spectra of rubrene single crystals. a,b, Absorption spectra of crystals 1 and 2 respectively, at both 0° and 30° degree incidence angle. The spectra of the excitation pulses are also shown.

5.3 Site-dependent anomalous photoluminescence behaviour

Figure 5.4a,b shows time-gated photoluminescence spectra, normalised at 607 nm, from crystals 1 and 2 following pulsed excitation at 500 nm. The pump was introduced at an incidence angle of 45° and therefore excites both the c- and ab-polarised absorption components. The pump spectrum is shown in Figure 5.3c. PL (in all polarisations) was collected at normal incidence to the ab crystal plane (see Section 5.5.3).

Figure 5.4c,d shows the dependence of the PL intensity (integrated from 0–2 µs) on the rotation angle of a linear polariser placed before the detector. In both cases, the intensity exhibits the expected $cos^2\theta$ pattern associated with dipole emission. The pattern is slightly less pronounced in crystal 1 (Figure 5.4c), perhaps due to some PL 'leakage' from the edges of the crystal being picked up by the collection lens.

We observe slight changes with time to the shape of the PL tail beyond 620 nm in Figure 5.4a,b which suggests small contributions from lower-lying excited states[282]. Similar low energy bands of varying intensity are commonly observed in the PL tail of rubrene single crystals[34,35,37,189,282–287]. The origin of such bands are debated; suggestions include oxygen-related mid-gap states[286] or amorphous regions within the crystal[282]. We note that the PL spectra from our crystals strongly resemble the spectra from 'pristine' rubrene single crystals in Ref. 34 (see Figure 5.7).

Crucially, we do not find any significant differences in temporal behaviour between 565 nm and 607 nm and therefore between the c- and ab-polarised emission components, suggesting that at the positions measured, both components

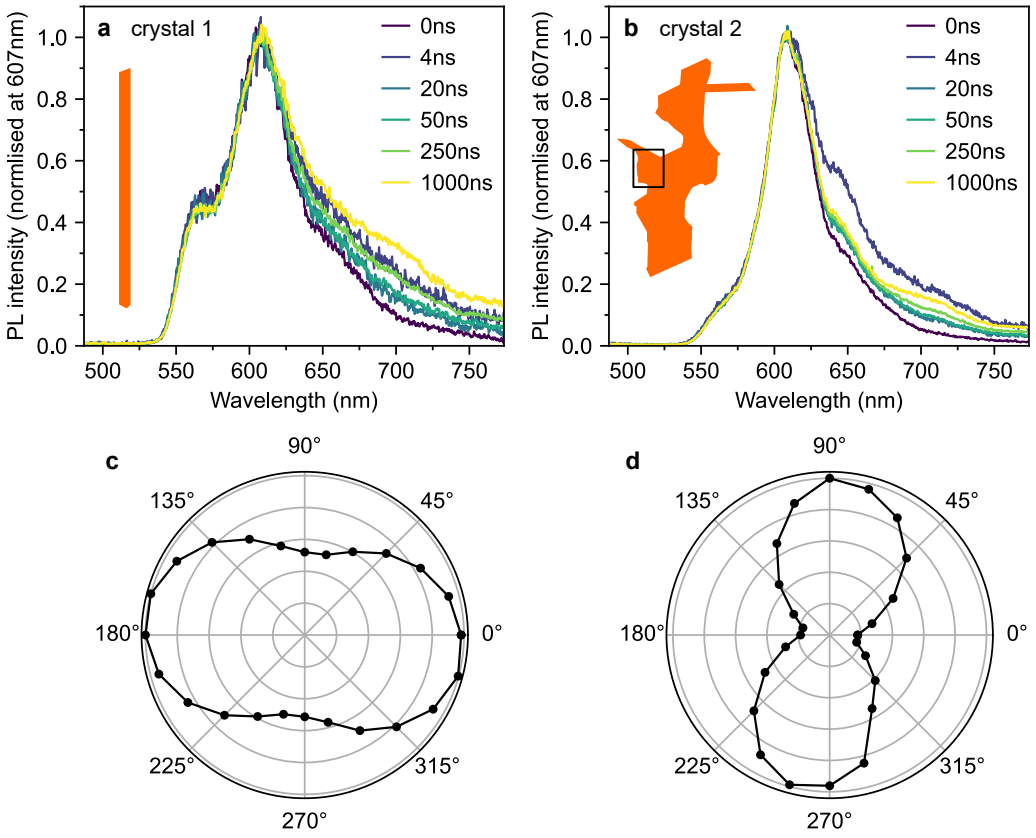

Figure 5.4 | Ordinary photoluminescence behaviour of rubrene crystals. **a,b**, Time-gated PL spectra, normalised at 607 nm, for crystal 1 (**a**) and crystal 2 (**b**). **c,d**, The dependence of the PL intensity at 607 nm on the rotation angle of a linear polariser placed before the detector. The excitation density was approximately 50 µJ cm^{-2} for all TRPL measurements reported in this chapter.

arise from the same excitonic species.

However, by scanning around the surface of crystal 2, we were able to find a spot that reproduced the behaviour observed in Ref. 33, which we denote crystal 2*. The time-gated spectra from this spot (Figure 5.5a) show a striking dependence on detection wavelength. A short-lived component that peaks at ∼565 nm (and is hence c-polarised only[34]) dominates during the first few nanoseconds, before giving way to a constant spectrum resembling the ab-polarised emission (plus the expected c-polarised 'leakage' due to experimental conditions[34]). These different dynamics are clearly evident when comparing the PL decay profiles in Figure 5.5b. Beyond 50 ns, the PL dynamics of crystal 2 and 2* are identical. Initially however, the band at 565 nm appears as an extra component with a lifetime of a few nanoseconds.

To investigate the origins of the two emission components evident in crystal 2*, we measured the detection polarisation anisotropy of the PL intensity, shown in Figure 5.6a,b. The long-lived, mainly ab-polarised component of crys-

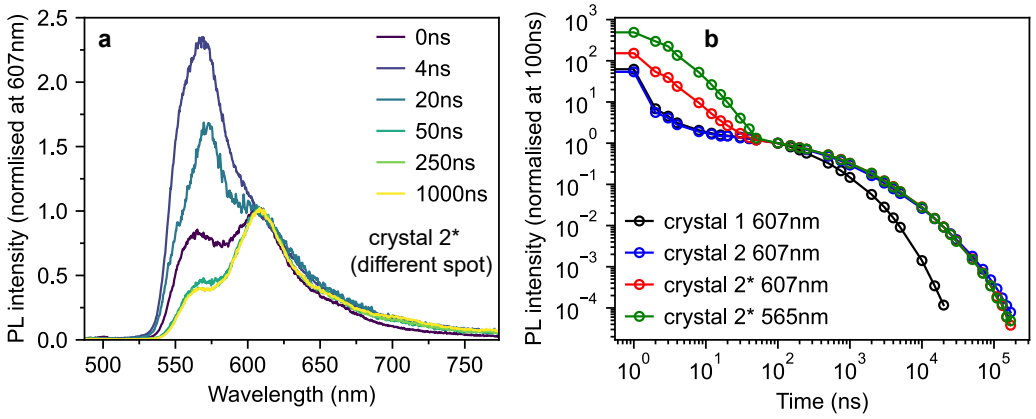

Figure 5.5 | Anomalous photoluminescence behaviour of rubrene crystals. **a**, Time-gated PL spectra, normalised at 607 nm, for crystal 2*, a different spot on the surface of crystal 2 that exhibited similar PL behaviour to that reported in Ref. 33. **b**, Time-dependence of the PL intensity from crystals 1, 2 and 2* at various detection wavelengths, normalised at 100 ns.

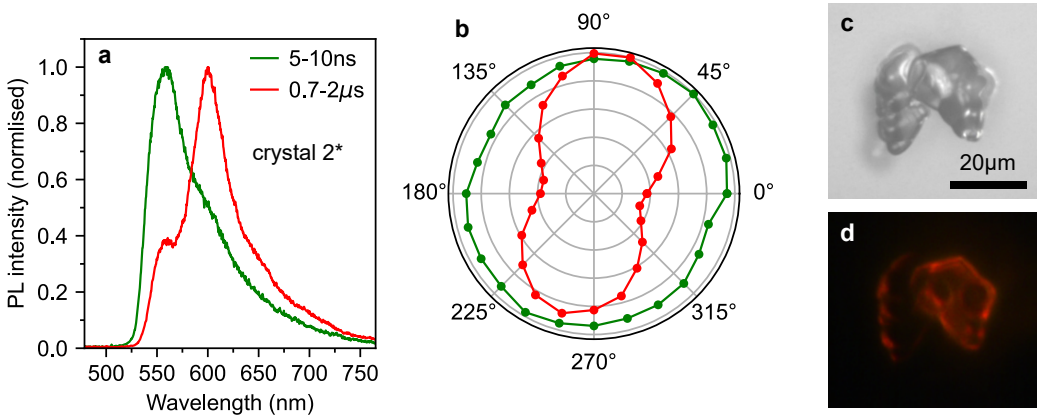

Figure 5.6 | Origins of anomalous photoluminescence behaviour of rubrene crystals. **a**, Normalised PL spectra from crystal 2*, gated from 5–10 ns (green) and 0.7–2 µs. **b**, The dependence of PL intensity (at 565 nm, green and 607 nm, red) on detection polariser angle for the two spectra shown in (**a**). **c**, Microscope image of a microcrystal defect on the surface of crystal 2. Such a defect is a candidate source of the emission from crystal 2*. **d**, Image of the photoluminescence from the defect shown in (**c**). The defect is much brighter than the bulk crystal.

tal 2* (red, Figure 5.6a,b) shows the same expected $cos^2\theta$ dipole dependence as crystals 1 and 2 (Figure 5.4c,d). In contrast, the short-lived, c-polarised component of crystal 2* (green, Figure 5.6a,b) is almost completely isotropic.

If ^{1}(TT) and S_1 respectively are the sources of the ab- and c-polarised emission components, we would not expect significant differences in their anisotropy, nor would we expect the c-polarised part to be observable only at specific sites on the crystal. Instead, the measurements in Figures 5.4-5.6 indicate that the short-lived, c-like component arises from a sub-population of singlet excitons

found only at certain points on the crystal due to morphological inhomogeneity.

This conclusion is in agreement with results in Ref. 34, where it was found that micrometer-sized defects on the crystal surface within the excitation/detection region resulted in a large enhancement in the PL shoulder at 565 nm. This was attributed to the scattering of c-polarised PL into the detector. Such scattering would explain why we measure this emission to be isotropic. Indeed an examination of the surface of crystal 2 (Figure 5.2b) reveals that several rough, micrometer-sized microcrystals are present on the surface. An example of such a surface microcrystal is shown in Figure 5.6c, and it is clear from the PL image* in Figure 5.6d that these microcrystals can be significantly brighter than the bulk crystal. It therefore seems likely that such microcrystals or defects, rather than singlet and triplet origins, are the cause of the curious results in Ref. 33.

5.4 Conclusions

We have demonstrated that there is no clear evidence of photoluminescence from the ^{1}(TT) state in rubrene single crystals, despite the small S_1-^{1}(TT) energy gap. Our photoluminescence experiments show that previously observed differences in the behaviour of c-polarised and ab-polarised emission components are found only at particular sites on rubrene crystals. We have shown that these sites are likely to correspond to microcrystal surface defects.

This result introduces something of a conundrum. If ^{1}(TT) is non-emissive in rubrene crystals, the matrix element that couples S_1 with ^{1}(TT) through vibrational modes in Equation 5.1 must be small. However, recent ultrafast experiments[35] have suggested that the vibronic coupling between S_1 and ^{1}(TT) is strong and that it enables ultrafast singlet fission (which is ordinarily forbidden due to the unique symmetry of the rubrene crystal[188]). We investigate this apparent discrepancy in the following chapter.

5.5 Methods

5.5.1 Rubrene single crystal growth

Rubrene single crystals were grown by Maik Matthiesen at the University of Heidelberg using physical vapour transport. Details can be found in Section 3.2.3.

*The PL image was recorded by Rahul Jayaprakash.

5.5.2 Ground state absorption

Ground state absorption spectra were recorded using the probe beam of the picosecond transient absorption setup described in Section 3.4.2. The probe spot size is less than 100 µm in diameter at the sample position which is less than the smallest dimension of crystal 1 (Figure 5.2). The transmission of the probe light was recorded through both the crystal and bare substrate (by translating the crystal laterally out of the beam focus) and the absorbance calculated from these two measurements.

5.5.3 Time-resolved photoluminescence

Narrowband 500 nm pump pulses were produced in a home-built non-collinear optical parametric amplifier (NOPA)[†], seeded by a Ti:sapphire regenerative amplifier (Solstice, Spectra-Physics, 800 nm, 90 fs FWHM, 1 kHz, 4 mJ). The NOPA produces broadband pulses spanning the range 500–700 nm; the narrowband pulses were obtained by passing the NOPA output through a 500 nm bandpass filter (FWHM 10 nm). The excitation was focussed onto the sample at a 45° incidence angle by an aspheric lens ($f = 32$ mm). The photoluminescence was collected by the same lens (reflection geometry) at normal incidence and recorded by the spectrograph and iCCD described in Section 3.4.1. Filters were used to eliminate pump scatter (longpass Schott OG550 for 500 nm excitation and 532 nm notch for 532 nm excitation). The pump polarisation was set parallel to the b-axis for crystal 1. For measurements of PL anisotropy, a rotatable linear polariser was placed before the spectrograph slit. The TRPL setup is illustrated in Figure 3.8a.

We note that following the laboratory closure during the COVID-19 pandemic, the wavelength calibration of our spectrograph became slightly off. The measurements presented in this chapter (and the next) were recorded after the laboratory reopened, but before the calibration issue was realised. Therefore, all spectra presented in this chapter have been shifted by 8.5 nm to correct for the miscalibration. In Figure 5.7, we compare such a corrected spectrum (crystal 1, 0–2 µs) against a spectrum from Ref. 34 measured for a pristine rubrene crystal under similar experimental conditions. We find that the 8.5 nm shift correction results in an extremely close match between our spectrum and the literature reference. The slight suppression of the blue edge of the spectrum in our measurement can be attributed to absorption by the 550 nm longpass filter used and the small differences around 650 nm may arise from the different

[†]The NOPA was built by Sayantan Bhattacharya.

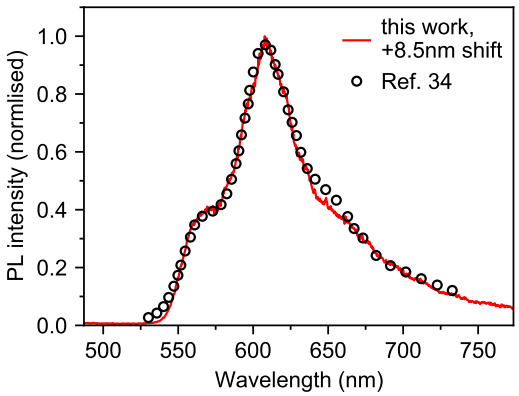

Figure 5.7 | Wavelength miscalibration and comparison with literature spectra. Normalised PL spectrum of crystal 1 (0–2 µs), recorded using our spectrograph and iCCD. The spectrum has been shifted by 8.5 nm to account for the wavelength miscalibration that occurred during a prolonged laboratory closure prior to the measurements in this chapter being taken. Our corrected spectrum closely matches an equivalent spectrum from Ref. 34, demonstrating that the 8.5 nm shift is sufficient to correct the miscalibration. Data shown by black circles adapted with permission from Reference 34; Copyright 2012 by the American Physical Society.

crystals studied, as discussed above.

Chapter 6

Triplet-pair formation in crystalline rubrene

In the previous chapter we found no evidence for emissive $^1(TT)$ states in rubrene single crystals despite the close energy level alignment of $^1(TT)$ and S_1. This implies that vibronic coupling between the two states must be weak. This conclusion is in direct contradiction with recent work, in which near instantaneous $^1(TT)$ formation in rubrene single crystals was explained by invoking strong vibronic coupling between S_1 and $^1(TT)$. In this chapter we attempt to resolve this conundrum. We perform transient absorption spectroscopy of rubrene single crystals at different excitation wavelengths and incidence angles and find no evidence of instantaneous $^1(TT)$ formation, suggesting, in line with calculations, that the vibronic coupling between S_1 and $^1(TT)$ is weak. Strikingly however, we discover that polycrystalline films exhibit pronounced instantaneous $^1(TT)$ formation. We suggest that ultrafast singlet fission in crystalline rubrene can instead be enabled by static disorder.

6.1 Introduction

Singlet fission ordinarily requires electronic coupling between S_1 and ^{1}(TT), possibly via charge transfer states as described in Section 2.6.3. In orthorhombic single crystals of rubrene however, the electronic coupling between ^{1}(TT) and S_1 (and charge transfer states) vanishes owing to the peculiar symmetry of the C_{2h} π-stacking[188]. As a result, singlet fission is forbidden at the equilibrium geometry and requires the action of vibrational modes to break the symmetry constraint[188]. Calculations of the singlet fission dynamics of rubrene crystals, based on this framework, show that singlet fission is incoherent, and that the ^{1}(TT) population rises from zero, reaching approximately 20% of the initial

photo-excited S_1 population by 1 ps[188].

Some transient absorption measurements[189,288] and transient grating pump-probe experiments[289] of rubrene crystals appear to support these calculations. They found that the ^{1}(TT) population, probed via its excited state absorption at 510 nm, initially increased approximately exponentially following photo-excitation, with a time constant of ∼2 ps (although the transient grating experiments reported this time constant to vary substantially with excitation wavelength).

In 2017 however, several studies reported near-instantaneous (instrument-limited, i.e. $<$ 25 fs) formation of ^{1}(TT) in rubrene single crystals[35–37] not predicted by the calculations[188] discussed above and in contrast to the other experimental results[189,288,289]. The explanations for this surprising observation differ. The details of the proposed mechanisms and the discrepancies between them are nicely described in a recent review article[191]. Here, we give an overview of the key points.

Miyata et al.[35] found that part of the total triplet-pair population was generated within the 25 fs instrument response time of their ultrafast transient absorption experiment. This initial ^{1}(TT) population was temperature independent and a subsequent, slower rise was found to be thermally activated. At 35 K, the authors observed vibrational coherences in both the ^{1}(TT) and S_1 transient absorption signals. Through analysis of these coherences, the authors proposed a mechanism whereby strong mixing between S_1 and ^{1}(TT) occurs near the Franck-Condon region (ground state minimum), enabled through a vibrational mode of appropriate symmetry. This mixing allows direct, coherent excitation of both S_1 and ^{1}(TT)[35] and is supported by recent calculations[186].

Breen et al.[36] performed both electronic transient absorption and 2D electronic spectroscopy at room temperature and found no evidence of coherent oscillations, despite observing the same $<$ 25 fs partial population of the ^{1}(TT) state. Instead, the authors found that a vibronic shoulder of the ^{1}(TT) excited state absorption spectrum decayed with a time constant of 2 ps which they assigned to relaxation of a vibrationally dressed ^{1}(TT) state, denoted ^{1}(TT)′. A mechanism was proposed whereby the initially excited state is a vibrationally dressed S_1 state, S_1′, that undergoes ultrafast equilibration with ^{1}(TT)′. The equilibration process was suggested to be mediated by weak couplings between S_1 and ^{1}(TT) with the ultrafast time constant ascribed to the resonance between the vibronic sublevels[36]. Interestingly, a similar mechanism was proposed by Ishibashi et al.[288], but instead with a 2 ps time constant.

The coherent vibronic coupling mechanism proposed by Miyata et al. implies

that ^{1}(TT) should be emissive in rubrene crystals[35,103]. However, in Chapter 5, we found no evidence of ^{1}(TT) photoluminescence signatures in our rubrene single crystals. In this chapter, we therefore aim to clarify the mechanism of ^{1}(TT) formation in rubrene single crystals.

6.2 Selective excitation of pristine rubrene crystals

We use the same 'pristine' rubrene crystals studied in Chapter 5 and shown in Figure 5.2. We judged our crystals to be pristine, particularly crystal 1, by comparing their PL spectra against those reported in Ref. 34, an extremely careful and comprehensive analysis of the absorption and emission properties of rubrene single crystals (see, for example, Figure 5.7). We note that the PL spectra reported by Miyata et al.[35] and Bera et al.[37] are both dominated by the 650 nm band indicative of defective rubrene crystals[34,282,286]. Furthermore, the PL spectrum (from platelet crystals very similar to ours) reported by Breen et al.[36] is dominated by a band at 565 nm. In Chapter 5, we showed, in accordance with Ref. 34, that such emission can arise from microcrystal defects on the crystal surface. The lack of experimental details surrounding the acquisition of the PL spectrum make interpretation difficult, however, we note that such defects can be clearly seen in the microscope image presented by Breen et al.[36]. In fact, of the transient absorption literature reviewed above, only Ishibashi et al.[288] report a PL spectrum consistent with pristine rubrene crystals[34]. We will see below that potentially defective crystals may have a substantial impact on the measured transient absorption data.

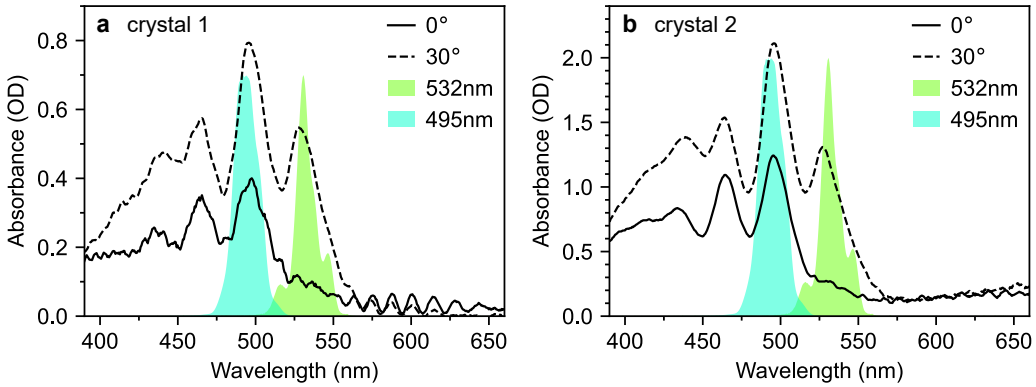

Figure 6.1 | Selective excitation of rubrene single crystals. a,b, Absorption spectra of rubrene single crystals 1 and 2 at incidence angles of 0° and 30°, reproduced from Figure 5.3. The 495 nm and 532 nm pump spectra used in the transient absorption experiments presented in this chapter are shown. The two pump wavelengths target the 0-1 and 0-0 vibronic transitions respectively.

Figure 6.1 reproduces the absorption spectra of crystals 1 and 2 from Figure 5.3. Alongside, we plot the spectra of two different pump pulses used in our transient absorption experiments (see Section 6.7.2). The pulse centred at 495 nm selectively excites the 0-1 transition, which includes both ab- and c-polarised components[34]. The pulse centred at 532 nm selectively excites the vibrationless 0-0 transition, which is exclusively c-polarised[34].

According to the coherent mechanism proposed by Miyata et al.[35], excitation using either of these pump pulses should result in instrument-limited ^{1}(TT) formation. In contrast, the incoherent pathway suggested by Breen et al.[36] should only be activated when the initial photo-excited state is a vibrationally dressed S_1 state. In that case, instrument-limited ^{1}(TT) formation should be observed only when pumping at 495 nm. Comparing the dynamics of the ^{1}(TT) population under these two excitation conditions should therefore enable us to distinguish between these two mechanisms. To obtain further confirmation of our conclusions in Chapter 5 that ^{1}(TT) is not responsible for the ab-polarised absorption component, we also performed experiments at both 0° and 30° incidence.

6.3 No instantaneous ^{1}(TT) formation in single crystals

Figure 6.2a,b show transient absorption spectra recorded in crystal 1 with 495 nm excitation at 0° incidence, and 532 nm excitation at 30° incidence, respectively. The band at 435 nm arises from the $S_1 \rightarrow S_3$ excited state absorption[189,278] whilst the band at 510 nm is characteristic of $T_1 \rightarrow T_3$[35,36,189,278,288]. In the probe region beyond 550 nm, both singlet and triplet excited state absorptions contribute[35,278,290]. Absorptions from charge separated states can also be present in the spectral region around 600–900 nm[291,292]. We discount them here because they are usually observed only under ultraviolet excitation[189,291,292] and are generally short-lived[292], unlike the persistent signal apparent at 660 nm in our measurements. We observe an isosbestic point between the singlet and triplet-pair absorption features, indicating that singlet fission is a one-to-one conversion between S_1 and ^{1}(TT)[189].

The transient absorption dynamics corresponding to Figure 6.2a,b are plotted in Figure 6.2c,d for probe wavelengths of 435 nm (mostly singlets), 660 nm (a mixture of singlets and triplet-pairs) and 510 nm (almost entirely triplet-pairs). The dynamics are normalised to the maximum signal at 435 nm. In Figure H.6, we demonstrate that the dynamics at 510 nm are almost entirely uncontaminated by spectral overlap with nearby singlet bands and are thus a

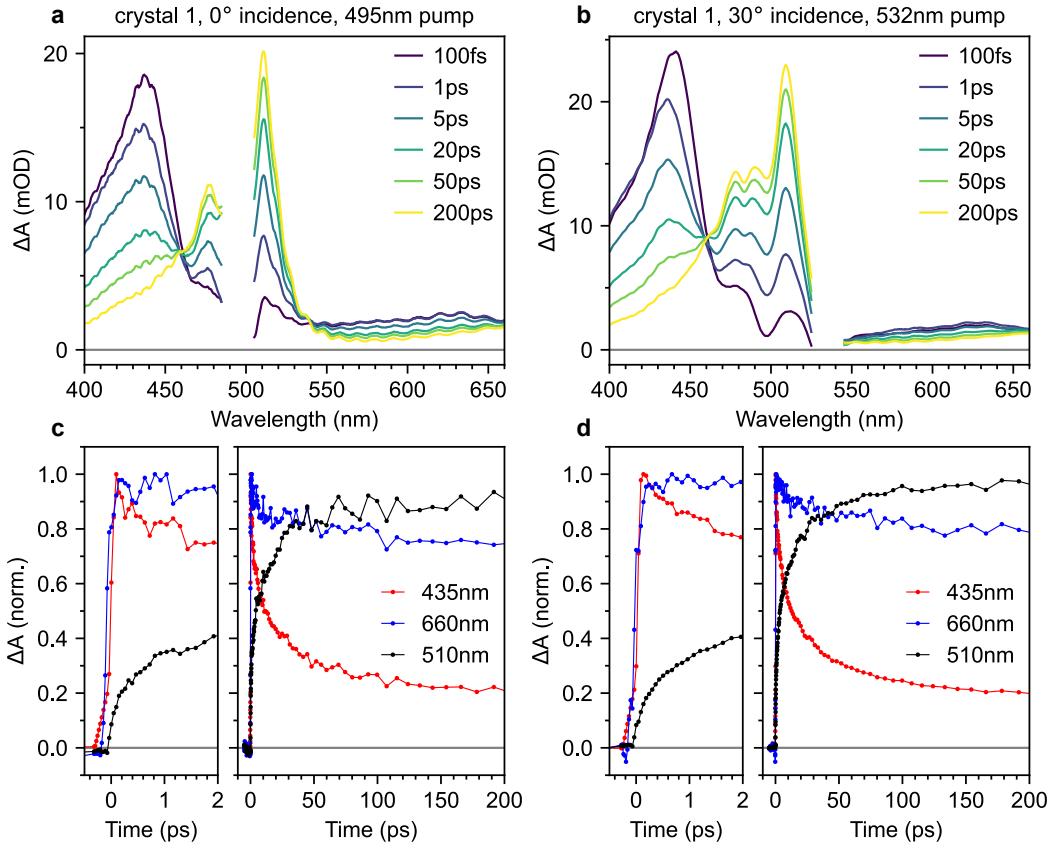

Figure 6.2 | Transient absorption spectroscopy of rubrene crystals. a,b, Transient absorption spectra measured on crystal 1 at different delay times for 495 nm excitation at 0° incidence (**a**) and 532 nm excitation at 30° incidence (**b**). **c,d**, Corresponding transient absorption dynamics at 435 nm (mostly S_1) 660 nm (mixture of S_1 and ^{1}(TT)) and 510 nm (almost entirely ^{1}(TT)). The excitation intensity was 70 µJ cm^{-2} for all experiments reported in this chapter.

good measure of triplet-pair population.

We find no clear evidence of instrument-limited ^{1}(TT) formation in Figure 6.2c,d. The rise in the triplet-pair population at 510 nm starts after, and is less steep than, the rise of the photo-excited singlet population at 435 nm. This cannot be an artefact of the chirp correction procedure (see Section 6.7.2) because it is also later, and less steep, than the rise of the signal at 660 nm. This behaviour is the same regardless of excitation wavelength.

In order to compare our measured triplet-pair dynamics with previous measurements, we attempted to extract time constants using multi-exponential fitting. We found that whilst a bi-exponential function gave a good fit, the extracted time constants varied significantly depending on the time window used for the fit. Moving to a tri-exponential function (Figure 6.5a, below) provided a much more robust set of fitting parameters. However, as a result of the large number of fitting parameters (six) and clear non-exponential behaviour, it does

not make sense to talk about time constants *per se*. Nevertheless, the fitting results are instructive, particularly when we come to compare the triplet-pair dynamics to those measured for a polycrystalline film below.

A tri-exponential fit to the triplet-pair dynamics of crystal 1 (532 nm excitation, 30° incidence), shown below in Figure 6.5a, yielded time constants of 0.25(3) ps (23(2) %), 1.8(4) ps (26(3) %) and 14(3) ps (51(2) %). These three values are similar to those extracted by Breen et al.[36] and the latter two time constants agree well with those reported by Ma et al.[189] and Ishibashi et al.[288] based on bi-exponential fitting. Our sub-picosecond component is slower than that of Ref. 36 by a factor of 2-3. This might reflect differences in the instrument response time, though we reiterate that our initial triplet-pair rise is slower than the rise time of the singlet exciton signal.

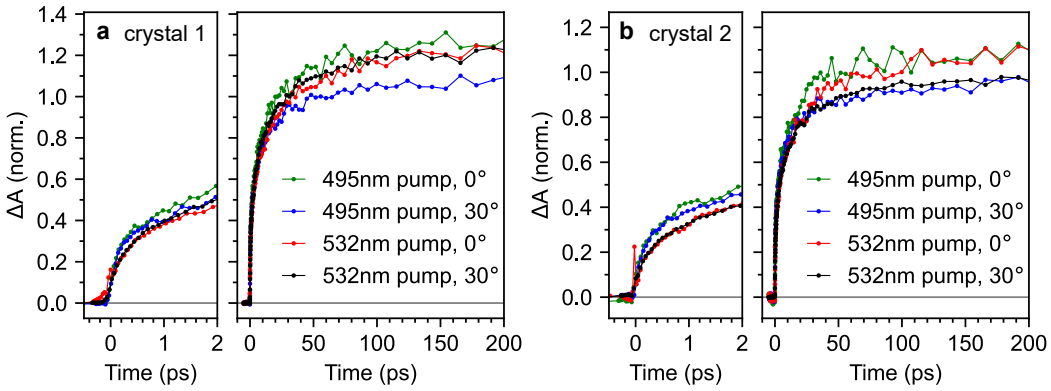

Figure 6.3 | Consistent triplet-pair dynamics in rubrene crystals. **a,b**, Triplet-pair dynamics, probed at 510 nm for single crystals 1 and 2 respectively. No major differences were observed between different crystals, excitation wavelengths or incidence angles.

For completeness, Figure 6.3 compares the triplet-pair dynamics probed at 510 nm for both crystals 1 and 2 under different excitation wavelengths and incidence angles. We find that the dynamics are very similar across both crystals, incidence angles and excitation wavelengths. It appears that the triplet-pair dynamics exhibit a very slightly more pronounced sub-picosecond component when the excitation wavelength is 495 nm, resulting in a marginally larger population at 2 ps. At first glance, this appears to support the conclusions of Breen et al.[36] that a vibrationally dressed photo-excited singlet state (only possible with 495 nm excitation in our experiment) is required to enable ultrafast ^{1}(TT) formation. However, it is noticeable from Figure 6.3 that the effect of excitation wavelength is more pronounced in crystal 2 than crystal 1. Crystal 2 is significantly more defective (see Figure 5.2), suggesting that this may not be an intrinsic bulk effect.

6.4 Clear instantaneous ^{1}(TT) formation in polycrystalline films

Since many of the rubrene crystals reported in the literature exhibit PL spectra indicative of defects, and since we find that the effect of excitation wavelength on sub-picosecond triplet-pair formation is more pronounced in a more defective crystal, we repeated our measurements on a polycrystalline thin film. The absorption spectrum is shown in Figure 6.4a and the microscope image in Figure 6.4b reveals a polycrystalline texture on the micrometer length scale.

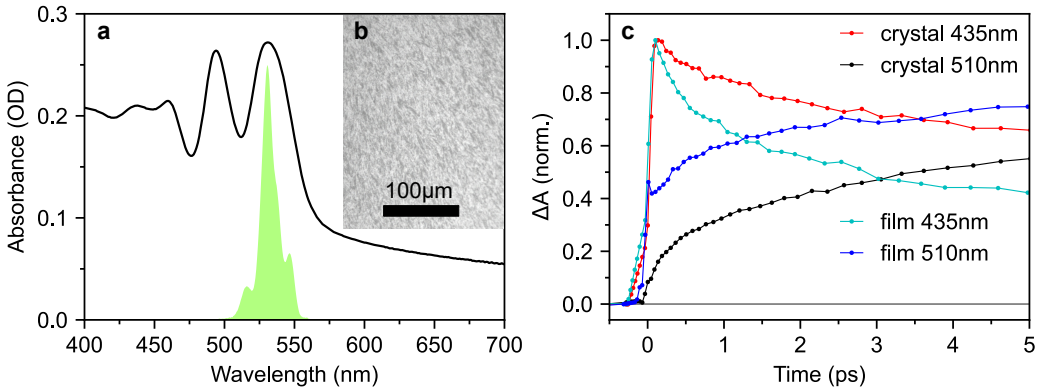

Figure 6.4 | Instantaneous triplet-pair formation in polycrystalline films. **a**, Absorption spectrum of a polycrystalline rubrene film prepared by thermal evaporation and annealing. **b**, Microscope image of the film surface, revealing a micrometer-scale polycrystalline texture. Many of the crystals appear to be oriented in the same direction. **c**, Comparison of transient absorption dynamics at probe wavelengths of 435 nm and 510 nm between crystal 1 (30° incidence) and the polycrystalline film. The excitation wavelength (532 nm) and intensity (70 µJ cm^{-2}) were the same in both cases.

Strikingly, when comparing the transient absorption dynamics of the film and crystal in Figure 6.4c, we find very clear evidence of instantaneous ^{1}(TT) formation in the polycrystalline sample. The initial rise of the triplet-pair signal at 510 nm exactly follows the rise of the photo-excited singlet at 435 nm, demonstrating ^{1}(TT) formation within the instrument response. We demonstrate in Figure H.7 that this observation is not an artefact of spectral overlap. We note that the instantaneous ^{1}(TT) formation in the polycrystalline film occurs even though the excitation wavelength is 532 nm. 532 nm is not sufficiently energetic to populate vibrationally dressed S_1 states, thereby casting doubt on the mechanism proposed by Breen et al.[36] to explain femtosecond singlet fission in rubrene.

We repeated the tri-exponential fitting for the triplet-pair dynamics on the polycrystalline film. The fit is shown in Figure 6.5a and we extracted time

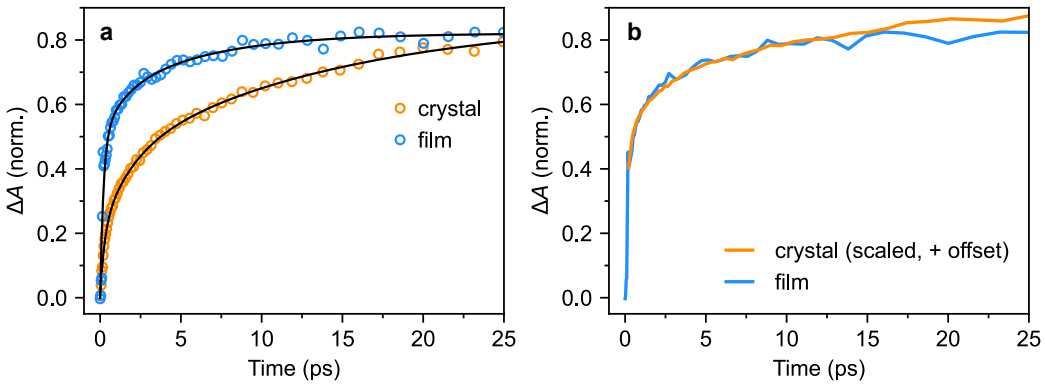

Figure 6.5 | Triplet-pair dynamics in crystals and films. **a**, Tri-exponential fits to the triplet-pair population dynamics of crystal 1 (532 nm excitation, 30° incidence) and a polycrystalline film (also 532 nm excitation). **b**, The triplet-pair dynamics of the polycrystalline film, following the instrument-limited rise to 50% of the maximum population, closely match those of the bulk single crystal when a constant offset is added to the latter.

constants of 0.21(5) ps (59(12) %), 1(3) ps (16(23) %) and 6(6) ps (25(27) %). The large errors on the latter two components illustrate the limitations of such fitting, but it is clear that the sub-picosecond component is significantly greater, and slightly faster, than in the bulk crystal. More instructively, in Figure 6.5b, we show that for the first few tens of picoseconds, the triplet-pair dynamics of the polycrystalline film can be explained as an instrument-limited initial offset of around 50% of the maximum population with subsequent dynamics that exactly match those of the bulk crystal.

6.5 Discussion

Our transient absorption results demonstrate that instantaneous, or instrument-limited, formation of ^{1}(TT) following photo-excitation of crystalline rubrene occurs in polycrystalline thin films but not in bulk single crystals. Following this ultrafast rise in the film, the ^{1}(TT) dynamics appear almost identical to those of the bulk crystal. The lack of femtosecond singlet fission in rubrene crystals is in line with expectations[188], raising the question of what factors enable it to occur in polycrystalline films.

One possibility is that ^{1}(TT) and S_1 are mixed at certain sites within the film morphology where the C_{2h} π-stacking symmetry breaks down due to static disorder, for example at grain boundaries or dislocations. At these sites, ^{1}(TT) can be formed extremely rapidly, whilst elsewhere, the formation dynamics mimic those of the bulk crystal, as shown in Figure 6.5b. It is perhaps curious then that singlet fission is reported to be completely suppressed in truly amorphous

solid rubrene[289], though this may simply be a result of weaker intermolecular couplings. Further experiments and calculations may be required to discover which intermolecular alignments are preferential for ultrafast singlet fission in rubrene.

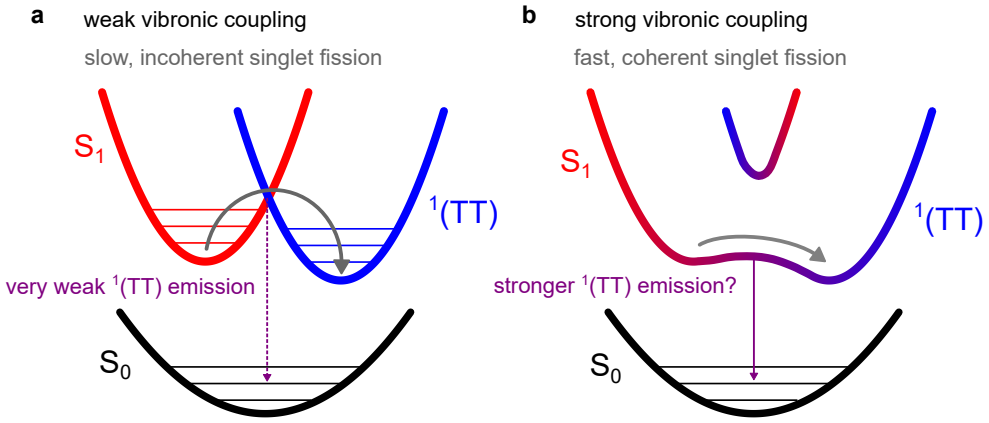

Figure 6.6 | Possible singlet fission pathways in crystalline rubrene. **a**, In bulk crystals, low energy modes provide weak vibronic coupling between S_1 and ^{1}(TT). As a result singlet fission is incoherent and slow (picosecond timescale). **b**, At sites where the symmetry is broken by static disorder, S_1 and ^{1}(TT) can become strongly mixed, allowing fast (femtosecond) coherent formation of both. We might expect the strength of any Herzberg-Teller emission from ^{1}(TT) to follow the strength of vibronic coupling (purple arrows).

These two proposed types of singlet fission, bulk and defect, are shown schematically in Figures 6.6a and 6.6b respectively. In the bulk (a), low-energy librational modes provide weak vibronic coupling between S_1 and ^{1}(TT), enabling incoherent singlet fission to occur with a picosecond time constant. At sites where the symmetry constraint is broken (b), ^{1}(TT) and S_1 may become substantially mixed. Photo-excitation at such sites results in a coherent superposition of S_1 and ^{1}(TT).

The pathways proposed in Figure 6.6 suggest that photoluminescence from ^{1}(TT), enabled by vibronic coupling, or Herzberg-Teller intensity borrowing, might be present in polycrystalline thin films but not in single crystals. To test this, we measured the time-resolved photoluminescence of our polycrystalline thin film under both 500 nm and 532 nm excitation (Figures 6.7a and 6.7b respectively).

Following 532 nm excitation (Figure 6.7b), we do observe a small shoulder grow in on a timescale of several nanoseconds at 630 nm. This is similar to a spectral feature previously assigned to ^{1}(TT) in rubrene thin films[74]. However, we observe no such behaviour following excitation at 500 nm (Figure 6.7a). The slight changes in behaviour with excitation wavelength may be due rather to

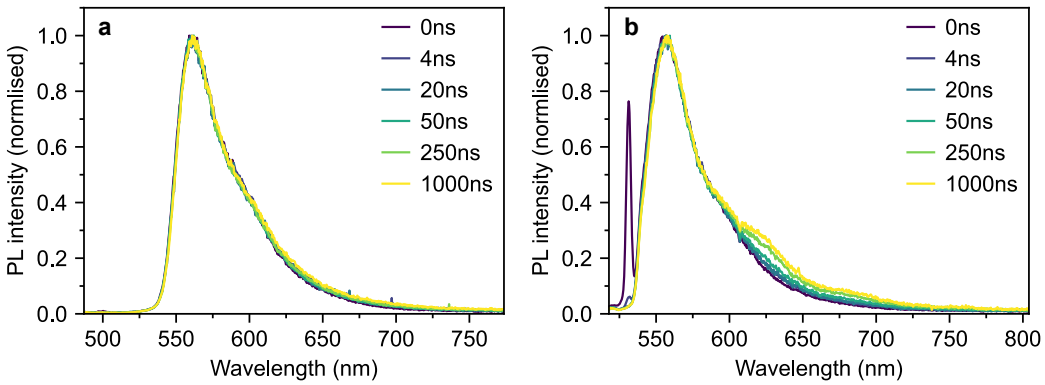

Figure 6.7 | TRPL of polycrystalline rubrene. a,b Time-gated photoluminescence spectra of a polycrystalline rubrene film following excitation at 500 nm (**a**) and 532 nm (**b**).

a different region of the film falling within the excitation spot across the two separate measurements. Furthermore, it is well known that defects in rubrene films can emit at around 630 nm (Ref. 34). Further experiments should therefore be performed before any assignment can be made.

In any case, even if ^{1}(TT) is notionally emissive in polycrystalline rubrene, it may not be possible to distinguish its spectral component from that of S_1 using time-resolved photoluminescence. If the two states are strongly mixed, we cannot necessarily talk in terms of separate diabatic S_1 and ^{1}(TT) states.

6.6 Conclusions

In this chapter, we have demonstrated that ultrafast instantaneous formation of ^{1}(TT) states in crystalline rubrene occurs in polycrystalline films but not in bulk crystals, in contrast to recent reports. Our results are consistent with calculations that showed singlet fission in rubrene crystals to be an incoherent process, occurring on the picosecond timescale, and driven by low energy vibrational modes that weakly couple S_1 to ^{1}(TT).

We proposed that the instantaneous ^{1}(TT) formation that we readily observe in polycrystalline films may arise from static disorder. At certain sites within the film morphology, molecules may be oriented in such a way as to break the symmetry and allow S_1 and ^{1}(TT) to mix. At such sites, singlet fission can be a coherent process.

We further hypothesised that such mixing might result in site-dependent Herzberg-Teller emission from the ^{1}(TT) state in polycrystalline rubrene. However, our time-resolved PL measurements found no clear evidence of this. These results highlight the need for more detailed experiments to investigate the de-

pendence of singlet fission on inter-molecular geometry in rubrene.

6.7 Methods

6.7.1 Sample preparation

Single crystal growth is described in Section 3.2.3. Rubrene thin films were prepared by thermal evaporation and annealing, as detailed in Section 3.2.2. The absorption spectrum of the rubrene film was recorded using a spectrophotometer (Cary60, Agilent).

6.7.2 Transient absorption spectroscopy

Transient absorption spectroscopy was performed using the setup described in Section 3.4.2. The chirp of the probe pulses was corrected for by measuring the coherent artefact of a bare substrate. Experiments were performed with the pump polarisation both parallel and perpendicular to the probe polarisation, allowing both the isotropic signal and anisotropy to be obtained[224,293]. Data presented in this chapter were taken in the parallel configuration; we show in Figure H.8 that these data are proportional to the isotropic signal (in other words, the anisotropy has no time dependence).

6.7.3 Time resolved photoluminescence

TRPL measurements were conducted as described in Section 5.5.3.

Chapter 7

On the spin statistics of triplet-triplet annihilation*

The preceding chapters have focussed on the formation and spectral signatures of the strongly exchange-coupled, spin-0 triplet-pair state $^1(TT)$. In Chapter 4, we found that $^1(TT)$ is formed via triplet-triplet annihilation and that this occurs via weakly bound (T...T) states. If $^1(TT)$ is similar in energy to S_1, as is the case for rubrene which we concentrated on in Chapters 5 and 6, then bright, spin-0 singlet excitons can be formed from two dark spin-1 triplets through triplet-triplet annihilation. The probability of obtaining a singlet state through such an interaction is given by the spin statistical factor, η. The value of η is therefore critical in determining the efficiency of devices that rely on triplet-triplet annihilation such as blue-emitting OLEDs and photon upconverters. In this chapter, we show that η is frequently incorrectly described in the literature. We use a combined theoretical and experimental approach, using rubrene as a model system, to investigate in detail the factors influencing the value of η and reveal several strategies for engineering materials with high values of η that have been largely overlooked to date.

7.1 Introduction

In Section 2.6, we saw how bright, emissive singlet excitons can be created from the fusion of two dark triplet excitons through the photophysical process of triplet-triplet annihilation (TTA)[97]. Efficient TTA is highly desirable for improving the performance of organic light emitting diodes (OLEDs)[295,296] and

*This chapter has been adapted from the following publication[294]: Bossanyi et al., *JACS Au* **1**, 12, 2188-2201 (2021). Some sample preparation was carried out by Yoichi Sasaki; all other work presented in this chapter is my own.

solar photovoltaics[13,14,20,106,107,202], as well as for biomedical applications[21,55] including targeted drug delivery[297] and optogenetics[23]. Furthermore, the interactions between triplet excitons that govern the TTA process are of fundamental interest to a variety of research areas such as the condensed phases of ground state triplet molecules[298–301], the physics of interacting bosons[302], quantum entanglement[31,117] and quantum information and computing based on organic molecules[303,304].

The probability that a pair of annihilating spin-1 triplet excitons results in a spin-0 singlet exciton is given by the spin statistical factor, η, with $0 \leq \eta \leq 1$. For OLEDs and TTA-mediated photon upconverters, materials systems with a high value of η would result in very efficient device performance[19,22,107,202,295,296]. However, despite its fundamental importance, the triplet-triplet interactions that govern the value of η are not, in general, fully understood or appreciated. As a result, several potential strategies for designing materials with a high value of η have been largely overlooked to date.

In Section 2.6.4, we discussed how, in the literature, the spin statistical factor of triplet-triplet annihilation, η, is almost always discussed in terms of nine pure-spin triplet-pair encounter complexes: one spin-0 singlet, three spin-1 triplets and five spin-2 quintets[22,38–42]. At first glance, this might suggest that $\eta = \frac{1}{9}$, however measurements of triplet-triplet annihilation upconversion (TTA-UC) efficiencies greatly exceeding this limit demonstrate that this is not the case[38,208] (recall that in TTA-UC, annihilating triplets are first sensitised on acceptor molecules by energy transfer from photo-excited donor species[19,22,107,202], as shown in Figure 2.19). As discussed further below, the quintet complexes readily dissociate again into individual triplets since molecular quintet states are energetically inaccessible in relevant molecules[209]. The triplet complexes on the other hand can undergo internal conversion to nearby triplet states, leading to the loss of one triplet of the pair[39,40]. If such internal conversion is efficient, this description yields $\eta = \frac{2}{5}$.

These conventional discussions of spin statistics overlook many of the subtleties of triplet-triplet interactions, studied initially by Merrifield and co-workers 50 years ago[102], further developed by others since[98,305] and explored in detail in Section 2.6.1. These interactions have been investigated in great depth more recently through research into singlet fission[29,30] which, as we demonstrated in Chapter 4, proceeds via the same intermediate triplet-pair states. Here we aim to bridge the apparent divide between the singlet fission and TTA-UC descriptions by demonstrating the profound effect of triplet-pair character, in particular the strength of inter-triplet exchange coupling, on

the spin statistical factor. Inspired by recent reports of high-level reverse intersystem crossing from T_2 to S_1[306], which could allow the loss associated with the formation of spin-1 triplet-pair complexes to be bypassed[307], we also investigate internal conversion rate constants and the fate of higher-lying triplet states and their impacts on the spin statistical factor.

We therefore begin by providing an overview of the spin physics of triplet-pair states in the context of TTA-UC. Next, we investigate the triplet-pair character, energy levels, internal conversion rates and reverse intersystem crossing in rubrene, the most common acceptor molecule for near-infrared-to-visible TTA-UC[42,107]. Based on these experimental results, we present an updated model for the spin statistics of upconversion that includes the effects of inter-triplet exchange coupling and orientation, as well as internal conversion rate constants, energy levels and reverse intersystem crossing. We find that variations in exchange energy and orientation can tune the spin statistical factor η within the range $\frac{2}{5} \leq \eta \leq \frac{2}{3}$, but that careful optimisation of the S_1, T_2 and T_1 energy levels may allow η to reach unity, thereby bypassing such considerations.

7.2 Theoretical background

In Section 2.6.1 we provided a detailed description of weakly and strongly exchange-coupled triplet-pair states and gave expressions for the governing spin Hamiltonian and the various spin wavefunctions. Here, we relate the spin physics of triplet-pair states to the spin statistical factor η of triplet-triplet annihilation.

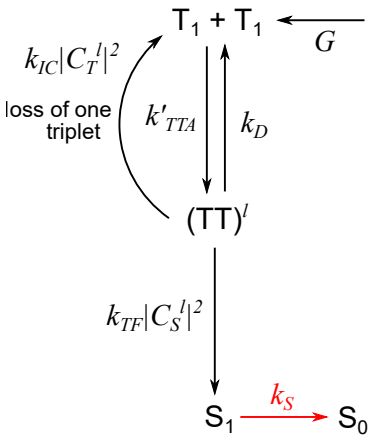

Figure 7.1 | The simplest kinetic model of TTA-UC. A schematic diagram of the simplest kinetic model for TTA-UC that considers triplet-pair spin character in a general way. The processes and rate constants are described in the text. This is referred to as model 1.

In order to understand the influence of triplet-pair character on the spin statistics of TTA-UC, we can construct a kinetic model based on the Johnson-Merrifield framework[102,124]. We note that while related analyses have been reported by Mezyk et al. in 2009[308] and more recently by Schmidt and Castellano[309], the effect of triplet-pair character on spin statistics was not explored in either work. Even in the work of Atkins and Evans[305], in which the inter-triplet exchange interaction was explicitly included, the spin statistical factor (written by them as λ_T) was incorporated only as a parameter and no expression for it was ever given.

The simplest possible such model is illustrated in Figure 7.1. Triplet states generated at rate G can annihilate to form triplet-pair states $(\mathrm{TT})^l$, whose spin wavefunctions $|\psi_l\rangle$ are determined by the spin Hamiltonian (Equation 2.70). We choose to consider an annihilation process that depends linearly rather than quadratically on the triplet population. This results in a linear set of rate equations with a simple analytical solution under steady-state conditions. TTA is therefore described by an effective annihilation rate constant k'_{TTA}.

The triplet-pair states formed can either dissociate back into independent triplets with rate constant k_D or form a singlet state with rate constant k_{TF}, modulated by the singlet character $|C_S^l|^2$. Recall that

$$|C_S^l|^2 = |\,\langle S|\psi_l\rangle\,|^2, \tag{7.1}$$

where $|S\rangle$ is the pure spin-0 triplet-pair state defined in (Equation 2.71). The $|\psi_l\rangle$ are obtained by diagonalising the spin Hamiltonian (Equation 2.70), hence the overall triplet-pair fusion rate is also dependent on the spin Hamiltonian.

We also include an internal conversion channel, with overall rate constant k_{IC}, that results in the loss of one triplet; participation in this channel requires non-zero triplet character so the rate constant is modulated by $|C_T^l|^2$. Following Ref. 308, we define $|C_T^l|^2$ in an analogous way to the singlet character. Now however, there are three possible pure spin-1 triplet-pair states (Equation 2.71) and so we write

$$|C_T^l|^2 = \sum_{m=x,y,z} |C_{Tm}^l|^2 = \sum_{m=x,y,z} |\,\langle T_m|\psi_l\rangle\,|^2. \tag{7.2}$$

Quintet triplet-pairs are approximately equal in energy to S_1 only when two chromophores are involved. Coalescence from a quintet triplet-pair to a single-chromophore molecular quintet state is energetically infeasible[209] (the corollary for singlets and triplets is opposite). The only fate of quintets is therefore

to simply break apart again into independent triplets[39] and so no process in the model depends explicitly on the quintet character of the triplet-pair states. Nevertheless, for completeness, we will define the total quintet character $|C_Q^l|^2$ as

$$|C_Q^l|^2 = \sum_{m=a,b,x,y,z} |C_{Qm}^l|^2 = \sum_{m=a,b,x,y,z} |\langle Q_m|\psi_l\rangle|^2, \tag{7.3}$$

where $|Q_m\rangle$ are the pure spin-2 triplet-pair states defined in Equation 2.71. Finally, the singlet S_1 states decay radiatively back to the ground state with rate constant k_S.

The rate equations describing the above processes can be written as follows:

$$\frac{d[\mathrm{T}_1]}{dt} = G + 2k_D \sum_{l=1}^{9}[(\mathrm{TT})^l] + k_{IC} \sum_{l=1}^{9} |C_T^l|^2[(\mathrm{TT})^l] - 2k'_{TTA}[\mathrm{T}_1] \tag{7.4}$$

$$\frac{d[(\mathrm{TT})^l]}{dt} = \frac{1}{9}k'_{TTA}[\mathrm{T}_1] - k_D[(\mathrm{TT})^l] - k_{IC}|C_T^l|^2[(\mathrm{TT})^l] - k_{TF}|C_S^l|^2[(\mathrm{TT})^l] \tag{7.5}$$

$$\frac{d[\mathrm{S}_1]}{dt} = k_{TF} \sum_{l=1}^{9} |C_S^l|^2[(\mathrm{TT})^l] - k_S[\mathrm{S}_1]. \tag{7.6}$$

Since the photoluminescence quantum yield (PLQY) is unity in this model and no other losses are present besides spin statistical effects, the spin statistical factor η can be evaluated analytically by solving the equations under steady-state conditions. We obtain

$$\eta = \frac{2k_S[\mathrm{S}_1]}{G} \tag{7.7}$$

$$= \frac{\sum_{l=1}^{9} \frac{k_{TF}|C_S^l|^2}{k_{TF}|C_S^l|^2 + k_{IC}|C_T^l|^2 + k_D}}{\sum_{l=1}^{9} \frac{k_{TF}|C_S^l|^2 + \frac{1}{2}k_{IC}|C_T^l|^2}{k_{TF}|C_S^l|^2 + k_{IC}|C_T^l|^2 + k_D}}. \tag{7.8}$$

Equation 7.8 is identical to the expression previously arrived at by Schmidt and Castellano[309], though it was not written out explicitly in their work. At the time however, the distinction between weak and strong exchange coupling within triplet-pair states was not so well understood, and the true implications were not fully grasped.

We can evaluate Equation 7.8 for the limits of strongly and weakly exchange-coupled triplet-pairs discussed above. We find:

$$\eta_{strong} = \left(1 + \frac{3}{2}\frac{k_{IC}k_{TF} + k_{IC}k_D}{k_{IC}k_{TF} + k_{TF}k_D}\right)^{-1} \tag{7.9}$$

$$\eta_{weak} = \left(1 + \frac{1}{2}\frac{k_{IC}k_{TF} + 3k_{IC}k_D}{k_{IC}k_{TF} + k_{TF}k_D}\right)^{-1}. \tag{7.10}$$

Assuming that the dissociation of triplet-pair states is considerably slower than fusion or internal conversion ($k_D \ll k_{TF}, k_{IC}$), we obtain, as expected[40,309], $\eta = \frac{2}{5}$ in the limit of strong exchange coupling. Interestingly however, the spin statistical factor rises to $\eta = \frac{2}{3}$ for weakly exchange-coupled triplet pair states. In both cases, $\eta = 1$ if $k_{IC} = 0$.

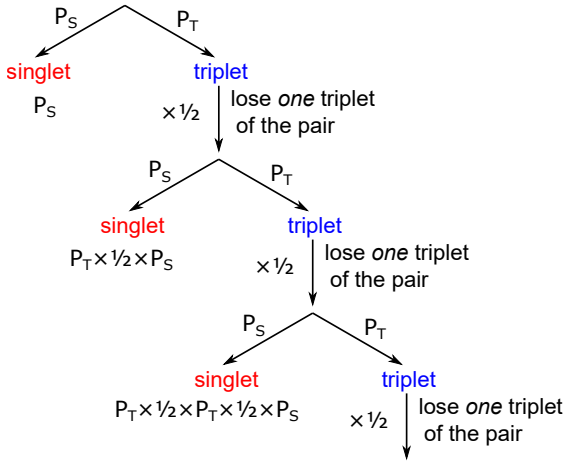

Figure 7.2 | Probability tree for TTA spin statistics. The spin statistical factor can be evaluated using a probability diagram when the triplet character is contained exclusively in pure spin-1 states (there is no triplet-quintet or triplet-singlet mixing, as is the case for molecules oriented parallel). P_S and P_T are the respective probabilities of forming a triplet-pair state with singlet or triplet character.

We can understand these limits more intuitively by considering the probability tree associated with triplet-pair formation events (Figure 7.2). Only triplet-pair states with singlet or triplet character are 'active' in TTA-UC and we let their probabilities of formation be P_S and P_T respectively. The spin statistical factor is then given by a geometric progression:

$$\eta = P_S \left[1 + \frac{1}{2}P_T + (\frac{1}{2}P_T)^2 + (\frac{1}{2}P_T)^3 + \ldots\right] \tag{7.11}$$

$$= \frac{P_S}{1 - \frac{1}{2}P_T}. \tag{7.12}$$

In the case of strong exchange coupling, the relevant triplet-pair states comprise one pure singlet and three pure triplets giving $P_S = \frac{1}{4}$ and $P_T = \frac{3}{4}$, and hence $\eta = \frac{2}{5}$. For weakly exchange coupled triplet-pair states (on parallel molecules) we again have three pure triplets. The singlet character is spread across three singlet-quintet mixtures. The quintet component does not affect the fate of these mixed spin states, and so we have $P_S = P_T = \frac{1}{2}$ and therefore $\eta = \frac{2}{3}$.

Equations 7.8-7.10 allow us to identify the key factors expected to affect the spin statistics of TTA-UC. First, the inter-triplet exchange energy J determines

the character of the triplet-pair spin wavefunctions. If J is negligible compared to other terms in the spin Hamiltonian (Equation 2.70), the finer details of the intra-triplet spin dipolar interactions, including intermolecular orientation, also play a role. Second, the rate constants of internal conversion from ^{3}(TT) to individual triplet states T_N, and the subsequent fate of T_N, have a profound effect. If the internal conversion is slow in comparison to triplet-pair fusion and separation, or if high-level reverse intersystem crossing[306,307,310,311] (HL-RISC) channels ^{3}(TT) states to S_1 via T_2, the spin statistical factor can approach unity[307]. In the following, we investigate these factors in turn in the context of rubrene, the most common acceptor molecule for near-infrared-to-visible TTA-UC.

7.3 Material system: rubrene

Figure 7.3a shows the molecular structure of rubrene. In crystalline rubrene, triplets are formed via singlet fission on the picosecond timescale[35,36,189], allowing their fusion behaviour to be studied without the presence of sensitizer species[216]. We perform the majority of our experiments on rubrene nanoparticles (NPs) dispersed in a poly(vinyl alcohol) (PVA) matrix (Figure 7.3b). Nanoparticles prepared in this way have an average diameter of 220 nm and show no sharp peaks in their X-ray diffraction pattern[203]. These nanoparticle films are the basis of recently reported solid-state TTA-UC systems[45,203] and we will investigate their photophysics in detail in Chapter 8.

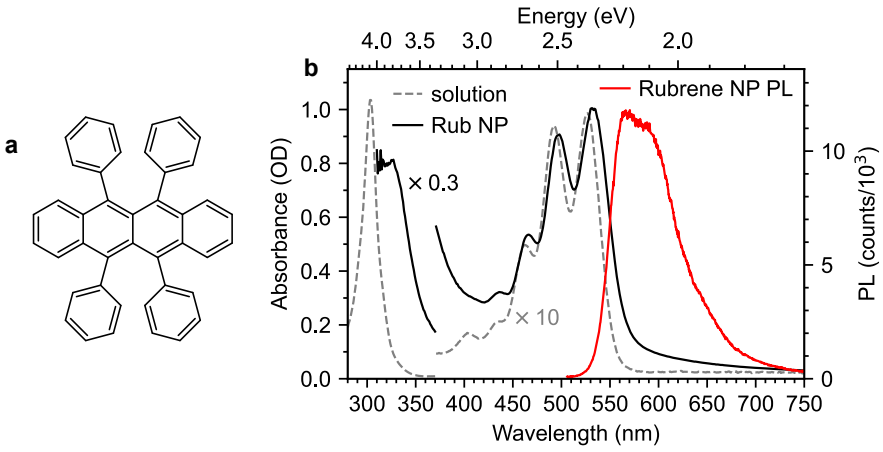

Figure 7.3 | Rubrene nanoparticle films. **a**, Molecular structure of rubrene. **b**, Absorption and emission spectra of rubrene nanoparticle films alongside the absorption spectrum of rubrene dissolved in toluene (1×10^{-4} M).

In Figure 7.3b we present the absorption and emission spectra of our rubrene

NPs alongisde the absorption spectrum of rubrene monomers in toluene. From these spectra, we confirm the S_1 energy level at between 2.32 eV and 2.23 eV based on the absorption and emission maxima. A small peak at 400 nm (3.1 eV) is clearly visible in the solution absorption spectrum which does not appear to follow the vibronic progression of the S_1 state. We suggest that this may be a signature of S_2. The strong absorption at around 300 nm (4.13 eV) corresponds to a higher-lying $S_0 \rightarrow S_N$ transition.

7.4 Triplet-pair character

Equations 7.8-7.10 demonstrate that the spin Hamiltonian of Equation 2.70, in particular the inter-triplet exchange coupling J, has a profound effect on the spin statistical factor η. In order to probe the inter-triplet interactions in our rubrene NPs, we measured the effects of magnetic fields on the delayed fluorescence during bimolecular triplet-triplet annihilation.

Figure 7.4a shows the time-resolved photoluminescence (PL) of a rubrene NP film at three different excitation intensities. Between 100 ns and 10 µs, we find that greater excitation density leads to a relative increase in measured PL. These dynamics are characteristic of bimolecular triplet-triplet annihilation that, via triplet-pair intermediates, repopulates the S_1 state. We found a similar signature in our measurements of diF-TES-ADT in Chapter 4.

To investigate the character of the triplet-pair states that are the initial product of bimolecular TTA, in Figure 7.4b we plot the change in PL intensity 0.5–1 µs after excitation as a function of applied magnetic field, at the same three excitation intensities as Figure 7.4a. We observe a small increase in the PL for fields < 50 mT followed by a decrease at higher fields. The overall magnitude of the effect increases with excitation intensity, demonstrating that the triplet-pairs responsible are products of bimolecular TTA.

Magnetic field effects (MFEs) such as those presented in Figure 7.4b are well-known to be characteristic of triplet-triplet annihilation and were first explained by Johnson and Merrifield 50 years ago[25,102]. In Section 2.6.2, we described how MFEs arise in the context of the Johnson-Merrifield model and we will revisit the key points here.

The Johnson-Merrifield model for the spin physics of singlet fission and triplet-triplet annihilation is based on the spin Hamiltonian (Equation 2.70) *but with no exchange term*, i.e. $J = 0$. Thus Johnson and Merrifield's rather vaguely defined 'TT' states are implicitly weakly exchange-coupled, though such terminology was not used at the time. As implied in the later work of Atkins

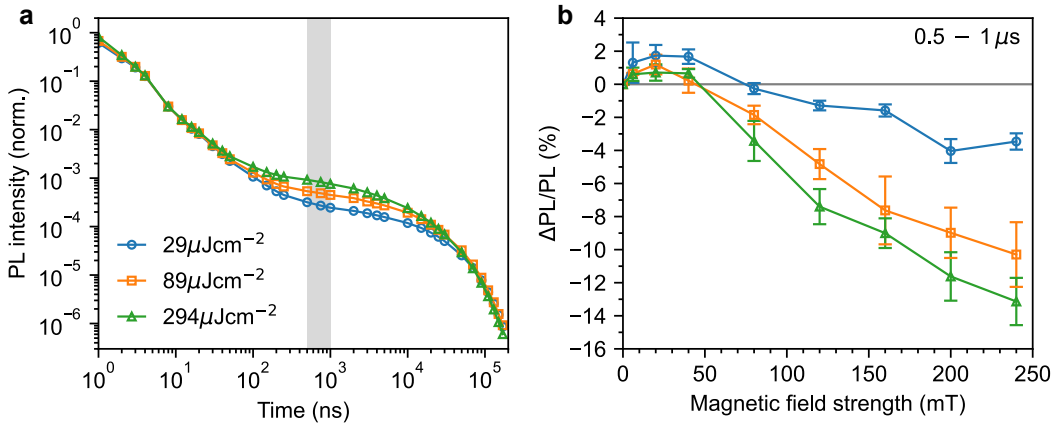

Figure 7.4 | Triplet-triplet annihilation and magnetic field effects. **a**, Time-resolved photoluminescence (PL) of a rubrene nanoparticle film at three different excitation intensities. The decays have been normalised at 8 ns. **b**, Magnetic field effects (MFEs) on fluorescence gated from 0.5–1 µs at the same three excitation intensities. Error bars reflect the variation between sweeping up and down in magnetic field and arise from slight photobleaching and small fluctuations in laser power.

and Evans[305], MFEs measured under fields of a few tens of mT are therefore signatures of weakly exchange-coupled triplet-pair states[115]. This can be readily understood by examining the spin Hamiltonian of Equation 2.70.

The zero-field splitting parameter D is typically around 10 µeV. For example, it is 6.45 µeV in tetracene[138] and is thought to be similar for rubrene[111]. The Zeeman term thus has a similar magnitude to the zero-field term when $g\mu_B B \sim D$, i.e. $B \sim 50$ mT. In the absence of other terms in the spin Hamiltonian of similar or greater magnitude, the competition between the Zeeman and zero-field terms at such fields leads to variations in the eigenstates $|\psi_l\rangle$ with magnetic field and hence to variations in the singlet character $|C_S^l|^2$ (Equation 2.75) of the triplet-pair states[102,124]. For example we have seen that when $B = 0$, three of the eigenstates ($|xx\rangle$, $|yy\rangle$ and $|zz\rangle$) have singlet character. If $g\mu_B B \gg D$, this falls to two[102], giving rise to the characteristic reduction in measured PL during triplet-triplet annihilation. If however, as is implicitly assumed in discussions of spin statistics for TTA-UC, the triplet-pairs formed are strongly exchange-coupled ($J \gg D$), we would not see any significant MFE until $g\mu_B B \sim J$, since the zero-field term now acts only as a tiny perturbation. This requires much higher field strengths and gives rise to very different types of MFE[114,115,119]. In acene materials, high-field MFEs have been reported in only one material, TIPS-tetracene[119] and the effect was observed only at 1.4 K.

MFEs corresponding to weakly exchange-coupled triplet-pairs, similar to ours in Figure 7.4b, have been measured during TTA-UC both in the solid state[308] and in solution[312–315]. Observations of these MFEs cannot prove that

all TTA events exclusively produce triplet-pair states that are initially weakly exchange-coupled since strongly exchange-coupled triplet-pairs do not contribute to the MFE at low (tens to hundreds of mT) magnetic field strengths. Nevertheless, the idea that triplet-pair states formed through bimolecular TTA are weakly exchange-coupled is supported by the results in Chapter 4 and it is demonstrably true for at least a proportion of TTA events. Below, we therefore explore the implications of this for the spin statistics of TTA-UC. First however, we investigate the other key factors that may impact the spin statistical factor: internal conversion, energy levels and reverse-intersystem crossing.

7.5 Energy levels and internal conversion

In order to estimate the rate constants of internal conversion from ^{3}(TT) to T_N, we must first determine the triplet energy levels. The energy of T_1 is well known to be 1.14 eV for rubrene[74,207,276]. We can therefore take the energy of ^{3}(TT) to be 2.28 eV in the absence of large inter-triplet binding. Reported values for the rubrene T_2 energy vary significantly[277,289,290,316]. For a precise determination of the higher lying triplet energies, we turn to transient absorption (TA) spectroscopy.

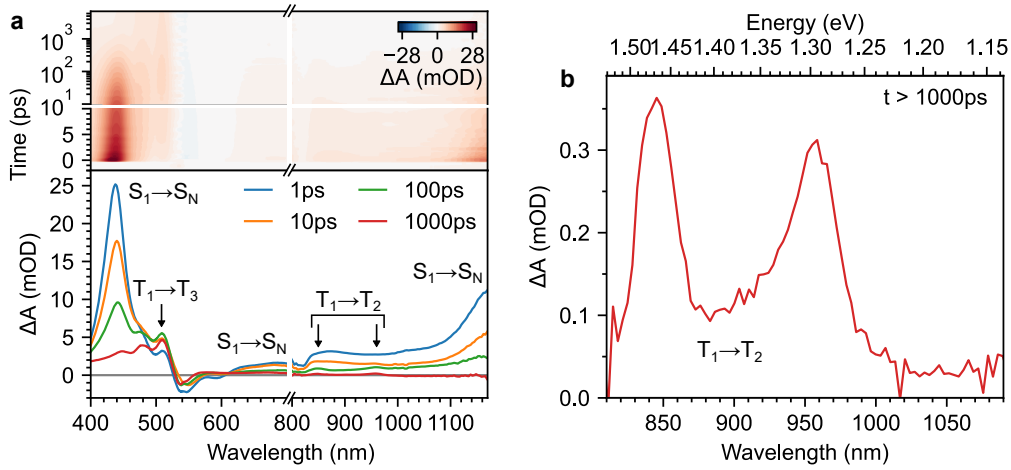

Figure 7.5 | Transient absorption spectroscopy of rubrene nanoparticle films. **a**, False-colour map showing transient absorption measurements of rubrene NP films pumped at 532 nm with an excitation intensity of 40 µJ cm^{-2}. **b**, Transient absorption spectra spanning the visible and near-infrared reveal singlet fission dynamics. Singlet photo-induced absorption (PIA) features at 440 nm, 680 nm and 1170 nm decay, accompanied by a rise in triplet PIA bands at 510 nm, 850 nm and 960 nm. The latter two peaks, highlighted in (**c**), correspond to the 0-0 and 0-1 bands of the $T_1 \rightarrow T_2$ transition. Given the T_1 energy of 1.14 eV, we calculate the T_2 and T_3 energy levels to be 2.43 eV and 3.57 eV respectively.

Figure 7.5 shows transient absorption spectra of a rubrene NP film pumped

at 532 nm. We find the characteristic signatures of singlet fission in rubrene: the singlet photo-induced absorption (PIA) at 440 nm decays rapidly, accompanied by a rise in the triplet PIA at 510 nm[189]. Broad PIA features at around 680 nm and 1170 nm decay with similar dynamics to the 440 nm band (Figure I.1) and we therefore assign them to $S_1 \rightarrow S_N$ transitions, as reported previously[35,74]. Finally, we observe two PIA peaks in the near-infrared at 960 nm and 850 nm (Figure 7.5c) whose dynamics match those of the well-known triplet PIA at 510 nm (Figure I.1). Similar peaks have previously been assigned to triplet states in rubrene[74]. Broad PIA features in the same spectral region have been explicitly assigned to $T_1 \rightarrow T_2$ transitions in rubrene[35], in agreement with calculations[317]. The two sharp peaks that we measure here are separated in energy by 0.17 eV, suggesting that they belong to a vibronic progression. We therefore assign them to the 0-0 and 0-1 vibronic peaks of the $T_1 \rightarrow T_2$ transition, putting the T_2 energy at 2.43 eV. The next triplet PIA is that at 510 nm, suggesting that T_3 lies at 3.57 eV.

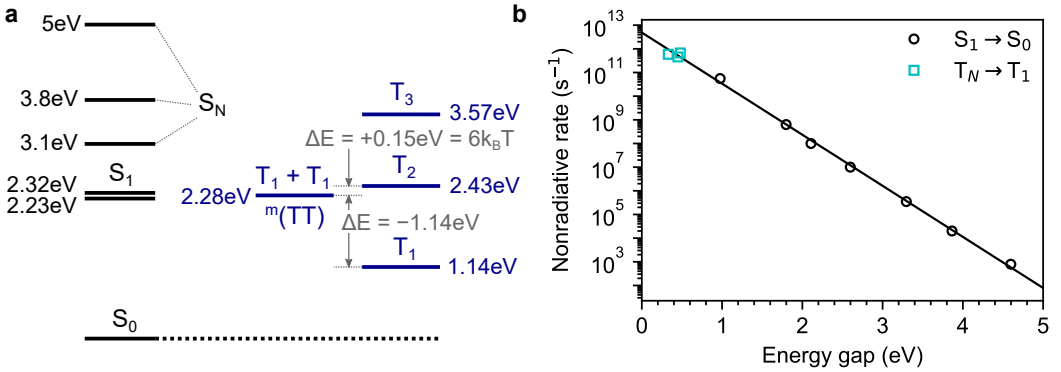

Figure 7.6 | Energy levels of rubrene and internal conversion in acenes. **a**, Energy level diagram for rubrene based on the transient absorption spectra in Figure 7.5. ^{3}(TT) $\rightarrow$ T_1 is exothermic by 1.14 eV and ^{3}(TT) $\rightarrow$ T_2 is endothermic by 150 meV $= 6k_BT$. **b**, $S_1 \rightarrow S_0$ nonradiative rates plotted against optical gap for acenes based on data in Refs. 318 and 319. We find excellent agreement with the energy gap law. Measurements of triplet-triplet internal conversion rate constants in erythrosin B, rose bengal and tetraphenylporphyrin[310] follow the same gap law.

We use the photo-induced absorptions from Figure 7.5 to construct the energy level diagram of rubrene shown in Figure 7.6a. Of particular importance for the spin statistics of upconversion are the energy differences between $2T_1 \approx {}^3$(TT), T_1 and T_2. ^{3}(TT) $\rightarrow$ T_1 is exothermic by 1.14 eV, whilst ^{3}(TT) $\rightarrow$ T_2 is endothermic by 150 meV $= 6k_BT$. To date, only the relative energy levels have been considered in determining whether the ^{3}(TT) $\rightarrow$ T_N loss channel is operational in TTA-UC[41]. Here, we aim to go a step further by estimating the rate constants of the internal conversions.

As discussed in Section 2.4.1, in the absence of strong vibronic or non-adiabatic coupling, the rate constant of internal conversion in organic molecules obeys the energy gap law[59], which we write here as

$$k_{IC} = A \exp\left(-\frac{\gamma \Delta E}{\hbar\omega_0}\right), \tag{7.13}$$

where ΔE is the energy gap between the electronic states, $\hbar\omega_0$ is the highest available vibrational frequency that couples to the electronic states (taken to be the symmetric vinyl stretching mode at 0.17 eV)[61] and γ and the prefactor A are material system dependent.

We begin by assuming that internal conversion in the triplet and singlet manifolds obeys the same energy gap law. For singlet internal conversions, we use the rate constants of the nonradiative $S_1 \rightarrow S_0$ transition. These have been determined experimentally for the acene family from benzene through to hexacene[318] and also for carbon nanotubes[319]. Following Ref. 29, we plot these internal conversion rate constants against their optical gaps in Figure 7.6b and find excellent correspondence with the energy gap law. This allows us to extract values of $A = (4.9 \pm 1.3) \times 10^{12}\,\mathrm{s}^{-1}$ and $\gamma = 0.845 \pm 0.015$ for molecules comprising fused aromatic rings. Experimental determinations of triplet-triplet internal conversions are much less common, though measurements do exist for erythrosin B, rose bengal and tetraphenylporphyrin[310]. Plotting these values on Figure 7.6b, we find good agreement with the energy gap law for singlet manifold internal conversions, providing some justification of our earlier assumption.

We use the values of A and γ extracted from Figure 7.6b in Equation 7.13 to estimate the triplet internal conversion rate constants in rubrene. For the exothermic $^3(\mathrm{TT}) \rightarrow T_1$ process, we find a rate constant of $(1.7 \pm 0.5) \times 10^{10}\,\mathrm{s}^{-1}$ or (60 ± 20) ps. The endothermic route via T_2 requires thermal activation, but can then proceed with an energy gap of zero. Thus the rate constant can be approximated by

$$k_{^3(\mathrm{TT})\rightarrow T_2} = A \exp\left(-\frac{\Delta E_{T_2 - {}^3(\mathrm{TT})}}{k_B T}\right), \tag{7.14}$$

which evaluates to $(1.2 \pm 0.3) \times 10^{10}\,\mathrm{s}^{-1}$ or (80 ± 20) ps at room temperature. The internal conversion rate constants are therefore expected to be similar for transitions to T_1 and T_2 despite the endothermic nature of the latter. This is highly significant: it has been recently reported that high-level reverse intersystem crossing (HL-RISC) from T_2 to S_1 can occur in rubrene[306], potentially providing a pathway from $^3(\mathrm{TT})$ to S_1 that could alleviate at least some of the

losses usually implied by the formation of ^{3}(TT)[307]. We therefore use pump-push-probe spectroscopy to investigate the fate of the T_2 state in rubrene.

7.6 High-level reverse intersystem crossing

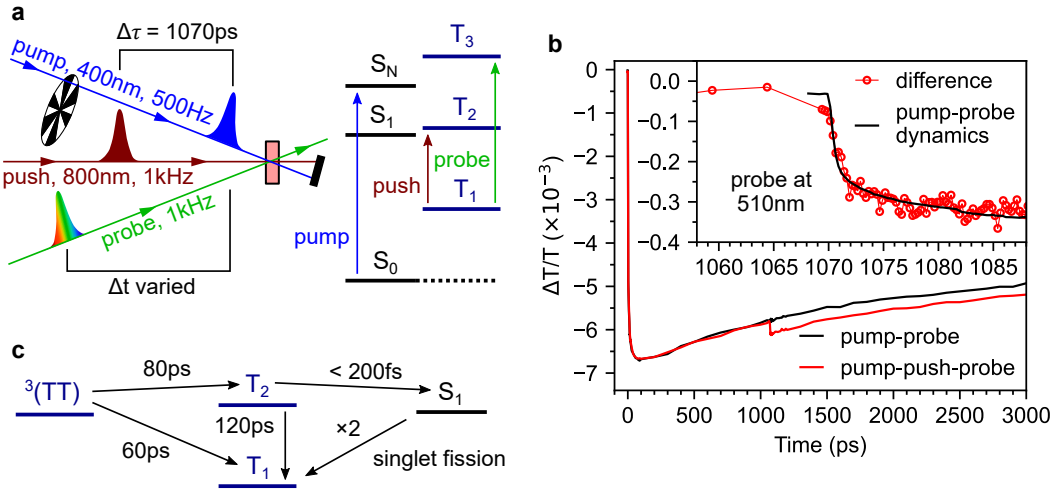

Figure 7.7 | Pump-push-probe spectroscopy of rubrene. **a**, Illustration of the pump-push-probe experiment and the electronic transitions targeted by each pulse. The pump initiates singlet fission. After 1 ns, the excited state population will be principally triplets, which are excited from T_1 to T_2 by the sub-bandgap push pulse. The probe is used to investigate the effect of the push pulses with and without the initial pump. **b**, Pump-probe and pump-push-probe data recorded at a probe wavelength of 510 nm (the $T_1 \rightarrow T_3$ transition) for a polycrystalline rubrene thin film. The push pulse causes an enhancement of the $T_1 \rightarrow T_3$ photo-induced absorption, with dynamics that match the initial singlet fission. **c**, Interpretation of the pump-push-probe data in terms of high-level reverse intersystem crossing from T_2 to S_1.

Figure 7.7a illustrates the pump-push-probe experiment and the transitions in rubrene targeted by each pulse. Full details of the experimental setup are given in Figure 3.13. The 400 nm pump pulses photo-excite the singlet manifold, thereby initiating singlet fission. The push pulses are delayed by a constant 1 ns with respect to the pump, by which time triplets are expected to be the dominant excited states. The sub-bandgap 800 nm push pulses are approximately resonant with the $T_1 \rightarrow T_2$ transition[290] and we monitor the probe transmission at 510 nm, which corresponds to $T_1 \rightarrow T_3$. Other probe wavelengths show no discernable push-induced effects due to reduced signal to noise (the triplet PIA is sharply peaked at around 510 nm). These are shown in Figure I.2. We halve the frequency of the pump pulses only, and record the differential transmission as a function of pump-probe delay.

We performed the pump-push-probe experiment on a polycrystalline thin

film (the same sample studied in Chapter 6 and characterised in Figure 6.4) rather than the rubrene NPs, since we found it to possess a stronger triplet excited state absorption at 510 nm, giving sufficient signal to noise to measure the push-induced effects. Figure 7.7b shows the results with (red) and without (black) the presence of the push pulses. We find that the push from T_1 to T_2 causes an increase, rather than a bleach, of the T_1 population. Furthermore, the dynamics of the push induced enhancement match the regular pump-probe dynamics of singlet fission, as shown in the inset of Figure 7.7b.

We consider several possibilities for the underlying photophysics, which we discuss in more detail in Appendix I. First, if the T_2 states populated by the push pulses simply undergo internal conversion to T_1, we would expect to see a bleach, and subsequent recovery of the T_1 population. Alternatively, the push could act as a second pump, perhaps through two-photon absorption[320,321]. In this case, the ground state population available to be 're-pumped' by the push is depleted by the first pump pulse, and we would again expect to see a reduction in signal when the push is present. Instead, we observe an enhancement.

We suggest that these results are consistent with recent reports of exothermic high-level reverse intersystem crossing from T_2 to S_1 in rubrene[306]. In this case, T_2 states populated by the push are converted, via S_1 and singlet fission, into pairs of triplets. This can only occur in the presence of the initial pump; it therefore manifests itself as an enhancement in the triplet signal rather than a bleach, since each T_2 state results in a pair of triplets. Quantitative calculations in Appendix I further support this assignment. We find that the HL-RISC mechanism should result in a push-induced $\Delta T/T$ signal of between -2.4×10^{-4} and -9.3×10^{-4}. Our measured signal of -3.5×10^{-4} falls within this predicted range. We note that the reverse intersystem crossing must occur within the instrument response of our setup ($\sim$ 200 fs) for the HL-RISC pathway to be consistent with our results. As shown in Figure 7.7c, we therefore expect HL-RISC to be the dominant fate of the T_2 excited state because internal conversion to T_1 is relatively slow owing to the large energy gap (we estimate a time constant of 120 ps from the energy gap law in Figure 7.6b). Furthermore, we expect singlet fission to be the dominant fate of the resulting S_1 states, since ISC back to T_2 is thermally activated and slow (on the order of 1 µs at room temperature[277,322]).

There is precedent for expecting HL-RISC to occur in rubrene. As mentioned above, it is well known that thermally activated intersystem crossing from S_1 to T_2 occurs in rubrene[277,316], though estimates of the Arrhenius parameters differ by several orders of magnitude between measurements in solution[277] and

solid glasses[316]. It must also be possible therefore for the exothermic HL-RISC process to occur. Furthermore, HL-RISC was proposed by several authors to explain high TTA-UC efficiencies in OLED devices based on rubrene[323] and substituted anthracenes[307,311,324] (though it is interesting to note that it does not occur in diphenylanthracene (DPA)[307], perhaps due to symmetry restrictions[325]). Recently, a detailed study of magnetic field effects in rubrene-based OLEDs confirmed that HL-RISC was occurring[306]. The sub-picosecond timescale is also plausible: HL-RISC rate constants for erythrosin B, rose bengal and tetraphenylporphyrin have been measured to be 1 ps or less[310]. The S_1-T_2 energy gaps in these three dyes are several hundred meV greater than in rubrene, so we might expect the HL-RISC rate constant in the latter to be even faster. Finally, we note that vibronic coupling effects have been calculated to increase RISC rate constants by several orders of magnitude in thermally activated delayed fluorescence molecules[326] and suggest that similar effects could help to enable sub-picosecond HL-RISC in rubrene.

7.7 Simulations and discussion

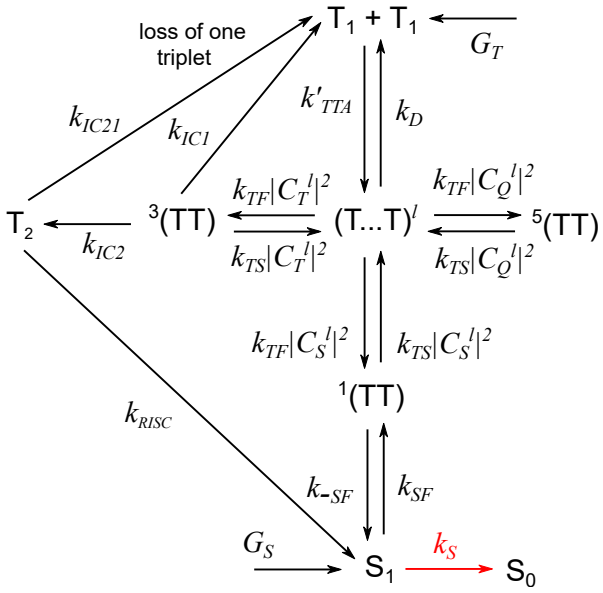

Figure 7.8 | An extended model of TTA-UC. Schematic diagram showing a refinement of the model in Figure 7.1. We differentiate between triplet-pairs formed directly through TTA, and strongly-exchange coupled pure spin triplet-pairs. In the limit of strong exchange coupling, these sets of states are identical. We also include a singlet fission channel. This is referred to as model 2.

Given that the initial products of TTA are weakly exchange-coupled triplet pairs, and given the important distinction between internal conversions from

^{3}(TT) to T_1 and T_2, we can extend our simple scheme (model 1) from Figure 7.1 into that shown in Figure 7.8 (model 2). Now we explicitly differentiate between triplet-pair states $(T...T)^l$ formed through TTA, which are governed by the spin Hamiltonian in Equation 2.70, and the pure spin states ^{1}(TT), ^{3}(TT) and ^{5}(TT), which couple to the $(T...T)^l$ states through their singlet, triplet and quintet character respectively. In the limit of $J \gg D$, these two sets of states will coincide. We also include a singlet fission channel, and add a distinct T_2 state that is permitted to undergo HL-RISC to form S_1.

The rate equations governing this extended model can be written as follows:

$$\begin{aligned}\frac{d[T_1]}{dt} &= G_T + 2k_D \sum_{l=1}^{9}[(T...T)^l] + k_{IC1} \sum_{m=x,y,z} |C_T^l|^2 [^3(TT)_m] \\ &\quad + k_{IC21}[T_2] - 2k'_{TTA}[T_1]\end{aligned} \tag{7.15}$$

$$\begin{aligned}\frac{d[(T...T)^l]}{dt} &= \frac{1}{9}k'_{TTA}[T_1] - k_{TF}\left(|C_S^l|^2 + |C_T^l|^2 + |C_Q^l|^2\right)[(T...T)^l] \\ &\quad + k_{TS}\Bigg(|C_S^l|^2[^1(TT)] + \sum_{m=x,y,z} |C_{Tm}^l|^2 [^3(TT)_m] \\ &\quad + \sum_{m=a,b,x,y,z} |C_{Qm}^l|^2 [^5(TT)_m]\Bigg) - k_D[(T...T)^l]\end{aligned} \tag{7.16}$$

$$\frac{d[^5(TT)_m]}{dt} = k_{TF} \sum_{l=1}^{9} |C_{Qm}^l|^2 [(T...T)^l] - k_{TS}\left(\sum_{l=1}^{9} |C_{Qm}^l|^2\right)[^5(TT)_m] \tag{7.17}$$

$$\begin{aligned}\frac{d[^3(TT)_m]}{dt} &= k_{TF} \sum_{l=1}^{9} |C_{Tm}^l|^2 [(T...T)^l] - k_{TS}\left(\sum_{l=1}^{9} |C_{Tm}^l|^2\right)[^3(TT)_m] \\ &\quad - (k_{IC1} + k_{IC2})[^3(TT)_m]\end{aligned} \tag{7.18}$$

$$\begin{aligned}\frac{d[^1(TT)]}{dt} &= k_{TF} \sum_{l=1}^{9} |C_S^l|^2 [(T...T)^l] - k_{TS}\left(\sum_{l=1}^{9} |C_S^l|^2\right)[^1(TT)] \\ &\quad + k_{SF}[S_1] - k_{-SF}[^1(TT)]\end{aligned} \tag{7.19}$$

$$\frac{d[S_1]}{dt} = G_S + k_{-SF}[^1(TT)] - k_{SF}[S_1] - k_S[S_1] + k_{RISC}[T_2] \tag{7.20}$$

$$\frac{d[T_2]}{dt} = k_{IC2} \sum_{m=x,y,z} |C_T^l|^2 [^3(TT)_m] - (k_{IC21} + k_{RISC})[T_2]. \tag{7.21}$$

Since we assumed an effective linear annihilation rate constant k'_{TTA}, we solved the equations (numerically) using linear algebra.

The quantum yield of TTA-UC is generally written as[22]

$$\Phi_{UC} = \frac{1}{2}\eta\Phi_{PL}\Phi_{TTA}\Phi_{TET}\Phi_{ISC}, \tag{7.22}$$

where Φ_{ISC}, Φ_{TET} and Φ_{PL} are the quantum yields of intersystem crossing (or more generally triplet production) on the donor species, triplet energy transfer from donor to acceptor and acceptor fluorescence respectively. The factor of $\frac{1}{2}$ reflects the fact that two triplets yield one singlet and Φ_{TTA} describes the competition between annihilation and decay for the fate of triplet states.

In model 2, by construction $\Phi_{TTA} = \Phi_{TET} = \Phi_{ISC} = 1$. As a result, the upconversion quantum yield can be calculated from

$$\Phi_{UC} = \frac{k_S[\mathrm{S}_1]}{G_T}, \ (G_S = 0), \tag{7.23}$$

whilst the photoluminescence quantum yield is given by

$$\Phi_{PL} = \frac{k_S[\mathrm{S}_1]}{G_S}, \ (G_T = 0), \tag{7.24}$$

where G_T and G_S are the generation rates for triplet and singlet states respectively. If the rate constant of singlet fission k_{SF} is non-zero, Φ_{PL} may not be unity and instead will depend on the spin statistical factor η, which in general can be calculated as

$$\eta = \frac{2\Phi_{UC}}{\Phi_{PL}}. \tag{7.25}$$

Order-of-magnitude values for the main rate constants are given in Table 7.1. As shown Figure I.3, the values of k'_{TTA} and k_{SF} have no effect on the model predictions and neither does $G_{i=S\,or\,T}$ since the equations are linear. The other rate constants can be varied significantly from the values in Table 7.1 with little impact. Large variations in k_{TF}, k_D and k_{IC} do have an effect on η but this is only to be expected[309] from equation 7.8. We thus consider the conclusions drawn from the model to be robust and highly general. In our simulations, we use the zero-field splitting parameters of monomeric tetracene[138], $D = 6.45 \times 10^{-6}\,\mathrm{eV}$ and $E = -6.45 \times 10^{-7}\,\mathrm{eV}$, which have been judged to be more suitable for such simulations than those for the crystal[111]. We note that the spin-dipolar term in Equation 2.70 can be formulated in various ways. Since the coupling strength X is thought to be on the order of $10\,\mathrm{neV}$[149,327], much less than D and E, the exact form is unimportant[111]. For simplicity, we use[112]

$$H_{dipole-dipole} \approx X\hat{\boldsymbol{S}}_A \cdot \hat{\boldsymbol{S}}_B \tag{7.26}$$

and take $X = D/1000$. Finally, we take the simplest case of parallel molecules, which corresponds to the π-stacking direction in acene crystals including rubrene, unless otherwise indicated.

Table 7.1 | Values and sources of the main rate constants.

Rate	**Value** (ns^{-1})	**Source**
k_S	0.0625	Refs. 67,289
k_{SF}	100	Approximated from TA data (Figures 7.5 and I.1)
k_{-SF}	100	Approximated from TA data (Figures 7.5 and I.1)
k_{TS}	10	Lower bound on triplet hopping rate, estimated from the TTA rate constant in Ref. 216, larger values have no effect (Figure I.3)
k_{TF}	5	$= k_{TS}/2$ for 1D diffusion
k_D	0.1	Approximate, estimated from onset of bimolecular TTA in Figure 7.4
k_{IC1}	17	Energy gap law (Figure 7.6)
k_{IC2}	12	Energy gap law (Figure 7.6)
k_{IC21}	8	Energy gap law (Figure 7.6)
k_{RISC}	5000	Approximate instrument response of pump-push-probe

Figures 7.9-7.11 show the key predictions from the model[†]. In order to investigate the effects of inter-triplet exchange coupling, we begin by switching off the HL-RISC channel and taking the simplest case of parallel molecules, which corresponds to the π-stacking direction in most acene crystals including rubrene. Next, we explore the effects of non-parallel molecular orientation and finally we introduce the HL-RISC channel.

Figure 7.9a shows the simulated MFE for triplet-triplet annihilation in the limits of strong (red) and weak (blue) exchange coupling. To demonstrate the generality of our model, we also show the (identical) predictions from model 1, incorporating a singlet fission channel (circles). As expected, we find that only in the limit of weak exchange coupling between triplets following TTA do we reproduce the experimentally measured MFE (Figure 7.4b). The lower panel of Figure 7.9a illustrates the origin of the $J = 0$ MFE by plotting the number of $(T...T)^l$ states with $|C_S^l|^2 > 5\%$ (i.e. more than 5% singlet character) as a function of magnetic field, along with equivalent numbers for triplet and quintet character. The threshold of 5% was chosen because it nicely illustrates the key

[†]The simulation code is freely available at https://github.com/davidbossanyi/spin-statistics.

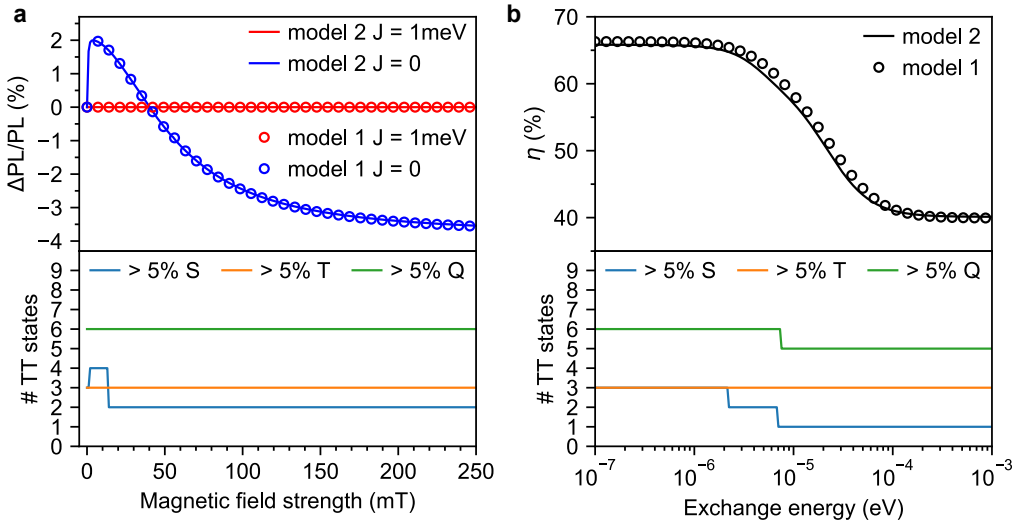

Figure 7.9 | Effects of exchange energy on spin statistics. a, Simulated MFE for parallel molecules comparing model 1 (Figure 7.1) and model 2 (Figure 7.8) for strongly ($J = 1\,\text{meV}$) and weakly ($J = 0$) exchange-coupled triplet-pairs. The lower panel shows changes in spin character of the $J = 0$ triplet-pairs with applied magnetic field. Note that >5% S means triplet-pair states with $|C_S^l|^2 > 5\%$, i.e. more than 5% singlet character, and similarly for triplet (T) and quintet (Q) character. The simulation shows that the experimental MFE (Figure 7.4b) can only be reproduced if the initial products of TTA are weakly exchange-coupled triplet-pairs. **b**, Simulated spin statistical factor η for parallel molecules as a function of inter-triplet exchange energy J. The lower panel again shows the changes in triplet-pair spin character. The simulation shows that, for parallel molecules and in the absence of HL-RISC, $\eta = \frac{2}{3}$ rather than the conventionally assumed $\frac{2}{5}$.

behaviours. At higher fields, two rather than three of the $(\text{T...T})^l$ triplet-pair states have appreciable singlet character, leading to reduced PL. We note that the HL-RISC channel would introduce further magnetic field effects: the S_1 states formed can undergo singlet fission, which gives an inverted MFE shape compared to TTA, and the RISC process itself carries a (negative) magnetic field effect[306] which is beyond the scope of our model.

In Figure 7.9b we plot the spin statistical factor for TTA-UC as a function of inter-triplet exchange energy. In the conventionally assumed but as we have explained, incorrect, case of strong exchange coupling we find the expected limit of $\eta = \frac{2}{5}$. As shown in the lower panel, this is the case for eigenstates that are pure spin states: 5 quintets, 3 triplets and 1 singlet. The spin statistical factor rises to $\frac{2}{3}$ as the exchange coupling is reduced, reflecting the increase (from 1 to 3) in the number of triplet-pair states possessing significant singlet character.

As discussed above, the spin character of weakly exchange-coupled triplet-pair states is dependent on the relative orientation of the two molecules involved[111,112,115]. This has a knock-on effect on the spin statistical factor, as

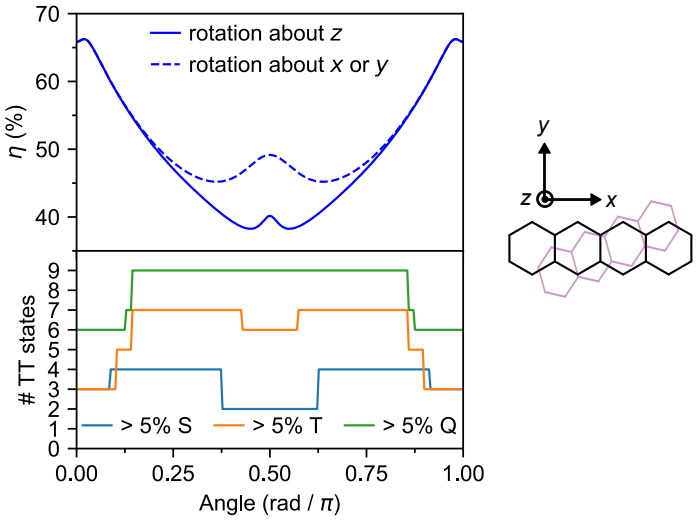

Figure 7.10 | Effects of molecular orientation on spin statistics. Model 2 simulation showing the variation of η with inter-molecular orientation, for $J = 0$ and $k_{RISC} = 0$. The lower panel shows triplet-pair spin character. Changes to singlet-triplet-quintet spin mixing causes η to vary between $\frac{2}{3}$ (parallel orientation) and $\frac{2}{5}$ (perpendicular orientation).

shown in Figure 7.10. Rotation of one molecule of the pair with respect to the other causes increased singlet-triplet-quintet mixing. In particular, the greater number of states possessing significant triplet character results in a higher probability for ^{3}(TT) $\rightarrow$ T_N internal conversions, thereby reducing the spin statistical factor (in the absence of efficient HL-RISC). The dependence of η on relative molecular orientation may help to explain differences in TTA efficiency between monomeric annihilators and rigid dimers[328]. Furthermore, it introduces an important consideration for the design of solid state upconversion systems. We find that the parallel orientations associated with close $\pi - \pi$ stacking (and hence rapid triplet diffusion[93]) in acene crystals also result in the best spin statistical factors.

Finally, in Figure 7.11, we explore the impact of HL-RISC on the spin statistical factor by plotting η against T_2 energy (relative to the ^{3}(TT) level) for several different cases. In solution, the common annihilator molecules rubrene and DPA are thought to form triplet-pair complexes in which the chromophores are oriented perpendicular to each other[309]. In this case, the spin-statistical factor is 40% in the absence of a HL-RISC channel, but we emphasise that this is a result of weakly interacting triplet-pair states with mixed singlet, triplet and quintet character and not because TTA forms pure singlet, triplet and quintet complexes in a 1:3:5 ratio. We suggest that this is the reason that DPA in solution is reported to give $\eta \sim 40\%$[107,202,307,309,330–334]. The range of experimentally

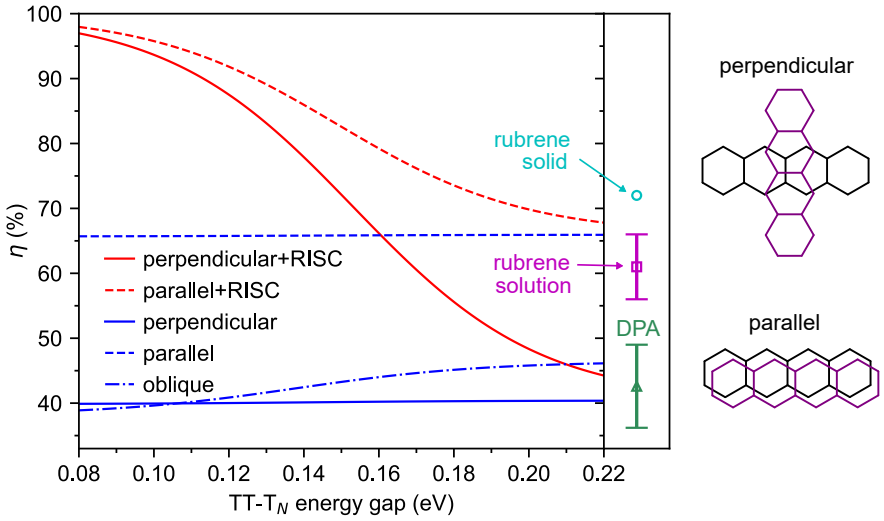

Figure 7.11 | Effects of reverse intersystem crossing on spin statistics. Model 2 simulation of η as a function of ^{3}(TT)-T_N energy gap (for rubrene, $N = 2$), for several different cases, all with $J = 0$. The presence of HL-RISC causes a sensitive dependence on T_2 energy, relative to ^{3}(TT), with smaller gaps leading to higher values of η. In the absence of HL-RISC, this dependence is much weaker and shows the opposite trend. The oblique case, corresponding to an inter-molecular geometry found in the DPA crystal[329], shows a more pronounced dependence, due to increased triplet-singlet and triplet-quintet mixing and hence greater variation in the internal conversion rates. These simulations show that differences in triplet-pair orientation, coupled with the presence or absence of HL-RISC, can explain the different values of η measured experimentally for rubrene and DPA, shown in the right-hand panel. These reported experimental ranges of η for DPA, rubrene in solution and rubrene in the solid state were obtained from the literature[37,38,42,74,208,277,307,323,330–335] and are given, together with reported values of the rubrene T_2 energy level, in Tables I.1 and I.2 respectively.

measured values of η for DPA are shown in the right-hand panel of Figure 7.11 and the values and references are given in Table I.1. There are two inequivalent molecules in the DPA crystal unit cell[329] and therefore two possible triplet-pair orientations, one parallel and one oblique. The oblique orientation results in spin statistical factors within the experimentally reported range.

In rubrene, the HL-RISC channel can contribute due to the favourable energy level alignment between $2 \times T_1$, T_2 and S_1, which raises the value of η close to the $\sim 60\%$ measured for rubrene in solution[38,208], indicated (with the reported experimental errors) in the right-hand panel of Figure 7.11. In solid rubrene, η has been reported to reach 72%[323], also shown in the right-hand panel of Figure 7.11. Again, our model can explain this value through a combination of parallel molecular geometry, weakly exchange-coupled triplet-pairs and a partially active HL-RISC channel. The effectiveness of the HL-RISC channel is highly sensitive to the relative energy levels due to the exponential

nature of the energy gap law and Boltzmann factors. Figure 7.11 shows that variations on the order of k_BT can have a large impact on η and as shown in Table I.2, there is a considerable spread in the reported T_2 energy level of rubrene. Finally, we note that in the absence of HL-RISC, η increases only weakly as T_2 is raised above ^{3}(TT) and never reaches 100% as has been suggested[41]. In the presence of HL-RISC however, $\eta = 100\%$ is attained when T_2 and ^{3}(TT) are very close in energy and regardless of inter-molecular orientation.

7.8 Conclusions

In this chapter we have shown how factors rarely considered in discussions the of TTA-UC spin statistics can have a profound effect on the efficiency. In particular, we have explained why the oft repeated statement that TTA produces pure singlet, triplet and quintet encounter complexes in a 1:3:5 ratio contains an implicit assumption that the triplet-pair states are strongly exchange-coupled. This is incompatible with experimentally measured magnetic field effects that can be explained only through weakly exchange-coupled triplet-pair states. When the triplet-pairs are weakly exchange-coupled, our simulations show that varying the inter-molecular orientation tunes the spin statistical factor from $\frac{2}{3}$ for parallel chromophores to $\frac{2}{5}$ for perpendicular chromophores, through variations in the spin mixing of the triplet-pair wavefunctions. We suggest that the origin of the commonly observed 40% value for acceptors such as DPA[107,202,307,309,330–334] is therefore considerably more subtle than has been assumed to date.

Our updated framework for calculating the spin statistical factor can also explain the higher values that have been measured for rubrene. Using transient absorption and pump-push-probe spectroscopy, we provided additional evidence for the recently reported high-level reverse intersystem crossing channel from T_2 to S_1 in rubrene. Based on the energy levels of T_1, T_2 and S_1, we modelled the effect of this channel and found that measured spin statistical factors of 60% for solution[38,208] and 72% in the solid state[323] can be readily understood in terms of chromophore orientation and high-level reverse intersystem crossing.

This work points the way towards strategies for exceeding the spin statistical limit of TTA-UC. Control of inter-molecular distance and geometry within the triplet-pair complexes can result in values up to $\frac{2}{3}$. Even better, harnessing high-level reverse intersystem crossing can make such considerations redundant, potentially allowing the spin statistical factor to reach unity. These findings therefore provide an important step in understanding that will pave the way

for significant efficiency improvements in photon upconverters for solar energy harvesting and light-driven biomedical applications, as well as in organic light-emitting diodes.

7.9 Experimental

7.9.1 Sample preparation

Films of rubrene nanoparticles dispersed in a PVA matrix were prepared by Yoichi Sasaki as described in Section 3.2.4. Polycrystalline thin films were fabricated by thermal evaporation as described in Section 3.2.2.

7.9.2 Ground state absorption and TRPL measurements

Ground state absorption spectra were recorded with a UV–vis spectrophotometer (Cary60, Agilent). A Ti:sapphire regenerative amplifier (Solstice, Spectra-Physics) providing 800 nm pulses (90 fs FWHM, 1 kHz, 4 mJ) was used to generate the pump beam for photoluminescence measurements. A portion of the 800 nm beam was frequency doubled in a BBO crystal to generate 400 nm pump pulses and focussed onto the sample. The photoluminescence was detected in reflection geometry using the time-gated iCCD described in detail in Section 3.4.1. A 435 nm long pass filter was used to eliminate pump scatter. Magnetic fields were applied transverse to the excitation beam using an electromagnet. Magnetic field strength was measured using a transverse Hall probe. The pump beam spot size was measured at the sample position by translating a razor blade through the focus and monitoring the transmitted power.

7.9.3 Picosecond transient absorption spectroscopy

Picosecond TA spectroscopy was carried out using the setup described in Section 3.4.2. The pump beam spot size was measured at the sample position using a CCD bean profiler (Thorlabs).

7.9.4 Pump-push-probe spectroscopy

Pump-push-probe spectroscopy was carried out using the setup described in Section 3.4.2. The 400 nm, 500 Hz pump pulses had an energy of $0.2\,\mathrm{mJ\,cm^{-2}}$ at the sample position whilst the 800 nm, 1 kHz push pulses had an energy of $1.2\,\mathrm{mJ\,cm^{-2}}$ at the sample position. The push pulses were delayed by a fixed 1070 ps with respect to the pump.

Chapter 8

Singlet energy collection in rubrene*

We have seen (Chapter 7) that triplet-triplet annihilation can produce singlet states in rubrene. We have also seen that singlet states in rubrene undergo singlet fission (Chapter 6), thereby, in principle, undoing the hard work of triplet-triplet annihilation. To counteract this, many groups have doped rubrene with small quantities of tetraphenyldibenzoperiflanthene (DBP), which can harvest and emit singlet energy from rubrene via Förster transfer. This has been shown to increase the photoluminescence quantum yield (PLQY) of rubrene by more than an order of magnitude and lead to much more efficient photon upconversion, an effect that has long been attributed rather vaguely to the suppression of singlet fission. In this chapter, we perform detailed time-resolved spectroscopy of rubrene nanoparticles doped with DBP. We find that energy transfer from rubrene to DBP does not outcompete the formation of triplet-pairs through singlet fission, despite the addition of DBP increasing the PLQY from 3% to 61%. Instead, it competes with triplet-pair separation and we rationalise these findings in the context of the well-known effects of triplet fusion and triplet-quenching defects on the photoluminescence yield of crystalline rubrene.

8.1 Introduction

As discussed in Section 2.6, triplet-triplet annihilation upconversion (TTA-UC) provides an attractive mechanism for converting near-infrared photons into visible photons[19,39,107]. Triplet excitons created on donor species following photon

*This chapter has been adapted from the following publication[336]: Bossanyi, Sasaki et al., *J. Mat. Chem. C* (2022). This work was the result of a fruitful collaboration with Yoichi Sasaki (Kyushu University, Japan). The majority of the work presented here is my own; Yoichi's contributions are explicitly noted.

absorption are transferred to acceptor molecules via Dexter transfer[337]. The subsequent annihilation of two sensitised triplets yields one singlet state which fluoresces, giving upconverted emission (Figure 2.19). TTA-UC has received a great deal of interest in recent years due to its potential to significantly enhance the power conversion efficiency of photovoltaics cells[14,40,106,338,339]. In addition, TTA-UC also has a variety of biomedical applications[21,55] including optogenetics[23] and targeted drug delivery[297].

In order to maximise the photon energy gain (anti-Stokes shift) during TTA-UC, it is desirable for the singlet energy level of the annihilator molecule to be as close as possible to twice the triplet energy. Rubrene fulfils this criterion[277], which partly explains its widespread use as the acceptor molecule for near-infrared-to-visible TTA-UC[19,22,38,43,107,202,205,207,340]. For example, a TTA-UC efficiency of 8% (out of a maximum 50%) has been reported for rubrene-mediated TTA-UC in solution[208]. However, photovoltaic and biomedical applications demand solid state TTA-UC material systems. In this case, the beneficial energy level alignment between S_1 and twice T_1 can become a hindrance to efficient upconversion. This is because the singlet states populated by TTA can undergo the reverse process of singlet fission[15,16], whereby they split into pairs of triplet excitons, rather than emitting their energy radiatively[43–46,341].

As a result, several strategies have recently been reported to mitigate the effects of singlet fission in solid rubrene-based TTA-UC systems. The addition of bulky side groups to increase intermolecular distances has been shown to improve the PLQY of rubrene several-fold[44,342,343], though the benefit to TTA-UC is severely tempered by reduced triplet diffusivity[343]. More commonly, rubrene is doped with the singlet energy collector tetraphenyldibenzoperiflanthene (DBP), which can harvest singlet energy from rubrene by Förster resonance energy transfer (FRET, discussed in Section 2.5.3)[43–46]. The effectiveness of this strategy appears to vary significantly with the type of sample studied. For example Wu et al. reported a 19-fold increase in the upconversion quantum yield upon doping with DBP[43], whilst Wieghold at el. reported that it had little effect[46].

Previous studies of rubrene-DBP TTA-UC systems include in some form the assertion that FRET from rubrene to DBP outcompetes singlet fission[43–46]. This simple statement appears to overlook the complexity of singlet fission and triplet fusion that occurs in solid rubrene, dynamics that have been extensively studied in orthorhombic single crystals[33–37,93,137,189,216,272,279,288,344–346] and to a lesser degree in more complex thin films[74,112,289,292,341,343,347,348].

Furthermore, as described in Chapter 6, transient absorption spectroscopy

of rubrene single crystals has shown that $S_1 \rightarrow {}^1(TT)$ occurs extremely rapidly, with reported time constants varying from 25 fs[35,36] to 2 ps[189,288]. FRET from rubrene to DBP is therefore very unlikely to outcompete this first singlet fission step for the majority of excitons. In Appendix J, we estimate the rubrene-DBP FRET rate to be 1.5 ps for nearest neighbours based on previous calculations of the Förster radius[349]. We also demonstrate that, since the DBP concentration is low (1 in 200[44,45]), the majority of photo-excited rubrene singlets will undergo singlet fission well before diffusing far enough to encounter a DBP molecule. If energy transfer from rubrene to DBP is not competitive with singlet fission, what role does DBP play that enables it to increase the PLQY of solid rubrene by such a large factor[43,44,203]?

In order to answer this question, we probe the excited-state dynamics of some of the most highly emissive solid-state rubrene samples developed to date[45,203], both with and without the DBP dopant. These are the nanoparticle films which, in their pure rubrene form, we measured in Chapter 7. To reiterate, the material system consists of solid rubrene nanoparticles prepared by reprecipitation and dispersed in an oxygen-blocking poly(vinyl alcohol) (PVA) matrix[45,203]. The nanoparticles are smooth and spherical with an average diameter of 220 nm and give no peaks in X-ray diffraction measurements[203], indicating a lack of any long-range molecular ordering. These rubrene nanoparticle films have proven to be an effective and versatile platform for realising in-air TTA-UC in solid rubrene, reaching an upconversion quantum efficiency of more than 2% when doped with an optimum 0.5 mol% DBP[45]. Perhaps most strikingly, the reported PLQY value of 84% for the rubrene-DBP nanoparticles[45] is several times greater than the 15% measured for equivalently doped polycrystalline films[44].

In rubrene-DBP systems, the details of exciton dynamics is yet to be discussed in terms of the triplet-pair intermediates and the concurrent nature of singlet fission and triplet fusion in rubrene. Here we use the high-performing rubrene NP films as a model system, combined with transient absorption and time-resolved photoluminescence spectroscopy, to explore and understand the true role of the DBP dopant. We also compare our results against a polycrystalline film reference. We begin by characterising the singlet fission and triplet fusion dynamics of pure rubrene NPs, allowing us to next identify which processes are affected by the addition of DBP. We find that FRET from rubrene to DBP does not outcompete the formation of triplet-pairs via singlet fission, but instead partially competes with triplet-pair separation. We further highlight the crucial effects of energy cycling through triplet fusion in the high PLQY of

DBP-doped rubrene.

8.2 Singlet fission and triplet fusion in rubrene: a brief review

Before presenting our results, it is useful to briefly review the extensive existing literature on singlet fission and triplet fusion in rubrene crystals and films. We begin with the best studied material system: vapour-grown orthorhombic single crystals[34,279].

In orthorhombic rubrene crystals, the electronic coupling between S_1 and ^{1}(TT) vanishes by symmetry[188]. As a result, some form of symmetry breaking is responsible for the first fission step, $S_1 \rightarrow {}^1$(TT), though the mechanism is debated[35,36,191] and reported time constants range from 25 fs[35,36] to 2 ps[189,288]. The formation of ^{1}(TT) via singlet fission in rubrene single crystals was extensively discussed in Chapter 6.

Next, ^{1}(TT) separates into (T...T) over tens of picoseconds[35,36,189,288], a process thought to occur by thermally-activated triplet hopping[193–196]. The overall singlet fission process is therefore commonly written as[169,228]

$$S_1 \rightarrow {}^1(\mathrm{TT}) \rightarrow (\mathrm{T...T}) \rightarrow T_1 + T_1, \tag{8.1}$$

where (T...T) denotes spatially separated triplet-pair states that retain their spin interactions[117] before eventually decohering into independent triplet excitons (see also Sections 2.6.1 and 2.6.3).

Observations of quantum beats (Section 2.6.2) in the delayed fluorescence[137] confirm the existence of ^{1}(T...T): a spatially separated triplet-pair state that retains its spin-0 singlet character[133,134,192,327]. ^{1}(T...T) subsequently undergoes spin evolution[112], resulting in the formation of mixed-spin triplet-pair states $(\mathrm{T...T})^l$, whose presence is confirmed by the observation of changes in PL with applied magnetic field[125]. The final products of singlet fission in rubrene single crystals are independent triplet excitons, which are formed with near-unity quantum yield[216,272]. These triplets possess a long excited state lifetime of 100 µs[272], enabling them to diffuse across distances of several microns[33,93].

Geminate and non-geminate fusion of triplet-pairs and triplets respectively results in pronounced delayed PL[216,272,344,345]. Geminate fusion of separated triplet-pairs gives rise to distinct power-law dynamics in the delayed PL, with exponents that depend on the dimensionality and anisotropy of the triplet diffusion[344,345]. Overall, triplet fusion in rubrene crystals is extremely efficient

and can contribute more than 90% of the total photoluminescence quantum yield (PLQY)[216]. The long diffusion length of the triplet excitons, coupled with dominant contribution of triplet fusion to the total PL, means that the PLQY of rubrene single crystals is extremely sensitive to triplet-quenching defects[346].

Rubrene single crystals are impractical for technological applications. Instead, rubrene-based TTA-UC systems are often based on thin film morphologies[43,44,46]. Similar to single crystals, singlet fission dynamics and delayed PL arising from triplet fusion have been reported in rubrene thin films, though the time constants measured vary widely and there is a clear dependence on sample morphology[74,112,289,292,341,343,347,348]. In particular, truly amorphous thin films show no evidence of singlet fission: the photoluminescence decays exponentially with a time constant of 15.2 ns[289], matching the radiative lifetime of singlet excitons in solution[67]. Even thin films that give no peaks in X-ray diffraction experiments exhibit singlet fission dynamics[112,347], suggesting that favourable molecular packing on a local scale can give rise to site-specific singlet fission[347].

8.3 Model system: rubrene nanoparticles

We prepared[†] rubrene and rubrene-DBP nanoparticles (NPs) using the reprecipitation method, dispersed them in a PVA matrix and cast them onto glass substrates as described in Section 3.2.4 and Refs. 203 and 45. Nanoparticle films prepared in this way have been characterised previously: the nanoparticles are spherical with an average diameter of 220 nm and there are no sharp peaks apparent in X-ray diffraction patterns indicating a lack of any long-range crystalline order[45,203]. We might therefore expect the NPs to behave differently to rubrene crystals.

We measured the absolute PLQY of our pure rubrene (Figure 8.1a) NP films[‡] to be 2.9–3.6 %, and rising to 61% when doped with an optimum[45] 0.5 mol% DBP (Figure 8.1b). The absolute PLQY values exhibited a small degree of sample-to-sample variation and dropped slightly over more than one year of sample storage in inert atmosphere. For example, we measured a PLQY of 46% for DBP-doped rubrene NPs 18 months after fabrication. These small variations are discussed in Appendix J, but we highlight that the photophysical behaviour did not change significantly with storage time (Figures J.3 and J.4).

The dramatic rise in PLQY upon doping with DBP is reflected in the steady-state PL spectra (Figure 8.1c). As described previously[43–46], for the DBP-doped

[†]Samples were prepared by Yoichi Sasaki, both at Kyushu University and during his visit to the University of Sheffield

[‡]PLQY values were measured by Yoichi Sasaki at Kyushu University

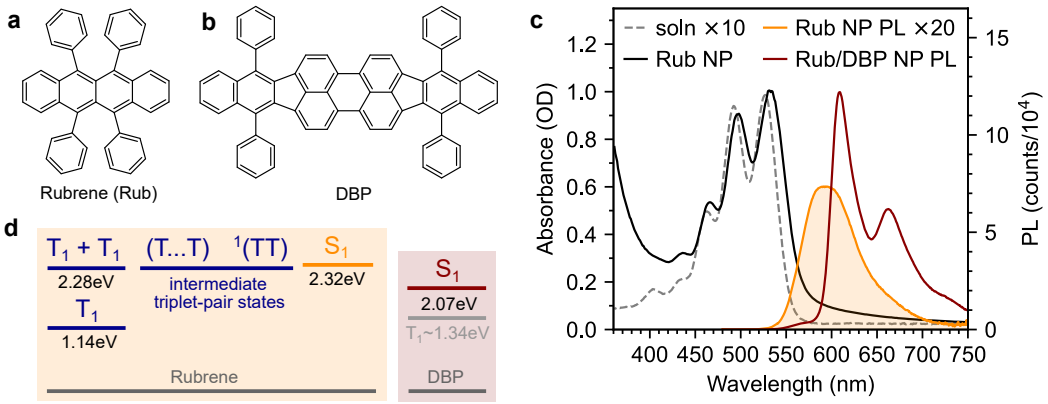

Figure 8.1 | Rubrene and DBP. Molecular structures of rubrene (**a**) and DBP (**b**). **c**, Absorption spectra of rubrene dissolved in anhydrous toluene (1×10^{-4} M) and as a nanoparticle (NP) film. The emission spectrum for pure rubrene nanoparticle films (orange) is affected by self-absorption due to their high optical density. When 0.5 mol% DBP is added, almost all of the PL comes from the DBP (red). **d**, The S_1 and triplet-pair energy levels in rubrene are isoenergetic, allowing for concurrent singlet fission and triplet fusion via various triplet-pair intermediates. The S_1 state of DBP lies approximately 200 meV lower. Calculations have shown that the triplet energy of DBP is approximately 0.2 eV above that of rubrene[43,323], so DBP acts as a singlet energy collector only.

NPs, almost all of the emission comes from DBP, with only a small residual contribution from rubrene. The absolute PLQY of our rubrene NP films is towards the higher end of values typically reported for polycrystalline rubrene films[44,342], for which the relatively low quantum yield has been attributed to the rapid formation of triplets through efficient singlet fission[112,342]. Previous works that saw a similar enhancement in PL yield upon doping with DBP attributed it to FRET outcompeting singlet fission[43–46]. As discussed in Appendix J, this seems unlikely given that singlet fission is expected to be considerably faster than FRET in rubrene-DBP systems[35,36,189,288,349].

To investigate the role of the DBP dopant in our rubrene NPs, we begin by characterising the singlet fission and triplet fusion processes in pure rubrene NPs. This gives us rate constants for all of the steps in the singlet fission process (Equation 8.1), thereby allowing us to understand which processes are affected by the presence of DBP.

8.4 Photophysics of pure rubrene nanoparticle films

Figure 8.2a-c(i) shows ultrafast transient absorption (TA) spectroscopy of a rubrene nanoparticle film, which we compare against data taken for a dilute solution (ii) and a spin-coated 50 nm thick polycrystalline film (iii) under the

same experimental conditions. Transient absorption data has been measured previously for rubrene in solution[189,348], films[292,343,348] and crystals[35,36,189,288] (see also Chapter 6) and we include them here simply as references.

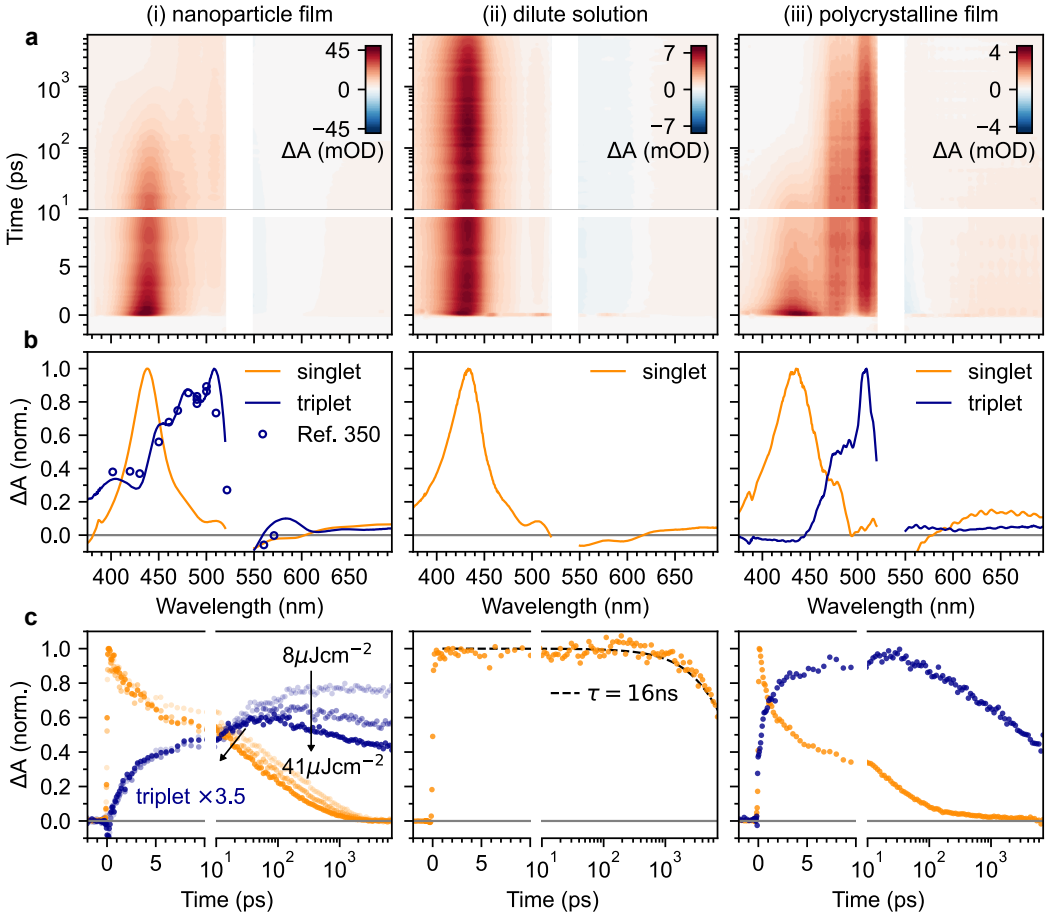

Figure 8.2 | Singlet fission in rubrene nanoparticles. a, False-colour maps of the transient absorption of rubrene as PVA-dispersed NPs (i), dilute (1×10^{-4} M) toluene solution (ii) and polycrystalline film (iii). The excitation intensity was 41 µJ cm^{-2} and the pump pulses were centred at 532 nm with a FWHM of 16 nm. Data in the spectral region of the pump have been removed. **b**, Transient absorption spectra of singlets (orange) and triplets (blue) in rubrene, extracted via MCR-ALS in (i) and (iii). The singlet and triplet excited state absorption spectra in the NPs are very similar to those of rubrene in solution[350]. **c**, Dynamics of singlets and triplets in rubrene, normalised to the initial singlet population. Panel **b**(i) adapted with permission from Reference 350; Copyright 1979 American Chemical Society.

In the rubrene NP film (Figure 8.2a-c(i)) we find signatures of singlet fission[189]. An extraction of the two components using Multivariate Curve Resolution Alternating Least Squares (MCR-ALS)[225,226] (see Sections 3.4.3 and 8.8.5) results in spectra (Figure 8.2b(i)) that closely match the excited state absorption (ESA) spectra of singlet and triplet excitons in solution[278,348,350]. From the extracted dynamics (Figure 8.2c(i)), we see that the singlet exciton life-

time is dramatically reduced from the 16 ns value measured in solution (Figure 8.2c(ii)). In the NP film, the singlet population initially decays exponentially with a time constant of 5 ps to half of its initial value, accompanied by a corresponding exponential rise in the triplet population, also with a time constant of 5 ps (Figure 8.3). These dynamics indicate (in the absence of rapid nonradiative decay to the ground state) that a roughly 50:50 equilibrium between S_1 and triplet-pair states is established within the first 10 ps. In addition, similar to rubrene single crystals[189], we find an isosbestic point between the singlet and triplet ESA spectra (Figure J.2), similar to that of Figure 6.2, indicating a single singlet to triplet transformation[189]. Taken together, these data suggest that the first step of singlet fission, $S_1 \leftrightarrow {}^1(TT)$ occurs in the nanoparticles with a time constant of 10 ps, and that the triplet yield is high, as it is in single crystals[189,216].

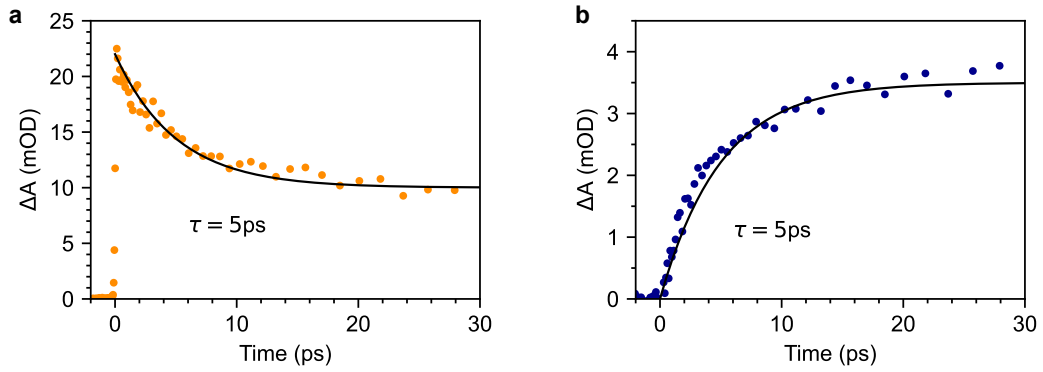

Figure 8.3 | Formation of a ~50:50 equilibrium between S_1 and $^1(TT)$. **a**, The singlet population decays to approximately half its initial value monoexponentially with a time constant of 5 ps. **b**, The triplet population rises monoexponentially with the same time constant. This represents the expected behaviour for the creation of a 50:50 equilibrium between S_1 and $^1(TT)$ with a singlet fission (and triplet-pair fusion) rate of 10 ps.

Given the similarity between the singlet fission dynamics of our rubrene NP films and rubrene single crystals[189,289], it is surprising that the singlet and triplet ESA spectra of the NPs so closely resemble those of rubrene in solution, and that the triplet ESA is four times weaker in the NPs than the polycrystalline film, relative to the initial singlet ESA. Since the spectra are similar, we estimated the triplet yield in our rubrene NP films from the ESA cross-sections previously measured in solution[278]. This procedure gives a yield of ~ 40% (out of a maximum of 200%), which would imply that only 1 in 5 singlet excitons undergoes fission. This is inconsistent with the population dynamics however: 50% of the initial S_1 population is lost within the first 10 ps, with an exponential decay that matches the rise of the triplet signal. The reasons for the

similarities and differences in ESA spectral shapes and cross sections between solution, crystals and NPs therefore remain unclear.

Moving beyond the first 10 ps, the triplet signal in the rubrene NP films continues to rise, accompanied by a reduction in singlet population (Figure 8.2c(i)). This could be a sign of the next step in the singlet fission process: the formation of spatially separated triplet-pairs from ^{1}(TT)[36,169,193]. There are alternative explanations for two-stage singlet fission dynamics, such as the co-existence of a direct parallel pathway $S_1 \rightarrow {}^1$(T...T) or exciton migration to singlet fission sites[192]. In Appendix J, we explain, with the help of further experimental evidence, why these are less likely than the simple sequential $S_1 \rightarrow {}^1$(TT) $\rightarrow {}^1$(T...T) pathway that has been well established for rubrene single crystals[35–37,189,288]. We show below that this sequential pathway quantitatively explains our experimental data with physically reasonable rate constants. Finally, we find a slight dependence of the singlet and triplet dynamics on excitation pulse energy, demonstrating that a small amount of singlet-singlet annihilation (SSA) is taking place. As shown in Figure J.11, SSA principally affects the dynamics within the first 10 ps, though this is somewhat unclear in the normalised dynamics of Figure 8.2c(i).

Given that initial singlet fission (∼10 ps) and triplet-pair separation (∼100 ps) are orders of magnitude faster than radiative decay (16 ns), triplet fusion must contribute significantly to the absolute PLQY of the rubrene nanoparticles, just as it does for rubrene single crystals[216]. We therefore turn to time-resolved measurements on nanosecond-millisecond timescales in order to investigate the triplet fusion dynamics in the rubrene NP films.

Figure 8.4a shows the photoluminescence decay (wavelength-integrated since the spectrum is time-independent) of the rubrene NPs measured using a combination of time-correlated single photon counting (TCSPC) and an electronically gated iCCD (see Section 8.8.3). Three regions are apparent. Following photoexcitation, the PL decays exponentially with an apparent time constant of 3 ns, though our TCSPC measurement does not have sufficient time resolution to give an accurate value. This subsequently gives way to a power law decay with an exponent of -1.3. On timescales of several hundred nanoseconds we find the onset of an enhancement to the delayed PL which grows with increasing excitation density. This latter region matches the triplet excited state dynamics shown in Figure 8.4b, measured using transient absorption spectroscopy. Beyond 100 ns, the slow decrease in triplet population is replaced by a more rapid decay, which gets faster with increasing excitation density. This is characteristic of non-geminate TTA[239], which here repopulates the S_1 state.

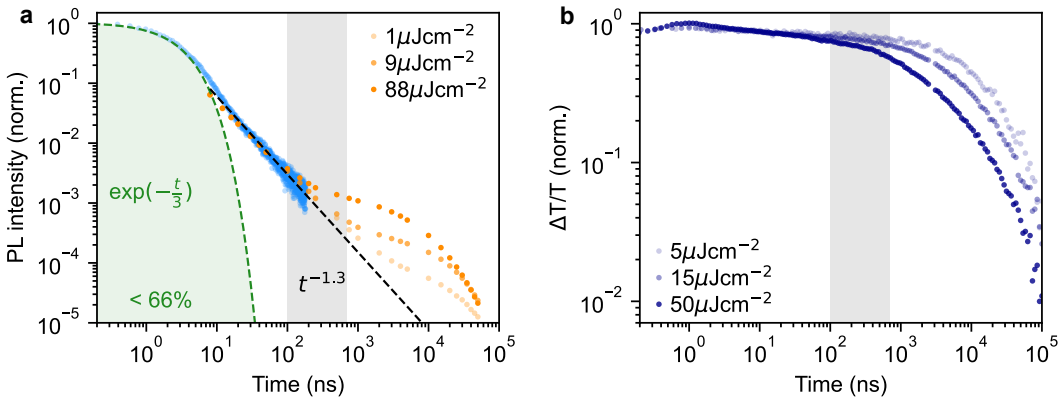

Figure 8.4 | Rubrene photoluminescence and triplet dynamics. **a**, Wavelength-integrated TRPL dynamics of rubrene NP films comprising TCSPC (blue, 470 nm excitation) and intensified gated CCD (orange, 532 nm excitation) measurements. The power-law behaviour is characteristic of geminate fusion of ^{1}(TT) and (T...T)[344,345]. We find an excitation density dependent enhancement to the delayed PL beyond 100 ns, that corresponds to the onset of bimolecular TTA determined by monitoring the triplet transient absorption signal at 510 nm (**b**).

The intermediate power law dynamics that we observe in the NP films are characteristic of geminate fusion of associated and separated triplet-pair states[344,345,351], i.e. ^{1}(TT) and (T...T). A random walk model for the triplet diffusion between fission and geminate fusion events predicts an exponent of -1.5 in the limits of 3D and 1D diffusion and -1 for 2D diffusion[345,351]. For example, Wolf et al.[344] have shown that a change in the power law exponent from -1.18 to -1.66 measured in rubrene single crystals is associated with a transition from 2D to 3D triplet diffusion. Our exponent lies in between these values, suggesting a mixture of 2D and 3D triplet diffusion occurs in the NP films on timescales of tens of nanoseconds.

We can estimate a lower bound on the contribution that triplet fusion makes to the total PL by integrating under the PL decay in Figure 8.4a. We find that the 'prompt' exponential part contributes at most 66% of the total emitted light if no non-geminate TTA takes place, and much less otherwise. The exponential region itself must contain contributions from ^{1}(TT) fusion since the singlet fission rate is 10 ps, thus ours is a conservative estimate. Triplet fusion following singlet fission therefore makes a very substantial contribution to the total PL emitted by the rubrene NP films, similar to rubrene single crystals in which more than 90% of the PLQY comes from triplet fusion[216].

To gain further insight into the nature of the triplet-pair intermediates in the rubrene NP films, we measured the effects of an applied magnetic field on the PL (Section 2.6.2) at two different time delays. These results are presented in Figure 8.5. At a delay of 20 ns, we observe an enhancement of the PL for fields

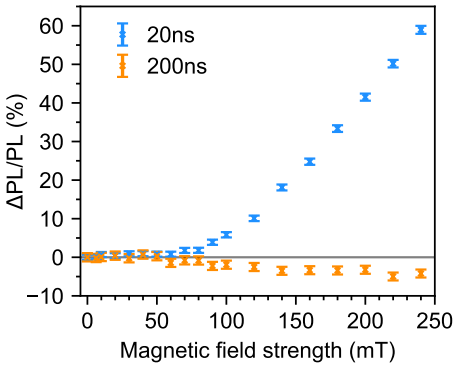

Figure 8.5 | Magnetic field effect in rubrene nanoparticles. Magnetic field effect on fluorescence at two different time delays. Error bars reflect the difference between sweeping up and down in magnetic field. At 20 ns we observe an enhancement in PL with magnetic field due to the formation of mixed-spin triplet-pair states. Recombination of these states results in the negative effect observed at 200 ns.

$>$ 70 mT. This is characteristic of the formation of weakly exchange-coupled triplet-pair states[102,112,124]. These triplet-pair states are not eigenstates of the total spin operator, thus spin is no longer a good quantum number and they instead possess mixed spin character. At zero applied field, three of the nine possible triplet-pair states have a degree of singlet character[102]. This falls to two at higher fields[102], thus reducing the probability that singlet energy is lost and increasing the measured PL. At a delay of 200 ns the magnetic field effect (MFE) is inverted, showing that fusion of mixed spin triplet-pair states dominates on this timescale. We note that the magnitude of the time-gated MFEs depends sensitively on the gate time and width in a non-trivial way, and it is the shapes and signs that are important here.

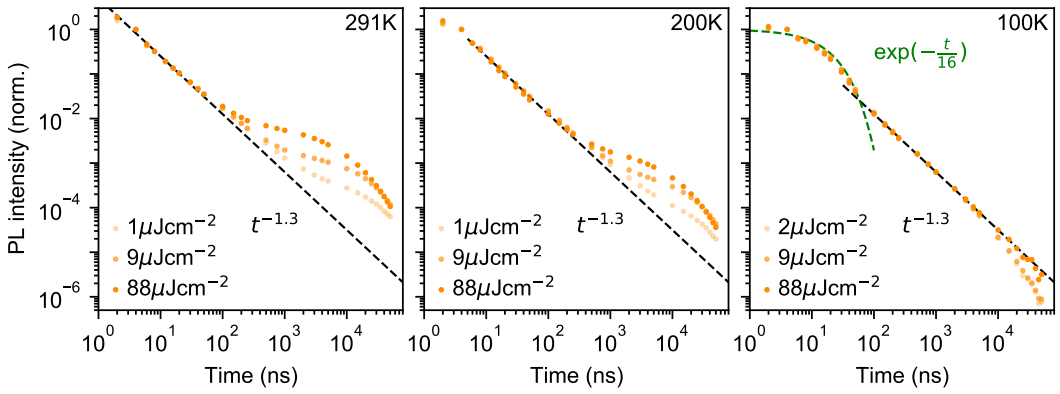

Figure 8.6 | Temperature dependence of triplet fusion. Wavelength-integrated time-resolved photoluminescence decays of the rubrene nanoparticles at 291 K, 200 K and 100 K. As the temperature is decreased, the contribution of non-geminate triplet recombination to the total PL reduces. At 100 K, all the triplet recombination is geminate and follows the expected power-law dynamics[344,345].

We further investigate the effects of triplet-pair dynamics on the NP photoluminescence through measurements of the PL decay as a function of temperature and excitation density, as shown in Figure 8.6. The PL dynamics at 100 K are considerably different to those at 200 K and room temperature. Firstly, we find that the initial decay becomes noticeably exponential with a time constant of 16 ns, matching the radiative rate of singlet excitons in rubrene[67,289]. A very similar feature is seen in the PL decay of rubrene single crystals at room temperature[345], where it corresponds to emission from the small percentage of singlet excitons that do not undergo fission[344]. Secondly, we find no dependence of the PL decay on excitation density, in stark contrast to the behaviour at room temperature and 200 K. Instead, the power law behaviour persists for many tens of microseconds, demonstrating that all subsequent triplet fusion is geminate at this temperature. Similar effects have been observed in tetracene derivatives[151] and we measured a similar effect in diF-TES-ADT films in Chapter 4.

The reduction in non-geminate triplet fusion with temperature implies that the triplet diffusion length is reduced at low temperature. This could be due to changes in the diffusion constant or the lifetime. The triplet lifetime in rubrene films shows little dependence on temperature[74]. In contrast, the hole mobility (mediated by a 1-electron Dexter transfer) in rubrene single crystals reduces by a factor of 30 on cooling from room temperature to 100 K[352]. Since triplet transfer is a 2-electron Dexter transfer process, we might expect the reduction in triplet mobility to be even greater. In rubrene thin films, the triplet hopping rate has been reported to decrease by approximately one order of magnitude over the same temperature range[353].

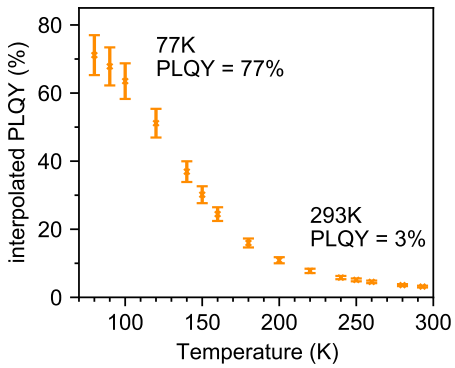

Figure 8.7 | Temperature dependence of PLQY. PLQY of the rubrene nanoparticles as a function of temperature. We calculated the interpolated PLQY values by normalising the integrated PL as a function of temperature to the measured absolute PLQY. Error bars reflect the discrepancy between normalising to the PLQY measured at 77 K and room temperature.

These low-temperature dynamics, caused by reduced triplet mobility, are ac-

companied by a striking 20-fold increase in the PLQY, shown in Figure 8.7. At 77 K, 77% of absorbed photons are re-emitted as PL. Singlet fission is still occurring at these temperatures since we observe significant delayed PL arising from geminate triplet fusion. Subsequent triplet-pair separation, which is reported to be thermally activated in rubrene[35] may also be reduced at low temperature.

The dramatic increase in PLQY accompanied by reduced triplet diffusion as the temperature is decreased suggests that substantial losses are associated with the formation of separated triplets following singlet fission, such as triplet quenching[354] and trapping[355,356], but that these losses are minimal at low temperature when triplet migration is inhibited. These results for our rubrene NP films are similar to reported single crystal measurements which show a reduction in the PL yield as the defect density is increased, attributed to the long diffusion lengths of triplet excitons and their dominant contribution to the total PL[346]. Confirming this idea, Figure J.8 shows how a faster decay of the total triplet population, and hence increased triplet losses in our polycrystalline rubrene films dramatically reduce their emitted PL compared to the NP samples.

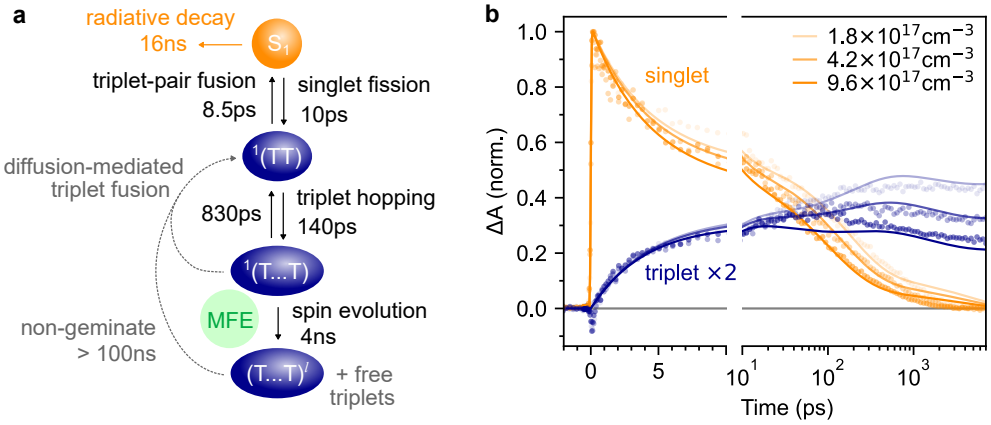

Figure 8.8 | Photophysics of rubrene nanoparticles. **a**, Schematic diagram summarising the photophysics of rubrene nanoparticles. **b**, The kinetic scheme in (**a**) provides a good description of the ps singlet and triplet dynamics. We have neglected the > 100 ns triplet fusion and included singlet-singlet annihilation ($k = 3 \times 10^{-8}\,\mathrm{cm^3\,s^{-1}}$) in the simulation.

Putting our results together, we arrive at the description of rubrene NP photophysics shown in Figure 8.8a which, with the addition of singlet-singlet annihilation, quantitatively reproduces the picosecond singlet and triplet dynamics as shown in Figure 8.8b (rate equations and constants are given in Appendix J). The kinetic scheme is consistent with the picture built up through measurements of crystalline rubrene[35,36,189,216,272,288,289,344–346] which we reviewed above. Here we focus on the rate constants of the different steps, which will be import-

ant when we come to consider the effect of the singlet energy collector DBP in the following section.

Interconversion between S_1 and ^{1}(TT) occurs within 10 ps. ^{1}(TT) subsequently separates into ^{1}(T...T) with a time constant of approximately 140 ps. This triplet hopping rate is consistent with the bimolecular triplet annihilation constant of $5 \times 10^{-12}\,\mathrm{cm^3\,s^{-1}}$ measured for rubrene single crystals[216] (see Section J.3). The rate of fusion from ^{1}(T...T) to ^{1}(TT) is roughly six times slower which is expected for triplet hopping in three dimensions. Spin evolution on a timescale of several nanoseconds results in triplet-pairs with mixed spin character. Not included in the simulation is the complicated diffusion-mediated triplet fusion that occurs on nanosecond timescales[344,345].

In our description of the photophysics of the rubrene NP films, we have neglected the possibility that rubrene monomers may exist in isolation within the PVA matrix. There are several reasons why any such contribution must be very small. Firstly, the PLQY of the NP films (around 3%) is similar to values reported for pure polycrystalline films[44,342,343]. Significant concentrations of monomeric rubrene, which has a PLQY of almost unity[67], would cause the PLQY to increase. Secondly, we find no evidence of the 16 ns exponential decay component of monomeric rubrene[67,289] in either the time-resolved fluorescence or transient absorption measurements. Thirdly, the large magnitude of the magnetic field effect shown in Figure 8.5 demonstrates that the majority of the fluorescence arises from solid, aggregated rubrene. The photoluminescence intensity of monomeric rubrene, which does not undergo singlet fission, is independent of magnetic field.

8.5 Addition of DBP does not suppress initial singlet fission

In the previous section we showed that the PLQY of the rubrene NPs depends heavily on triplets, as it does for rubrene single crystals[216]. To investigate the effect of the DBP dopant on the photophysics of rubrene, we compare transient absorption measurements of DBP-doped NP films with those of pure rubrene NPs, recorded under the same experimental conditions.

We begin by determining the transient absorption signatures of DBP singlet states by performing measurements of monomers in solution. In Figure 8.9 we see that the TA data is comprised principally of negative ground state bleach and stimulated emission features. These decay uniformly with a time constant of 4 ns and we therefore assign them to the singlet exciton.

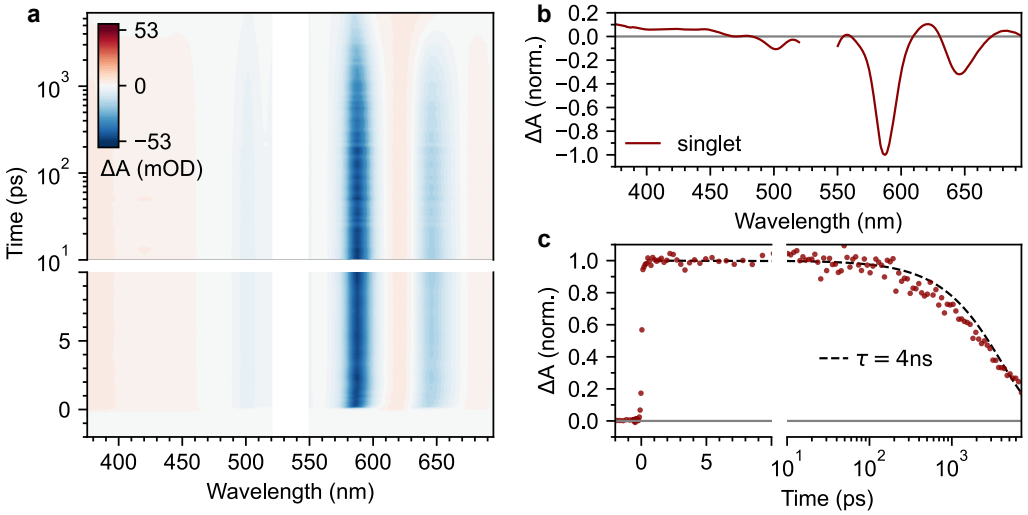

Figure 8.9 | Transient absorption of DBP monomers in solution. **a**, Ultrafast TA spectroscopy of DBP dissolved in anhydrous tetrahydrofuran (THF) at a concentration of 10^{-4}M. We observed a single spectral feature that decayed uniformly with time and is assigned to the S_1 state. **b**, TA spectrum associated with the S_1 state of DBP obtained by averaging the TA data from 10 ps onwards. **c**, Normalised TA dynamics at 587 nm give the approximately exponential decay of the S_1 state of DBP monomers. The lifetime is ∼4 ns.

Figure 8.10a-b shows ultrafast transient absorption data for rubrene NPs containing 0.5 mol% DBP. In addition to the spectral features corresponding to the singlet and triplet excited states of rubrene, we observe a new, negative feature that grows in over several tens of picoseconds. This feature closely matches the TA spectrum of DBP monomers in solution (Figure 8.9b) and we therefore assign it to the singlet state of DBP, which includes both ground state bleach and stimulated emission. We used the singlet spectra measured in solution measurements as references in our global extraction of the singlet, triplet and DBP dynamics using MCR-ALS, as described in Section 8.8.5.

The kinetics of the singlet and triplet states of rubrene resulting from this procedure are shown in Figure 8.10c. Strikingly, we find that there is very little change to the excited state dynamics of pure rubrene NPs (grey squares) upon the addition of DBP. In particular, initial singlet fission, that is $S_1 \rightarrow {}^1(TT)$, still occurs with the same initial yield and rate. We see the same lack of change for polycrystalline films containing the same 0.5% mole fraction of DBP (Figure J.9). On timescales of tens to hundreds of picoseconds, the singlet and triplet populations do appear to decay slightly faster in the DBP-doped nanoparticles, indicating that energy transfer to DBP occurs predominantly on these longer timescales.

Indeed, this is borne out by the kinetics of the DBP singlet state, shown by

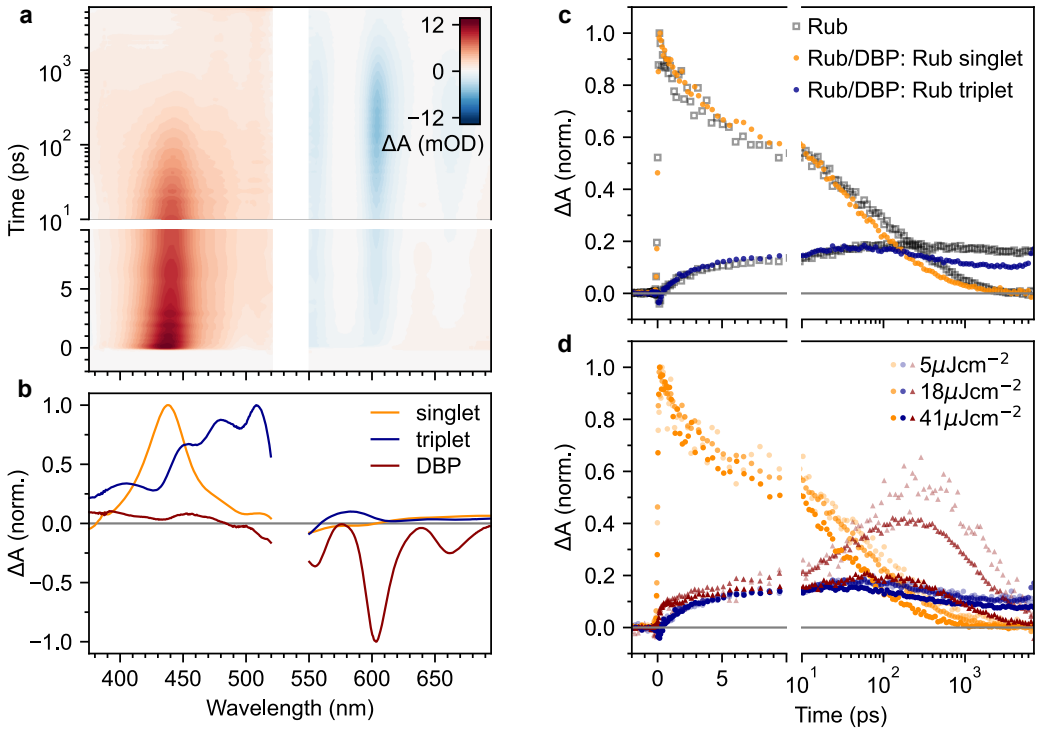

Figure 8.10 | The addition of DBP does not suppress initial singlet fission. **a**, Ultrafast TA of rubrene nanoparticles doped with 0.5 mol% DBP. Data is shown for an excitation density of 18 µJ cm^{-2}. We extracted spectral components using a global MCR-ALS procedure based on measured reference spectra, giving the rubrene singlet (orange), rubrene triplet (blue) and DBP singlet (red) spectra shown in (**b**). **c**, The corresponding dynamics of the rubrene singlet and triplet populations in the DBP-doped NPs are almost identical to those in the pure NPs (both shown for an excitation density of 18 µJ cm^{-2}). We find a small reduction in the singlet and triplet populations beyond 50 ps. **d**, The principal rise in the DBP singlet population occurs well after initial singlet fission has taken place and is strongly dependent on excitation density. Some DBP molecules are directly photo-excited by the 532 nm pump pulses, which were the same as those used to excite the pure rubrene NP films.

red triangles in Figure 8.10d. We find that following photo-excitation (which populates the singlet state of both rubrene and DBP), the DBP singlet mainly grows in on timescales of several tens to hundreds of picoseconds, after the first step of singlet fission has taken place. Thus the addition of DBP does not suppress initial singlet fission. Instead, FRET from the rubrene S_1 to the DBP S_1 is competitive with the subsequent step of triplet-pair separation (see Figure 8.8a).

The yield of DBP singlet is heavily dependent on the excitation density, which on picosecond timescales affects the dynamics only through singlet-singlet annihilation (Figure 8.10d). If there is a distribution of singlet exciton diffusivity within the NPs, singlets with greater mobility are more likely to transfer their energy to the DBP molecules, but it is these same mobile singlets that are

quenched by singlet-singlet annihilation in our experiments.

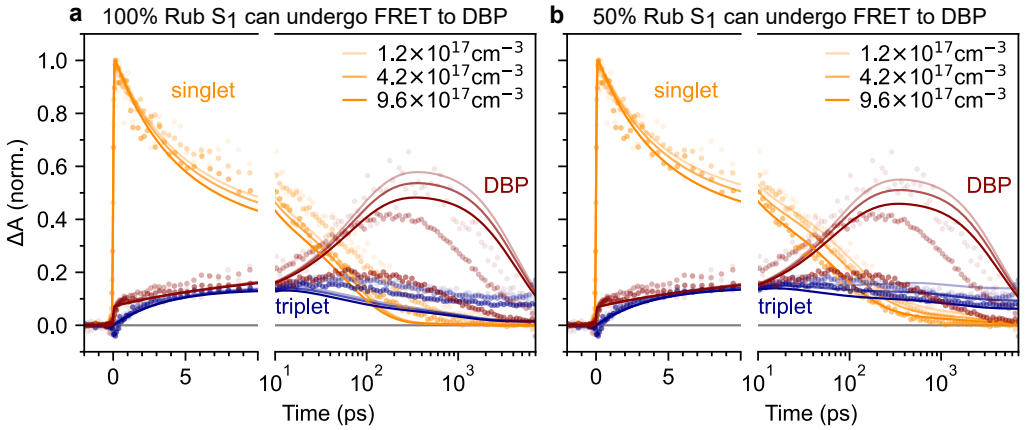

Figure 8.11 | Modelling the inclusion of DBP in rubrene NPs. a, If all the rubrene singlets are able to undergo FRET to DBP, the depletion of the singlet and triplet populations is overestimated. **b**, If instead only half of the rubrene singlets are able to undergo FRET to DBP, the dynamics are reasonably well described. In both cases the effect of singlet-singlet annihilation on the DBP dynamics is underestimated. We suggest that this is because the same mobile singlets that preferentially undergo FRET are also most affected by singlet-singlet annihilation.

This hypothesis supported by our kinetic modelling[§] (Figure 8.11). To simulate the inclusion of DBP, we initially included a single rubrene-DBP FRET rate of $20\,\mathrm{ns}^{-1}$. Note that since DBP molecules also absorbed the 532 nm pump pulses, we split the initial photoexcitation between rubrene S_1 and DBP S_1 states in the ratio 10:1. The mole fraction (0.5%) of DBP in the sample and the ratio of molar absorptivity at the excitation wavelength (1:10)[45,203] give a ratio of 20:1. We found that 10:1 better reproduced the data, though we note that the model does not reproduce the large effect of singlet-singlet annihilation on the DBP population dynamics so there is some uncertainty in this ratio.

Under the simple assumption that all of the rubrene singlet states are able to undergo FRET to DBP, we obtain the simulation shown in Figure 8.11a. In this case, the model underestimates the effect of singlet-singlet annihilation on the DBP population dynamics, but overestimates the depletion of the rubrene singlet and triplet populations. This is consistent with the interpretation that the less mobile singlets are not able to find DBP molecules, whilst the more mobile ones that can are particularly susceptible to singlet-singlet annihilation.

We can therefore assume instead that (somewhat arbitrarily) only 50% of the singlet excitons in rubrene can undergo FRET to DBP. To model this we take the average of two simulations, one with $k_{fret} = 0$ and one with $k_{fret} = 20\,\mathrm{ns}^{-1}$.

[§]The code used for the simulations in Figures 8.8 and 8.11 is freely available at https://github.com/davidbossanyi/rubrene-nanoparticle-dynamics

In this case we can reproduce the singlet, triplet and DBP dynamics reasonably well as shown in Figure 8.11b, though again, the excitation density dependence of the DBP dynamics is still not captured. This is to be expected since the model does not include diffusion processes.

In line with our calculations of FRET rates and exciton diffusion lengths in Appendix J, plenty of singlet excitons evidently do undergo both singlet fission and triplet separation. This is evidenced by the substantial triplet signal that persists for several nanoseconds after the DBP population has mostly decayed away. The residual triplet signal, relative to the initial photo-excited singlet, is at least half that of pure rubrene NPs, yet we find that the addition of DBP increases the absolute PLQY by a factor of 20. This can nevertheless be rationalised by taking into account the recycling of excitation energy through triplet fusion[216], which we explore in the following section.

8.6 Singlet energy collection in rubrene nanoparticles

Figure 8.12a compares the PL dynamics of rubrene nanoparticles with and without the addition of DBP. The initial 'prompt' decay is more pronounced for DBP-containing nanoparticles and makes a larger contribution to the total PL than for pure rubrene NPs. Beyond 30 ns, a slightly faster roll-off of singlet population generated from bimolecular TTA is observed for rubrene-DBP NPs. A comparison of the triplet dynamics, shown in Figure 8.12b, reveals almost identical behaviour regardless of the presence of DBP. The underlying photophysics in both cases is therefore predominantly that of concurrent singlet fission and triplet fusion in rubrene. We suggest the following hypothesis to explain the 20-fold increase in PLQY upon doping with DBP.

DBP acts to increase the probability of radiative decay when excitation energy returns to the $S_1 \leftrightarrow {}^1(TT)$ equilibrium. Correspondingly, the probability of non-radiative decay of fission generated independent triplets is reduced. Since energy is continually moving back and forth between singlets and triplets, including when DBP is present, the cumulative effect results in a substantial increase to the PLQY, from 3% to 61%, as shown in Figure 8.12c. Our measurements of polycrystalline rubrene films are also consistent with this conclusion (Figure J.9), which we summarise schematically in Figure 8.13.

Since less energy is lost through nonradiative triplet decay in DBP-doped rubrene, Figure 8.12c shows a much more modest increase in PLQY at low temperature than that measured for pure rubrene. Reducing the temperature is a different way to avoid non-radiative triplet decay, but instead through sup-

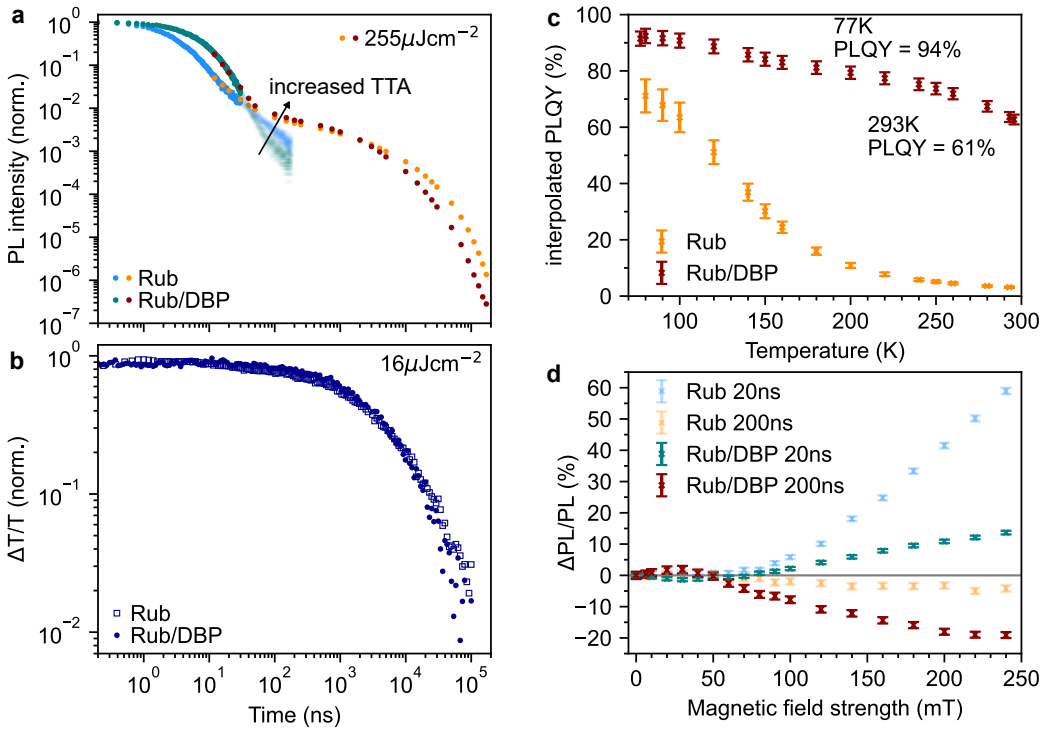

Figure 8.12 | Energy transfer to DBP competes with triplet-pair separation. **a**, TRPL dynamics of rubrene NP films with and without DBP comprising TCSPC (470 nm excitation) and intensified gated CCD (532 nm excitation) measurement. DBP-doped nanoparticles show increased prompt PL and a slightly faster roll-off of singlet population on the microsecond timescales associated with TTA. Very similar triplet fusion dynamics are observed on these timescales, as shown by transient absorption measurements at 510 nm in (**b**). Note that the overlap between the TCSPC and iCCD data is not perfect owing to the very different pulse energies used, and that the TCSPC data for the DBP-containing nanoparticles was detected at 640 nm. **c**, DBP-doped nanoparticles have a much higher PLQY than pure rubrene nanoparticles at room temperature that increases only moderately for low temperatures. **d**, Magnetic field effect on time-gated fluorescence with and without the addition of DBP.

pression of triplet diffusion which reduces the likelihood that triplets encounter defects.

The change in the MFE shown in Figure 8.12d is consistent with this description of the role of the singlet energy collector in rubrene. The reduced probability that triplet-pairs separate and undergo spin evolution causes a decrease in the magnitude of the MFE at 20 ns delay. At 200 ns delay, the negative MFE associated with triplet fusion is stronger because the positive contribution from triplet separation and subsequent spin evolution is reduced.

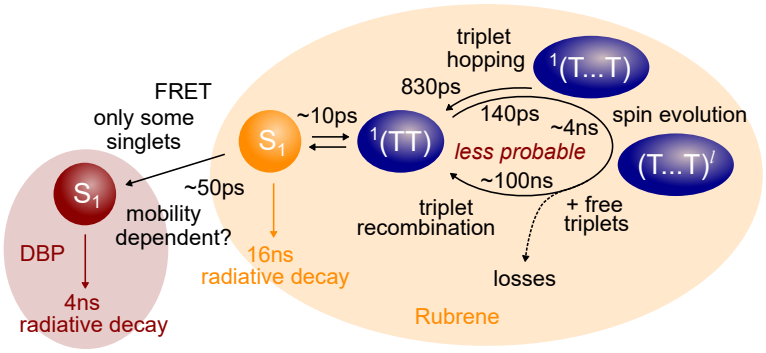

Figure 8.13 | Proposed role of DBP doping in rubrene photophysics. Schematic diagram summarising the suggested interplay between singlet energy collection, singlet fission and triplet recombination in rubrene-based nanoparticles. The addition of DBP increases the probability that singlet energy decays radiatively by (partially) competing with triplet separation. This increased emission probability is encountered every time excitation energy is recycled through triplet recombination, leading to a large increase in PLQY at room temperature.

8.7 Conclusions

In this chapter we have presented a detailed photophysical characterisation of recently developed rubrene nanoparticle films. Our most striking finding is that the addition of 0.5 mol% of the singlet energy collector DBP has very little discernable effect on the singlet and triplet population dynamics in rubrene, despite increasing the photoluminescence quantum yield by a factor of 20 to 61% at room temperature. We suggest that this behaviour can be rationalised by considering the roles of geminate and non-geminate triplet fusion, which have been extensively studied in rubrene crystals over the last decade.

In rubrene NP films, we have shown that similar concurrent singlet fission and triplet fusion dynamics to those in rubrene crystals[35,36,189,216,272,288,289,344–346] occur. This is surprising, given the lack of peaks in the X-ray diffraction patterns of the rubrene NPs[45,203] and the similarity between their excited state absorption spectra and those measured for singlets and triplets in solution[350].

It is well known that triplet-quenching defects substantially reduce the PLQY of rubrene crystals[346], and we find that similar defects are also the likely cause of the modest 3% PLQY of pure rubrene NP films. We suggested that the effect of the DBP dopant is to reduce the probability that triplets encounter such defects by providing a radiative channel for singlets ($\sim$ 50 ps) that competes not with the formation of triplet-pairs (10 ps) as is usually implied, but with their subsequent separation ($\sim$ 140 ps).

These results point to alternative strategies for achieving efficient TTA-UC

in solid rubrene. Whilst singlet fission can be completely suppressed in rubrene by making it amorphous[289], or adding bulky side groups[343], the disruption this causes to the crystal structure seriously hinders the long-range triplet diffusion required[20] and leads, overall, to lower upconversion efficiencies[343]. We suggest instead that efforts should focus on controlling triplet-pair separation and eliminating triplet-quenching defects. Such a strategy could increase the PLQY whilst maintaining the crystallinity required for triplet diffusion. It may even be possible to forego the addition of DBP altogether, thereby avoiding the associated 200 meV reduction in the upconversion anti-Stokes shift.

8.8 Methods

8.8.1 Sample preparation

Films of rubrene and DBP-doped rubrene nanoparticles dispersed in a PVA matrix were prepared by Yoichi Sasaki as described in Section 3.2.4. Polycrystalline films of rubrene and DBP-doped rubrene were solution processed as described in Section 3.2.2.

8.8.2 Steady-state absorption and photoluminescence

Ground state absorption spectra were recorded with a UV–vis spectrophotometer (Cary60, Agilent). Temperature-dependent PL spectra were measured by Yoichi Sasaki using a spectrofluorometer (FP-8300 and CSH-831, JASCO) combined with a liquid nitrogen cryostat (Optistat DN2, Oxford Instruments). The absolute photoluminescence quantum yield was measured by Yoichi Sasaki in an integrating sphere using a Hamamatsu Photonics absolute quantum yield measurement system.

For comparisons of room temperature static PL intensity, excitation was provided by a 532 nm continuous wave laser diode (CPS532, Thorlabs). PL was collected via optical fibre and detected with a CCD spectrometer (AvaSpec, Avantes). The excitation intensity was $\sim$1 W cm^{-2}. A 532 nm notch filter was used to reduce laser scatter in the measured spectra.

8.8.3 Time-resolved photoluminescence

Time correlated single photon counting (TCSPC) measurements were carried out by Yoichi Sasaki using a lifetime spectroscopy system (Quantaurus-Tau C11367-02, Hamamatsu). The excitation wavelength was 470 nm. Nanosecond-millisecond TRPL measurements were carried out using our iCCD setup, de-

scribed in detail in Section 3.4.1. Excitation took the form of 532 nm pump pulses (temporal width < 500 ps, 5 kHz) provided by the frequency-doubled output of a Q-switched Nd:YVO_4 laser (Picolo-AOT, Innolas). A 532 nm notch filter was used to eliminate pump scatter. For low-temperature measurements samples were situated in the helium exchange gas of a nitrogen bath cryostat (Optistat DN, Oxford Instruments). The pump beam spot size was measured at the sample position by translating a razor blade through the focus and monitoring the transmitted power.

For magnetic field dependent TRPL measurements, a different excitation source was used, owing to its superior power stability over time. A Ti:sapphire regenerative amplifier (Solstice, Spectra-Physics) providing 800 nm pulses (90 fs FWHM, 1 kHz, 4 mJ) was used to generate the pump pulses. A portion of the 800 nm beam was frequency doubled in a BBO crystal to generate 400 nm excitation. The excitation intensity used was 25 µJ cm^{-2}.

8.8.4 Transient absorption spectroscopy

Transient absorption spectroscopy was performed using both the picosecond and nanosecond setups described in Sections 3.4.2 and 3.4.2 respectively.

8.8.5 Spectral deconvolution of TA data

We extracted the spectra and dynamics of the different excited state species from our ultrafast TA data using Multivariate Curve Resolution Alternating Least Squares (MCR-ALS)[225,226], the basic principles of which are discussed in Section 3.4.3. We generated reference spectra, used to act as starting points for the fitting procedure, in the following ways. We obtained the rubrene singlet spectrum from the measurement of rubrene monomers in solution, by averaging the data from 10 ps onwards. This is the spectrum plotted in Figure 8.2b(ii). This spectrum was then redshifted in energy by 32.7 meV such that the peak coincided with the maximum of the S_1 spectral feature in the solid samples. We obtained the DBP singlet spectrum in an exactly analogous way from the measurement of DBP monomers in solution (Figure 8.9b). In this case the required redshift was 55.9 meV. We estimated the rubrene triplet spectrum for the nanoparticle (NP) samples by averaging the pure rubrene NP TA data (18 µJ cm^{-2}) from 5 ns onwards. Beyond 5 ns the spectral shape remained unchanged because the singlet component had decayed, thus we judged the remaining spectral features to be representative of excited triplet species. We used the same procedure to obtain a starting spectrum for the triplets in the polycrystalline films.

Next, we grouped all of our ultrafast TA measurements by sample type. For the nanoparticle (NP) samples, this gave six datasets in total: rubrene NPs with and without the 0.5 mol% DBP additive, measured with pump intensities of $8\,\mu J\,cm^{-2}$, $18\,\mu J\,cm^{-2}$ and $41\,\mu J\,cm^{-2}$. For the polycrystalline films, we had three datasets: films with 0, 0.1 and 0.5 mol% DBP measured with pump intensities of $41\,\mu J\,cm^{-2}$.

We ran the MCR-ALS algorithm only once for each group of datasets, since the spectral components are common to all samples. Note that the DBP component was excluded for samples of pure rubrene. Grouping the datasets in this way provides a much more tightly constrained deconvolution. We used the reference spectra as described above for the initial point of the fitting procedure. The algorithm was run until convergence was achieved.

Chapter 9

Summary and Outlook

In this chapter we review the key findings of the work presented in this thesis and place them in the context of the wider research field. We identify a range of open questions and propose future studies that may begin to answer them.

9.1 Summary

This thesis has investigated intermediate triplet-pair states in singlet fission and triplet-triplet annihilation. Building on the recent wave of research in these areas, we have studied a variety of material systems in order to clarify the nature and behaviour of different kinds of triplet-pair states and how they impact the photophysical mechanisms of exciton fission and fusion.

In Chapter 4, we investigated emission signatures of the strongly exchange-coupled spin-0 triplet-pair state, ^{1}(TT). Previous works had assigned redshifted features in emission spectra to the ^{1}(TT) state but these signatures varied from vibronically structured photoluminescence attributed to the Herzberg-Teller intensity borrowing mechanism to broad unstructured features assigned to excimer states. It had also been shown that the excimer-like emission features were observed only during singlet fission and not during the triplet-triplet annihilation, casting doubt on the role of ^{1}(TT) as a real intermediate state.

We conducted time-resolved photoluminescence measurements on two material systems: polycrystalline films of diF-TES-ADT, for which singlet fission is slightly endothermic and single crystals of pentacene, for which it is exothermic. In both cases, we were able to measure clear structured photoluminescence signatures consistent with ^{1}(TT) states formed directly via triplet-triplet annihilation and emitting through the Herzberg-Teller mechanism. In diF-TES-ADT, we showed that these spectral signatures of ^{1}(TT) are distinct from excimers, suggesting that observations of excimer emission are not necessarily evidence of

^{1}(TT). Our analysis of the emission spectra of our pentacene single crystals took us back to the 1980s, when redshifted photoluminescence features in pentacene and tetracene were instead assigned to self-trapped excitons. We demonstrated that these previous assignments were inconsistent, and used our time-resolved photoluminescence measurements, the first to be conducted on pentacene single crystals, to identify ^{1}(TT), formed through triplet-triplet annihilation, as the source of the redshifted emission.

Our results add weight to the notion that ^{1}(TT) is a real, observable intermediate state in both singlet fission and triplet-triplet annihilation and that this is generally true for all polyacenes. We demonstrated that time-resolved photoluminescence spectroscopy can be used to track the ^{1}(TT) population decay with high sensitivity over many orders of magnitude. Indeed, in doing so we identified contributions from weakly exchange-coupled triplet-pair states and confirmed their involvement through magnetic field effects.

Based on the conclusions of Chapter 4, we hypothesised that Herzberg-Teller emission from ^{1}(TT) might be particularly bright in single crystals of rubrene owing to the close energetic alignment between S_1 and ^{1}(TT). This hypothesis was suggested in part by curious photoluminescence behaviour previously reported in rubrene single crystals. We therefore studied the time-resolved photoluminscence behaviour of rubrene single crystals in Chapter 5, but found no evidence of emission from ^{1}(TT) states. Instead, we found that previous reports of anomalous photoluminescence behaviour are likely to be a result of defects sometimes present on crystal surfaces.

The role of defects in rubrene came to the fore in Chapter 6. Surprised by recent reports of ultrafast ^{1}(TT) formation in rubrene single crystals, we used transient absorption spectroscopy at different excitation wavelengths and incidence angles to investigate the formation of ^{1}(TT) states. We found that ^{1}(TT) was formed 'instantaneously' only in polycrystalline films and not in bulk single crystals. The results from this chapter allow us to contribute to the debate surrounding the time constant of singlet fission in bulk crystalline rubrene[191]. Recall that some groups report a rate of ~ 25 fs for the initial formation of ^{1}(TT) from S_1[35–37], while others give a value of ~ 2 ps[189,288,289]. We suggest that the latter value is likely to be correct in the sense that the 2 ps time constant represents the singlet fission rate intrinsic to pure, bulk rubrene crystals, as indeed is predicted by calculations[188]. We have shown that significantly faster singlet fission on the order of tens of femtoseconds can occur in crystalline rubrene, but only when the morphology differs from that of ideal crystals, for example in polycrystalline films.

In Chapter 7, we continued our investigations of rubrene but now focussing on the probability of obtaining a spin-0 singlet state from the annihilation of two spin-1 triplets, a quantity known as the spin statistical factor, η. Our results in Chapter 4 had suggested that triplet-triplet annihilation forms first weakly, then strongly exchange-coupled triplet-pair states. We confirmed this for rubrene in Chapter 7 using magnetic field dependent measurements, and explained why most discussions of η in the literature have considered only strongly exchange coupled triplet-pairs. For example, it is usually assumed that the probability of a pair of triplets annihilating to form a singlet is $\frac{2}{5}$. By happy coincidence this matches the measured spin statistical factor for the archetypal DPA molecule in solution. Our results show that this is only a coincidence, and is based on the false premise that the interacting triplets are initially strongly exchange-coupled.

Because of the weak exchange interaction initially found between annihilating triplets, we showed that the molecular geometry of the encounter complex can dramatically alter the spin statistical factor, varying it from $\frac{2}{5}$ to $\frac{2}{3}$. In addition, we demonstrated that the spin statistical factor can be overcome in materials such as rubrene by high-level reverse intersystem crossing. With careful molecular engineering, therefore, our results show that 100% of all triplet annihilation events could result in a bright singlet exciton. These findings uncover several potential strategies for engineering materials with favourable spin statistical factors for use in OLEDs and photon upconverters.

Finally, in Chapter 8, we showed how knowing the dynamics of different triplet-pair states is key to understanding the interplay between singlet fission and singlet energy collection via FRET to a dopant molecule in rubrene nanoparticles. We used transient absorption spectroscopy and time-resolved photoluminescence measurements to demonstrate that singlet energy collection does not outcompete singlet fission, as previously supposed, but instead competes with triplet-pair separation. This finding will help direct future efforts in maximising the photon upconversion quantum yield in rubrene-based systems.

9.2 Unanswered questions

The research presented in this thesis raises a range of questions and future research directions which we group below into five areas. Building on the experiments and simulations in Chapters 4-8, we propose possible avenues for future work that might begin to tackle these questions.

The emission spectrum of rubrene

In Chapter 5, we showed that ^{1}(TT) is not responsible for the ab-polarised absorption/emission component in rubrene single crystals. In the introduction, we suggested that instead, it could arise due to Herzberg-Teller intensity borrowing from a higher-lying singlet state. Raman spectroscopy, coupled with calculations, may help to confirm this hypothesis.

More fundamentally, during our investigations of rubrene in Chapters 5-8, we came to the realisation that the emission spectrum of rubrene remains poorly understood, particularly its temperature dependence. For example, in Figure J.10, we clearly observe that the apparent vibrational energy increases dramatically with decreasing temperature from around 135 meV at room temperature to around 170 meV at 80 K. The vibrational energy we extract from the absorption spectrum is also around 170 meV but this is independent of temperature[353,357]. We have confirmed that this behaviour also occurs in polycrystalline thin films, and it has been reported elsewhere[353]. Surprisingly, we cannot find a measured temperature dependence of the absorption and emission spectra of rubrene monomers (for example dissolved in a glass-forming solvent such as 2-methyltetrahydrofuran) in the literature. Such an experiment should be performed to determine whether the changes in vibrational energy with temperature seen in the PL spectrum are intrinsic to the rubrene molecule.

Even in solution at room temperature, there appears to be no satisfactory explanation for the much reduced vibrational energy required to fit the PL spectrum compared to the absorption spectrum[357,358]. It is thought that the rubrene backbone is twisted in solution, and possibly in thin films as well[359]. Perhaps rubrene planarises in the excited state, leading to a different potential energy surface compared to the ground state. Combining temperature dependent absorption and emission measurements with ground state and resonant Raman spectroscopy, alongside theoretical calculations, may help to answer such questions.

Fundamentals of singlet fission

Our measurements of bright, long-lived emission from the ^{1}(TT) state in diF-TES-ADT at 100 K suggest that this system may be an ideal platform to unravel the spin physics of singlet fission. In Section 2.6.3 we outlined the uncertainty surrounding the role of the strongly exchange coupled quintet states ^{5}(TT) that have been observed in trEPR measurements. By combining time-resolved photoluminescence measurements of ^{1}(TT) with trEPR measurements of ^{5}(TT),

it may be possible to determine whether ^{5}(TT) acts as an intermediate state between ^{1}(TT) and free triplets[141,145,147] or whether it is formed as a by-product via weakly exchange-coupled triplet pairs (which are singlet-quintet mixtures).

The role of morphology

Our results from Chapters 5 and 6 were inconclusive regarding the possibility of ^{1}(TT) photoluminescence from disordered, polycrystalline rubrene. We suggested that ^{1}(TT) may be formed extremely rapidly at disordered sites where symmetry breaking promotes S_1-^{1}(TT) mixing. Such mixing may also promote brighter ^{1}(TT) emission. Spatially-resolved TRPL measurements, combined with calculations, may help to determine exactly which type of molecular misalignment is required for ultrafast singlet fission in rubrene.

This leads us to a more general question with as yet, no clear answer: how does morphology impact singlet fission and, by extension, triplet-triplet annihilation? Going further, how does this dependence manifest itself in materials with different molecular packing geometries? For example, S_1-^{1}(TT) couplings are non-zero in brickwork-packed TIPS-pentacene, but zero in orthorhombic rubrene[188]. In addition to our studies of rubrene in Chapter 6, recent work[171] employed spatially resolved transient absorption spectroscopy to suggest that singlet fission occurred preferentially at the edges and defects of TIPS-pentacene crystals, sites that were also associated with a different crystal packing and lower S_1 energy.

We suggest that spatially- and time-resolved photoluminescence measurements of diF-TES-ADT at low temperature could provide a clear dataset for investigating the role of morphology on singlet fission. At 100 K for example, we have shown that S_1 and ^{1}(TT) are both bright and spectrally highly distinct (Chapter 4). As such the rate and yield of triplet-pair formation could be spatially imaged and correlated against morphological features or other spatially-resolved measurements, such as the S_1 and ^{1}(TT) energies and linewidths.

Similarly, our results in Chapter 6 indicate that spatially-resolved transient absorption of polycrystalline rubrene may help to unravel the effects of molecular alignment on singlet fission. Going further, impulsive vibrational spectroscopy could be used to probe the role of vibrational modes in enabling singlet fission at different sites. It would then be interesting to investigate whether the same morphological features that encourage rapid and efficient singlet fission are also associated with increased or reduced TTA-UC.

Rubrene nanoparticle morphology

The rubrene nanoparticles introduced in Chapter 7 and studied in detail in Chapter 8 exhibited a number of curious properties that we were not able to satisfactorily explain. Firstly, we found that the dynamics and lifetime of triplet species were similar to those found in bulk rubrene single crystals, in contrast to polycrystalline films which exhibit instantaneous ^{1}(TT) formation and considerably shorter triplet lifetimes. However, the excited state absorption spectrum of triplet excitons in the nanoparticles was remarkably similar to that measured for rubrene in solution[350], and very different to that of single crystals. Furthermore, either the cross-section of this absorption, or the singlet fission yield, are lower than in single crystals and polycrystalline films. These apparent contradictions call for detailed investigations of the nanoparticle morphology, especially given their potential as an air-stable material system for TTA-UC applications.

Annihilator molecules for TTA-UC

One of the conclusions of Chapter 7 is that relative molecule orientation should impact the spin statistical limit of TTA-UC through the spin Hamiltonian. A future study could investigate this prediction experimentally. Dimers have been successfully used to study the fundamental physics of triplet-pair states in singlet fission[166,167,360,361] and they have recently been shown to perform well for TTA-UC[362]. We suggest that a series of rigid annihilator dimers exhibiting a range of inter-chromophore geometries and separations could be used to test our hypothesis in sensitized TTA-UC experiments.

In addition to intermolecular orientation, our simulations in Chapter 7 demonstrated that materials exhibiting HL-RISC can potentially exceed any spin statistical limit for TTA-UC. Computational and synthetic chemists could explore ways to create molecules possessing efficient HL-RISC for blue-emitting OLEDs and photon upconverters.

9.3 Future directions for research into triplet-pair states

Some of the most potentially fruitful experiments to further elucidate the nature and character of triplet-pair states are likely to be those that aim to understand the impact of morphology. As we alluded to above, a promising series of experiments could aim to link spatially-resolved transient absorption and photoluminescence measurements to the results of other spatially-resolved experiments

recorded on the same areas of the same samples. The large, multidimensional datasets generated by such experiments would lend themselves to analysis using statistical methods, allowing the contribution of different morphological factors to the time-resolved behaviour of the excited states to be determined.

As suggested above, diF-TES-ADT thin films at low temperature could be a sensible starting point for such a series of experiments. One could imagine mapping the spatial distribution of parameters obtained from time-resolved spectroscopy, such as time constants, linewidths and excited state energies against, to begin with, basic morphological structures such as grain boundaries identified by microscopy techniques.

9.4 Future applications for exciton fission and fusion

Much of the recent research into exciton fission and fusion has been motivated by the potential to create spectral converters for photovoltaics. Even if efficient spectral conversion systems based on exciton fission or fusion could be created, to be commercially appealing to the photovoltaics industry such systems would need to meet a host of stringent requirements relating to cost, toxicity and long-term stability and performance under harsh environmental conditions. One can't help feeling that this may never come to pass.

Nevertheless, spectral converters based on exciton fission and fusion could still be valuable in other ways. We have already mentioned the biomedical applications of TTA-UC in this thesis. Going further, spectral converters could, for example, be used to enhance the wavelength range of photodetectors, act as ultraviolet light sources with antimicrobial properties or manipulate the light transmitted into greenhouses in order to optimise the solar spectrum for the growth of different plants.

Appendix A

Time-dependent perturbation theory

Consider the Hamiltonian H_0 of an unperturbed system. The eigenstates obey the time-independent Schrödinger equation

$$H_0 |n\rangle = E_n |n\rangle \tag{A.1}$$

and vary in time only by a phase term

$$|n(t)\rangle = e^{-iE_n t/\hbar} |n\rangle . \tag{A.2}$$

We now introduce a time-dependent perturbation to the system so that the total Hamiltonian becomes

$$H = H_0 + H_1(t) \tag{A.3}$$

and the quantum state of the perturbed system $|\psi(t)\rangle$ obeys the time-dependent Schrödinger equation

$$H |\psi(t)\rangle = i\hbar \frac{\partial}{\partial t} |\psi(t)\rangle . \tag{A.4}$$

The quantum state $|\psi(t)\rangle$ can be constructed from a linear combination of the eigenbasis of H_0, giving

$$|\psi(t)\rangle = \sum_n c_n(t) e^{-iE_n t/\hbar} |n\rangle . \tag{A.5}$$

Substituting Equation A.5 into Equation A.4, using the product rule and Equation A.1, we find that the zero-order terms cancel, leaving

$$\sum_n \left(i\hbar \frac{dc_n(t)}{dt} - c_n(t) H_1(t) \right) e^{-iE_n t/\hbar} |n\rangle = 0. \tag{A.6}$$

Left multiplying by $\langle k|$ and using the orthonormality of the eigenbasis, we find

$$\frac{dc_k(t)}{dt} = \frac{1}{i\hbar} \sum_n \langle k| H_1(t) |n\rangle c_n(t) e^{-i(E_n - E_k)t/\hbar}, \tag{A.7}$$

which integrated yields

$$c_k(t) = c_k(0) + \frac{1}{i\hbar} \sum_n \int_0^t \langle k| H_1(t') |n\rangle c_n(t') e^{-i(E_n - E_k)t'/\hbar} dt'. \tag{A.8}$$

Iterative substitution into the right hand side gives, to first order in H_1,

$$c_k(t) = c_k(0) + \frac{1}{i\hbar} \sum_n \int_0^t \langle k| H_1(t') |n\rangle c_n(0) e^{-i(E_n - E_k)t'/\hbar} dt'. \tag{A.9}$$

If the perturbation is turned on at $t = 0$ when the system is in initial state $|i\rangle$ we have $c_n(0) = \delta_{in}$ giving, for $k \neq i$,

$$c_k(t) = \frac{1}{i\hbar} \int_0^t \langle k| H_1(t') |i\rangle e^{-i(E_i - E_k)t'/\hbar} dt'. \tag{A.10}$$

Equation A.10 is a key result from first-order time-dependent perturbation theory. We next use it to derive expressions for the Fermi Golden Rule.

Consider an oscillatory perturbation of angular frequency ω of the general form

$$H_1(t) = V e^{-i\omega t} + V^* e^{i\omega t}. \tag{A.11}$$

We can treat each term separately. For example considering the first term we find that

$$c_k(t) = \frac{1}{i\hbar} \langle k| V |i\rangle \int_0^t e^{i(\omega_{ki} - \omega)t'} dt' \tag{A.12}$$

where $\omega_{ki} = E_k - E_i$ is the difference between the energies of the initial state $|i\rangle$ and the state $|k\rangle$. Performing the integration gives

$$c_k(t) = \frac{1}{\hbar(\omega_{ki} - \omega)} \langle k| V |i\rangle \left(1 - e^{i(\omega_{ki} - \omega)t}\right) \tag{A.13}$$

which can be re-written as

$$c_k(t) = \frac{-2}{\hbar} \langle k| V |i\rangle e^{i(\omega_{ki}-\omega)t/2} \frac{\sin\left((\omega_{ki}-\omega)t/2\right)}{(\omega_{ki}-\omega)}. \tag{A.14}$$

Thus the probability of the transition $|i\rangle \rightarrow |k\rangle$ is given by

$$P_{i\rightarrow k} = |c_k(t)|^2 = \frac{4}{\hbar^2} |\langle k| V |i\rangle|^2 \frac{\sin^2\left((\omega_{ki}-\omega)t/2\right)}{(\omega_{ki}-\omega)^2}. \tag{A.15}$$

Using the definition of the Dirac delta function

$$\lim_{t\rightarrow\infty} \frac{\sin^2(\Omega t/2)}{\Omega^2 t} = \frac{\pi}{2}\delta(\Omega) \tag{A.16}$$

we find that for $t \rightarrow \infty$

$$P_{i\rightarrow k} = \frac{2\pi}{\hbar} |\langle k| V |i\rangle|^2 \delta(E_k - E_i - \hbar\omega)t, \tag{A.17}$$

where we have written the delta function in terms of energy rather than angular frequency. Thus the rate of the transition is given by

$$\Gamma_{i\rightarrow k} = \frac{\partial P_{i\rightarrow k}}{\partial t} = \frac{2\pi}{\hbar} |\langle k| V |i\rangle|^2 \delta(E_k - E_i - \hbar\omega). \tag{A.18}$$

Including both terms from Equation A.11 we obtain, for real V,

$$\Gamma^{\pm}_{i\rightarrow k} = \frac{2\pi}{\hbar} |\langle k| V |i\rangle|^2 \delta(E_k - E_i \pm \hbar\omega), \tag{A.19}$$

where $\Gamma^{-}_{i\rightarrow k}$ corresponds to a process in which the system gains energy from the perturbation such that $E_k = E_i + \hbar\omega$ (for example the absorption of a photon) and $\Gamma^{+}_{i\rightarrow k}$ corresponds to a process in which the system loses energy back into the perturbation such that $E_k = E_i - \hbar\omega$ (for example the stimulated emission of a photon). This is Fermi's Golden Rule.

In reality, the exact energy matching required for the transition rate to be non-zero is never met. Instead, rather than considering two discrete energy levels, we introduce a *density of final states*, $\rho(E_k)$, where $\rho(E_k)dE_k$ gives the number of final states with energy in the interval $(E_k, E_k + dE_k)$. By integrating the transition rate over the density of states, we obtain a more useful form of Fermi's Golden Rule:

$$\Gamma^{\pm}_{i\rightarrow k} = \frac{2\pi}{\hbar} |\langle k| V |i\rangle|^2 \rho(E_k) \delta(E_k - E_i \pm \hbar\omega), \tag{A.20}$$

where the delta function ensures energy conservation. Finally, we consider the

case of a constant, time-invariant perturbation $H_1(t) = V'$ that turns on at $t = 0$. In this case, we can simply set $\omega = 0$, giving

$$\Gamma_{i\to k} = \frac{2\pi}{\hbar} |\langle k| V' |i\rangle|^2 \rho(E_k)\delta(E_k - E_i). \tag{A.21}$$

Appendix B

The Born-Oppenheimer approximation

The Born-Oppenheimer approximation is based on the fact that nuclei are more than three orders of magnitude heavier than electrons. Electrons dynamics are therefore very 'fast' compared to the movements of the nuclei and hence we introduce an electronic state $|\psi(\mathbf{r};\mathbf{R})\rangle$ that depends only *parametrically* on the nuclear coordinates $\mathbf{R} = \{\mathbf{R}\}$. In other words the electronic state $|\psi(\mathbf{r};\mathbf{R})\rangle$ is determined by a given set of static nuclear coordinates.

We likewise extract from the total molecular Hamiltonian defined in Equations 2.2-2.5 a part that depends parametrically on the nuclear coordinates, given by

$$H_{BO}(\mathbf{R}) = H_{el-el} + H_{el-nuc} + V_{nuc-nuc}, \tag{B.1}$$

where the only term not included is the nuclear kinetic energy term, T_{nuc}. The states $|\psi(\mathbf{r};\mathbf{R})\rangle$ are eigenstates of H_{BO} and so

$$H_{BO}(\mathbf{R})\,|\psi_k(\mathbf{r};\mathbf{R})\rangle = E_k(\mathbf{R})\,|\psi_k(\mathbf{r};\mathbf{R})\rangle\,. \tag{B.2}$$

Given this set of *adiabatic* electronic wavefunctions $|\psi(\mathbf{r};\mathbf{R})\rangle$, we can write the total molecular wavefunction as

$$|\Psi(\mathbf{r},\mathbf{R})\rangle = \sum_k |\psi_k(\mathbf{r};\mathbf{R})\rangle\,\chi_k(\mathbf{R}) \tag{B.3}$$

where $\chi_k(\mathbf{R})$ are expansion coefficients dependent only on the positions of the nuclei. We could of course also expand the total molecular wavefunction in

terms of the nuclear wavefunctions $|\chi_{kl}(\mathbf{R})\rangle$, for example:

$$|\Psi(\mathbf{r},\mathbf{R})\rangle = \sum_{kl} c_{kl} \, |\psi_k(\mathbf{r};\mathbf{R})\rangle \, |\chi_{kl}(\mathbf{R})\rangle \,, \tag{B.4}$$

though this requires extra expansion coefficients. From here on, we drop the $\mathbf{r}$ and $\mathbf{R}$ dependency labels for clarity and recall simply that the $|\psi_k\rangle$ depend on $\mathbf{r}$ and parametrically on $\mathbf{R}$, whilst the χ_k depend on $\mathbf{R}$.

Inserting Equation B.3 into Schrödinger's equation for the entire molecule (Equation 2.1) gives

$$\begin{aligned} H \, |\Psi\rangle &= (H_{BO} + T_{nuc}) \sum_k |\psi_k\rangle \, \chi_k \\ &= \sum_k E_k \, |\psi_k\rangle \, \chi_k + \sum_k T_{nuc} \, |\psi_k\rangle \, \chi_k \\ &= E \sum_k |\psi_k\rangle \, \chi_k . \end{aligned} \tag{B.5}$$

Left multiplying by $\langle\psi_j|$ and using the orthonormality of the $|\psi_k\rangle$ and Equation B.2, we obtain

$$E_j \chi_j + \sum_k \langle\psi_j| \, T_{nuc} \, |\psi_k\rangle \, \chi_k = E \chi_j . \tag{B.6}$$

Using the definition of T_{nuc} from Equation 2.4, we can evaluate $T_{nuc} \, |\psi_k\rangle \, \chi_k$ using the chain rule,

$$\begin{aligned} T_{nuc} \, |\psi_k\rangle \, \chi_k &= \sum_\alpha \frac{\mathbf{P}_\alpha^2}{2M_\alpha} \, |\psi_k\rangle \, \chi_k \\ &= \sum_\alpha \frac{1}{2M_\alpha} \left\{ |\psi_k\rangle \, \mathbf{P}_\alpha^2 \chi_k + \left[\mathbf{P}_\alpha^2 \, |\psi_k\rangle\right] \chi_k + 2\mathbf{P}_\alpha \, |\psi_k\rangle \, \mathbf{P}_\alpha \chi_k \right\} , \end{aligned} \tag{B.7}$$

giving, for the second term in Equation B.6,

$$\sum_k \langle\psi_j| \, T_{nuc} \, |\psi_k\rangle \, \chi_k = T_{nuc} \chi_j + \sum_k \Theta_{jk} \chi_k , \tag{B.8}$$

where we have defined the nonadiabatic coupling as

$$\Theta_{jk} = \langle\psi_j| \, T_{nuc} \, |\psi_k\rangle + \sum_\alpha \frac{1}{M_\alpha} \langle\psi_j| \, \mathbf{P}_\alpha \, |\psi_k\rangle \, \mathbf{P}_\alpha . \tag{B.9}$$

Inserting B.8 into B.6, we obtain a set of coupled equations for the coefficients

χ_j:

$$(E_j + T_{nuc} + \Theta_{ii} - E)\,\chi_j = -\sum_{k \neq j} \Theta_{jk}\chi_k. \tag{B.10}$$

Thus far the treatment is exact. The Born-Oppenheimer approximation is to set the nonadiabatic coupling on the right hand side to zero. The diagonal term Θ_{ii}, known as the Born-Oppenheimer diagonal correction, is typically very small and therefore also ignored. This gives a simple eigenvalue equation for χ_k:

$$(E_k + T_{nuc})\,\chi_k = E\chi_k. \tag{B.11}$$

Thus under the Born-Oppenheimer approximation, the electronic and nuclear motions are decoupled. We therefore write the many body wavefunction as the product of electronic and nuclear wavefunctions,

$$|\Psi_{k,\nu}(\mathbf{r},\mathbf{R})\rangle = |\psi_k(\mathbf{r};\mathbf{R})\rangle\,|\chi_{k,\nu}(\mathbf{R})\rangle\,, \tag{B.12}$$

where ν are the vibrational quantum numbers associated with each adiabatic electronic state k. We have shown that, provided we neglect the nonadiabatic terms, this wavefunction is an eigenstate of the total molecular Hamiltonian:

$$H\,|\psi_k(\mathbf{r};\mathbf{R})\rangle\,|\chi_{k,\nu}(\mathbf{R})\rangle \approx (E_k(\mathbf{R}) + T_{nuc})\,|\psi_k(\mathbf{r};\mathbf{R})\rangle\,|\chi_{k,\nu}(\mathbf{R})\rangle\,. \tag{B.13}$$

$E_k(\mathbf{R})$ is the adiabatic potential energy surface associated with electronic state k and is the effective potential experienced by the nuclei.

Finally we address the validity of the Born-Oppenheimer approximation. Perturbation theory tells us that the nonadiabatic coupling (Equation B.9) can be safely neglected provided that the matrix elements $\langle\Psi_j|\,\Theta_{jk}\,|\Psi_k\rangle$ are much smaller than the energy difference $E_j - E_k$ between the electronic states. The Born-Oppenheimer approximation therefore breaks down in situations where

(i) the adiabatic potential energy surfaces of different electronic states approach each other or intersect, or

(ii) the electronic wavefunction changes rapidly as a function of the nuclear coordinates.

For example situation (i) is encountered at a conical intersection whilst situation (ii) occurs during internal conversion.

Appendix C

Normal mode coordinates

The nuclear Hamiltonian can be expressed as

$$H_k(\mathbf{R}) = \sum_i \frac{\mathbf{P}_i^2}{2M_i} + V_k(\mathbf{R}), \tag{C.1}$$

where k labels the electronic states and $V_k(\mathbf{R}) = E_k(\mathbf{R})$ is the nuclear potential, or adiabatic potential energy surface. For simplicity we will work in one dimension, in which case

$$H_k(x) = -\sum_i \frac{\hbar^2}{2M_i}\frac{\partial^2}{\partial x_i^2} + V_k(x). \tag{C.2}$$

For small nuclear motions, we can expand the potential about some equilibrium geometry x_0, giving

$$H_k(x) = -\sum_i \frac{\hbar^2}{2M_i}\frac{\partial^2}{\partial x_i^2} + \frac{1}{2}\sum_{ij}\frac{\partial V_k}{\partial x_i \partial x_j}(x_i - x_{0i})(x_j - x_{0j}) + \ldots, \tag{C.3}$$

where we have set $V_k(x_0) = 0$ without loss of generality. Next, we introduce relative coordinates scaled by the nuclear masses

$$x_i - x_{0i} \to \frac{1}{\sqrt{M_i}}\bar{x}_i \implies \frac{\partial}{\partial x_i} \to \sqrt{M_i}\frac{\partial}{\partial \bar{x}_i} \tag{C.4}$$

giving

$$H_k(\bar{x}) = -\sum_i \frac{\hbar^2}{2}\frac{\partial^2}{\partial \bar{x}_i^2} + \frac{1}{2}\sum_{ij}\mathcal{H}_{ij}\bar{x}_i\bar{x}_j + \ldots, \tag{C.5}$$

where $\mathcal{H}_{ij}$ is the mass-weighted Hessian matrix

$$\mathcal{H}_{ij} = \frac{1}{\sqrt{M_i}\sqrt{M_j}}\frac{\partial V_k}{\partial x_i \partial x_j}. \tag{C.6}$$

We define normal coordinates Q_α through the orthonormal transformation

$$\bar{x}_i = \sum_\alpha D_{\alpha i} Q_\alpha \qquad \mathbf{D}^T\mathbf{D} = \mathbf{1}. \tag{C.7}$$

The transformation matrix $\mathbf{D}$ is the matrix of eigenvectors of $\mathcal{H}$. The diagonal eigenvalue matrix $\mathbf{w}$ is defined by

$$\mathbf{D}\mathcal{H}\mathbf{D}^T = \mathbf{w} \tag{C.8}$$

and we will write its elements as

$$w_{\alpha\beta} = \omega_\alpha^2 \delta_{\alpha\beta}, \tag{C.9}$$

where, as we shall see shortly, ω_α are the frequencies of the normal modes. The eigenvectors of $\mathcal{H}$ are orthonormal and so

$$\sum_i \frac{\partial^2}{\partial \bar{x}_i^2} = \sum_\alpha \frac{\partial^2}{\partial Q_\alpha^2} \tag{C.10}$$

allowing us to write the nuclear Hamiltonian in terms of the normal mode coordinates as

$$H_k(Q_k) = \frac{1}{2}\sum_\alpha \left(P_\alpha^2 + \omega_{k,\alpha}^2 Q_{k,\alpha}^2\right), \tag{C.11}$$

which corresponds to that of a set of quantum harmonic oscillators of unit mass. We recall that the eigenvalues of each mode are given by

$$E_{k,\alpha}^\nu = \left(\nu + \frac{1}{2}\right)\hbar\omega_{k,\alpha} \tag{C.12}$$

for vibrational quantum numbers $\nu = 0, 1, 2, \ldots$ and the wavefunctions by

$$\chi_{k,\alpha}^\nu(Q_{k,\alpha}) = \frac{1}{\sqrt{2^\nu \nu!}}\left(\frac{\omega_{k,\alpha}}{\pi\hbar}\right)^{\frac{1}{4}} \exp\left(-\frac{\omega_{k,\alpha}Q_{k,\alpha}^2}{2\hbar}\right) H_\nu\left(\sqrt{\frac{\omega_{k,\alpha}}{\hbar}}Q_{k,\alpha}\right), \tag{C.13}$$

where H_ν are the Hermite polynomials,

$$H_\nu(z) = (-1)^\nu e^{z^2}\frac{d^\nu}{dz^\nu}\left(e^{-z^2}\right). \tag{C.14}$$

Appendix D

Herzberg-Teller intensity borrowing

Consider the dipole matrix element for spin-allowed transitions between adiabatic Born-Oppenheimer states

$$\mu_{mn,\nu\nu'} = \langle \Psi_{m,\nu} | \, \mathbf{p} \cdot \hat{\epsilon} \, | \Psi_{n,\nu'} \rangle = \langle \chi_{m,\nu} | \, \mu^e_{mn} \, | \chi_{n,\nu'} \rangle \, . \tag{D.1}$$

Expanding to first order about some equilibrium geometry Q_0 we find

$$\mu_{mn,\nu\nu'} = \mu^e_{mn}(Q_0) \, \langle \chi_{m,\nu} | \chi_{n,\nu'} \rangle + \sum_\alpha \left(\frac{\partial \mu^e_{mn}}{\partial Q_\alpha} \right)_{Q_0} \langle \chi_{m,\nu} | \, Q_\alpha \, | \chi_{n,\nu'} \rangle + \ldots \tag{D.2}$$

Transitions from $|\Psi_{n,\nu'}\rangle$ to $|\Psi_{m,\nu}\rangle$ are formally dipole-forbidden if $\mu^e_{mn}(Q_0) = 0$. Recalling that

$$\mu^e_{mn} = \langle \psi_m | \, \mathbf{p} \cdot \hat{\epsilon} \, | \psi_n \rangle = \langle \psi_m | \, p \, | \psi_n \rangle \, , \tag{D.3}$$

we can evaluate the derivative of the electronic dipole matrix element using the chain rule

$$\left(\frac{\partial \mu^e_{mn}}{\partial Q_\alpha} \right)_{Q_0} = \left(\langle \psi_m | \, p \, | \frac{\partial \psi_n}{\partial Q_\alpha} \rangle + \langle \frac{\partial \psi_m}{\partial Q_\alpha} | \, p \, | \psi_n \rangle \right)_{Q_0} \tag{D.4}$$

In order to evaluate the derivatives of the wavefunctions, we turn to perturbation theory. Consider the action of a normal mode Q_α acting as a perturbation to the Hamiltonian. To first order, we have

$$H = H(Q_0) + \sum_\alpha \left(\frac{\partial H_{el-nuc}}{\partial Q_\alpha} \right)_{Q_0} Q_\alpha \tag{D.5}$$

where we have noted that only the Hamiltonian corresponding to Coulomb repulsion between the electrons and nuclei is perturbed by vibrational motion.

We can therefore write the perturbed electronic wavefunctions as

$$|\psi_n\rangle = |\psi_n\rangle (Q_0) + \sum_{\alpha} \sum_{i \neq n} \left(\frac{\langle \psi_i | \frac{\partial H_{el-nuc}}{\partial Q_\alpha} |\psi_n\rangle}{E_i - E_n} \right)_{Q_0} |\psi_i\rangle Q_\alpha \tag{D.6}$$

Allowing us to identify the derivative of the wavefunction

$$\left(\frac{\partial \psi_n}{\partial Q_\alpha} \right)_{Q_0} = \sum_{i \neq n} \left(\frac{\langle \psi_i | \frac{\partial H_{el-nuc}}{\partial Q_\alpha} |\psi_n\rangle}{E_i - E_n} \right)_{Q_0} |\psi_i\rangle . \tag{D.7}$$

If we assume that ψ_m represents the electronic ground state, we can neglect the term $\frac{\partial \psi_m}{\partial Q_\alpha}$ in equation D.4 because the energy denominators in equation D.7 will always be large[75]. Substituting equations D.4 and D.7 into equation D.2, we arrive at the following expression for the Herzberg-Teller dipole matrix element

$$\mu_{mn,\nu\nu'} = \sum_{\alpha} \sum_{i \neq n} \mu^e_{mi}(Q_0) \left(\frac{\langle \psi_i | \frac{\partial H_{el-nuc}}{\partial Q_\alpha} |\psi_n\rangle}{E_i - E_n} \right)_{Q_0} \langle \chi_{m,\nu} | Q_\alpha | \chi_{n,\nu'} \rangle . \tag{D.8}$$

Appendix E

Supplementary information for Chapter 4

E.1 Transient absorption of diF-TES-ADT

Figure E.1a shows transient absorption (TA) spectra of a dilute solution of diF-TES-ADT (1×10^{-4} M in anhydrous toluene, sealed under nitrogen atmosphere inside a 1 mm path length quartz cuvette). All excited state absorption, ground state bleach and stimulated emission features decay mono-exponentially with a time constant of ∼12 ns (Figure E.1b). They are therefore assigned to the singlet exciton.

Figure E.1c shows TA spectra of a diF-TES-ADT thin film. The spectra are broadly similar to those found in dilute solution, yet now there are spectral changes with time, indicating that more than one species is present (for example, compare 430 nm with 495 nm at 1 ps and 1 ns). To begin with everything decays with a time constant of 100 ps (Figure E.1d); this is attributed to singlet fission which rapidly depletes the singlet exciton population[74]. We speculate that a longer lived species evident at 495 nm arises from triplet-pairs. Note that the oscillations in the TA spectra present in the NIR arise from optical interference effects related to the encapsulating glass coverslip.

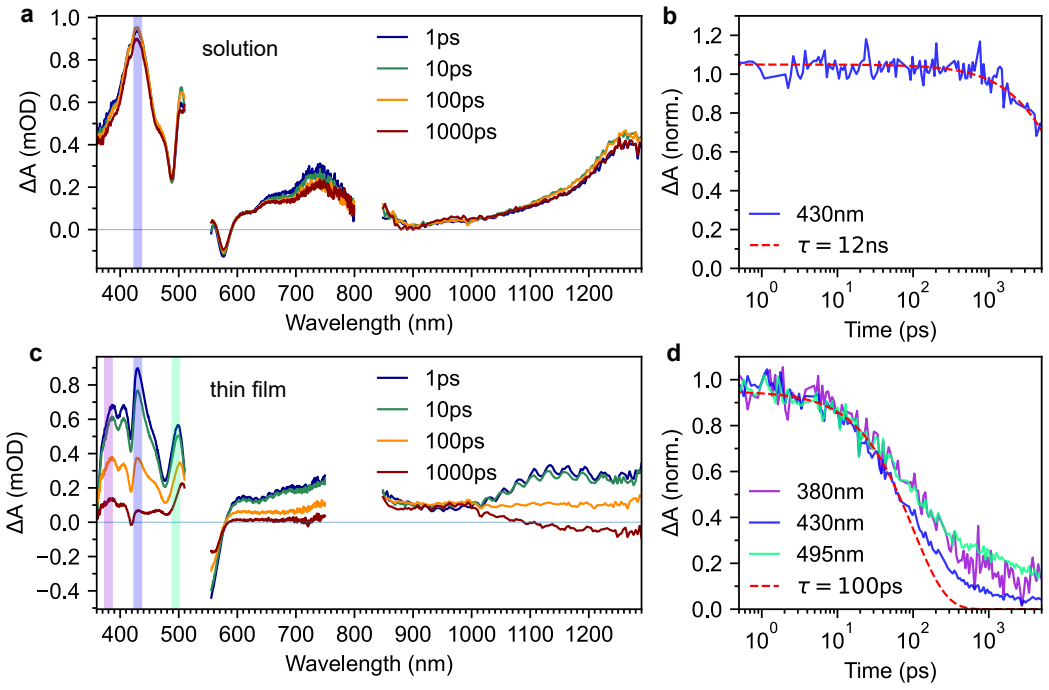

Figure E.1 | Transient absorption spectroscopy of diF-TES-ADT. **a**, TA spectra of dilute solution. **b**, Dynamics at 430 nm, corresponding to the singlet exciton. **c**, TA spectra of a diF-TES-ADT thin film. **d**, TA dynamics captured at various wavelengths (indicated by coloured bars in (**c**)), showing fast singlet fission (100 ps) followed by longer lived triplet-pairs (evident at 495 nm). Note that the spectral region around 532 nm has been removed due to pump scatter.

E.2 TRPL datasets for diF-TES-ADT

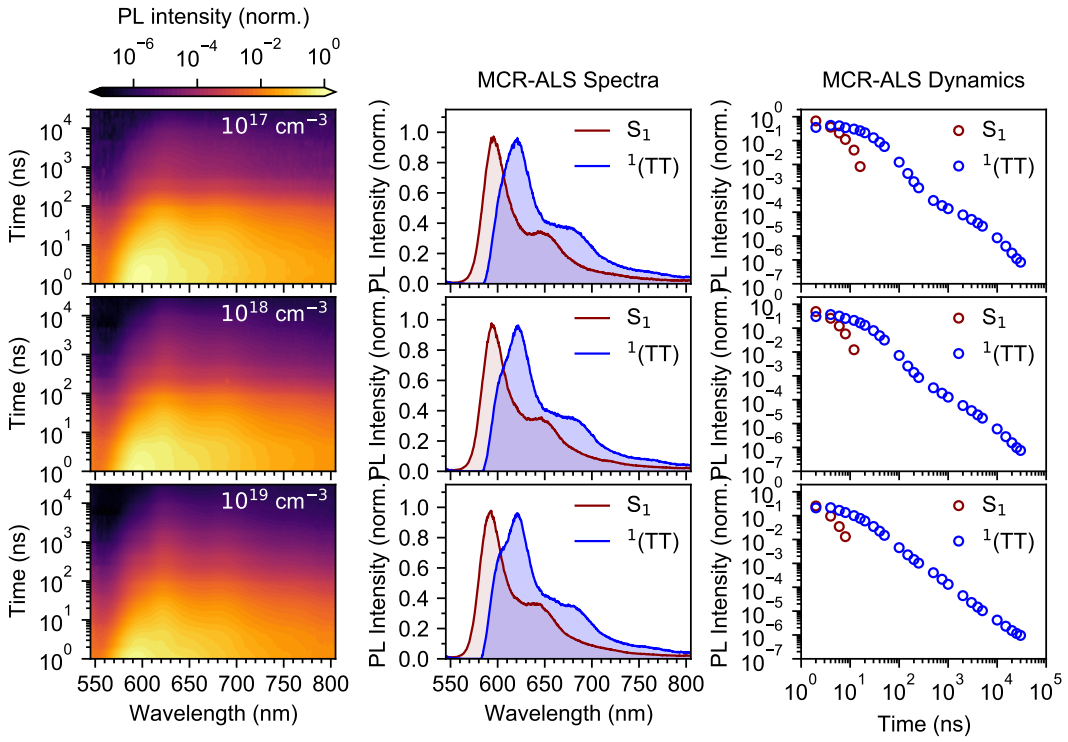

Figure E.2 | diF-TES-ADT TRPL at 77 K. 2D maps of the normalised TRPL data are shown in the left column, extracted spectra in the central column and extracted dynamics, normalised at 4 ns, in the right column. Initial exciton density varies from 10^{17}cm^{-3} (top row) through 10^{18}cm^{-3} (middle row) to 10^{19}cm^{-3} (bottom row).

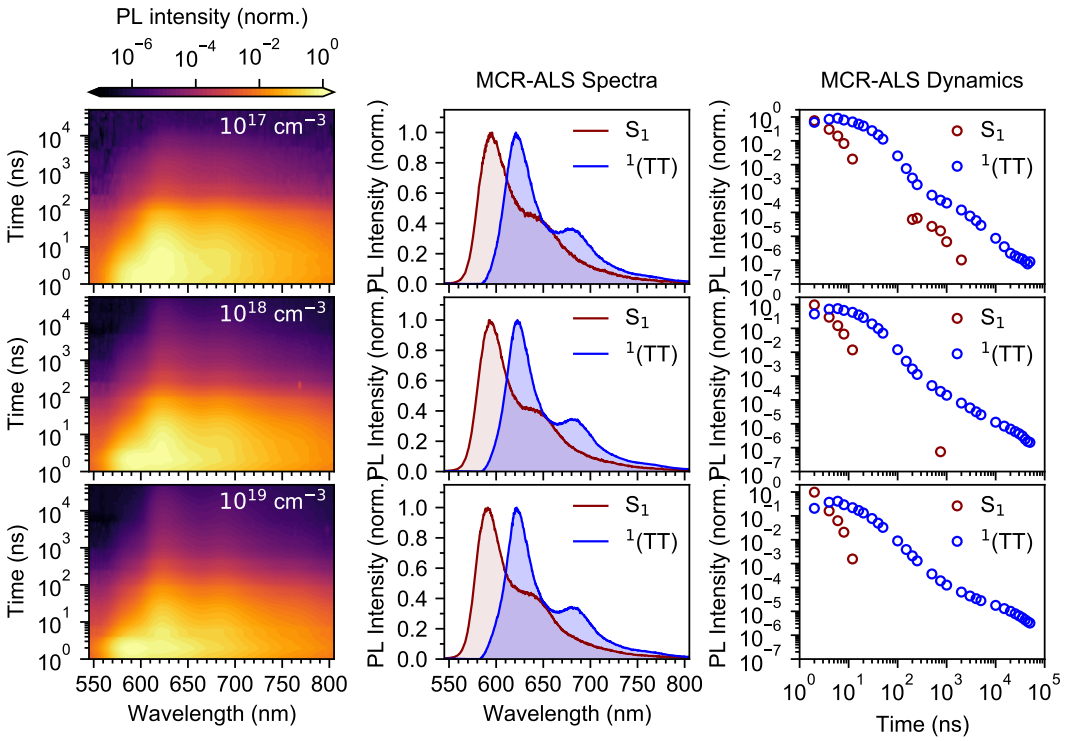

Figure E.3 | diF-TES-ADT TRPL at 100 K. 2D maps of the normalised TRPL data are shown in the left column, extracted spectra in the central column and extracted dynamics, normalised at 4 ns, in the right column. Initial exciton density varies from 10^{17}cm^{-3} (top row) through 10^{18}cm^{-3} (middle row) to 10^{19}cm^{-3} (bottom row).

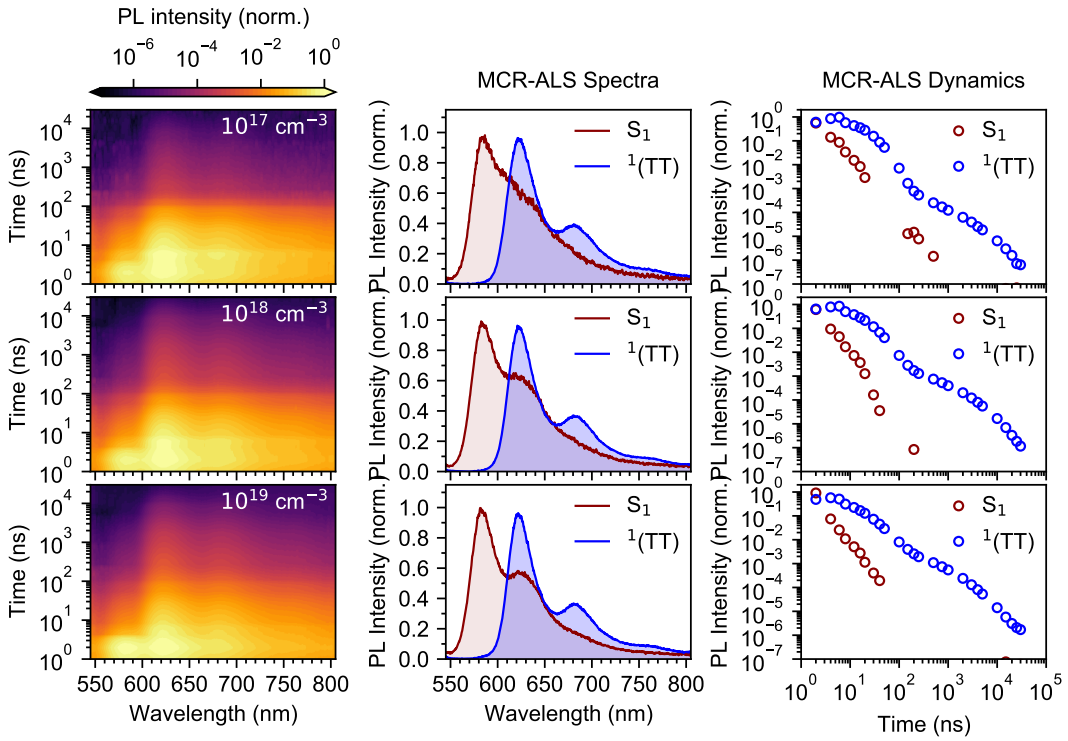

Figure E.4 | diF-TES-ADT TRPL at 150 K. 2D maps of the normalised TRPL data are shown in the left column, extracted spectra in the central column and extracted dynamics, normalised at 4 ns, in the right column. Initial exciton density varies from 10^{17}cm^{-3} (top row) through 10^{18}cm^{-3} (middle row) to 10^{19}cm^{-3} (bottom row).

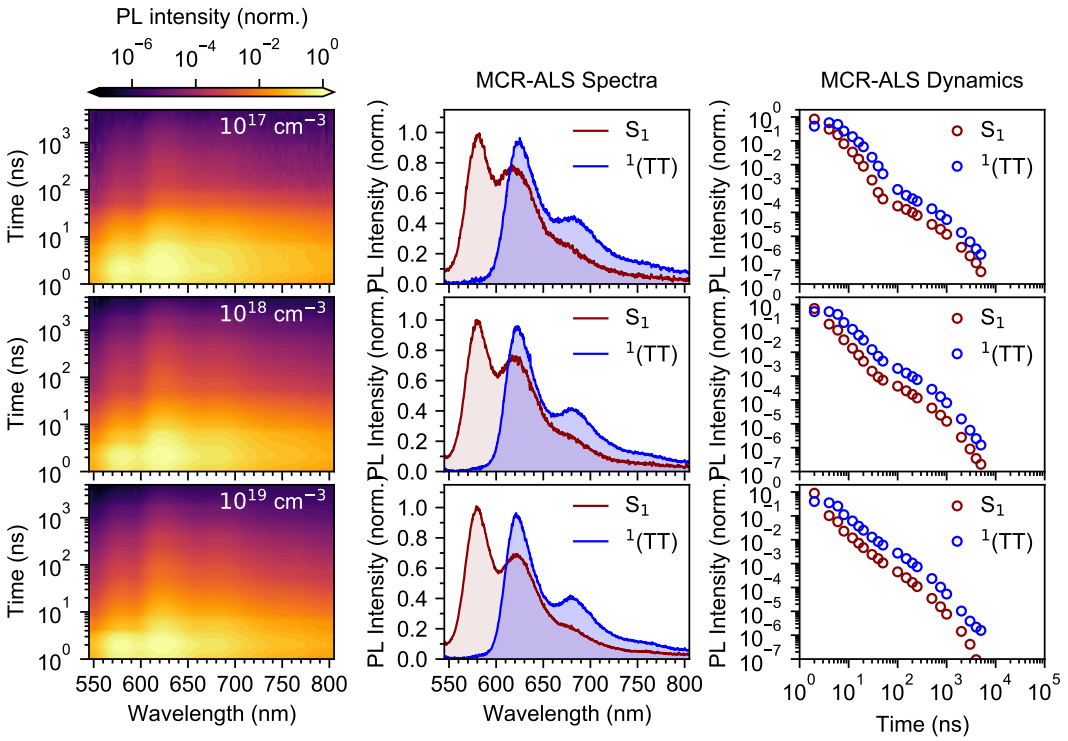

Figure E.5 | diF-TES-ADT TRPL at 200 K. 2D maps of the normalised TRPL data are shown in the left column, extracted spectra in the central column and extracted dynamics, normalised at 4 ns, in the right column. Initial exciton density varies from 10^{17}cm^{-3} (top row) through 10^{18}cm^{-3} (middle row) to 10^{19}cm^{-3} (bottom row).

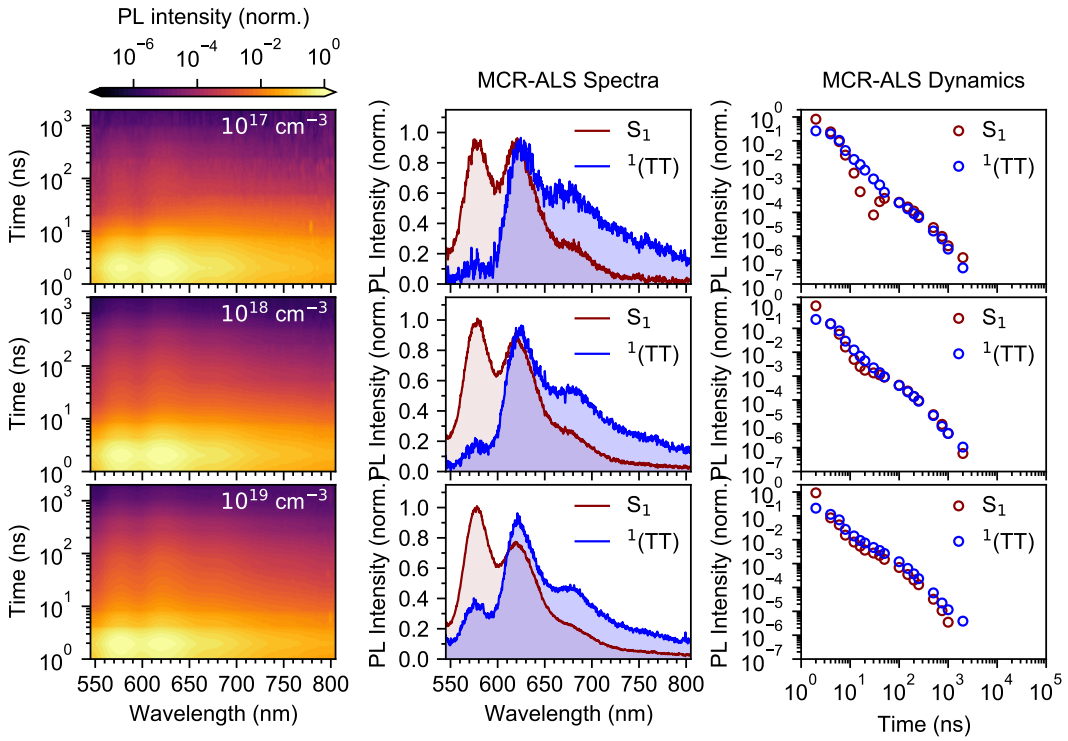

Figure E.6 | diF-TES-ADT TRPL at 250 K. 2D maps of the normalised TRPL data are shown in the left column, extracted spectra in the central column and extracted dynamics, normalised at 4 ns, in the right column. Initial exciton density varies from 10^{17}cm^{-3} (top row) through 10^{18}cm^{-3} (middle row) to 10^{19}cm^{-3} (bottom row).

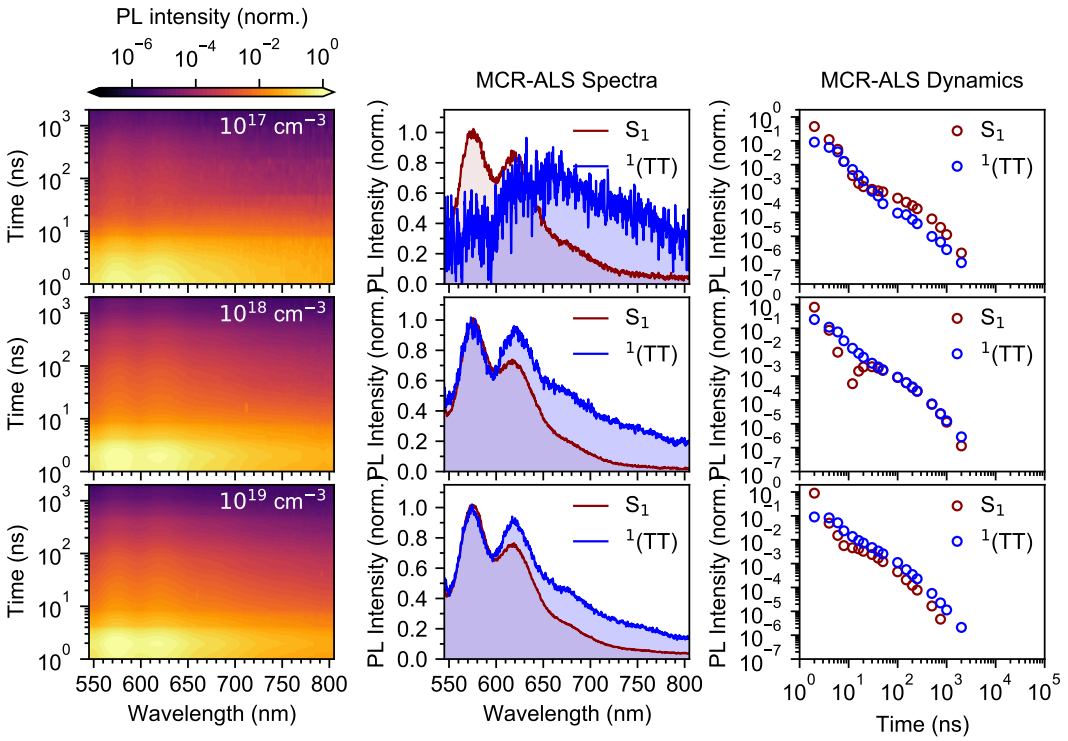

Figure E.7 | diF-TES-ADT TRPL at 291 K. 2D maps of the normalised TRPL data are shown in the left column, extracted spectra in the central column and extracted dynamics, normalised at 4 ns, in the right column. Initial exciton density varies from 10^{17}cm^{-3} (top row) through 10^{18}cm^{-3} (middle row) to 10^{19}cm^{-3} (bottom row).

E.3 Kinetic modelling for diF-TES-ADT

E.3.1 The Merrifield model

The most well known kinetic model of singlet fission was originally proposed by Johnson and Merrifield in 1970 in order to explain the changes in prompt and delayed luminescence with applied magnetic field in anthracene crystals[102]. The model is described in detail in Section 2.6.1. The rates equations for the Merrifield model can be written as follows:

$$\frac{d[\mathrm{S_1}]}{dt} = -\left(k_{sf}\sum_{l=1}^{9}|C_S^l|^2 + k_{snr}\right)[\mathrm{S_1}] + k_{-sf}\sum_{l=1}^{9}|C_S^l|^2[(\mathrm{TT})^l] \tag{E.1}$$

$$\begin{aligned}\frac{d[(\mathrm{TT})^l]}{dt} &= k_{sf}|C_S^l|^2[\mathrm{S_1}] - \left(k_{-sf}|C_S^l|^2 + k_{hop} + k_{ttnr}\right)[(\mathrm{TT})^l] \\ &\quad + \frac{1}{9}k_{tta}[\mathrm{T_1}]^2\end{aligned} \tag{E.2}$$

$$\frac{d[\mathrm{T_1}]}{dt} = 2k_{hop}\sum_{l=1}^{9}[(\mathrm{TT})^l] - 2k_{tta}[\mathrm{T_1}]^2 - k_{tnr}[\mathrm{T_1}] \tag{E.3}$$

Triplet-pair states can dissociate through k_{hop} to form pairs of free triplets which can subsequently annihilate with rate k_{tta} to re-form the triplet-pairs. This is a bimolecular, non-geminate process. Note that this process will populate the 9 triplet pair states with equal probability. Finally, the model includes decay of the excited states to the ground state through k_{snr}, k_{ttnr} and k_{tnr}, which in practice are the sum of the radiative and non-radiative rates.

We again highlight that one of the key assumptions underlying this model is that there is no electronic interaction between the triplets comprising each of the $(\mathrm{TT})^l$ states. We cannot therefore directly apply this model to datasets in which we clearly measure PL from two distinct singlet states, $\mathrm{S_1}$ and $^1(\mathrm{TT})$. To start, therefore, we take the same approach as for pentacene (see main text). We use simple 3-state models that explicitly include $^1(\mathrm{TT})$. Finding these to be inadequate, and since we also wish to simulate magnetic field effects, we subsequently make modifications to Merrifield's model and find that simply by explicitly including $^1(\mathrm{TT})$ as an intermediate between $\mathrm{S_1}$ and $(\mathrm{T...T})^l$, where $(\mathrm{T...T})^l$ are identical to Merrifield's $(\mathrm{TT})^l$, we are able to obtain a quantitative description of our full temperature- and excitation density-dependent TRPL (Figure 4.11), as well as the room-temperature magnetic field effect (Figure 4.12).

E.3.2 Simple 3-state models are insufficient for diF-TES-ADT

Figure E.8a shows a schematic diagram of a simple 3-state model similar to that used to describe the excited-state dynamics in pentacene single crystals (see main text). The rate equations are as follows:

$$\frac{d[\mathrm{S_1}]}{dt} = -(k_{sf} + k_{snr})[\mathrm{S_1}] + k_{-sf}[^1(\mathrm{TT})] \tag{E.4}$$

$$\frac{d[^1(\mathrm{TT})]}{dt} = k_{sf}[\mathrm{S_1}] - (k_{-sf} + k_{ttnr} + k_{hop})[^1(\mathrm{TT})] + k_{tta}[\mathrm{T_1}]^2 \tag{E.5}$$

$$\frac{d[\mathrm{T_1}]}{dt} = k_{hop}[^1(\mathrm{TT})] - 2k_{tta}[\mathrm{T_1}]^2 - k_{tnr}[\mathrm{T_1}] \tag{E.6}$$

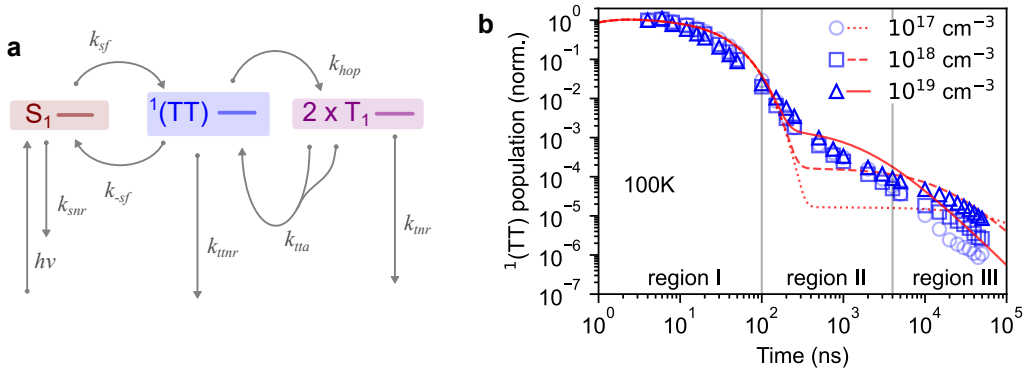

Figure E.8 | Merrifield model and diF-TES-ADT at 100 K. **a**, Schematic diagram of the kinetic model. **b**, The simulated ^{1}(TT) population (red lines) fails to capture the 3 distinct regions of measured emission dynamics. The onset of excitation-dependence occurs immediately after the mono-exponential decay of region I, i.e. the model cannot simulate region II.

Figure E.8b shows the result of attempting to fit this model to the measured decay of the ^{1}(TT) emission. Naturally, the initial portion of the data can be explained, however the model fails to capture the dynamics beyond 100 ns. Indeed, we find that it is only possible to generate regions I and III using this model, i.e. the initial exponential decay of the ^{1}(TT) population and the onset of an exciton density dependence arising from bimolecular TTA.

We suggest that the reason for the poor performance of the model is due to its inherent inability to consider geminate, monomolecular TTA as well as the non-geminate, bimolecular process. Put another way, with only a single 'triplet-pair' species explicitly included in the equations, there is no way to keep track of triplet-pairs that never fully separate. In this model, once ^{1}(TT) has separated to form two free triplets, any information regarding the origin of those two triplets is lost.

The simplest way to mimic the effect of geminate TTA might be to include a monomolecular pathway from free triplets to ^{1}(TT). Thus we add the process $T_1 + T_1 \rightarrow {}^1(TT)$ to the kinetic scheme, but with a rate k_{-hop} that depends only linearly on the free triplet population (Figure E.9a). The rate equations become:

$$\frac{d[S_1]}{dt} = -(k_{sf} + k_{snr})[S_1] + k_{-sf}[^1(TT)] \tag{E.7}$$

$$\frac{d[^1(TT)]}{dt} = k_{sf}[S_1] - (k_{-sf} + k_{ttnr} + k_{hop})[^1(TT)] + k_{-hop}[T_1] + k_{tta}[T_1]^2 \tag{E.8}$$

$$\frac{d[T_1]}{dt} = k_{hop}[^1(TT)] - 2k_{tta}[T_1]^2 - (2k_{-hop} + k_{tnr})[T_1] \tag{E.9}$$

Applying this scheme to our data, we find that, just as for the first model, it is unable to reproduce the dynamics beyond 100 ns (Figure E.9b). It would seem that simply including a monomolecular pathway from free triplets to triplet-pairs is not a reasonable approximation to geminate recombination.

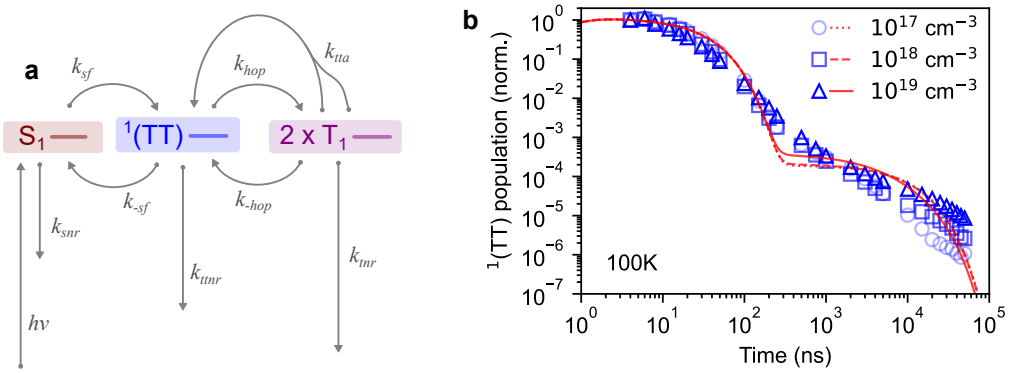

Figure E.9 | 3-state kinetic models cannot describe diF-TES-ADT at 100 K. **a**, Schematic diagram of the kinetic model: the same as above but including a monomolecular triplet recombination pathway. **b**, The simulated ^{1}(TT) population (red lines) still fails to capture the 3 distinct regions of measured emission dynamics. Together with Figure E.8, this suggests that an additional excited state species is required in the kinetic scheme in order to successfully reproduce the excited state dynamics.

E.3.3 Spin-lattice relaxation has little effect

We can remove the process of spin-lattice relaxation in order to see how much of an effect this has on the model's ability to reproduce the experimental data. The fitted results are shown in Figure E.10a. The quality of the fit is almost unchanged, despite having one less parameter to vary.

The temperature dependencies of the rate constants (Figure E.10b), are also very similar. The principal difference is the value of k_{tta} at 77 K. Since complete separation of triplet-pairs is largely suppressed at this temperature (lack of exciton density dependence in the dynamics) the rate of free triplet annihilation is in any case not well defined.

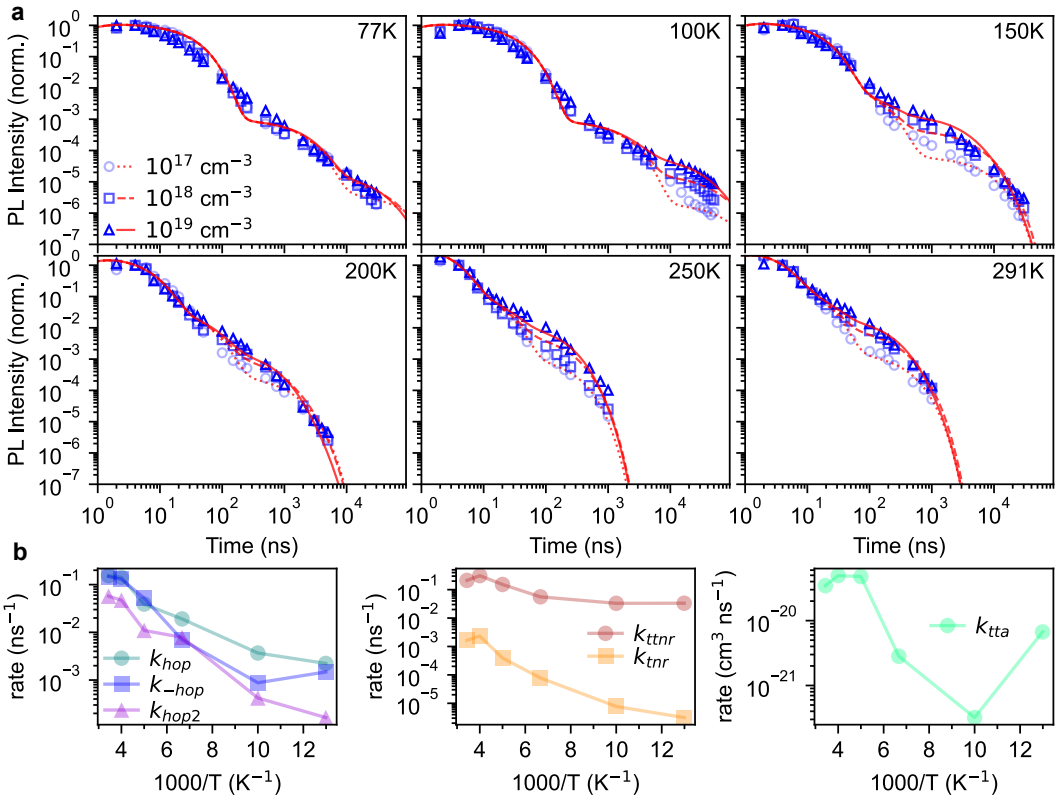

Figure E.10 | Spin-lattice relaxation rate has little effect. **b**, Application of the model (red lines) to the TRPL data (blue markers). The model is able to adequately describe the data even with one fewer free parameters. **b**, Extracted rate constants as a function of temperature.

E.3.4 Uncertainty estimation for rate constants

Uncertainty in each rate constant (for the kinetic model presented in Figure 4.9a was estimated by individually varying each one about its optimised (or fixed) value, whilst keeping all others constant and monitoring the effect on a cost function. The cost function, χ, was the same as was minimised during the rate constant optimisation process and was defined as:

$$\chi = \frac{1}{2N} \sum_{i=1}^{N} \left(\log_{10} y_i - \log_{10} f_i \right)^2 \tag{E.10}$$

where $i = 1, 2, ..., N$ runs over every time point at all three exciton densities measured and y_i and f_i are the measured and simulated ^{1}(TT) populations respectively. The normalisation by N is included to allow comparison between cost functions at different temperatures, for which different numbers of time points were measured. The logarithms were taken in order to give equal weight across all timescales measured.

The uncertainty in each rate constant was calculated as the lower and upper values which caused an increase of 20% in the cost function. The choice of 20% as a threshold is of course arbitrary, but it allows for a comparison of the uncertainties between rate constants.

Figures E.11-E.16 on the following two pages illustrate the process for calculating the uncertainty in each rate constant for temperatures of 77 K to 291 K. Black lines show the variation of χ with each rate constant. The dashed horizontal grey line shows the value of the optimized cost function, the solid one shows the 20% threshold. Vertical grey lines indicate the optimised value for each rate constant. Red circles indicate the lower and upper bounds. Note that though shown, k_{sf}, k_{-sf} and k_{snr} were not varied during the optimisation.

Unsurprisingly, given that singlet fission is much faster than our instrument response, we find that the values of k_{sf}, k_{-sf} and k_{snr} have negligible effect on the model output. We further find that k_{relax} has no lower bound for temperatures above 100 K, which is to say that it only has a significant role at low temperature. In contrast, k_{hop}, k_{-hop}, k_{hop2}, k_{tta}, k_{ttnr} and k_{tnr} are generally very tightly constrained. Note that at 77 K there is very little dependence of the ^{1}(TT) decay with excitation density, indicating that complete triplet separation is largely suppressed at this temperature. As a result, k_{hop2} and k_{tta} are relatively poorly constrained at 77 K.

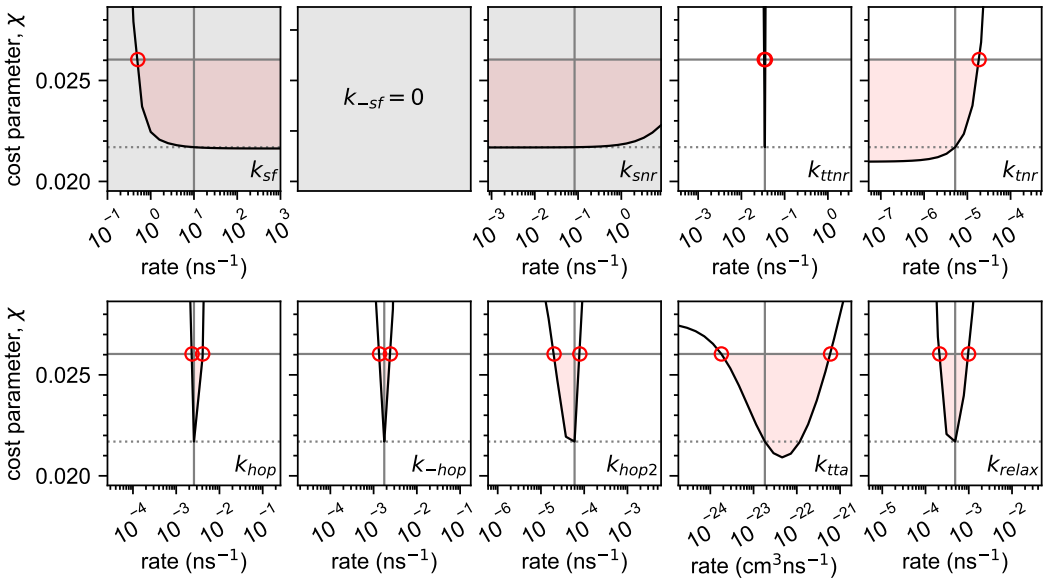

Figure E.11 | Uncertainty estimation for the diF-TES-ADT rate constants at 77 K. Note that k_{-sf} is not included in the analysis since it was set to zero. Grey shading indicates rate constants that were not varied. Each rate constant was individually varied about its optimised value; uncertainty was estimated as the lower and upper values that caused a 20% increase in the cost parameter.

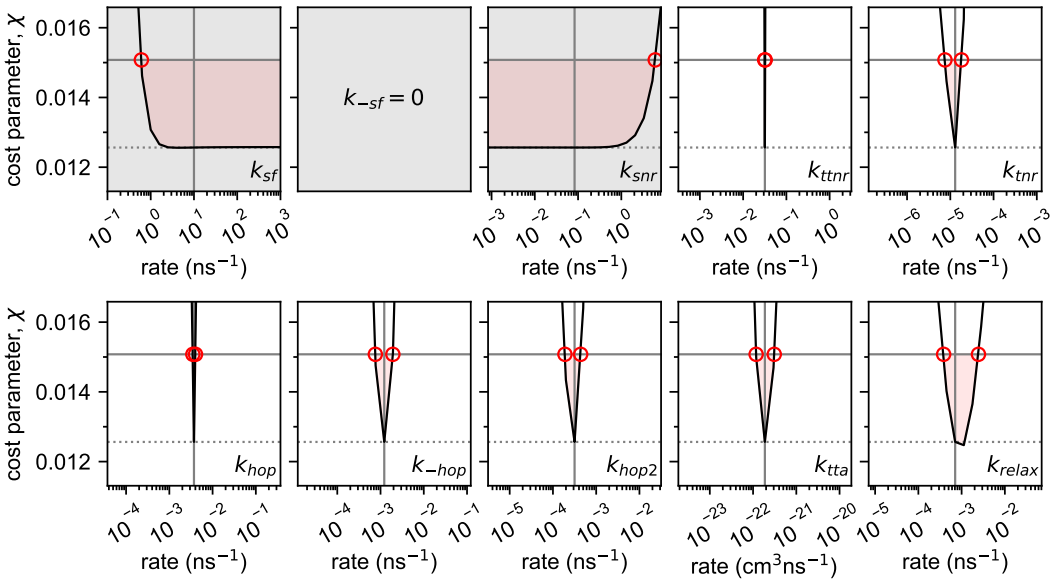

Figure E.12 | Uncertainty estimation for the diF-TES-ADT rate constants at 100 K. Note that k_{-sf} is not included in the analysis since it was set to zero. Grey shading indicates rate constants that were not varied. Each rate constant was individually varied about its optimised value; uncertainty was estimated as the lower and upper values that caused a 20% increase in the cost parameter.

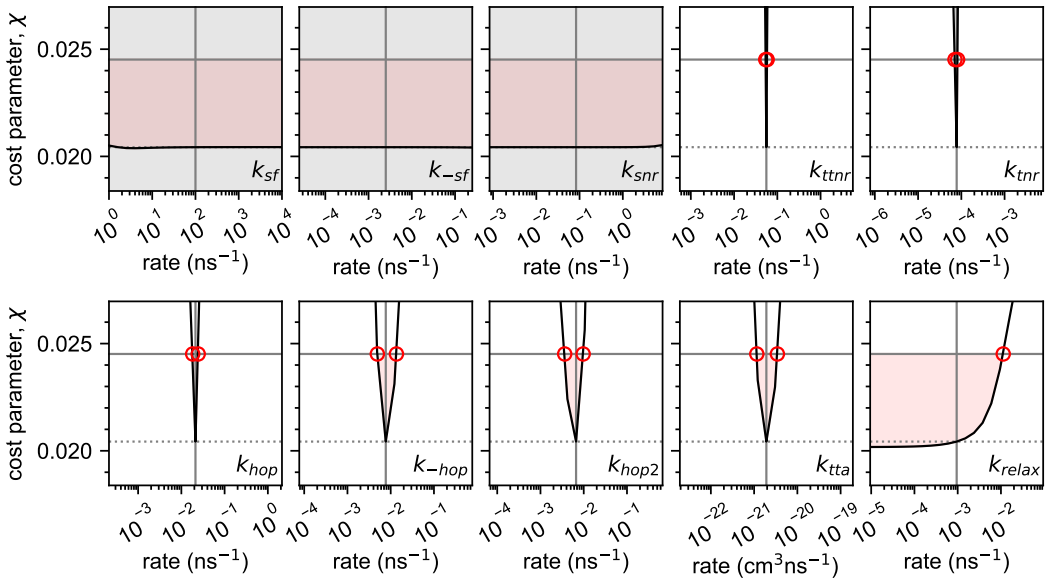

Figure E.13 | Uncertainty estimation for the diF-TES-ADT rate constants at 150 K. Grey shading indicates rate constants that were not varied. Each rate constant was individually varied about its optimised value; uncertainty was estimated as the lower and upper values that caused a 20% increase in the cost parameter.

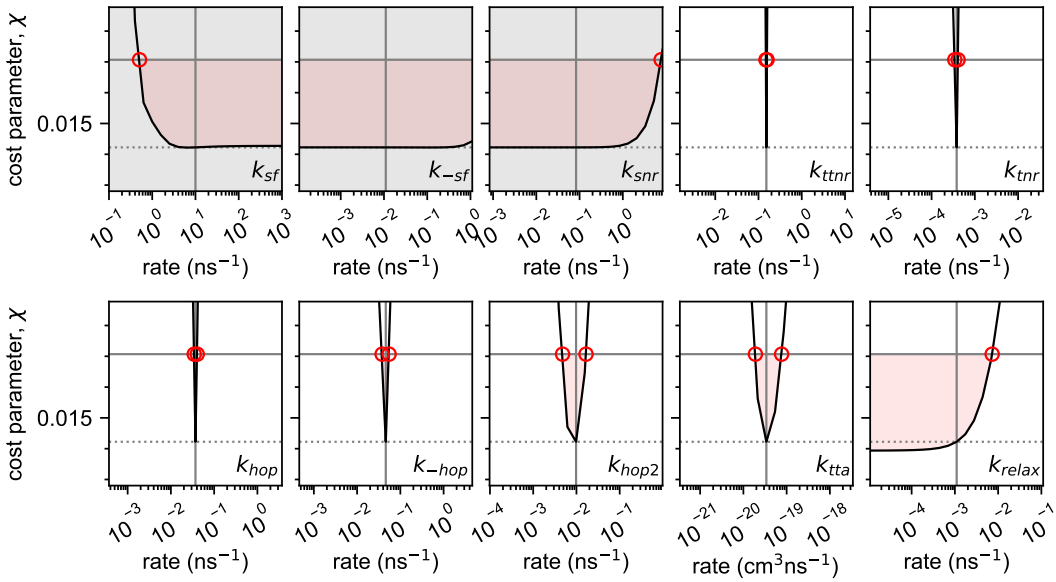

Figure E.14 | Uncertainty estimation for the diF-TES-ADT rate constants at 200 K. Grey shading indicates rate constants that were not varied. Each rate constant was individually varied about its optimised value; uncertainty was estimated as the lower and upper values that caused a 20% increase in the cost parameter.

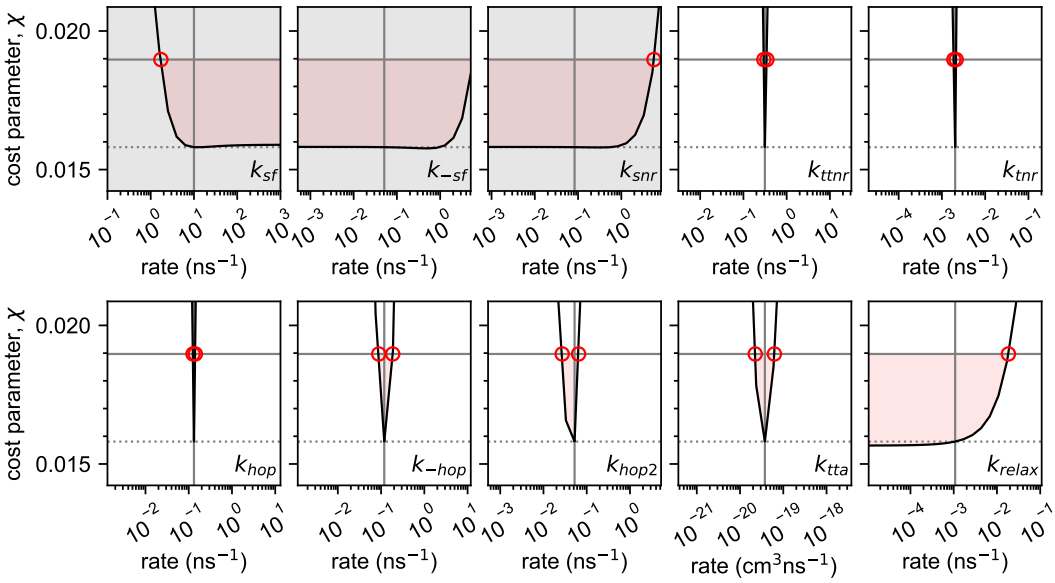

Figure E.15 | Uncertainty in diF-TES-ADT rate constants at 250 K. Grey shading indicates rate constants that were not varied. Each rate constant was individually varied about its optimised value; uncertainty was estimated as the lower and upper values that caused a 20% increase in the cost parameter.

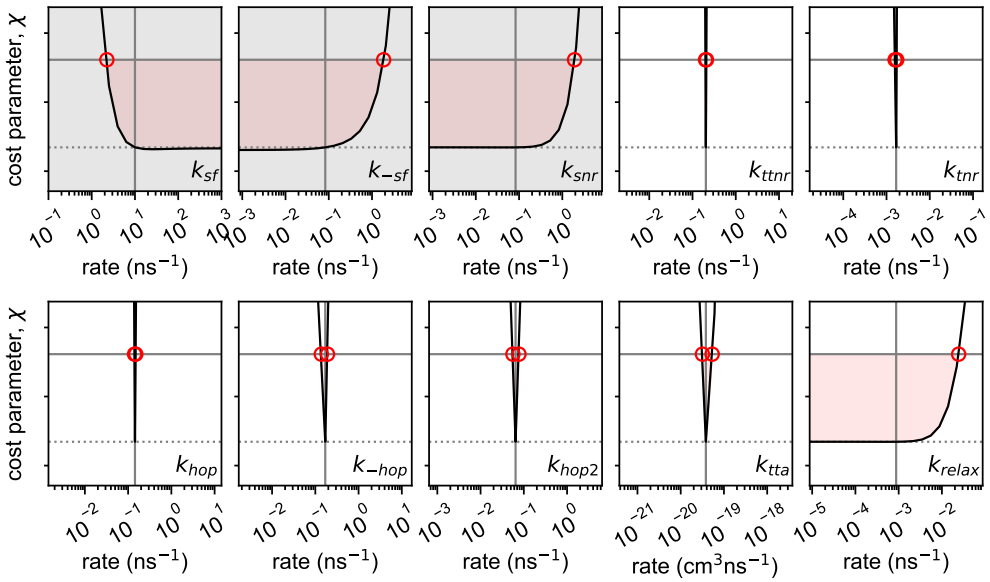

Figure E.16 | Uncertainty estimation for the diF-TES-ADT rate constants at 291 K. Grey shading indicates rate constants that were not varied. Each rate constant was individually varied about its optimised value; uncertainty was estimated as the lower and upper values that caused a 20% increase in the cost parameter.

E.4 Pentacene single crystal PL

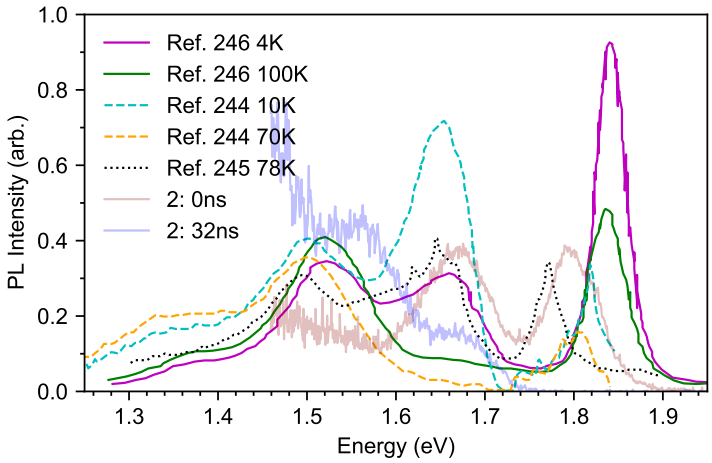

Figure E.17 | Comparison of measured pentacene emission spectra. Our time-gated spectra (faint red and blue lines) are plotted against previously reported steady-state spectra from single crystals[244,245] and high-quality thin films[246]. All the features in our time-resolved data can be found in the literature spectra. Purple and green lines adapted from Reference 246, with the permission of AIP Publishing. Blue and orange dashed lines adapted from Reference 244 with the permission of World Scientific Publishing Co. Black dashed line adapted from Reference 245, with the permission of AIP Publishing.

Figure E.17 shows a comparison of our time-gated spectra with literature steady-state spectra. There are small amounts of variation between the different measurements. Nevertheless, all show the same four emission bands at around 1.85 eV, 1.65 eV, 1.5 eV and 1.35 eV.

E.4.1 Raw data

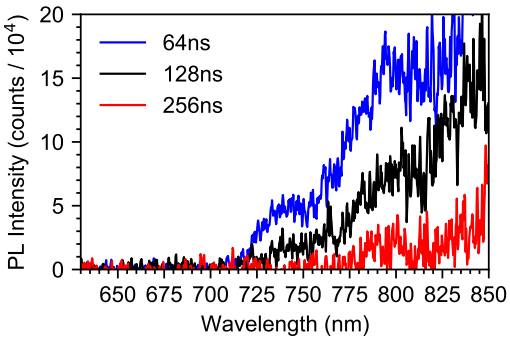

Figure E.18 | Pentacene TRPL on long timescales. Spectra are shown for the last 3 data points in Figure 4.17b, which have the worst signal to noise ratio. The noise in these spectra is reflected in the error bars of Figure 4.17b.

Figure E.18 shows the raw data for the PL kinetics measured on pentacene single crystal **2** at the three longest delay times. These spectra, together with the error bars on the data presented in Chapter 4, give a good idea of the fidelity of the dataset.

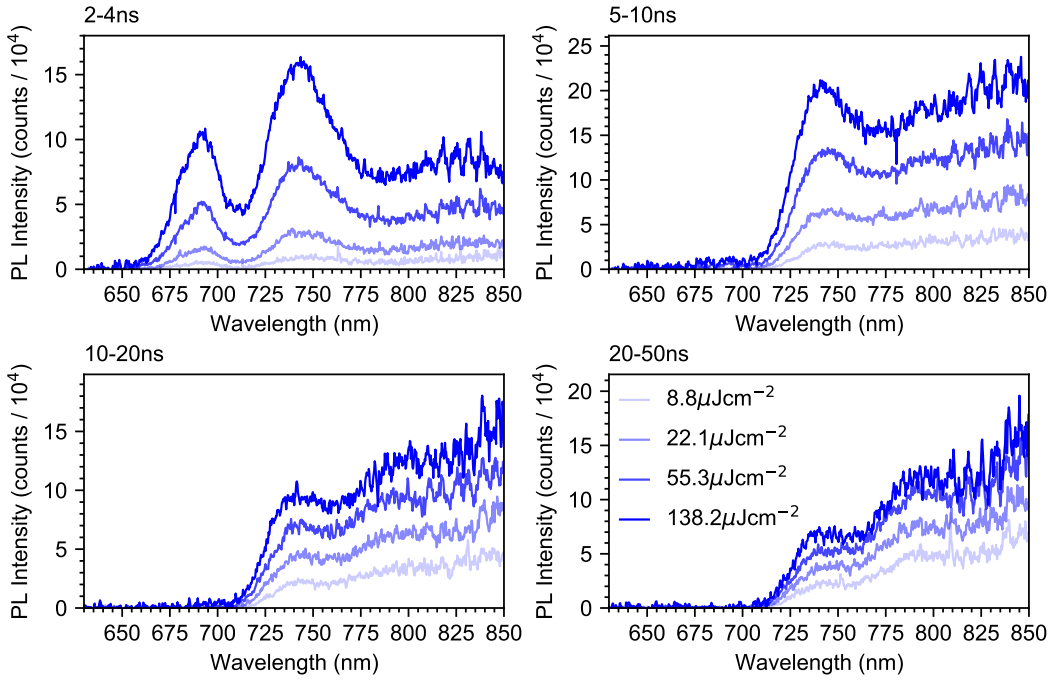

Figure E.19 | Pentacene time-gated fluence dependence. PL spectra as a function of laser pulse energy at delay times of 2–4 ns (**a**), 5–10 ns (**b**), 10–20 ns (**c**) and 20–50 ns (**d**). The good signal to noise ratio of all the spectra is reflected in the small error bars of Figure 4.17c.

Figure E.19 shows the raw data from which the fluence dependence reported in the main text was calculated. The signal to noise ratio at 750 nm is reasonably good for all fluences measured.

Appendix F

Phthalocyanine-sensitised TTA in diF-TES-ADT

We attempted to gain further confirmation that ^{1}(TT) is formed through bimolecular TTA by conducting triplet sensitisation experiments. The aim of these experiments was to add weight to the conclusion that bimolecular TTA does not proceed via S_1. Due to a variety of difficulties, outlined below, the experiments were not nearly as conclusive as we had hoped.

F.1 Methods

The triplet sensitizer palladium (II) octabutoxyphthalocyanine (PdPc - see Section 3.1.2) with triplet energy $E_{T_1} = 1.24\,\text{eV}$ has been shown to effectively sensitise triplets in rubrene ($E_{T_1} = 1.14\,\text{eV}$)[207]. For the case of diF-TES-ADT ($E_{T_1} = 1.08\,\text{eV}$[74]), triplet energy transfer is expected to be exothermic by approximately 160 meV.

Narrowband pump pulses at 725 nm were generated by frequency doubling the 1450 nm output of an optical parameteric amplifier (TOPAS Prime, Light Conversion) seeded with 800 nm pulses from a Ti:Sapphire regenerative amplifier (Solstice, Spectra Physics) in a BBO crystal. These pulses were then passed through a shortpass filter (Schott KG3), to remove residual infrared, an off-axis 750 nm bandpass filter, to spectrally clean the pulses and a 695 nm longpass filter, to ensure that no wavelengths that could directly excite diF-TES-ADT were present in the pulse. Time-gated PL spectra were measured using our iCCD detector (see Section 3.4.1). A 700 nm shortpass filter (FES700, Thorlabs) was used to reduce scattered pump light.

725 nm light is well below the optical gap of diF-TES-ADT, but sufficient to excite the $S_0 \rightarrow S_1$ transition of PdPc. We controlled for 2-photon absorption

by repeating our measurements on a pure diF-TES-ADT film. This turned out to be important: using femtosecond pulses resulted in significant upconverted emission arising from 2-photon absorption even in the pure diF-TES-ADT film. We highlight that upconversion emission from 2-photon absorption can carry the same quadratic intensity dependence as that expected from bimolecular TTA. We therefore passed the 725 nm pump light through a 10 cm quartz rod and 2 m optical fibre to temporally stretch the pulses. As a result of this modification, we were able to measure upconverted emission only in the diF-TES-ADT film doped with PdPc and not in the pure film (Figure F.1b).

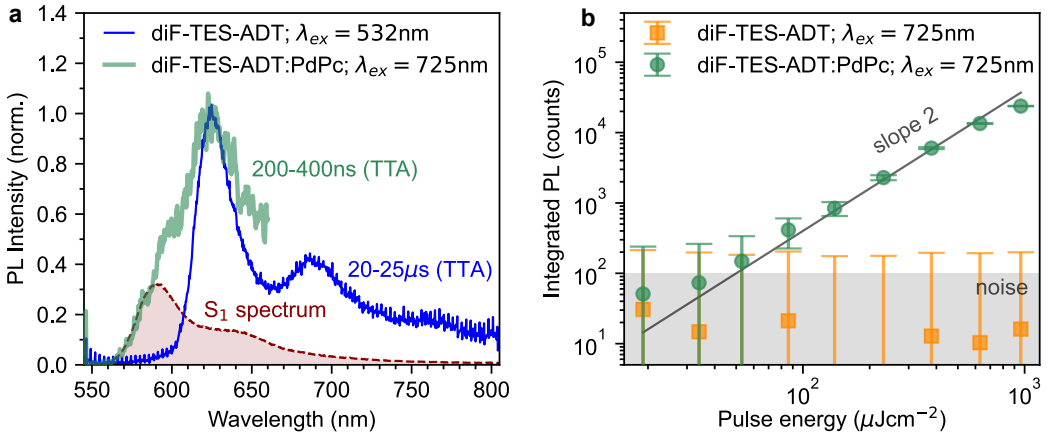

Figure F.1 | Sensitised TTA in diF-TES-ADT. a, Spectrum of upconverted emission (green line) compared to prompt (red dashed line) and delayed (blue line) PL in diF-TES-ADT at 100 K. The upconverted PL contains contributions from both S_1 and ^{1}(TT). The S_1 contribution is likely to arise from exothermic triplet transfer from a sensitiser aggregate onto a neighbouring diF-TES-ADT molecule that has already received a triplet. The excess energy then allows S_1 to be accessed. **b**, The dependence of the upconverted PL on pulse energy shows the expected quadratic relationship. No upconverted PL was observed in pure diF-TES-ADT films allowing us to rule out 2-photon absorption effects.

F.2 Results and discussion

Figure F.1a shows spectra from pure diF-TES-ADT pumped at 532 nm. The prompt emission (red) arises predominantly from S_1, whilst that at 20 µs is from ^{1}(TT) at a time delay where bimolecular TTA dominates (blue). The upconverted emission, gated from 200–400 ns, arising from sensitised TTA (green) contains contributions from both S_1 and ^{1}(TT). Figure F.1b shows the dependence of upconverted emission on laser power. The slope is 2, but no emission was observed for the pure film, confirming that TTA upconversion is the mechanism at play.

The two spectra that arise from TTA are different: in the sensitisation experiment, a small amount of emission from S_1 is present, in addition to the expected ^{1}(TT) emission. This is consistent with the scenario presented in the preceeding section, whereby the annihilation of two triplets forms an S_1 state that subsequently undergoes exciton fission to produce ^{1}(TT). Indeed, running the same model shown in Figure 4.10a, yet starting with an initial population of triplets rather than singlets to mimic the sensitisation, yields an expected 14% contribution of S_1 to the total PL on a timescale of 200–400 ns, similar to the contribution shown in Figure 4.10a. This is similar to what we observe in Figure F.1a.

How, then, does the discrepancy arise between the two 'TTA' spectra (blue and green lines in Figure F.1a)? We propose that different, non-bimolecular TTA events dominate the recombination in the sensitised film. It is well known that porphyrin or phthalocyanine based triplet sensitisers aggregate and undergo phase separation when blended into crystalline films[107,132,363] and that this can be a major problem in solid-state upconversion systems leading to, for example, sensitiser-sensitiser annihilation and triplet quenching[107,132]. It is therefore quite likely that in our film, TTA occurs predominantly at these aggregates and may include contributions from sensitiser-sensitiser and sensitiser-acceptor TTA. In both of these cases, since triplet transfer from PdPc to diF-TES-ADT is exothermic by approximately 160 meV, annihilation events carry more than enough excess energy to enable the ^{1}(TT) $\rightarrow$ S_1 transition, which is thermally activated in diF-TES-ADT, as demonstrated here and in previous work[74].

In an attempt to alleviate this problem of 'hot' TTA, we turned to a different type of triplet sensitiser: inorganic quantum dots (QDs) (sometimes called colloidal semiconductor nanocrystals)[43,364]. Colloidal PbS QDs possessing exceptionally narrow linewidths and with their triplet energies tuned to be equal to or very slightly above that of diF-TES-ADT were synthesised by Philippe Green in the group of Professor Mark Wilson at the University of Toronto, following the methods in their recent publication[206]. We fabricated two types of samples by either (1) blending a small molar fraction of the QDs in solution with diF-TES-ADT before spin coating or (2) spin-coating a thin layer ($\sim$ 5 dots) of QDs onto the substrate and thermally evaporating the same thickness $\sim$ 60 nm of diF-TES-ADT on top, forming a bilayer.

The QD-diF-TES-ADT samples were excited using the 1064 nm fundamental of our sub-ns Q-switched Nd:YVO4 laser (Picolo-AOT, Innolas). The films were maintained at 100 K in the same cryostat-PL setup depicted in Figure 3.8.

However, we were unable to measure any upconverted emission from any of the samples. We suspect that this may be due to very poor triplet transfer from the QD to the diF-TES-ADT, which is well known to be hindered by the oleic acid ligands that are attached to the surface of the QDs[337]. Further experiments using the QDs are ongoing.

Appendix G

Supplementary information for Chapter 5

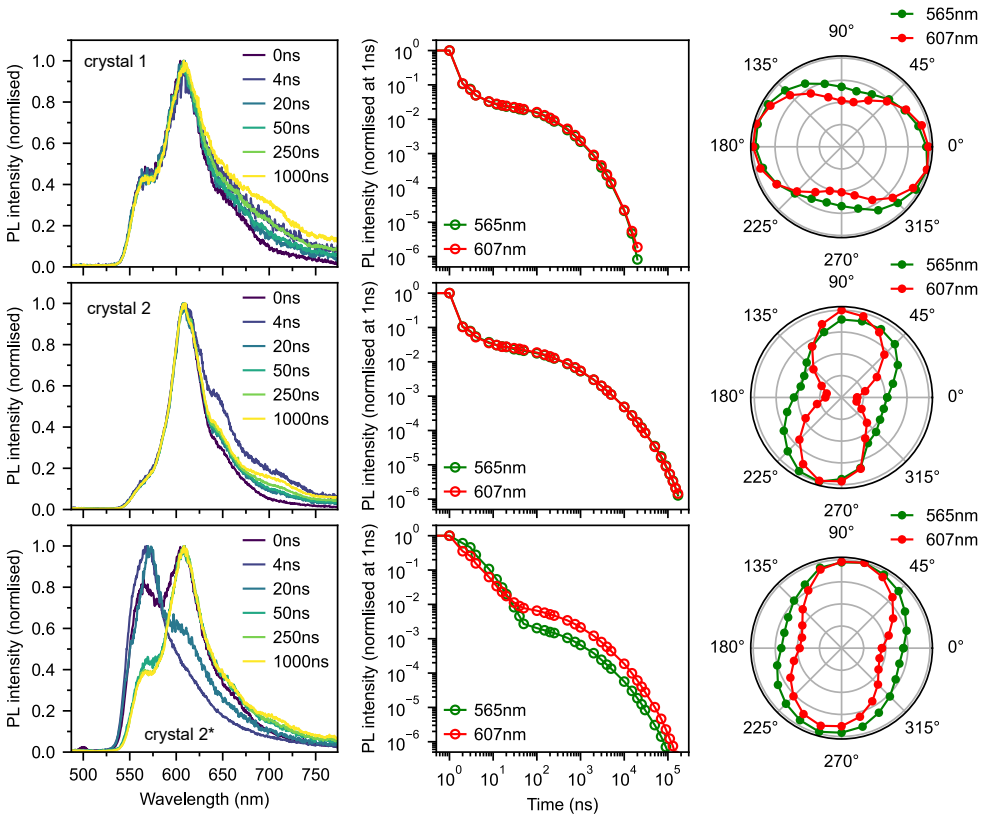

Figure G.1 | Rubrene crystal TRPL with 500 nm excitation. Time-gated PL spectra (left column), TRPL kinetics at 565 nm and 607 nm (middle column) and dependence of quasi steady-state PL intensity (0–2 µs) on detection polariser angle (right column) for crystal 1, crystal 2 and crystal 2* (rows). The excitation wavelength was 500 nm.

Figure G.1 shows the complete time resolved photoluminescence datasets with 500 nm excitation for crystals 1 and 2. Data for crystal 2* (a different

spot on the surface of crystal 2) is also shown. As a control, we also recorded similar datasets using 532 nm excitation; these are shown in Figure G.2. We saw no evidence of different temporal behaviours between 565 nm and 607 nm using 532 nm excitation.

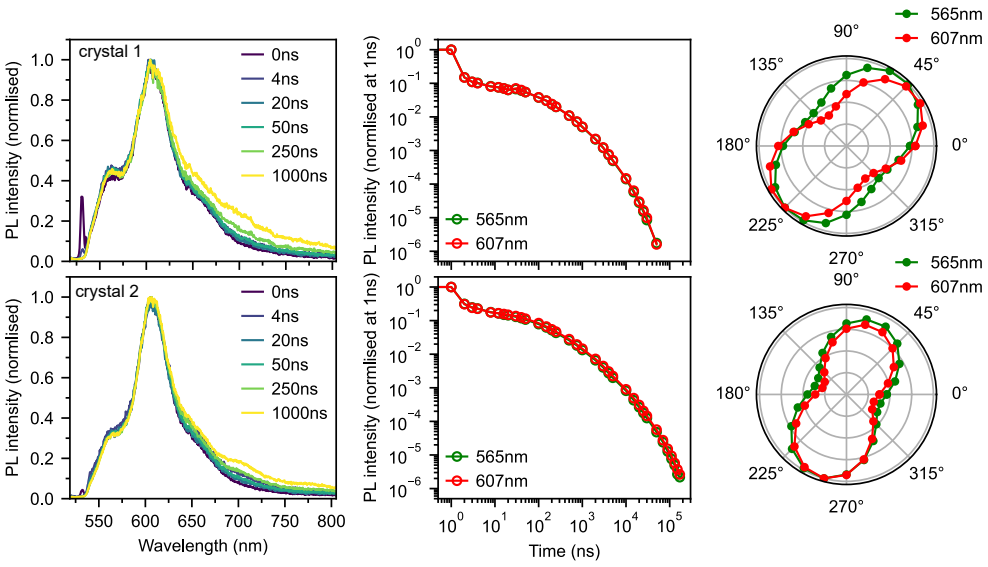

Figure G.2 | Rubrene crystal TRPL with 532 nm excitation. Time-gated PL spectra (left column), TRPL kinetics at 565 nm and 607 nm (middle column) and dependence of quasi steady-state PL intensity (0–2 µs) on detection polariser angle (right column) for crystal 1 and crystal 2 (rows). The excitation wavelength was 532 nm.

Appendix H

Supplementary information for Chapter 6

H.1 Complete transient absorption datasets

Figures H.1-H.5 display the complete transient absorption datasets for crystals 1 and 2 and the polycrystalline film.

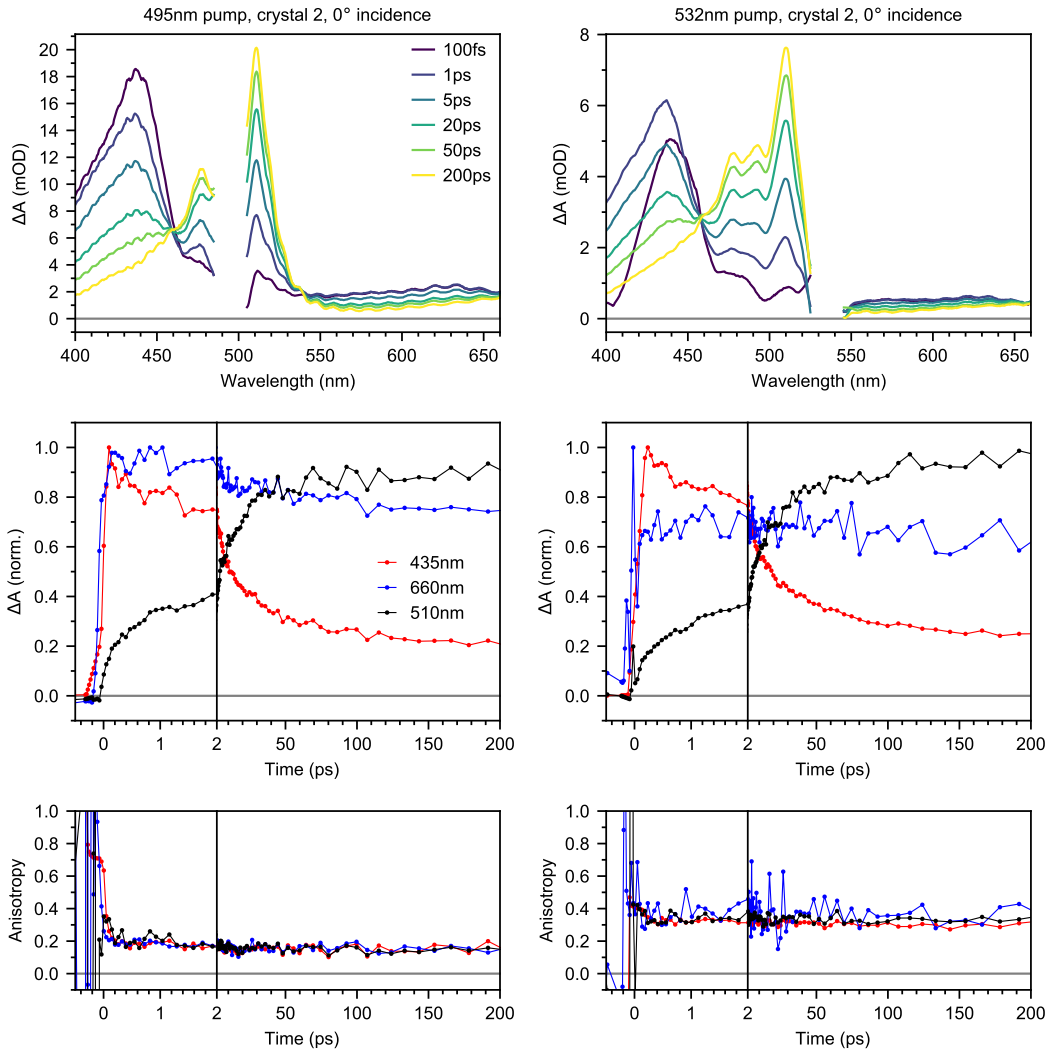

Figure H.1 | TA datasets for crystal 1, 0° incidence. Transient absorption of crystal 1 at 0° incidence, excited with 495 nm and 532 nm pumps (left and right columns respectively). Spectra (top row) show a clear evolution from singlets ($S_1 \rightarrow S_3$ excited state absorption at 435 nm) to triplet-pairs ($T_1 \rightarrow T_3$ excited state absorption at 510 nm). The conversion is approximately one-to-one, evidenced by the isosbestic point at 460 nm. The dynamics (middle row) and anisotropy (bottom row) are shown for probe wavelengths of 435 nm (mostly singlets, some triplets), 660 nm (mixture of singlets and triplets) and 510 nm (almost entirely triplets).

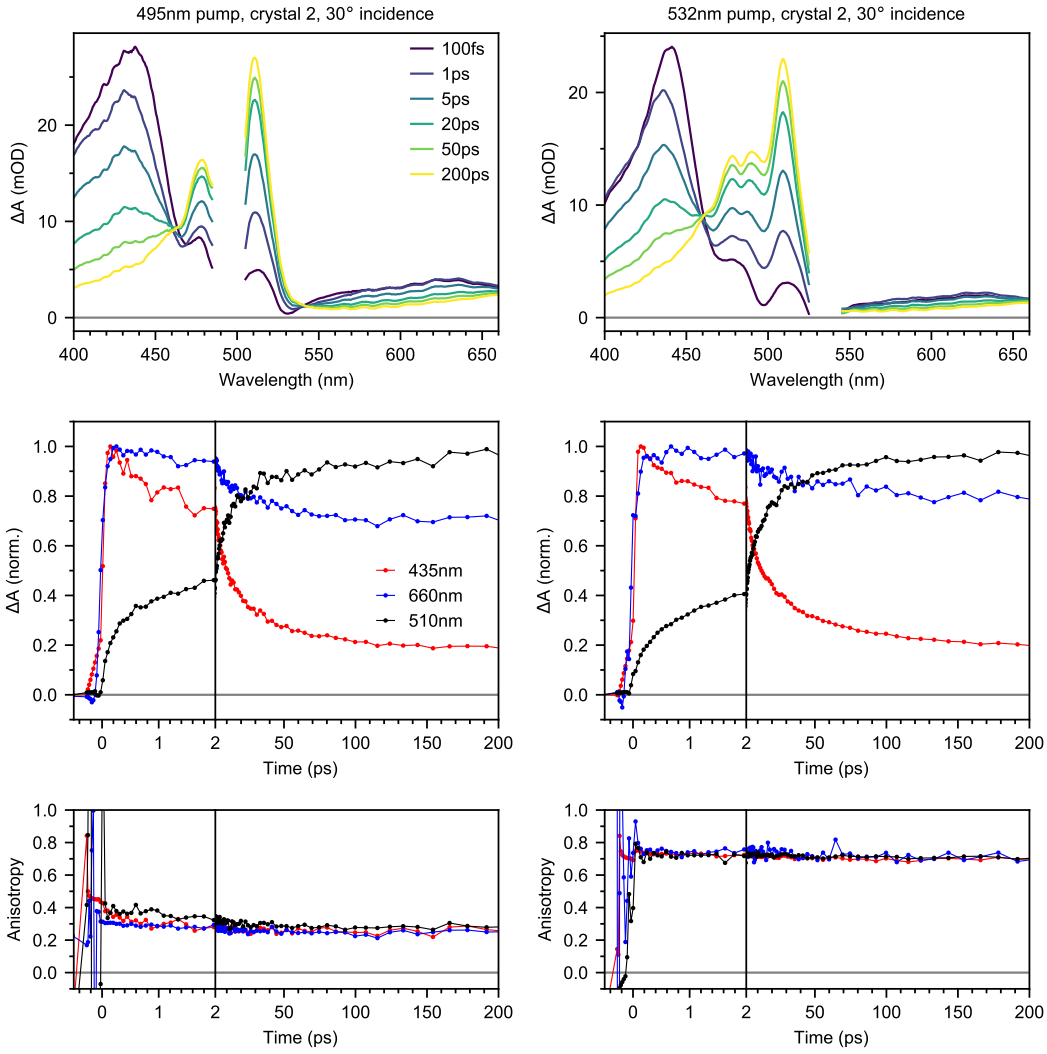

Figure H.2 | TA datasets for crystal 1, 30° incidence. Transient absorption of crystal 1 at 30° incidence, excited with 495 nm and 532 nm pumps (left and right columns respectively). Spectra (top row) show a clear evolution from singlets ($S_1 \rightarrow S_3$ excited state absorption at 435 nm) to triplet-pairs ($T_1 \rightarrow T_3$ excited state absorption at 510 nm). The conversion is approximately one-to-one, evidenced by the isosbestic point at 460 nm. The dynamics (middle row) and anisotropy (bottom row) are shown for probe wavelengths of 435 nm (mostly singlets, some triplets), 660 nm (mixture of singlets and triplets) and 510 nm (almost entirely triplets).

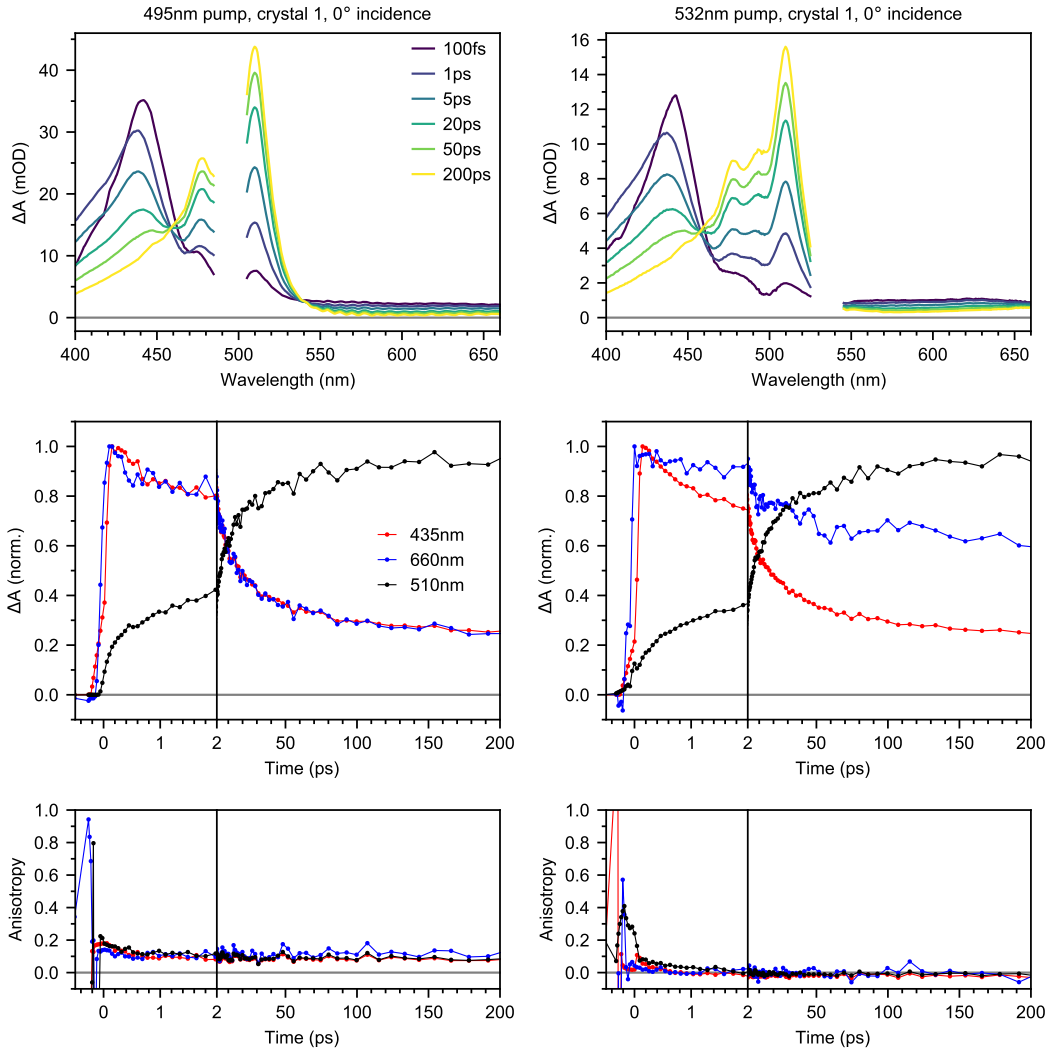

Figure H.3 | TA datasets for crystal 2, 0° incidence. Transient absorption of crystal 2 at 0° incidence, excited with 495 nm and 532 nm pumps (left and right columns respectively). Spectra (top row) show a clear evolution from singlets ($S_1 \rightarrow S_3$ excited state absorption at 435 nm) to triplet-pairs ($T_1 \rightarrow T_3$ excited state absorption at 510 nm). The isosbestic point at 460 nm is slightly less pronounced than in crystal 1. The dynamics (middle row) and anisotropy (bottom row) are shown for probe wavelengths of 435 nm (mostly singlets, some triplets), 660 nm (mixture of singlets and triplets) and 510 nm (almost entirely triplets).

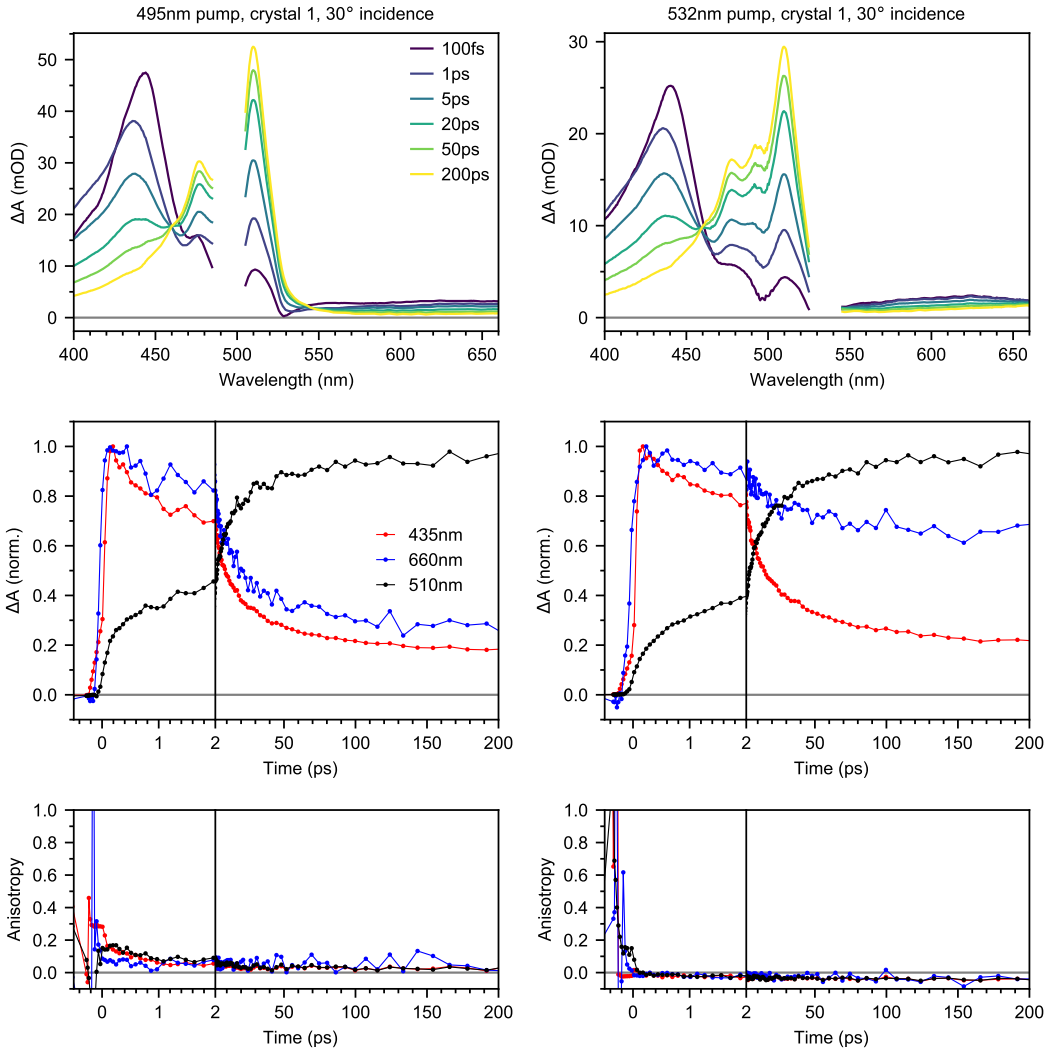

Figure H.4 | TA datasets for crystal 2, 30° incidence. Transient absorption of crystal 2 at 30° incidence, excited with 495 nm and 532 nm pumps (left and right columns respectively). Spectra (top row) show a clear evolution from singlets ($S_1 \rightarrow S_3$ excited state absorption at 435 nm) to triplet-pairs ($T_1 \rightarrow T_3$ excited state absorption at 510 nm). The isosbestic point at 460 nm is slightly less pronounced than in crystal 1. The dynamics (middle row) and anisotropy (bottom row) are shown for probe wavelengths of 435 nm (mostly singlets, some triplets), 660 nm (mixture of singlets and triplets) and 510 nm (almost entirely triplets).

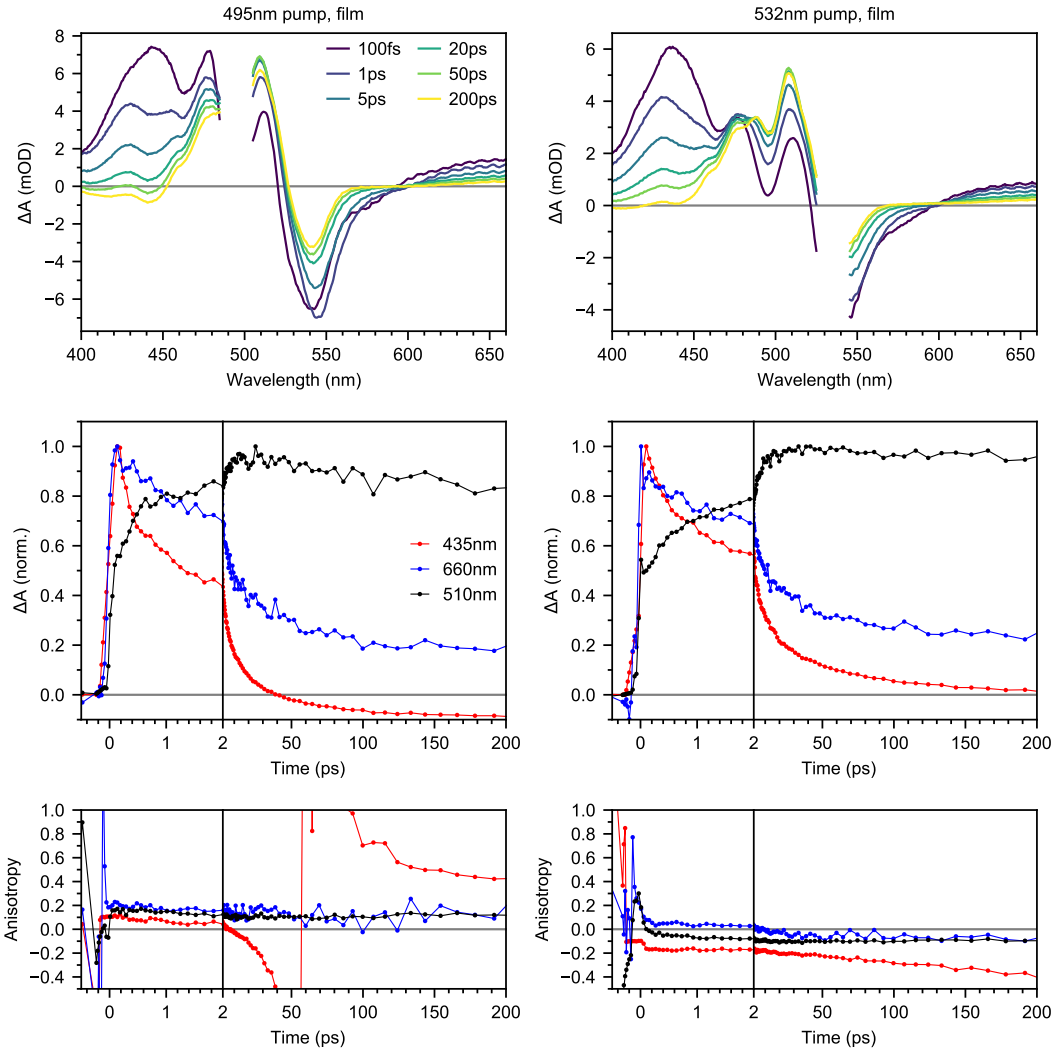

Figure H.5 | TA datasets for a polycrystalline film. Transient absorption of the polycrystalline film at 0° incidence, excited with 495 nm and 532 nm pumps (left and right columns respectively). Spectra (top row) show a clear evolution from singlets ($S_1 \rightarrow S_3$ excited state absorption at 435 nm) to triplet-pairs ($T_1 \rightarrow T_3$ excited state absorption at 510 nm). The ground state bleach is much more pronounced than in the crystals. The dynamics (middle row) and anisotropy (bottom row) are shown for probe wavelengths of 435 nm (mostly singlets, some triplets), 660 nm (mixture of singlets and triplets) and 510 nm (almost entirely triplets). The anisotropy at 435 nm, for the 495 nm excitation diverges at around 50 ps because the signal crosses from positive to negative ΔA at that time.

H.2 510 nm probe wavelength for triplet-pair population

Figure H.6 demonstrates that the transient absorption data, shown for crystal 1 with 532 nm excitation and at 30° incidence, in Figure H.6a can be faithfully reproduced by an MCR-ALS[225,226] reconstruction containing a singlet and triplet spectral component (Figure H.6b). The residuals are well below 5% except in the vicinity of time-zero and the pump scatter (Figure H.6c). Figure H.6d shows that the kinetics at a probe wavelength of 510 nm closely match the triplet population dynamics extracted via MCR-ALS. This indicates that the kinetics at 510 nm are uncontaminated by spectral overlap from the singlet excited state absorption. The same is not true of the kinetics at 435 nm, which contain both singlet and triplet contributions.

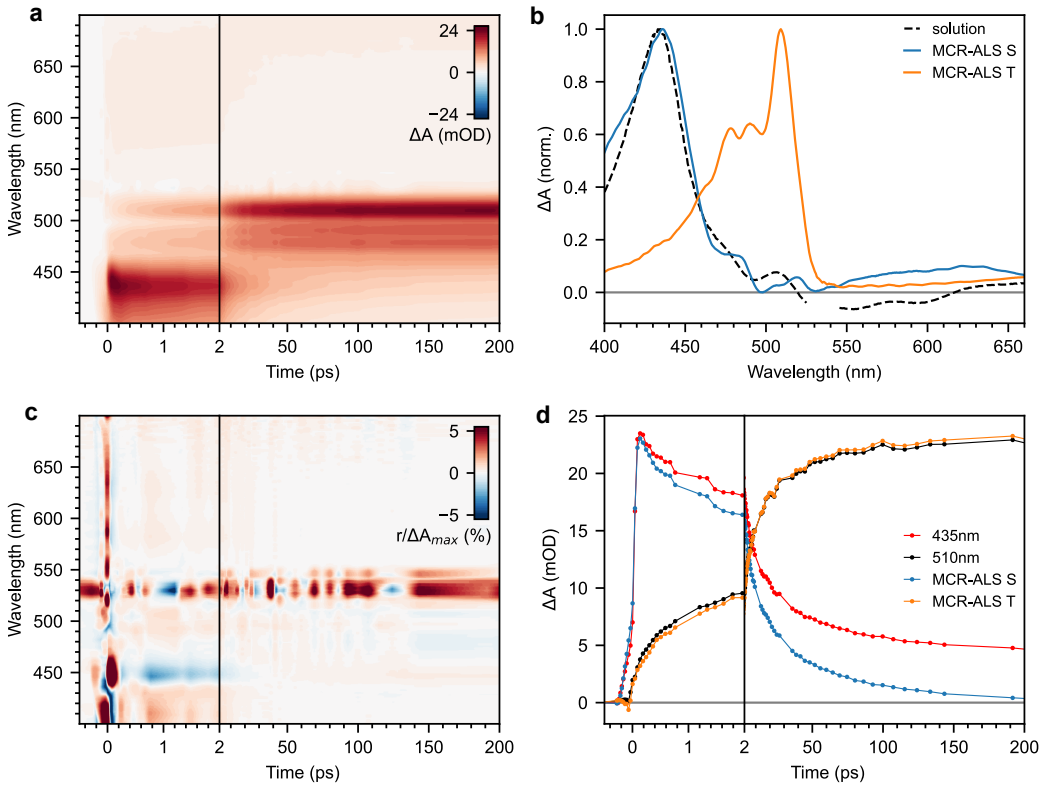

Figure H.6 | MCR-ALS of crystal 1 TA data. **a**, Transient absorption spectroscopy of crystal 1 excited at 532 nm at 30° incidence. **b**, Singlet and triplet spectral components extracted via MCR-ALS. A spectrum measured for rubrene solution (1×10^{-4} M toluene), in which only singlets are present, is shown for comparison. **c**, Residuals between the data (**a**) and the MCR-ALS reconstruction, normalised to the maximum signal. The residuals are well below 5% except in the vicinity of the pump scatter and time-zero. **d**, Kinetics at probe wavelengths of 435 nm and 510 nm compared against the singlet and triplet population dynamics extracted via MCR-ALS.

Figure H.7 shows a repeat of the MCR-ALS analysis for the polycrystalline film excited at 532 nm. Again, a good reconstruction is obtained by MCR-ALS. There is more spectral overlap between the singlet and triplet excited state absorption spectra (Figure H.7b) at 510 nm due to the increased ground state bleach in the film as compared to the crystals. As a result, the match between kinetics at a probe wavelength of 510 nm and the true triplet population dynamics is not quite as close as for the crystal. Crucially however, we find that the instantaneous formation of ^{1}(TT) observed at 510 nm does not arise from spectral overlap with the S_1 signal.

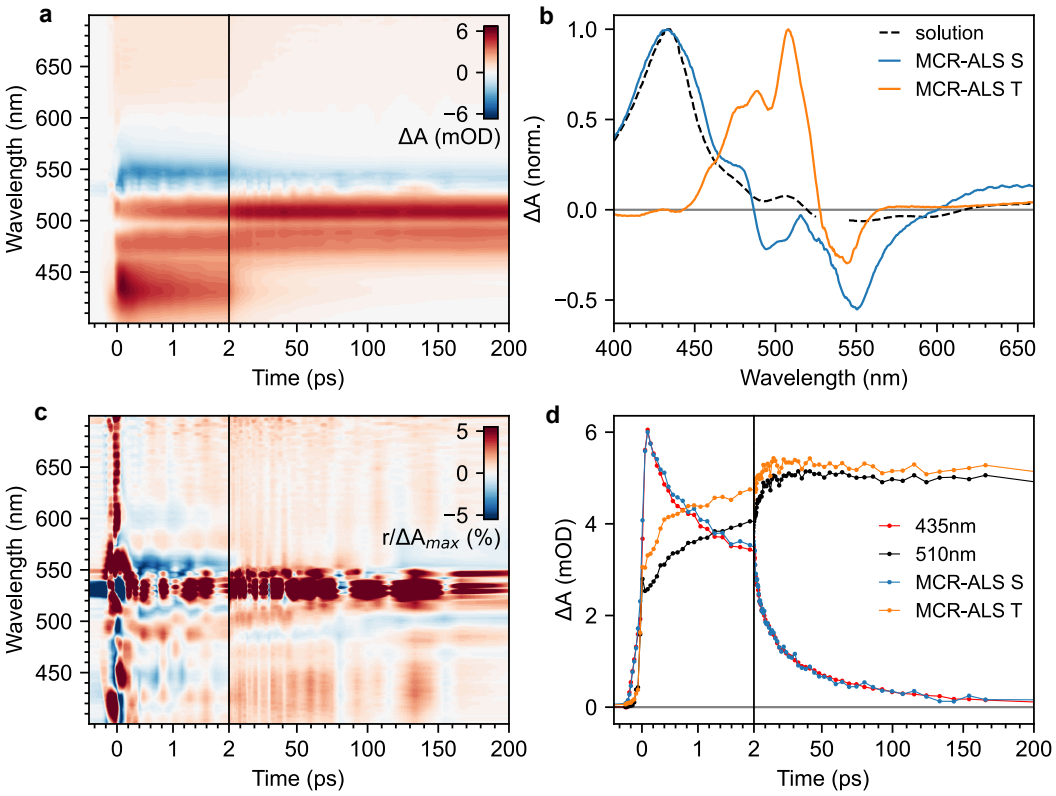

Figure H.7 | MCR-ALS of polycrystalline film TA data. a, Transient absorption spectroscopy of a polycrystalline rubrene film excited at 532 nm. **b**, Singlet and triplet spectral components extracted via MCR-ALS. A spectrum measured for rubrene solution (1×10^{-4} M toluene), in which only singlets are present, is shown for comparison. **c**, Residuals between the data (**a**) and the MCR-ALS reconstruction, normalised to the maximum signal. The residuals are well below 5% except in the vicinity of the pump scatter and time-zero. **d**, Kinetics at probe wavelengths of 435 nm and 510 nm compared against the singlet and triplet population dynamics extracted via MCR-ALS.

H.3 TA anisotropy

Figure H.8a,b shows a comparison between the parallel and isotropic TA kinetics for crystal 1 and the polycrystalline film. The parallel data, $\Delta A_{\parallel}$, was recorded with the pump and probe polarisations parallel. Data was also recorded with pump and probe polarisations perpendicular, $\Delta A_{\perp}$. The isotropic signal, proportional to that measured at the magic angle, can then be recovered through[293]

$$\Delta A_{iso} = \Delta A_{\parallel} + 2\Delta A_{\perp}. \tag{H.1}$$

For crystal 1, the anisotropy is entirely independent of time, giving perfect agreement between $\Delta A_{\parallel}$ and ΔA_{iso} as shown in Figure H.8a. For the polycrystalline film, the anisotropy exhibits a small time dependence, thus the agreement is not perfect. However, we note that all important features of the data, in particular the instrument-limited rise at 510 nm, are the same regardless of polarisation.

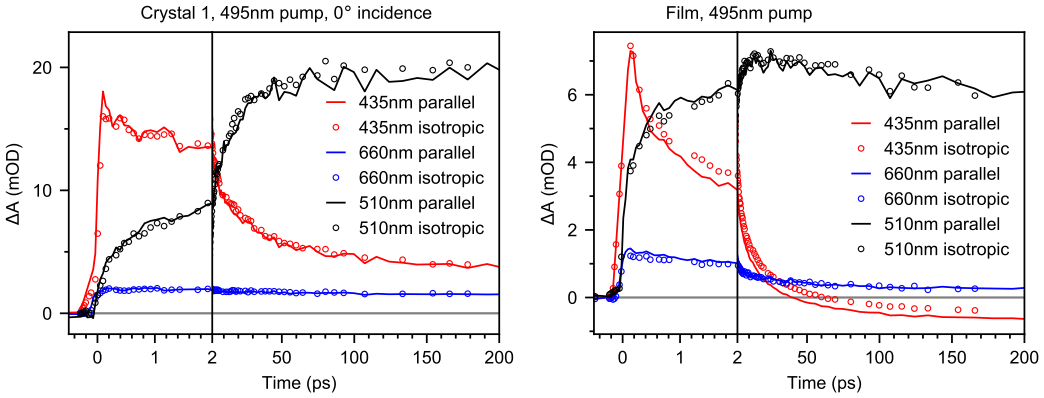

Figure H.8 | TA anisotropy. **a**, TA kinetics for rubrene single crystal 1 excited at 495 nm at 0° incidence. Both the parallel and isotropic data are shown. The isotropic data have been scaled by a constant factor. **b**, As for (**a**), but for the polycrystalline film excited at 495 nm.

Appendix I

Supplementary information for Chapter 7

I.1 Further analysis of transient absorption data

We confirm our assignments (to singlet or triplet states) of spectral features in our transient absorption data by comparing the dynamics.

Figure I.1a shows singlet and triplet PIA spectra in the visible spectral region extracted using multivariate curve resolution alternating least squares (MCR-ALS)[225,226]. Reference spectra used as the starting point of the deconvolution were obtained by time-averaging the data from 0.5–1 ps and 3–7 ns. The concentrations were constrained to be non-negative. The spectra resulting from the MCR-ALS procedure agree well with the measured singlet and reported triplet[350] absorption spectra for rubrene in solution.

The singlet and triplet dynamics extracted using MCR-ALS (Figure I.1b) are characteristic of singlet fission[189]. The triplet population rises with a time constant of approximately 3 ps, accompanied by a 50% reduction in the singlet population with a similar time constant. This suggests that singlet fission ($S_1 \rightarrow {}^1(TT)$) and triplet-pair fusion (${}^1(TT) \rightarrow S_1$) occur simultaneously with a time constant of $2 \times 3\,\text{ps} = 6\,\text{ps} \sim 10\,\text{ps}$.

In Figure I.1c, we show that the PIA bands at 680 nm and 1170 nm match the singlet dynamics, although an additional fast component is present at 1170 nm. Figure I.1d shows the dynamics at 850 nm and 960 nm, each with the dynamics at 1170 nm, weighted by the absorbance difference between the two wavelengths, subtracted. This removes the singlet component, yielding the residual triplet dynamics, which match those extracted in the visible region by MCR-ALS. This confirms that the peaks at 850 nm and 960 nm arise from triplet excited states.

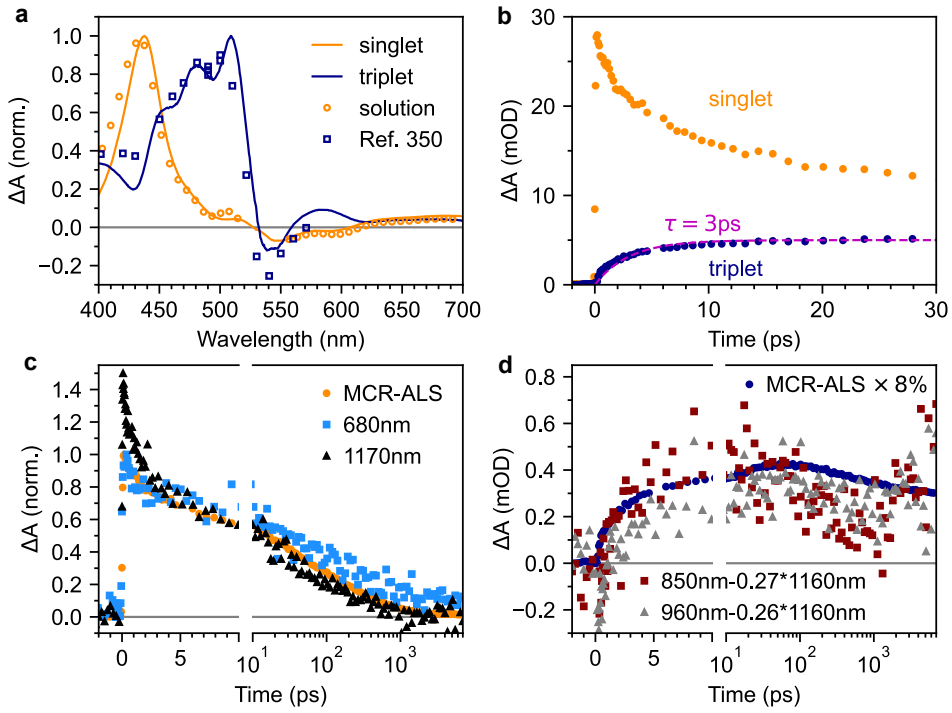

Figure I.1 | Transient absorption dynamics. **a**, Singlet and triplet PIA spectra extracted in the visible region using MCR-ALS[225,226]. The spectra match the singlet from measurements in dilute solution (Figure 8.2b(ii)) and the previously reported triplet spectrum for rubrene in solution[350]. **b**, Extracted singlet and triplet dynamics. **c**, Comparison of singlet PIA dynamics. **d**, Comparison of triplet PIA dynamics. The singlet component has been removed from the dynamics at 850 nm and 960 nm by subtracting the (suitably scaled) dynamics at 1170 nm. Panel **a** adapted with permission from Reference 350; Copyright 1979 American Chemical Society.

I.2 Pump-push-probe spectroscopy of a polycrystalline rubrene film

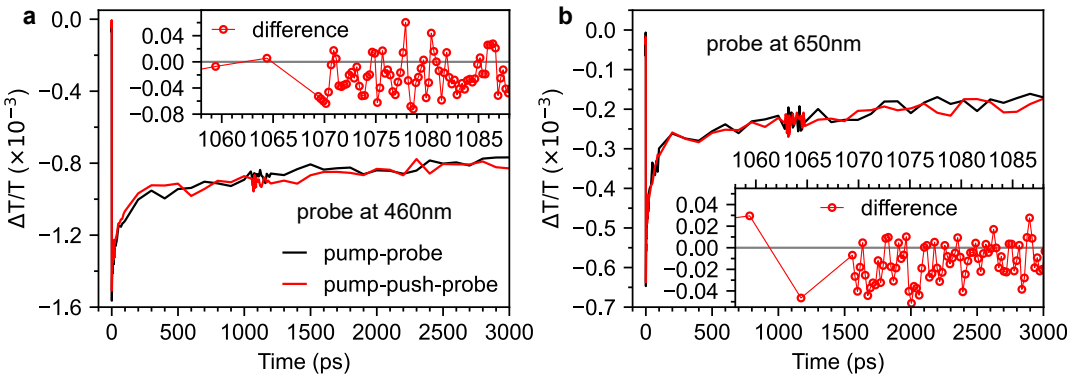

Figure I.2 | Pump-push-probe spectroscopy at different probe wavelengths. Pump-push-probe spectroscopy for probe wavelengths of 460 nm (**a**) and 650 nm (**b**) show no discernable push-induced effects, in contrast to the data at 510 nm (Figure 7.7b).

I.2.1 Alternative explanations for the pump-push-probe data

We find that the effect of our 800 nm push pulses is to enhance the T_1 to T_3 photo-induced absorption (PIA) when the 400 nm pump is present. In this section we investigate the predicted change in triplet PIA for three possible scenarios and show that only the proposed HL-RISC can give rise to an enhancement.

Let the triplet PIA signal X induced by the 400 nm pump have magnitude A at some arbitrary delay time. Then we have

$$X_{0,0} = 0 \tag{I.1}$$

$$X_{1,0} = A, \tag{I.2}$$

where $X_{i,j}$ denotes the signal with the pump on ($i = 1$), pump off ($i = 0$), push on ($j = 1$) or push off ($j = 0$). Then, for example, the pump-probe signal is given by:

$$X_{pump-probe} = X_{1,0} - X_{0,0} = A - 0 = A. \tag{I.3}$$

The push acts as a second pump

The first case we consider is that the push pulse acts as a pump from S_0 to S_N (for example through two-photon absorption) or even from S_0 to T_1. Let the

triplet PIA signal induced by the push alone have magnitude B at the same arbitrary delay time:

$$X_{0,1} = B. \tag{I.4}$$

When the push is preceded by the 400 nm pump pulse, some of the ground state has already been depleted by the first pump pulse. As a result, the magnitude of the push-induced triplet PIA will be less than B, by an amount δ_1, giving

$$X_{1,1} = X_{1,0} + X_{0,1} - \delta_1 = A + B - \delta_1. \tag{I.5}$$

The pump-push-probe signal in this case is

$$X_{pump-push-probe} = X_{1,1} - X_{0,1} = A + B - \delta_1 - B = A - \delta_1, \tag{I.6}$$

and so even if the push pulse acts as a second pump, the effect is to reduce the pump-push-probe signal rather than enhance it.

Internal conversion from T_2 to T_1

The second case to consider is that the push pulse excites the T_1 to T_2 transition but that T_2 undergoes internal conversion to T_1. In this case, the push pulse has no effect in the absence of the pump:

$$X_{0,1} = 0, \tag{I.7}$$

but causes a reduction δ_2 in the pump-induced PIA due to depletion of the T_1 state:

$$X_{1,1} = X_{1,0} - \delta_2 = A - \delta_2, \tag{I.8}$$

and therefore again resulting in a reduced pump-push-probe signal

$$X_{pump-push-probe} = X_{1,1} - X_{0,1} = A - \delta_2 - 0 = A - \delta_2, \tag{I.9}$$

where the magnitude δ_2 of the signal reduction would decrease to zero as the T_1 state is repopulated by internal conversion from T_2.

HL-RISC from T_2 to S_1

In this case, the push pulse excites the T_1 to T_2 transition and T_2 undergoes rapid HL-RISC to form S_1. S_1 then undergoes singlet fission, forming T_1+T_1.

In the absence of the pump, the push pulse has no effect:

$$X_{0,1} = 0. \tag{I.10}$$

When the pump pulse is present, T_1 is again depleted by amount δ_3. However, since each S_1 state formed by the subsequent HL-RISC produces two T_1 states through singlet fission, the triplet PIA is enhanced by an amount $2\delta_3$, giving

$$X_{1,1} = X_{1,0} - \delta_3 + 2\delta_3 = A + \delta_3, \tag{I.11}$$

and hence a pump-push-probe signal of

$$X_{pump-push-probe} = X_{1,1} - X_{0,1} = A + \delta_3 - 0 = A + \delta_3. \tag{I.12}$$

Thus, HL-RISC is predicted to produce an enhancement of the triplet PIA, and the dynamics of the enhancement should match the pump-probe singlet fission dynamics.

I.2.2 Quantitative analysis of the pump-push-probe signal magnitude

Having demonstrated that HL-RISC is the most likely explanation for the push-induced enhancement of the triplet PIA, we can estimate the expected magnitude of the enhancement from known and estimated triplet absorption cross sections and measured pulse intensities.

First, we estimate the density of triplet excitons responsible for a given $\Delta T/T$ signal at 510 nm. We can write the triplet PIA absorbance at 510 nm as

$$\Delta A = -\log_{10} e^{-\alpha d} = n_T \sigma d \log_{10}(e), \tag{I.13}$$

where α and σ are the triplet absorption coefficient and cross section, respectively, at 510 nm, d is the film thickness and n_T is the number density of triplet excitons.

Transforming into the measurement units of $\Delta T/T$ gives the following expression for the number density of triplet excitons:

$$n_T = \frac{-\log_{10}\left(1 + \frac{\Delta T}{T}\right)}{\sigma d \log_{10}(e)}. \tag{I.14}$$

The triplet absorption cross section in the vicinity of 510 nm has been measured as $1.2 \times 10^{-16}\,\mathrm{cm}^2$ for rubrene in solution[278]. Using this value, and our film

thickness of 125 nm, gives $n_T = 4.5 \times 10^{18}\,\mathrm{cm}^{-3}$ for our maximum $\Delta T/T$ signal of -0.0067 and $n_T = 3.9 \times 10^{18}\,\mathrm{cm}^{-3}$ for $\Delta T/T = -0.0058$, the value just before the arrival of the push pulse (see Figure 7.7b).

We can cross check these triplet exciton densities against the singlet exciton density calculated from the measured pump pulse intensity and the absorption of the film at 400 nm. In general, we have

$$n_S = F_A(1 - F_S)P\frac{\lambda}{hc}\frac{1}{d} \tag{I.15}$$

where F_A and F_S are the fraction of incident $\lambda = 400$ nm light absorbed and scattered/reflected by the film, respectively, and P is the pump pulse intensity in units of $\mathrm{J\,cm}^{-2}$. By fitting a scattering background to the absorption spectrum of the film shown in Figure 6.4a, we estimate $F_A \sim 0.1$ and $F_S \sim 0.3$ (from absorbances of 0.05 and 0.15). We measured P to be $0.2\,\mathrm{mJ\,cm}^{-2}$ (see Section 7.9.4). Using these values in Equation I.15 results in an initial photoexcited singlet exciton density of $n_S \sim 2.3 \times 10^{18}\,\mathrm{cm}^{-3}$. Assuming that singlet fission forms triplet excitons with a yield of 200%, we would expect a maximum triplet exciton density of $n_T \sim 4.6 \times 10^{18}\,\mathrm{cm}^{-3}$, which agrees very well with the values calculated above from the solution cross section and the measured $\Delta T/T$ signal.

We are now in a position to estimate the number density of triplet excitons that are re-excited by the push pulse, n_T', and hence obtain estimates for the push-induced $\Delta T/T$ signal from Equation I.14.

The number density of triplets re-excited by the push can be evaluated from Equation I.15, where P now represents the $\lambda = 800$ nm push pulse intensity which we measured to be $1.2\,\mathrm{mJ\,cm}^{-2}$. F_S is now the fraction of 800 nm light that is scattered by the film which we again obtain from the absorption spectrum, finding $F_S \sim 0.09$. The unknown parameter is F_A, the fraction of 800 nm light absorbed by the $T_1 \rightarrow T_2$ transition in the film. We have

$$F_A = 1 - 10^{-A_{800}}, \tag{I.16}$$

where the triplet-triplet absorbance at 800 nm is given by:

$$A_{800} = n_T\sigma' d\log_{10}(e) = n_T\sigma\frac{\sigma'}{\sigma}d\log_{10}(e). \tag{I.17}$$

Here σ and σ' are the triplet absorption cross sections at 510 nm and 800 nm respectively and $n_T = 3.9 \times 10^{18}\,\mathrm{cm}^{-3}$ (see above) is the triplet exciton density just before the arrival of the push pulse.

The ratio of triplet-triplet absorption cross sections at 510 nm and 800 nm

can be estimated from measured triplet PIA spectra for rubrene. We find significant variation between different measurements. For example the triplet PIA spectrum reported by Miyata et al.[35] for rubrene single crystals gives $\sigma'/\sigma \sim 0.3$. We suggest that this is an upper bound, given the significant spectral overlap between singlet and triplet PIA bands in the vicinity of 800 nm in their data. We can obtain a lower bound from our own transient absorption data in Figure 7.5. Although we cannot use the data at 800 nm due to residual fundamental in that probe region, we can take the ratio of the PIA signal at 510 nm and 850 nm (for $t > 1000$ ps) as a lower bound, giving $\sigma'/\sigma \sim 0.08$.

These upper and lower bounds for the triplet-triplet cross section ratio result in a range of $1.6 \times 10^{17}\,\mathrm{cm}^{-3} < n'_T < 6.2 \times 10^{17}\,\mathrm{cm}^{-3}$ for the push-induced triplet density, in other words the T_2 exciton density caused by the push pulse. In the HL-RISC picture, pushing from T_1 to T_2 results in the net gain of one T_1. This is because the push removes one T_1 state but HL-RISC from T_2 to S_1, followed by singlet fission from S_1 to T_1+T_1, adds back two T_1 states.

Thus we can simply convert n'_T into an expected push-induced $\Delta T/T$ signal at 510 nm by rearranging Equation I.14. Assuming that all T_2 states populated by the push undergo HL-RISC, we predict that the magnitude of the push-induced $\Delta T/T$ signal should lie between -2.4×10^{-4} and -9.3×10^{-4}. Our measured value of -3.5×10^{-4} (see Figure 7.7b) lies within this range, providing additional justification for our interpretation of the pump-push-probe data in terms of HL-RISC.

I.3 Sensitivity of the model to rate constant values

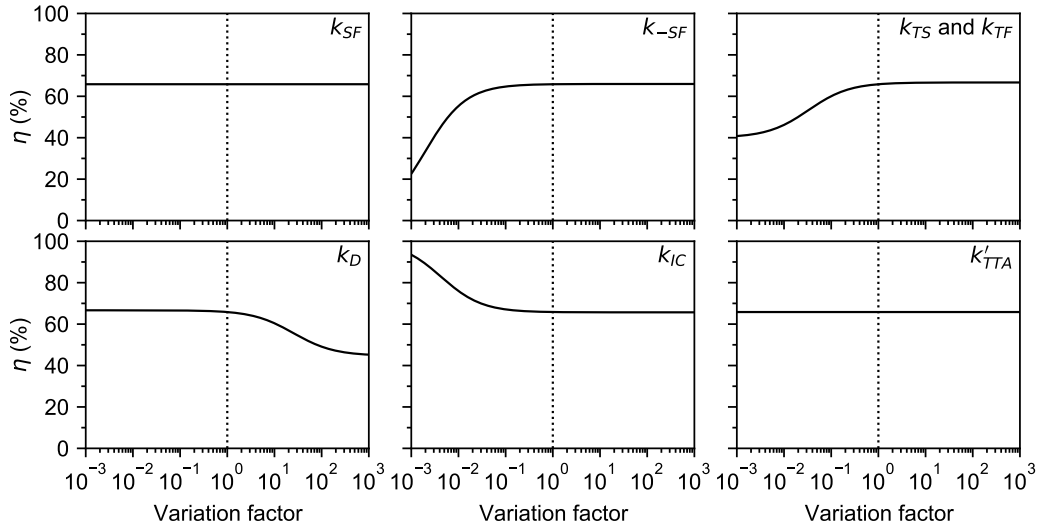

Figure I.3 | Sensitivity of model 2 to different rate constants. Each rate constant was varied by ±3 orders of magnitude about its original value and the effect on η monitored. In particular, we highlight that the value of η does not depend on k_{sf} or k'_{tta} and that increasing the triplet hopping rates further also has little impact.

I.4 Literature values of spin statistical factors and energy levels

Tables I.1 and I.2 give non-exhaustive experimental literature values for the spin statistical factor of diphenylanthracene (DPA) and rubrene and the T_2 energy in rubrene. These values were used to indicate the spread of reported experimental values shown in Figure 7.11.

Table I.1 | Experimental values of the spin statistical factor for rubrene and DPA.

Annihilator	**System**	η (%)	**Reference**
DPA	thin film	37	307
DPA	solution	44[a]	330
DPA	solution	36[a]	331
DPA	solution	45	332
DPA	solution	36[a]	333
DPA	solution	48[a]	334
DPA	solution	52	335
rubrene	solid	72	323
rubrene	solution	61(5)[b]	38,208
rubrene	solution	15[c]	42

[a]The value given is the upconversion quantum yield, which is very close to η since the other efficiencies are near unity.

[b]The value and error are taken from the measurements in Ref. 38. Very similar values were reported in Ref. 208

[c]It is unclear why the values reported in Ref. 42 are so much lower than the others.

Table I.2 | Experimental values of the T_2 energy level in rubrene. Note that only near-infrared (NIR) transient absorption (TA) data is included: some authors report the $T_1 \rightarrow T_2$ transition at 800 nm[35,290], giving a T_2 energy of 2.69 eV however their probe spectra do not extend far enough into the NIR to determine the true transition energy. ISC stands for intersystem crossing.

System	**Method**	**T_2 energy (eV)**	**Reference**
solution	thermally activated ISC	2.38-2.40	277
thin film	NIR TA	2.40	74
nanoparticle film	NIR TA	2.43	This work
crystal	NIR TA	2.55	37

Appendix J

Supplementary information for Chapter 8

J.1 Further analysis of transient absorption data

Figure J.1 shows that anisotropy changes and peak shifts, which are characteristic signatures of exciton migration in transient absorption[224], occur faster than, or on a similar timescale to, initial singlet fission. We note that monitoring the singlet excited state absorption (ESA) peak wavelength beyond 200 ps is impossible due to spectral overlap with the triplet ESA. Interestingly, the timescale of the singlet ESA shift is similar to the timescale of the first singlet fission step, suggesting that exciton migration to fission sites, resulting in ^{1}(TT) formation, may be occurring within the first 10 ps.

Beyond 20 ps however, both the singlet ESA peak position and the anisotropy are constant, suggesting that the ∼100 ps secondary rise time that we observe for the triplet signal in transient absorption is not due to exciton migration to fission sites. Instead, the fission dynamics are consistent with the formation of a ∼50:50 equilibrium between S_1 and triplet-pair states within 10 ps (Figure 8.3). Although we cannot with certainty say whether the initial triplet-pair states are strongly interacting ^{1}(TT) states or, as has been recently suggested[192], weakly interacting ^{1}(T...T) states, we believe that the former is more likely in this case for several reasons.

Firstly, $S_1 \rightarrow {}^1$(TT) $\rightarrow {}^1$(T...T) is the generally accepted pathway for singlet fission[169,193], including in rubrene[35–37]. Secondly, as shown below, we would expect a triplet hopping rate of around 100 ps based on the annihilation rate constant; this is consistent with the second time constant of the triplet dynamics, suggesting that the first (10 ps) component reflects the formation of ^{1}(TT). Lastly, our sequential model is consistent with the model in Ref. 345, which the

authors use to predict the same power law photoluminescence dynamics that we measure (Figure 8.4)a.

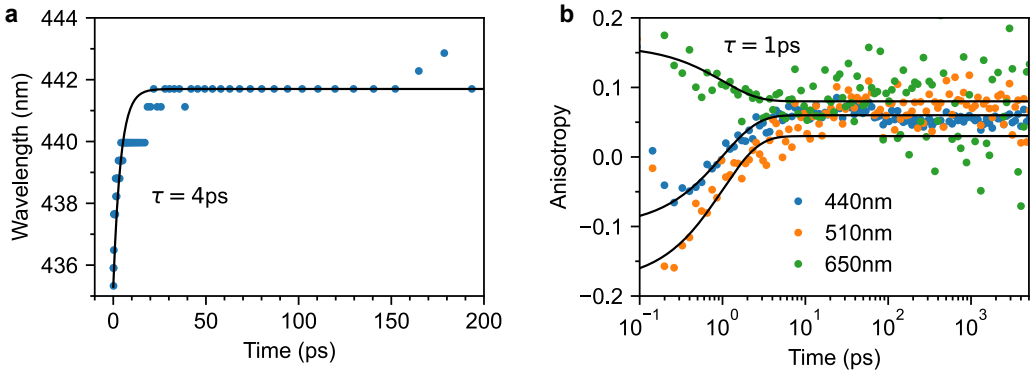

Figure J.1 | Signatures of exciton migration are similar to, or faster than, singlet fission dynamics. **a**, The slight redshift of the singlet excited state absorption (ESA) feature that occurs after photo-excitation has a time constant of around 4 ps. **b**, The initial change in anisotropy has a 1 ps time constant. These time constants are much faster than the 100 ps secondary rise in triplet-pair population observed by transient absorption.

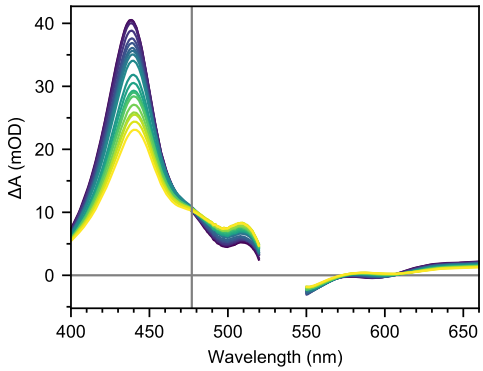

Figure J.2 | Isosbestic point during singlet fission in rubrene NP films. The presence of an isosbestic point between the singlet and triplet excited state absorptions suggests that the singlet fission yield is high in the rubrene NP films. Data is shown for an excitation density of 41 $\mu J\,cm^{-2}$.

J.2 Sample-to-sample variations

We find that the absolute PLQY values are slightly sensitive to the sample preparation conditions, and that they decrease over time. Table J.1 summarises the sample-to-sample variation in measured PLQY. For DBP-doped rubrene NPs, we quote the value of 61% since we were able to reproduce this number reliably in freshly-prepared samples. We observe only small changes to the measured excited state dynamics, as shown in Figures J.3 and J.4.

Table J.1 | Measured values of absolute PLQY for different samples.

Sample	Time before PLQY measurement	PLQY (%)
Rub	<1 month	7.6, 5.9, 4.2
Rub	18 months	3.6, 2.9
Rub/DBP	<1 month	59, 63, 64, 61
Rub/DBP	18 months	46, 44

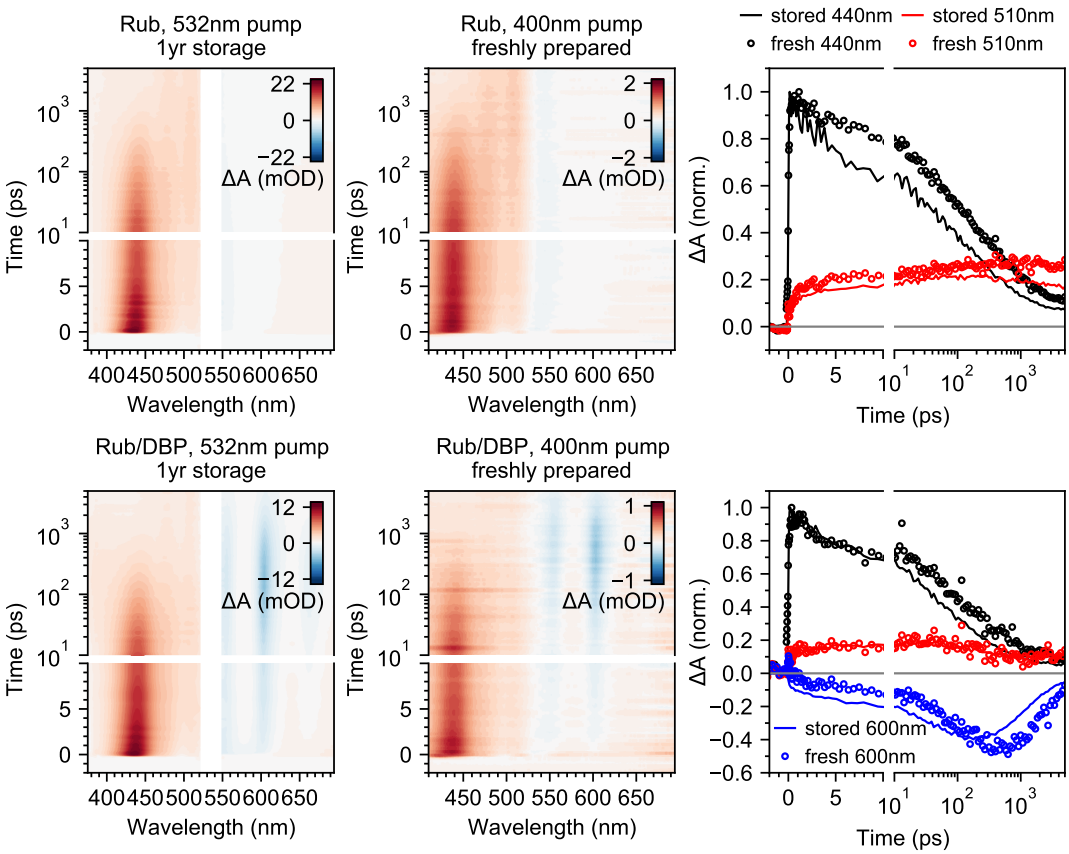

Figure J.3 | Picosecond photophysics are similar for fresh and aged samples. Although a direct comparison is impossible owing to the different pump wavelength and excitation density, we measure similar photophysics for both freshly prepared samples and samples kept in a glovebox for one year.

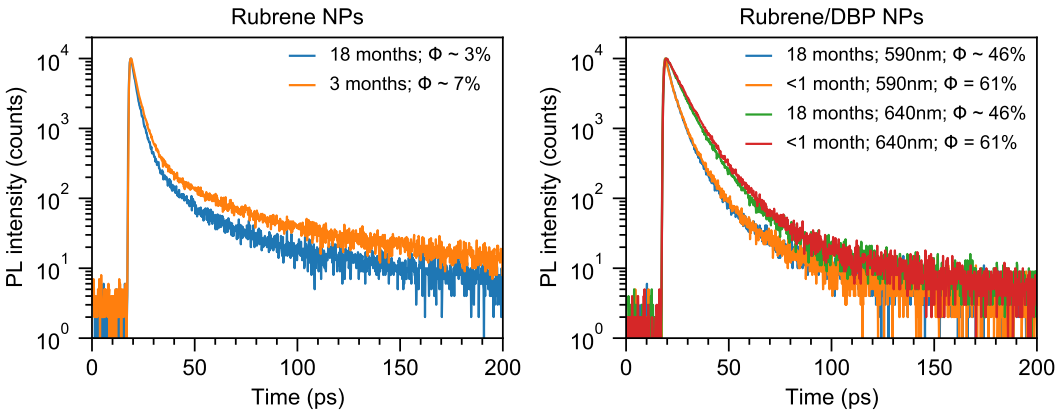

Figure J.4 | TCSPC decays are similar for fresh and aged samples. **a**, For pure rubrene NPs, the initial decay is slightly faster (and the PLQY correspondingly slightly lower) than for samples stored longer. The behaviour on longer timescales is very similar. **b**, For DBP-doped rubrene NPs, there is very little observable change in the PL decay between fresh and stored samples, although we find that the absolute PLQY decreases from 61% to 46%.

J.3 Estimation of the triplet hopping rate in rubrene

As discussed in Section 2.5.4, the bimolecular triplet-triplet annihilation rate constant γ is related to the triplet diffusivity D in three dimensions through[100]

$$\gamma = 4\pi D R_a \tag{J.1}$$

where R_a is the annihilation radius. The diffusion constant can be written in terms of the triplet hopping rate k and the hopping distance R. In three dimensions[365]

$$D = \frac{kR^2}{6}. \tag{J.2}$$

For simplicity we will assume that the annihilation radius is equal to the hopping distance since triplets are fairly localised in rubrene[366]. This gives us a simple relationship between the annihilation constant and time constant for triplet hopping:

$$\tau = \frac{1}{k} \approx \frac{2\pi R^3}{3\gamma} \tag{J.3}$$

Taking $R = 7.18\,\text{Å}$, the b-axis lattice constant of orthorhombic rubrene[34] and using the measured value of $\gamma = 5 \times 10^{-12}\,\text{cm}^3\,\text{s}^{-1}$ for rubrene single crystals[216] gives a hopping time of $\tau \approx 150\,\text{ps}$.

We can also estimate a lower bound for the annihilation constant on our rubrene nanoparticles from the excitation density dependent triplet dynamics of the rubrene NPs, shown in Figure 8.4b of the main text. In the simplest case we can assume that the triplet population dynamics $T(t)$ are governed by only triplet decay and bimolecular annihilation, giving[239]

$$\frac{dT(t)}{dt} = -k_T T(t) - \gamma T^2(t), \tag{J.4}$$

where k_T is the inverse of the triplet lifetime. The solution of this rate equation can be linearised[96],

$$\frac{1}{T(t)} = \left(\frac{1}{T(0)} + \frac{\gamma}{k_T}\right) \exp\left(k_T t\right) - \frac{\gamma}{k_T}, \tag{J.5}$$

where $T(0)$ is the triplet population at $t = 0$. From the simulation presented in Figure 8.8a, we obtained the ratio of singlet and triplet populations a few ns following excitation, giving us a conversion factor from measured pulse energy at 532 nm in units of $\mu\text{J}\,\text{cm}^{-2}$ to triplet excitation density in units of cm^{-3}. The conversion factor was then multiplied by two since there are two triplets per triplet-pair state. This procedure gave us a conversion factor of $9.2 \times$

$10^{17}\,\mu J^{-1}\,cm^{-1}$, which we used to convert our measured triplet TA signal at 510 nm into a population density. The inverse of these populations are plotted in Figure J.5 against $\exp(k_T t)$, where we have taken $k_T = 1 \times 10^{-5}\,ns^{-1}$ (Ref. 272).

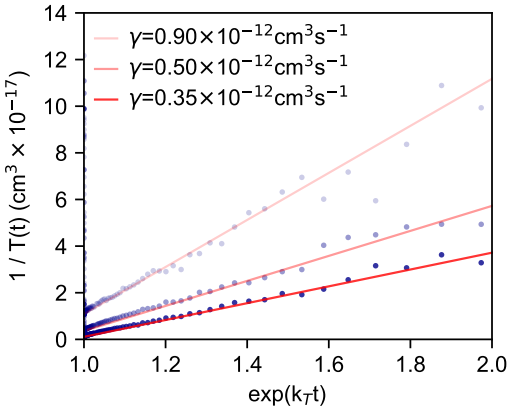

Figure J.5 | Triplet-triplet annihilation in rubrene nanoparticles. The triplet annihilation dynamics cannot be described by a single annihilation rate constant as suggested by Equations J.4 and J.5. This is because the interplay with other excited states, such as triplet-pair states, is not considered. Nevertheless, we can extract order-of-magnitude values for the annihilation rate constant that are similar to that measured for single crystal rubrene.

Applying Equation J.5 to the linearised data in Figure J.5 was not possible for a single value of γ. This is in part because the simple rate model in Equation J.4 assumes that triplet-triplet annihilation is a loss channel when in fact it can efficiently form triplet-pair states which also contribute to the measured triplet signal[216]. Nevertheless, as shown in Figure J.5, we find that the annihilation rate constants obtained using this over-simplified model are a similar order of magnitude to that measured for rubrene single crystals[216].

J.4 MCR-ALS residuals

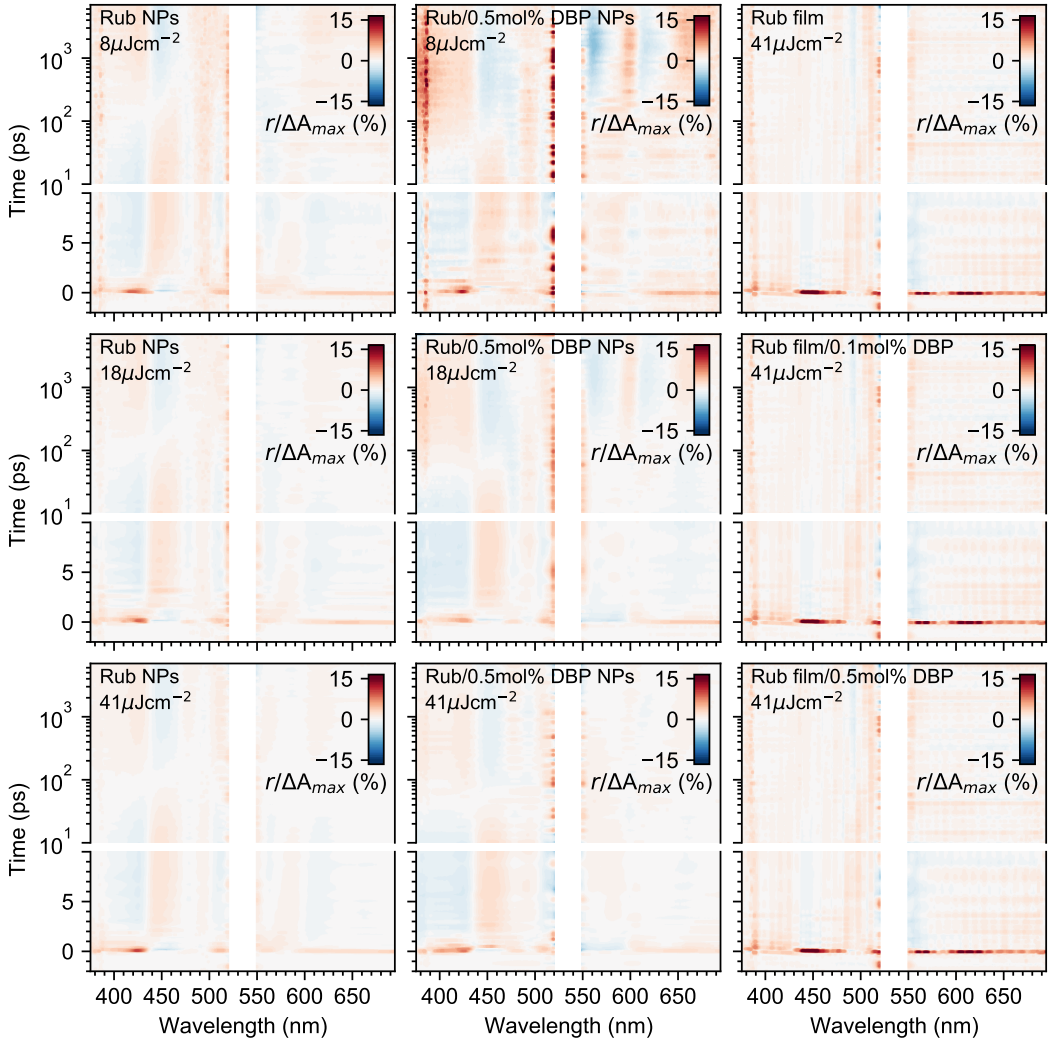

Figure J.6 | MCR-ALS residuals. We evaulated the quality of the MCR-ALS reconstructions by plotting the residuals between fitted and measured data. The residuals r are normalised to the maximum TA signal ΔA_{max} for each dataset. The residuals are small in all cases, except around $t = 0$ where coherent artefacts are present in the data, and in the vicinity of the pump scatter.

J.5 Polycrystalline rubrene films

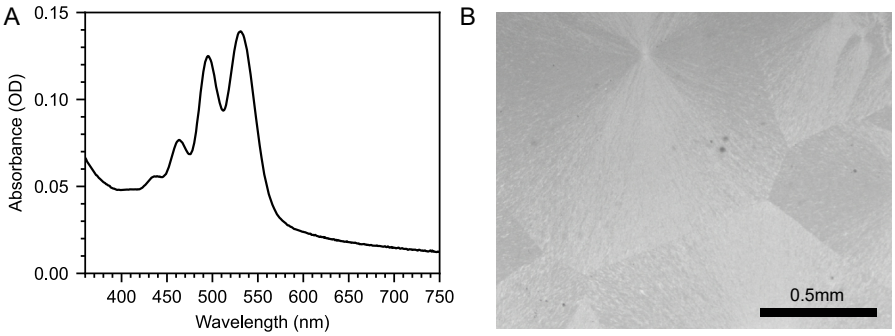

Figure J.7 | Polycrystalline rubrene films. **a**, Absorption spectrum of a 50 nm thick spin-coated polycrystalline rubrene film. **b**, Optical micrograph of the film showing spherulite crystal structures and visible micron-scale crystalline domains.

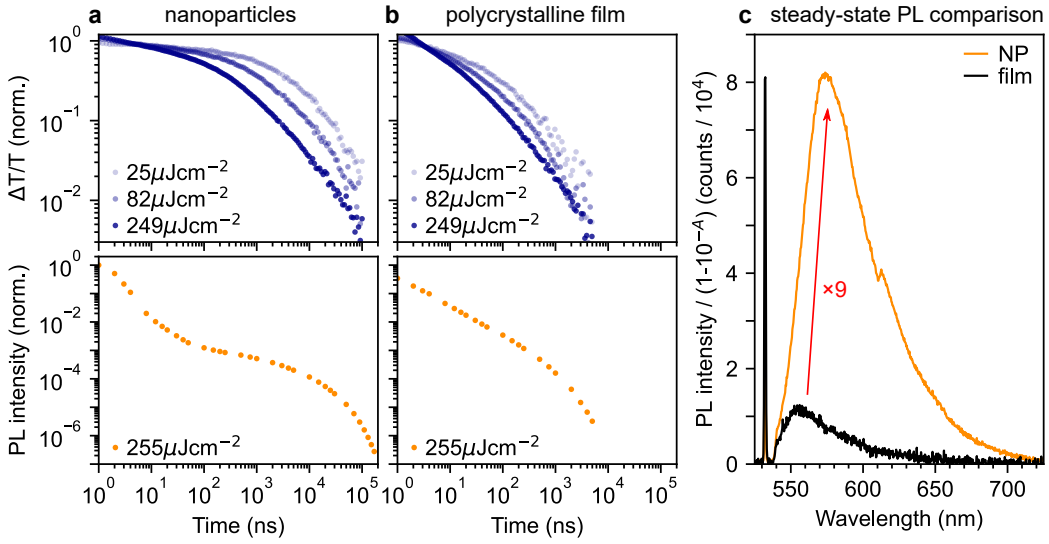

Figure J.8 | Triplet losses dramatically reduce the PLQY of rubrene. **a**, Triplet and singlet dynamics of rubrene NPs measured by TA (at 510 nm) and TRPL (wavelength integrated) respectively. **b**, Triplet and singlet dynamics of a polycrystalline rubrene film. The triplet decay is more rapid, reflecting increased triplet trapping and/or quenching compared to the NPs. This is reflected in the PL dynamics, which also decay more quickly, particularly on microsecond timescales. **c**, This results in a dramatic reduction in the steady-state PL of the rubrene film compared to the nanoparticles. The key to obtaining high PLQY in rubrene is therefore to encourage efficient singlet formation through triplet recombination following singlet fission.

Figure J.8 highlights the importance of triplet energy losses in rubrene. The triplet population in the polycrystalline film drops of considerably more rapidly with time than in the nanoparticles. This is reflected in the PL dynamics, which also decay more quickly. As a result, the steady-state PL (normalised for the different absorbances of the samples) is reduced by a factor of nine. This

highlights the critical role of triplet recombination in determining the absolute PLQY of rubrene and suggests that polycrystalline morphologies may be associated with increased triplet energy losses, perhaps due to the concentration of grain boundaries.

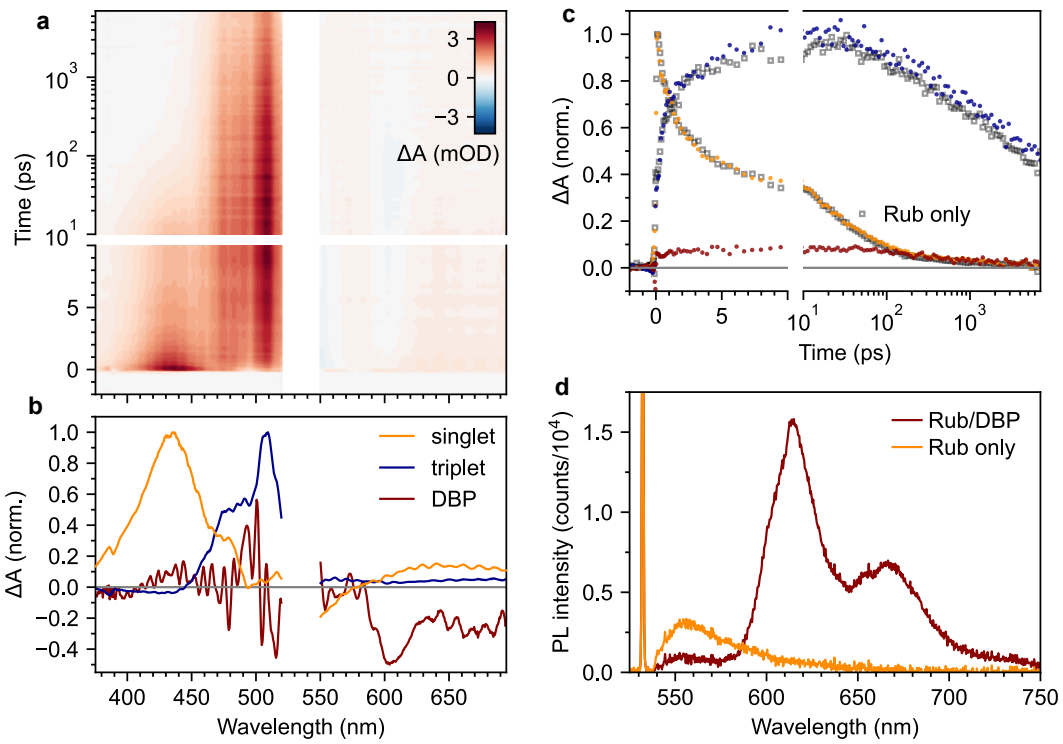

Figure J.9 | Addition of DBP does not suppress initial singlet fission in polycrystalline films. **a**, False-colour map of the transient absorption of a polycrystalline rubrene film containing 0.5 mol% DBP. The triplet signal at 510 nm is very pronounced. **b**, MCR-ALS spectra corresonding to the rubrene singlet (orange) rubrene triplet species (blue) and DBP singlet (red). **c**, The singlet and triplet dynamics are unchanged despite the addition of DBP. There is only a small amount of energy transfer to DBP, evidenced by the slight rise in the DBP population during the first few tens of picoseconds. Some DBP molecules were photo-excited by the 532 nm pump pulses. **d**, Despite the apparent lack of energy transfer to DBP occurring on picosecond timescales, and no evidence of singlet fission suppression, most of the photoluminescence comes from DBP rather than rubrene, and it is considerably brighter than the pure rubrene film. This highlights an important point: DBP does not suppress initial singlet fission, instead it reduces the probability of encountering losses associated with triplets and provides a more effective radiative sink for singlet energy.

J.6 Rate equations and constants

We modelled the ultrafast TA data using the simple kinetic scheme shown in Figure 8.8a. The rate equations governing the populations of the singlet [S_1], strongly-exchange coupled singlet triplet-pair [^{1}(TT)], weakly exchange-coupled singlet triplet-pair [^{1}(T...T)], mixed spin triplet-pairs [(T...T)] and singlet energy collector DBP [S_{1c}] are given by

$$\frac{d[S_1]}{dt} = -\left(k_r + k_{fret} + k_{sf}\right)[S_1] - k_{ssa}[S_1]^2 + k_{tf}[^1(TT)] \tag{J.6}$$

$$\frac{d[^1(TT)]}{dt} = k_{sf}[S_1] - \left(k_{hop} + k_{tf}\right)[^1(TT)] + k_{-hop}[^1(T...T)] \tag{J.7}$$

$$\frac{d[^1(T...T)]}{dt} = k_{hop}[^1(TT)] - \left(k_{-hop} + k_{spin} + k_t\right)[^1(T...T)] \tag{J.8}$$

$$\frac{d[(T...T)]}{dt} = k_{spin}[^1(T...T)] - k_t[(T...T)] \tag{J.9}$$

$$\frac{d[S_{1c}]}{dt} = k_{fret}[S_1] - k_{rc}[S_{1c}], \tag{J.10}$$

where square brackets denote concentrations of excited state species in units of cm^{-3}. We write rubrene singlets as [S_1] and DBP singlets as [S_{1c}].

The definitions and values of the rate constants are given in Table J.2. The values of the rate constants are well constrained by the measured TA data and the optimisation procedure (global least squares fitting to the excitation density dependent singlet and triplet dynamics) was performed principally for cosmetic reasons. We note that values of k_{hop} and k_{-hop} were checked against the expected values based on diffusion mediated triplet hopping in the rubrene nanoparticles.

The initial population of the photo-excited singlet state was estimated from the measured power P, spot radius at sample position r and known repetition rate f and wavelength λ of the excitation laser of the experimental setup using

$$N_0 \approx \frac{P}{f\pi r^2}\frac{\lambda}{hc}\frac{1}{d}\left(1 - 10^{-OD}\right), \tag{J.11}$$

where the absorbing sample thickness d was estimated from the measured optical density (OD) and known molar absorptivity[203]. A precise measurement of absorbing thickness was impossible since the samples comprised nanoparticles dispersed in a PVA matrix, rather than a continuous film.

We obtained the simulated excited state dynamics corresponding to different experimental measurements by integrating the rate equations using custom-made python code. Note that triplet transient absorption signals were assumed

Table J.2 | Values and sources of the rate constants used in the model. Note that the optimisation procedure was largely cosmetic: the values of the rate constants are well constrained by the measured TA data.

Rate constant	Value	Source
k_{sf}	$104\,\mathrm{ns}^{-1}$	TA data, then optimised
k_{tf}	$118\,\mathrm{ns}^{-1}$	TA data, then optimised
k_{hop}	$7\,\mathrm{ns}^{-1}$	TA data, then optimised
k_{-hop}	$1.2\,\mathrm{ns}^{-1}$	optimised, subject to constraint
k_{spin}	$0.25\,\mathrm{ns}^{-1}$	MFE data, Ref. 137, fixed
k_{fret}	$20\,\mathrm{ns}^{-1}$	TA data, fixed
k_{ssa}	$3 \times 10^{-17}\,\mathrm{cm}^3\,\mathrm{ns}^{-1}$	manually adjusted, then fixed
k_r	$0.0625\,\mathrm{ns}^{-1}$	TA data, fixed
k_{rc}	$0.25\,\mathrm{ns}^{-1}$	TA data, fixed
k_t	$1 \times 10^{-5}\,\mathrm{ns}^{-1}$	Ref. 272, fixed

to be proportional to $[^1(\mathrm{TT})] + [^1(\mathrm{T...T})] + [(\mathrm{T...T})]$. The simulated populations were convolved with a Gaussian function with a FWHM of 100 fs to mimic the instrument response of the experimental setup. Since the TA cross sections are unknown for our samples, the triplet and DBP populations were scaled by constant factors to match the experimental data.

J.7 Temperature-dependent PL of rubrene/DBP nanoparticles

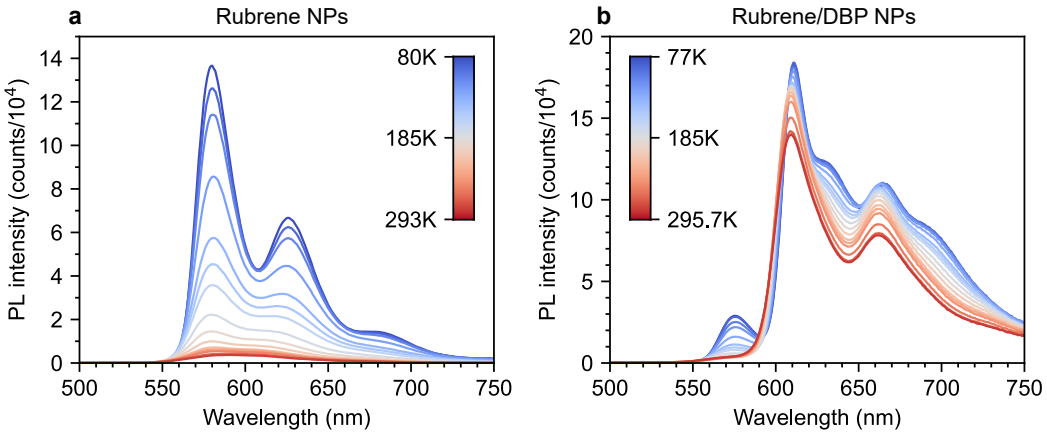

Figure J.10 | Temperature dependence of steady-state PL. a, PL spectra of rubrene NPs at temperatures between 80 K and room temperature. **b**, PL spectra of rubrene/DBP NPs.

J.8 Timescales of singlet-singlet annihilation

Figure J.11 shows the effect of normalisation choice on the apparent timescales of singlet-singlet annihilation. In reality, singlet-singlet annihilation affects the dynamics most strongly within the first ten picoseconds, but this is less clear when normalising to the signal maximum.

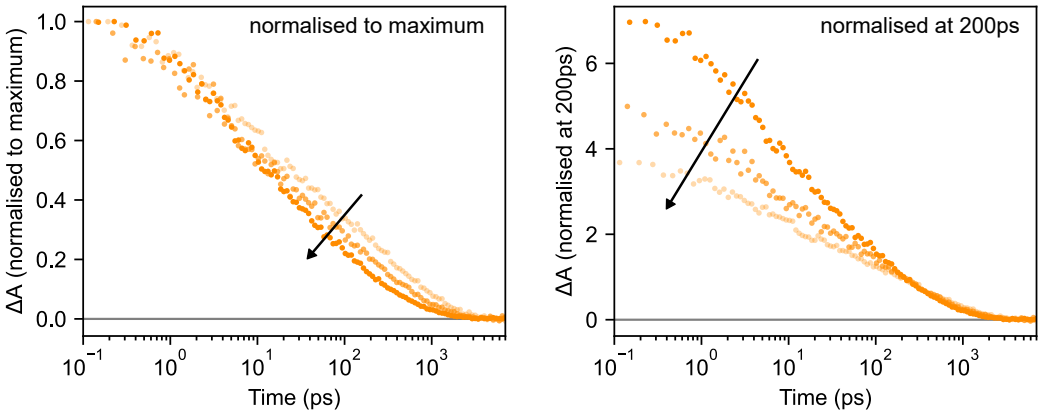

Figure J.11 | Timescales of singlet-singlet annihilation. Singlet population at three different excitation densities normalised to the signal maximum (left) and to the signal at 200 ps (right). The effect of singlet-singlet annihilation is most pronounced during the first 10 ps, but this is obscured somewhat when normalising to the maximum signal.

J.9 Estimations of FRET rates

The rate of Förster resonance energy transfer (FRET) between a donor D and acceptor A is given by[203]

$$k = \frac{1}{\tau}\left(\frac{R_F}{R}\right)^6 \tag{J.12}$$

where τ is the radiative lifetime of the donor, in this case the 16 ns radiative lifetime of rubrene singlet excitons[67,289], R is the intermolecular distance and the Förster radius R_F is given by[203]

$$R_F = 0.2108\left[\frac{\kappa^2\Phi_D}{n^4}\int_0^\infty I_D(\lambda)\epsilon_A(\lambda)\lambda^4 d\lambda\right]^{\frac{1}{6}} \tag{J.13}$$

where κ is an orientational factor, Φ_D is the fluorescence quantum yield of the (isolated) donor, n is refractive index, I_D is the normalised fluorescence spectrum of the donor and ϵ_A is the molar absorption coefficient of the acceptor.

Figure J.12 shows the molar absorption coefficients of rubrene and DBP, measured in Refs. 203 and 45 respectively alongside the fluorescence spectrum of rubrene taken from Ref. 203. From the spectral overlaps, we estimate that the rubrene-to-DBP FRET rate is approximately 50 times greater than the rubrene-to-rubrene FRET rate, if all other parameters are equal. This difference can be attributed to the much greater oscillator strength and spectral overlap of DBP.

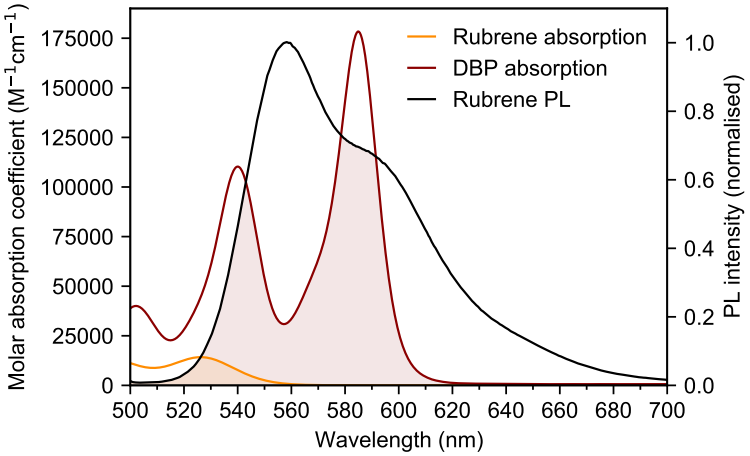

Figure J.12 | Spectral overlap between rubrene and DBP. Molar absorption coefficients of rubrene and DBP are shown together with their overlap with the rubrene photoluminescence spectrum. From the spectral overlaps, we estimate rubrene-to-DBP FRET to be approximately 50 times faster than rubrene self-FRET.

The Förster radius has been previously calculated as 4.7 nm for the rubrene-DBP pair in solid systems[349]. Based on the relative spectral overlap integ-

rals, we estimate the rubrene-rubrene Förster radius to be 2.5 nm. Taking the smallest intermolecular centre-of-mass separation of 7.2 Å in orthorhombic rubrene[279] as a lower bound for R, we estimate a rubrene-rubrene FRET rate of 10 ps, similar to the singlet fission rate.

We do not know how rubrene molecules pack around DBP molecules, but a centre-of-mass distance of 1 nm would seem reasonable, given the significantly larger size of the DBP molecule. This results in an estimated rubrene-DBP FRET rate of 1.5 ps. At 2 nm separation, this rises to 95 ps.

Photo-excited singlet excitons generated on rubrene molecules directly adjacent to a DBP molecule are therefore expected to transfer their energy to DBP before singlet fission takes place. However, since the concentration of DBP molecules is low (1 in 200), most photo-generated rubrene singlets are not nearest neighbours with DBP sites. These excitons must therefore diffuse by rubrene-rubrene FRET in order to get close enough to a DBP molecule to transfer their energy.

Whilst a kinetic Monte Carlo simulation, or similar, would be needed to quantitatively determine the likelihood of a randomly generated exciton transferring its energy to DBP via FRET rather than undergoing singlet fission, we can get a sense of how unlikely this is from simple calculations.

In a time t after photo-excitation, a singlet exciton diffusing via rubrene-rubrene FRET has an average mean-squared displacement of

$$\langle r^2 \rangle \approx k a^2 t \tag{J.14}$$

where k is the rubrene-rubrene FRET rate and a is the distance of a single hop. Let us take the time t when a fraction f of initially generated excitons have undergone singlet fission:

$$1 - f = e^{-k_{sf} t}. \tag{J.15}$$

Rearranging for t and inserting into our expression for the mean square displacement, we find

$$\langle r^2 \rangle \approx a^2 \frac{k}{k_{sf}} \ln\left(\frac{1}{1-f}\right). \tag{J.16}$$

Since we estimate the rubrene-rubrene FRET rate to be approximately equal to the singlet fission rate, the root mean square displacement is approximately

$$r_{rms} \sim a\sqrt{\ln\left(\frac{1}{1-f}\right)}. \tag{J.17}$$

Again taking a to be 7.2 Å, we find that by the time 99% of excitons have

undergone singlet fission ($f = 0.99$) the root mean square displacement of a typical exciton is only around 1.5 nm, or just over two intermolecular separations. Thus we would expect singlet fission to outcompete rubrene-DBP FRET fairly comprehensively and indeed the experiments presented in this work clearly demonstrate that this is the case.

To cross-check this analysis, we estimate the root mean square displacement of rubrene singlet excitons when the elapsed time t corresponds instead to the 16 ns radiative lifetime of rubrene. In this case, we obtain a value of 29 nm, in very close agreement with the reported singlet exciton diffusion length of (35 ± 2) nm for disordered, solid rubrene[349].

References

[1] Hulme, M. 1.5°C and climate research after the Paris Agreement. *Nat. Clim. Change* **6**, 222–224 (2016).

[2] Intergovernmental Panel on Climate Change (IPCC). *Global Warming of 1.5˚C: An IPCC Special Report on the Impacts of Global Warming of 1.5˚C Above Pre-Industrial Levels and Related Global Greenhouse Gas Emission Pathways, in the Context of Strengthening the Global Response to the Threat of Climate Change,* (World Meteorological Organization, Geneva, 2018).

[3] Hoegh-Guldberg, O. *et al.* The human imperative of stabilizing global climate change at 1.5°C. *Science* **365**, eaaw6974 (2019).

[4] Breyer, C. *et al.* On the role of solar photovoltaics in global energy transition scenarios. *Prog. Photovoltaics Res. Appl.* **25**, 727–745 (2017).

[5] Wilson, G. M. *et al.* The 2020 photovoltaic technologies roadmap. *J. Phys. D. Appl. Phys.* **53**, 493001 (2020).

[6] Creutzig, F. *et al.* The underestimated potential of solar energy to mitigate climate change. *Nat. Energy* **2**, 17140 (2017).

[7] Elshurafa, A. M., Albardi, S. R., Bigerna, S. & Bollino, C. A. Estimating the learning curve of solar PV balance–of–system for over 20 countries: Implications and policy recommendations. *J. Clean. Prod.* **196**, 122–134 (2018).

[8] Shockley, W. & Queisser, H. J. Detailed balance limit of efficiency of p-n junction solar cells. *J. Appl. Phys.* **32**, 510–519 (1961).

[9] Green, M. A. *et al.* Solar cell efficiency tables (version 53). *Prog. Photovoltaics Res. Appl.* **27**, 3–12 (2019).

[10] McCandless, B. E. & Sites, J. R. Cadmium telluride solar cells. *Handb. Photovolt. Sci. Eng.* 600–641 (2011).

[11] Petrus, M. L. *et al.* Capturing the sun: A review of the challenges and perspectives of perovskite solar cells. *Adv. Energy Mater.* **7**, 1700264 (2017).

[12] Al-Ashouri, A. *et al.* Monolithic perovskite/silicon tandem solar cell with >29% efficiency by enhanced hole extraction. *Science* **370**, 1300–1309 (2020).

[13] Day, J., Senthilarasu, S. & Mallick, T. K. Improving spectral modification for applications in solar cells: A review. *Renew. Energy* **132**, 186–205 (2019).

[14] Tayebjee, M. J. Y., McCamey, D. R. & Schmidt, T. W. Beyond Shockley–Queisser: Molecular approaches to high-efficiency photovoltaics. *J. Phys. Chem. Lett.* **6**, 2367–2378 (2015).

[15] Smith, M. B. & Michl, J. Singlet fission. *Chem. Rev.* **110**, 6891–6936 (2010).

[16] Smith, M. B. & Michl, J. Recent advances in singlet fission. *Annu. Rev. Phys. Chem.* **64**, 361–386 (2013).

[17] Rao, A. & Friend, R. H. Harnessing singlet exciton fission to break the Shockley–Queisser limit. *Nat. Rev. Mater.* **2**, 17063 (2017).

[18] Einzinger, M. *et al.* Sensitization of silicon by singlet exciton fission in tetracene. *Nature* **571**, 90–94 (2019).

[19] Singh-Rachford, T. N. & Castellano, F. N. Photon upconversion based on sensitized triplet–triplet annihilation. *Coord. Chem. Rev.* **254**, 2560–2573 (2010).

[20] Frazer, L., Gallaher, J. K. & Schmidt, T. W. Optimizing the efficiency of solar photon upconversion. *ACS Energy Lett.* **2**, 1346–1354 (2017).

[21] Zhou, J., Liu, Q., Feng, W., Sun, Y. & Li, F. Upconversion luminescent materials: Advances and applications. *Chem. Rev.* **115**, 395–465 (2015).

[22] Bharmoria, P., Bildirir, H. & Moth-Poulsen, K. Triplet–triplet annihilation based near infrared to visible molecular photon upconversion. *Chem. Soc. Rev.* **49**, 6529–6554 (2020).

[23] Sasaki, Y. *et al.* Near-infrared optogenetic genome engineering based on photon-upconversion hydrogels. *Angew. Chemie Int. Ed.* **58**, 17827–17833 (2019).

[24] Geacintov, N., Pope, M. & Vogel, F. Effect of magnetic field on the fluorescence of tetracene crystals: Exciton fission. *Phys. Rev. Lett.* **22**, 593–596 (1969).

[25] Johnson, R. C., Merrifield, R. E., Avakian, P. & Flippen, R. B. Effects of magnetic fields on the mutual annihilation of triplet excitons in molecular crystals. *Phys. Rev. Lett.* **19**, 285–287 (1967).

[26] Dexter, D. Two ideas on energy transfer phenomena: Ion-pair effects involving the OH stretching mode, and sensitization of photovoltaic cells. *J. Lumin.* **18-19**, 779–784 (1979).

[27] Hanna, M. C. & Nozik, A. J. Solar conversion efficiency of photovoltaic and photoelectrolysis cells with carrier multiplication absorbers. *J. Appl. Phys.* **100**, 074510 (2006).

[28] Sibbett, W., Lagatsky, A. A. & Brown, C. T. A. The development and application of femtosecond laser systems. *Opt. Express* **20**, 6989 (2012).

[29] Musser, A. J. & Clark, J. Triplet-pair states in organic semiconductors. *Annu. Rev. Phys. Chem.* **70**, 323–351 (2019).

[30] Miyata, K., Conrad-Burton, F. S., Geyer, F. L. & Zhu, X.-Y. Triplet pair states in singlet fission. *Chem. Rev.* **119**, 4261–4292 (2019).

[31] Bardeen, C. J. Time dependent correlations of entangled states with nondegenerate branches and possible experimental realization using singlet fission. *J. Chem. Phys.* **151**, 124503 (2019).

[32] Dover, C. B. *et al.* Endothermic singlet fission is hindered by excimer formation. *Nat. Chem.* **10**, 305–310 (2018).

[33] Najafov, H., Lee, B., Zhou, Q., Feldman, L. C. & Podzorov, V. Observation of long-range exciton diffusion in highly ordered organic semiconductors. *Nat. Mater.* **9**, 938–943 (2010).

[34] Irkhin, P., Ryasnyanskiy, A., Koehler, M. & Biaggio, I. Absorption and photoluminescence spectroscopy of rubrene single crystals. *Phys. Rev. B* **86**, 085143 (2012).

[35] Miyata, K. *et al.* Coherent singlet fission activated by symmetry breaking. *Nat. Chem.* **9**, 983–989 (2017).

[36] Breen, I. *et al.* Triplet separation drives singlet fission after femtosecond correlated triplet pair production in rubrene. *J. Am. Chem. Soc.* **139**, 11745–11751 (2017).

[37] Bera, K., Douglas, C. J. & Frontiera, R. R. Femtosecond Raman microscopy reveals structural dynamics leading to triplet separation in rubrene singlet fission. *J. Phys. Chem. Lett.* **8**, 5929–5934 (2017).

[38] Cheng, Y. Y. *et al.* Kinetic analysis of photochemical upconversion by triplet-triplet annihilation: Beyond any spin statistical limit. *J. Phys. Chem. Lett.* **1**, 1795–1799 (2010).

[39] Zhao, J., Ji, S. & Guo, H. Triplet–triplet annihilation based upconversion: from triplet sensitizers and triplet acceptors to upconversion quantum yields. *RSC Adv.* **1**, 937–950 (2011).

[40] Schulze, T. F. & Schmidt, T. W. Photochemical upconversion: present status and prospects for its application to solar energy conversion. *Energy Environ. Sci.* **8**, 103–125 (2015).

[41] Hoseinkhani, S., Tubino, R., Meinardi, F. & Monguzzi, A. Achieving the photon up-conversion thermodynamic yield upper limit by sensitized triplet–triplet annihilation. *Phys. Chem. Chem. Phys.* **17**, 4020–4024 (2015).

[42] Radiunas, E. *et al.* Understanding the limitations of NIR-to-visible photon upconversion in phthalocyanine-sensitized rubrene systems. *J. Mater. Chem. C* **8**, 5525–5534 (2020).

[43] Wu, M. *et al.* Solid-state infrared-to-visible upconversion sensitized by colloidal nanocrystals. *Nat. Photonics* **10**, 31–34 (2016).

[44] Radiunas, E. *et al.* Impact of t-butyl substitution in a rubrene emitter for solid state NIR-to-visible photon upconversion. *Phys. Chem. Chem. Phys.* **22**, 7392–7403 (2020).

[45] Kinoshita, M. *et al.* Photon upconverting solid films with improved efficiency for endowing perovskite solar cells with near-infrared sensitivity. *ChemPhotoChem* **4**, 5271–5278 (2020).

[46] Wieghold, S., Bieber, A. S., VanOrman, Z. A., Rodriguez, A. & Nienhaus, L. Is disorder beneficial in perovskite-sensitized solid-state upconversion? The role of DBP doping in rubrene. *J. Phys. Chem. C* **124**, 18132–18140 (2020).

[47] Blankenship, R. E. *Molecular mechanisms of photosynthesis* (John Wiley & Sons, 2014).

[48] Webb, A. R. Who, what, where and when—influences on cutaneous vitamin D synthesis. *Prog. Biophys. Mol. Biol.* **92**, 17–25 (2006).

[49] Turro, N. J., Ramamurthy, V. & Scaiano, J. C. *Modern Molecular Photochemistry of Organic Molecules* (University Science Books, 2010).

[50] Nelson, J. A. *The physics of solar cells* (World Scientific Publishing Company, 2003).

[51] Adachi, C. Third-generation organic electroluminescence materials. *Jpn. J. Appl. Phys.* **53**, 60101 (2014).

[52] Chénais, S. & Forget, S. Recent advances in solid-state organic lasers. *Polym. Int.* **61**, 390–406 (2012).

[53] Sirringhaus, H. 25th anniversary article: Organic field-effect transistors: The path beyond amorphous silicon. *Adv. Mater.* **26**, 1319–1335 (2014).

[54] Dou, L. *et al.* 25th anniversary article: A decade of organic/polymeric photovoltaic research. *Adv. Mater.* **25**, 6642–6671 (2013).

[55] Huang, L. *et al.* Designing next generation of photon upconversion: Recent advances in organic triplet-triplet annihilation upconversion nanoparticles. *Biomaterials* **201**, 77–86 (2019).

[56] Barford, W. *Electronic and optical properties of conjugated polymers*, vol. 159 (Oxford University Press, 2013).

[57] Grosso, G. & Pastori Parravicini, G. *Solid state physics* (Elsevier, Waltham, Massachusetts, 2014), second edn.

[58] Lim, S.-H., Bjorklund, T. G., Spano, F. C. & Bardeen, C. J. Exciton delocalization and superradiance in tetracene thin films and nanoaggregates. *Phys. Rev. Lett.* **92**, 107402 (2004).

[59] Köhler, A. & Bässler, H. Triplet states in organic semiconductors. *Mater. Sci. Eng. R Reports* **66**, 71–109 (2009).

[60] Xu, S. *et al.* Tuning the singlet-triplet energy gap: a unique approach to efficient photosensitizers with aggregation-induced emission (AIE) characteristics. *Chem. Sci.* **6**, 5824–5830 (2015).

[61] Spano, F. C. The spectral signatures of frenkel polarons in H- and J-aggregates. *Acc. Chem. Res.* **43**, 429–439 (2010).

[62] Nesbitt, D. J. & Field, R. W. Vibrational energy flow in highly excited molecules: Role of intramolecular vibrational redistribution. *J. Phys. Chem.* **100**, 12735–12756 (1996).

[63] Hochstrasser, R. M. & Li, T.-Y. Spectral manifestations of nonradiative processes in azulene. *J. Mol. Spectrosc.* **41**, 297–301 (1972).

[64] Yang, X., Dykstra, T. E. & Scholes, G. D. Photon-echo studies of collective absorption and dynamic localization of excitation in conjugated polymers and oligomers. *Phys. Rev. B - Condens. Matter Mater. Phys.* **71**, 1–15 (2005).

[65] Scholes, G. D., Larsen, D. S., Fleming, G. R., Rumbles, G. & Burn, P. L. Origin of line broadening in the electronic absorption spectra of conjugated polymers: Three-pulse-echo studies of MEH-PPV in toluene. *Phys. Rev. B* **61**, 13670–13678 (2000).

[66] Karabunarliev, S., Baumgarten, M., Bittner, E. R. & Müllen, K. Rigorous Franck–Condon absorption and emission spectra of conjugated oligomers from quantum chemistry. *J. Chem. Phys.* **113**, 11372–11381 (2000).

[67] Strickler, S. J. & Berg, R. A. Relationship between absorption intensity and fluorescence lifetime of molecules. *J. Chem. Phys.* **37**, 814–822 (1962).

[68] Kasha, M. Characterization of electronic transitions in complex molecules. *Discuss. Faraday Soc.* **9**, 14–19 (1950).

[69] Verhoeven, J. W. Glossary of terms used in photochemistry (IUPAC recommendations 1996). *Pure Appl. Chem.* **68**, 2223–2286 (1996).

[70] Siebrand, W. Radiationless transitions in polyatomic molecules. I. Calculation of Franck—Condon factors. *J. Chem. Phys.* **46**, 440–447 (1967).

[71] Yarkony, D. R. Conical intersections: Diabolical and often misunderstood. *Acc. Chem. Res.* **31**, 511–518 (1998).

[72] Beljonne, D., Shuai, Z., Pourtois, G. & Bredas, J. L. Spin-orbit coupling and intersystem crossing in conjugated polymers: A configuration interaction description. *J. Phys. Chem. A* **105**, 3899–3907 (2001).

[73] Tatchen, J., Gilka, N. & Marian, C. M. Intersystem crossing driven by vibronic spin–orbit coupling: a case study on psoralen. *Phys. Chem. Chem. Phys.* **9**, 5209–5221 (2007).

[74] Yong, C. K. *et al.* The entangled triplet pair state in acene and heteroacene materials. *Nat. Commun.* **8**, 15953 (2017).

[75] Orlandi, G. & Siebrand, W. Theory of vibronic intensity borrowing. Comparison of Herzberg-Teller and Born-Oppenheimer coupling. *J. Chem. Phys.* **58**, 4513–4523 (1973).

[76] Albrecht, A. C. On the theory of Raman intensities. *J. Chem. Phys.* **34**, 1476–1484 (1961).

[77] Kasha, M., Rawls, H. R. & Ashraf El-Bayoumi, M. The exciton model in molecular spectroscopy. *Pure Appl. Chem.* **11**, 371–392 (1965).

[78] Spano, F. C. The fundamental photophysics of conjugated oligomer herringbone aggregates. *J. Chem. Phys.* **118**, 981–994 (2002).

[79] Spano, F. C. Temperature dependent exciton emission from herringbone aggregates of conjugated oligomers. *J. Chem. Phys.* **120**, 7643–7658 (2004).

[80] Spano, F. C. Modeling disorder in polymer aggregates: The optical spectroscopy of regioregular poly(3-hexylthiophene) thin films. *J. Chem. Phys.* **122**, 234701 (2005).

[81] Spano, F. C., Clark, J., Silva, C. & Friend, R. H. Determining exciton coherence from the photoluminescence spectral line shape in poly(3-hexylthiophene) thin films. *J. Chem. Phys.* **130**, 074904 (2009).

[82] Clark, J., Chang, J.-F., Spano, F. C., Friend, R. H. & Silva, C. Determining exciton bandwidth and film microstructure in polythiophene films using linear absorption spectroscopy. *Appl. Phys. Lett.* **94**, 163306 (2009).

[83] Spano, F. C. & Silva, C. H- and J-aggregate behavior in polymeric semiconductors. *Annu. Rev. Phys. Chem.* **65**, 477–500 (2014).

[84] Hestand, N. J. & Spano, F. C. Molecular aggregate photophysics beyond the Kasha model: Novel design principles for organic materials. *Acc. Chem. Res.* **50**, 341–350 (2017).

[85] Hestand, N. J. & Spano, F. C. Expanded theory of H- and J-molecular aggregates: The effects of vibronic coupling and intermolecular charge transfer. *Chem. Rev.* **118**, 7069–7163 (2018).

[86] Hestand, N. J. *et al.* Polarized absorption in crystalline pentacene: Theory vs experiment. *J. Phys. Chem. C* **119**, 22137–22147 (2015).

[87] Förster, T. Zwischenmolekulare energiewanderung und fluoreszenz. *Ann. Phys.* **437**, 55–75 (1948).

[88] Laquai, F., Park, Y.-S., Kim, J.-J. & Basché, T. Excitation energy transfer in organic materials: From fundamentals to optoelectronic devices. *Macromol. Rapid Commun.* **30**, 1203–1231 (2009).

[89] Hedley, G. J., Ruseckas, A. & Samuel, I. D. W. Light harvesting for organic photovoltaics. *Chem. Rev.* **117**, 796–837 (2017).

[90] Dexter, D. L. A theory of sensitized luminescence in solids. *J. Chem. Phys.* **21**, 836–850 (1953).

[91] Yost, S. R., Hontz, E., Yeganeh, S. & Van Voorhis, T. Triplet vs singlet energy transfer in organic semiconductors: The tortoise and the hare. *J. Phys. Chem. C* **116**, 17369–17377 (2012).

[92] Mikhnenko, O. V., Blom, P. W. M. & Nguyen, T.-Q. Exciton diffusion in organic semiconductors. *Energy Environ. Sci.* **8**, 1867–1888 (2015).

[93] Irkhin, P. & Biaggio, I. Direct imaging of anisotropic exciton diffusion and triplet diffusion length in rubrene single crystals. *Phys. Rev. Lett.* **107**, 017402 (2011).

[94] Akselrod, G. M. *et al.* Visualization of exciton transport in ordered and disordered molecular solids. *Nat. Commun.* **5**, 3646 (2014).

[95] Tamai, Y., Matsuura, Y., Ohkita, H., Benten, H. & Ito, S. One-dimensional singlet exciton diffusion in poly(3-hexylthiophene) crystalline domains. *J. Phys. Chem. Lett.* **5**, 399–403 (2014).

[96] Shaw, P. E., Ruseckas, A. & Samuel, I. D. W. Exciton diffusion measurements in poly(3-hexylthiophene). *Adv. Mater.* **20**, 3516–3520 (2008).

[97] Kepler, R. G., Caris, J. C., Avakian, P. & Abramson, E. Triplet excitons and delayed fluorescence in anthracene crystals. *Phys. Rev. Lett.* **10**, 400–402 (1963).

[98] Suna, A. Kinematics of exciton-exciton annihilation in molecular crystals. *Phys. Rev. B* **1**, 1716–1739 (1970).

[99] Torney, D. C. & McConnell, H. M. Diffusion-limited reactions in one dimension. *J. Phys. Chem.* **87**, 1941–1951 (1983).

[100] Chandrasekhar, S. Stochastic problems in Physics and Astronomy. *Rev. Mod. Phys.* **15**, 1–89 (1943).

[101] Kroeze, J. E., Savenije, T. J., Vermeulen, M. J. W. & Warman, J. M. Contactless determination of the photoconductivity action spectrum, exciton diffusion length, and charge separation efficiency in polythiophene-sensitized TiO_2 bilayers. *J. Phys. Chem. B* **107**, 7696–7705 (2003).

[102] Johnson, R. C. & Merrifield, R. E. Effects of magnetic fields on the mutual annihilation of triplet excitons in anthracene crystals. *Phys. Rev. B* **1**, 896–902 (1970).

[103] Kim, H. & Zimmerman, P. M. Coupled double triplet state in singlet fission. *Phys. Chem. Chem. Phys.* **20**, 30083–30094 (2018).

[104] Sanders, S. N. *et al.* Understanding the bound triplet-pair state in singlet fission. *Chem* **5**, 1988–2005 (2019).

[105] Swenberg, C. E. & Stacy, W. T. Bimolecular radiationless transitions in crystalline tetracene. *Chem. Phys. Lett.* **2**, 327–328 (1968).

[106] Goldschmidt, J. C. & Fischer, S. Upconversion for photovoltaics - a review of materials, devices and concepts for performance enhancement. *Adv. Opt. Mater.* **3**, 510–535 (2015).

[107] Gray, V., Moth-Poulsen, K., Albinsson, B. & Abrahamsson, M. Towards efficient solid-state triplet–triplet annihilation based photon upconversion: Supramolecular, macromolecular and self-assembled systems. *Coord. Chem. Rev.* **362**, 54–71 (2018).

[108] Wilson, M. W. B. *et al.* Ultrafast dynamics of exciton fission in polycrystalline pentacene. *J. Am. Chem. Soc.* **133**, 11830–11833 (2011).

[109] Burgos, J., Pope, M., Swenberg, C. E. & Alfano, R. R. Heterofission in pentacene-doped tetracene single crystals. *Phys. status solidi* **83**, 249–256 (1977).

[110] Wilson, M. W. B. *et al.* Temperature-independent singlet exciton fission in tetracene. *J. Am. Chem. Soc.* **135**, 16680–16688 (2013).

[111] Tapping, P. C. & Huang, D. M. Comment on "Magnetic field effects on singlet fission and fluorescence decay dynamics in amorphous rubrene". *J. Phys. Chem. C* **120**, 25151–25157 (2016).

[112] Piland, G. B., Burdett, J. J., Kurunthu, D. & Bardeen, C. J. Magnetic field effects on singlet fission and fluorescence decay dynamics in amorphous rubrene. *J. Phys. Chem. C* **117**, 1224–1236 (2013).

[113] Steiner, U. E. & Ulrich, T. Magnetic field effects in chemical kinetics and related phenomena. *Chem. Rev.* **89**, 51–147 (1989).

[114] Yago, T., Ishikawa, K., Katoh, R. & Wakasa, M. Magnetic field effects on triplet pair generated by singlet fission in an organic crystal: Application of radical pair model to triplet pair. *J. Phys. Chem. C* **120**, 27858–27870 (2016).

[115] Bayliss, S. L. *et al.* Spin signatures of exchange-coupled triplet pairs formed by singlet fission. *Phys. Rev. B* **94**, 045204 (2016).

[116] Taffet, E. J., Beljonne, D. & Scholes, G. D. Overlap-driven splitting of triplet pairs in singlet fission. *J. Am. Chem. Soc.* **142**, 20040–20047 (2020).

[117] Scholes, G. D. Correlated pair states formed by singlet fission and exciton–exciton annihilation. *J. Phys. Chem. A* **119**, 12699–12705 (2015).

[118] Kollmar, C. Electronic structure of diradical and dicarbene intermediates in short-chain polydiacetylene oligomers. *J. Chem. Phys.* **98**, 7210–7228 (1993).

[119] Bayliss, S. L. *et al.* Site-selective measurement of coupled spin pairs in an organic semiconductor. *Proc. Natl. Acad. Sci.* **115**, 5077–5082 (2018).

[120] Wakasa, M. *et al.* What can be learned from magnetic field effects on singlet fission: Role of exchange interaction in excited triplet pairs. *J. Phys. Chem. C* **119**, 25840–25844 (2015).

[121] Ishikawa, K., Yago, T. & Wakasa, M. Exploring the structure of an exchange-coupled triplet pair generated by singlet fission in crystalline diphenylhexatriene: Anisotropic magnetic field effects on fluorescence in high fields. *J. Phys. Chem. C* **122**, 22264–22272 (2018).

[122] Merrifield, R. E., Avakian, P. & Groff, R. P. Fission of singlet excitons into pairs of triplet excitons in tetracene crystals. *Chem. Phys. Lett.* **3**, 155–157 (1969).

[123] Merrifield, R. E. Theory of magnetic field effects on the mutual annihilation of triplet excitons. *J. Chem. Phys.* **48**, 4318–4319 (1968).

[124] Burdett, J. J., Piland, G. B. & Bardeen, C. J. Magnetic field effects and the role of spin states in singlet fission. *Chem. Phys. Lett.* **585**, 1–10 (2013).

[125] Tarasov, V. V., Zoriniants, G. E., Shushin, A. I. & Triebel, M. M. The role of spin-lattice relaxation in magnetic field effects on the luminescence of amorphous and polycrystalline rubrene films. *Chem. Phys. Lett.* **267**, 58–64 (1997).

[126] Pedersen, J. B. Theory of chemically induced dynamic electron polarization. I. *J. Chem. Phys.* **58**, 2746 (1973).

[127] Pedersen, J. B. & Freed, J. H. Theory of chemically induced dynamic electron polarization. II. *J. Chem. Phys.* **59**, 2869–2885 (1973).

[128] Hu, B., Yan, L. & Shao, M. Magnetic-field effects in organic semiconducting materials and devices. *Adv. Mater.* **21**, 1500–1516 (2009).

[129] Kingma, H., van Grondelle, R. & Duysens, L. Magnetic-field effects in photosynthetic bacteria. II. Formation of triplet states in the reaction center and the antenna of Rhodospirillum rubrum and Rhodopseudomonas sphaeroides. Magnetic-field effects. *Biochim. Biophys. Acta - Bioenerg.* **808**, 383–399 (1985).

[130] Rodgers, C. T. Magnetic field effects in chemical systems. *Pure Appl. Chem.* **81**, 19–43 (2009).

[131] Ern, V. & Merrifield, R. E. Magnetic field effect on triplet exciton quenching in organic crystals. *Phys. Rev. Lett.* **21**, 609–611 (1968).

[132] Lin, T.-A., Perkinson, C. F. & Baldo, M. A. Strategies for high-performance solid-state triplet–triplet-annihilation-based photon upconversion. *Adv. Mater.* **32**, 1908175 (2020).

[133] Wang, Z. *et al.* Weakly coupled triplet pair states probed by quantum beating in delayed fluorescence in tetracene crystals. *J. Chem. Phys.* **151**, 134309 (2019).

[134] Burdett, J. J. & Bardeen, C. J. Quantum beats in crystalline tetracene delayed fluorescence due to triplet pair coherences produced by direct singlet fission. *J. Am. Chem. Soc.* **134**, 8597–8607 (2012).

[135] Chabr, M., Wild, U., Fünfschilling, J. & Zschokke-Gränacher, I. Quantum beats of prompt fluorescence in tetracene crystals. *Chem. Phys.* **57**, 425–430 (1981).

[136] Lukman, S. *et al.* Efficient singlet fission and triplet-pair emission in a family of zethrene diradicaloids. *J. Am. Chem. Soc.* **139**, 18376–18385 (2017).

[137] Wolf, E. A., Finton, D. M., Zoutenbier, V. & Biaggio, I. Quantum beats of a multiexciton state in rubrene single crystals. *Appl. Phys. Lett.* **112**, 83301 (2018).

[138] Yarmus, L., Rosenthal, J. & Chopp, M. EPR of triplet excitions in tetracene crystals: spin polarization and the role of singlet exciton fission. *Chem. Phys. Lett.* **16**, 477–481 (1972).

[139] Weiss, L. R. *et al.* Strongly exchange-coupled triplet pairs in an organic semiconductor. *Nat. Phys.* **13**, 176–181 (2017).

[140] Tayebjee, M. J. Y. *et al.* Quintet multiexciton dynamics in singlet fission. *Nat. Phys.* **13**, 182–188 (2017).

[141] Lubert-Perquel, D. *et al.* Identifying triplet pathways in dilute pentacene films. *Nat. Commun.* **9**, 4222 (2018).

[142] Chen, M. *et al.* Quintet-triplet mixing determines the fate of the multiexciton state produced by singlet fission in a terrylenediimide dimer at room temperature. *Proc. Natl. Acad. Sci.* **116**, 8178–8183 (2019).

[143] Bae, Y. J. *et al.* Spin dynamics of quintet and triplet states resulting from singlet fission in oriented terrylenediimide and quaterrylenediimide films. *J. Phys. Chem. C* **124**, 9822–9833 (2020).

[144] Pun, A. B. *et al.* Ultra-fast intramolecular singlet fission to persistent multiexcitons by molecular design. *Nat. Chem.* **11**, 821–828 (2019).

[145] Papadopoulos, I. *et al.* Varying the interpentacene electronic coupling to tune singlet fission. *J. Am. Chem. Soc.* **141**, 6191–6203 (2019).

[146] Basel, B. S. *et al.* Evidence for charge-transfer mediation in the primary events of singlet fission in a weakly coupled pentacene dimer. *Chem* **4**, 1092–1111 (2018).

[147] Basel, B. S. *et al.* Unified model for singlet fission within a non-conjugated covalent pentacene dimer. *Nat. Commun.* **8**, 15171 (2017).

[148] Kumarasamy, E. *et al.* Tuning singlet fission in π-bridge-π chromophores. *J. Am. Chem. Soc.* **139**, 12488–12494 (2017).

[149] Bayliss, S. L. *et al.* Geminate and nongeminate recombination of triplet excitons formed by singlet fission. *Phys. Rev. Lett.* **112**, 238701 (2014).

[150] Stern, H. L. *et al.* Identification of a triplet pair intermediate in singlet exciton fission in solution. *Proc. Natl. Acad. Sci.* **112**, 7656–7661 (2015).

[151] Stern, H. L. *et al.* Vibronically coherent ultrafast triplet-pair formation and subsequent thermally activated dissociation control efficient endothermic singlet fission. *Nat. Chem.* **9**, 1205–1212 (2017).

[152] Burdett, J. J., Müller, A. M., Gosztola, D. & Bardeen, C. J. Excited state dynamics in solid and monomeric tetracene: The roles of superradiance and exciton fission. *J. Chem. Phys.* **133**, 144506 (2010).

[153] Tayebjee, M. J. Y., Clady, R. G. C. R. & Schmidt, T. W. The exciton dynamics in tetracene thin films. *Phys. Chem. Chem. Phys.* **15**, 14797–14805 (2013).

[154] Bakulin, A. A. *et al.* Real-time observation of multiexcitonic states in ultrafast singlet fission using coherent 2D electronic spectroscopy. *Nat. Chem.* **8**, 16–23 (2016).

[155] Josue, J. S. & Frank, H. A. Direct determination of the S_1 excited-state energies of xanthophylls by low-temperature fluorescence spectroscopy. *J. Phys. Chem. A* **106**, 4815–4824 (2002).

[156] Petek, H. *et al.* The 2^1A_g state of trans,trans-1,3,5,7-octatetraene in free jet expansions. *J. Chem. Phys.* **98**, 3777–3794 (1993).

[157] Mauck, C. M. *et al.* Singlet fission via an excimer-like intermediate in 3,6-bis(thiophen-2-yl)diketopyrrolopyrrole derivatives. *J. Am. Chem. Soc.* **138**, 11749–11761 (2016).

[158] Hu, J. *et al.* New insights into the design of conjugated polymers for intramolecular singlet fission. *Nat. Commun.* **9**, 2999 (2018).

[159] Thampi, A. *et al.* Elucidation of excitation energy dependent correlated triplet pair formation pathways in an endothermic singlet fission system. *J. Am. Chem. Soc.* **140**, 4613–4622 (2018).

[160] Feng, X., Luzanov, A. V. & Krylov, A. I. Fission of entangled spins: An electronic structure perspective. *J. Phys. Chem. Lett.* **4**, 3845–3852 (2013).

[161] Feng, X. & Krylov, A. I. On couplings and excimers: lessons from studies of singlet fission in covalently linked tetracene dimers. *Phys. Chem. Chem. Phys.* **18**, 7751–7761 (2016).

[162] Chien, A. D. & Zimmerman, P. M. Recovering dynamic correlation in spin flip configuration interaction through a difference dedicated approach. *J. Chem. Phys.* **146**, 014103 (2017).

[163] Khan, S. & Mazumdar, S. Theory of transient excited state absorptions in pentacene and derivatives: Triplet–triplet biexciton versus free triplets. *J. Phys. Chem. Lett.* **8**, 5943–5948 (2017).

[164] Khan, S. & Mazumdar, S. Optical probes of the quantum-entangled triplet-triplet state in a heteroacene dimer. *Phys. Rev. B* **98**, 165202 (2018).

[165] Khan, S. & Mazumdar, S. Free triplets versus bound triplet–triplet biexciton in intramolecular singlet fission materials: Structure–property correlations. *J. Phys. Chem. C* **124**, 1171–1177 (2020).

[166] Sanders, S. N. *et al.* Quantitative intramolecular singlet fission in bipentacenes. *J. Am. Chem. Soc.* **137**, 8965–8972 (2015).

[167] Sanders, S. N. *et al.* Intramolecular singlet fission in oligoacene heterodimers. *Angew. Chemie* **128**, 3434–3438 (2016).

[168] Sanders, S. N. *et al.* Singlet fission in polypentacene. *Chem* **1**, 505–511 (2016).

[169] Pensack, R. D. *et al.* Observation of two triplet-pair intermediates in singlet exciton fission. *J. Phys. Chem. Lett.* **7**, 2370–2375 (2016).

[170] Pensack, R. D. *et al.* Striking the right balance of intermolecular coupling for high-efficiency singlet fission. *Chem. Sci.* **9**, 6240–6259 (2018).

[171] Jones, A. C., Kearns, N. M., Ho, J.-J., Flach, J. T. & Zanni, M. T. Impact of non-equilibrium molecular packings on singlet fission in microcrystals observed using 2D white-light microscopy. *Nat. Chem.* **12**, 40–47 (2020).

[172] Zimmerman, P. M., Zhang, Z. & Musgrave, C. B. Singlet fission in pentacene through multi-exciton quantum states. *Nat. Chem.* **2**, 648–652 (2010).

[173] Zimmerman, P. M., Bell, F., Casanova, D. & Head-Gordon, M. Mechanism for singlet fission in pentacene and tetracene: From single exciton to two triplets. *J. Am. Chem. Soc.* **133**, 19944–19952 (2011).

[174] Zimmerman, P. M., Musgrave, C. B. & Head-Gordon, M. A correlated electron view of singlet fission. *Acc. Chem. Res.* **46**, 1339–1347 (2013).

[175] Renaud, N., Sherratt, P. A. & Ratner, M. A. Mapping the relation between stacking geometries and singlet fission yield in a class of organic crystals. *J. Phys. Chem. Lett.* **4**, 1065–1069 (2013).

[176] Berkelbach, T. C., Hybertsen, M. S. & Reichman, D. R. Microscopic theory of singlet exciton fission. I. General formulation. *J. Chem. Phys.* **138**, 114102 (2013).

[177] Berkelbach, T. C., Hybertsen, M. S. & Reichman, D. R. Microscopic theory of singlet exciton fission. II. Application to pentacene dimers and the role of superexchange. *J. Chem. Phys.* **138**, 114103 (2013).

[178] Berkelbach, T. C., Hybertsen, M. S. & Reichman, D. R. Microscopic theory of singlet exciton fission. III. Crystalline pentacene. *J. Chem. Phys.* **141**, 074705 (2014).

[179] Greyson, E. C., Vura-Weis, J., Michl, J. & Ratner, M. A. Maximizing singlet fission in organic dimers: Theoretical investigation of triplet yield in the regime of localized excitation and fast coherent electron transfer. *J. Phys. Chem. B* **114**, 14168–14177 (2010).

[180] Lukman, S. *et al.* Tuneable singlet exciton fission and triplet-triplet annihilation in an orthogonal pentacene dimer. *Adv. Funct. Mater.* **25**, 5452–5461 (2015).

[181] Johnson, J. C., Nozik, A. J. & Michl, J. The role of chromophore coupling in singlet fission. *Acc. Chem. Res.* **46**, 1290–1299 (2013).

[182] Yost, S. R. *et al.* A transferable model for singlet-fission kinetics. *Nat. Chem.* **6**, 492–497 (2014).

[183] Chan, W.-L. *et al.* Observing the multiexciton state in singlet fission and ensuing ultrafast multielectron transfer. *Science* **334**, 1541 LP – 1545 (2011).

[184] Chan, W.-L., Ligges, M. & Zhu, X.-Y. The energy barrier in singlet fission can be overcome through coherent coupling and entropic gain. *Nat. Chem.* **4**, 840–845 (2012).

[185] Chan, W.-L. *et al.* The quantum coherent mechanism for singlet fission: Experiment and theory. *Acc. Chem. Res.* **46**, 1321–1329 (2013).

[186] Duan, H.-G. *et al.* Intermolecular vibrations mediate ultrafast singlet fission. *Sci. Adv.* **6**, eabb0052 (2020).

[187] Musser, A. J. *et al.* Evidence for conical intersection dynamics mediating ultrafast singlet exciton fission. *Nat. Phys.* **11**, 352–357 (2015).

[188] Tamura, H., Huix-Rotllant, M., Burghardt, I., Olivier, Y. & Beljonne, D. First-principles quantum dynamics of singlet fission: Coherent versus thermally activated mechanisms governed by molecular π-stacking. *Phys. Rev. Lett.* **115**, 107401 (2015).

[189] Ma, L. *et al.* Singlet fission in rubrene single crystal: direct observation by femtosecond pump–probe spectroscopy. *Phys. Chem. Chem. Phys.* **14**, 8307–8312 (2012).

[190] Ma, L. *et al.* Fluorescence from rubrene single crystals: Interplay of singlet fission and energy trapping. *Phys. Rev. B* **87**, 201203 (2013).

[191] Kim, W. & Musser, A. J. Tracking ultrafast reactions in organic materials through vibrational coherence: vibronic coupling mechanisms in singlet fission. *Adv. Phys. X* **6**, 1918022 (2021).

[192] Cruz, C. D., Chronister, E. L. & Bardeen, C. J. Using temperature dependent fluorescence to evaluate singlet fission pathways in tetracene single crystals. *J. Chem. Phys.* **153**, 234504 (2020).

[193] Grieco, C. *et al.* Triplet transfer mediates triplet pair separation during singlet fission in 6,13-bis(triisopropylsilylethynyl)-pentacene. *Adv. Funct. Mater.* **27**, 1703929 (2017).

[194] Lee, T. S. *et al.* Triplet energy transfer governs the dissociation of the correlated triplet pair in exothermic singlet fission. *J. Phys. Chem. Lett.* **9**, 4087–4095 (2018).

[195] Munson, K. T. *et al.* Ultrafast triplet pair separation and triplet trapping following singlet fission in amorphous pentacene films. *J. Phys. Chem. C* **124**, 23567–23578 (2020).

[196] Lee, T. S., Lin, Y. L., Kim, H., Rand, B. P. & Scholes, G. D. Two temperature regimes of triplet transfer in the dissociation of the correlated triplet pair after singlet fission. *Can. J. Chem.* **97**, 465–473 (2019).

[197] Srimath Kandada, A. R., Petrozza, A. & Lanzani, G. Ultrafast dissociation of triplets in pentacene induced by an electric field. *Phys. Rev. B* **90**, 75310 (2014).

[198] Yablon, L. M. *et al.* Persistent multiexcitons from polymers with pendent pentacenes. *J. Am. Chem. Soc.* **141**, 9564–9569 (2019).

[199] Korovina, N. V., Chang, C. H. & Johnson, J. C. Spatial separation of triplet excitons drives endothermic singlet fission. *Nat. Chem.* **12**, 391–398 (2020).

[200] Collins, M. I., McCamey, D. R. & Tayebjee, M. J. Y. Fluctuating exchange interactions enable quintet multiexciton formation in singlet fission. *J. Chem. Phys.* **151**, 164104 (2019).

[201] Eaton, S. W. *et al.* Singlet exciton fission in thin films of tert-butyl-substituted terrylenes. *J. Phys. Chem. A* **119**, 4151–4161 (2015).

[202] Gray, V., Dzebo, D., Abrahamsson, M., Albinsson, B. & Moth-Poulsen, K. Triplet–triplet annihilation photon-upconversion: Towards solar energy applications. *Phys. Chem. Chem. Phys.* **16**, 10345–10352 (2014).

[203] Amemori, S., Sasaki, Y., Yanai, N. & Kimizuka, N. Near-infrared-to-visible photon upconversion sensitized by a metal complex with spin-forbidden yet strong S_0–T_1 absorption. *J. Am. Chem. Soc.* **138**, 8702–8705 (2016).

[204] Sasaki, Y., Amemori, S., Kouno, H., Yanai, N. & Kimizuka, N. Near infrared-to-blue photon upconversion by exploiting direct S–T absorption of a molecular sensitizer. *J. Mater. Chem. C* **5**, 5063–5067 (2017).

[205] Huang, Z. *et al.* Hybrid molecule–nanocrystal photon upconversion across the visible and near-infrared. *Nano Lett.* **15**, 5552–5557 (2015).

[206] Green, P. B., Li, Z. & Wilson, M. W. PbS nanocrystals made with excess $PbCl_2$ have an intrinsic shell that reduces their Stokes shift. *J. Phys. Chem. Lett.* **10**, 5897–5901 (2019).

[207] Singh-Rachford, T. N. & Castellano, F. N. Pd(II) phthalocyanine-sensitized triplet-triplet annihilation from rubrene. *J. Phys. Chem. A* **112**, 3550–3556 (2008).

[208] Cheng, Y. Y. *et al.* On the efficiency limit of triplet–triplet annihilation for photochemical upconversion. *Phys. Chem. Chem. Phys.* **12**, 66–71 (2010).

[209] Dick, B. & Nickel, B. Accessibility of the lowest quintet state of organic molecules through triplet-triplet annihilation; an indo ci study. *Chem. Phys.* **78**, 1–16 (1983).

[210] Subramanian, S. *et al.* Chromophore fluorination enhances crystallization and stability of soluble anthradithiophene semiconductors. *J. Am. Chem. Soc.* **130**, 2706–2707 (2008).

[211] Jurchescu, O. D. *et al.* Organic single-crystal field-effect transistors of a soluble anthradithiophene. *Chem. Mater.* **20**, 6733–6737 (2008).

[212] Gundlach, D. J. *et al.* Contact-induced crystallinity for high-performance soluble acene-based transistors and circuits. *Nat. Mater.* **7**, 216–221 (2008).

[213] Hallani, R. K. *et al.* Structural and electronic properties of crystalline, isomerically pure anthradithiophene derivatives. *Adv. Funct. Mater.* **26**, 2341–2348 (2016).

[214] Nelson, S. F., Lin, Y.-Y., Gundlach, D. J. & Jackson, T. N. Temperature-independent transport in high-mobility pentacene transistors. *Appl. Phys. Lett.* **72**, 1854–1856 (1998).

[215] Sundar, V. C. *et al.* Elastomeric transistor stamps: Reversible probing of charge transport in organic crystals. *Science* **303**, 1644 LP – 1646 (2004).

[216] Biaggio, I. & Irkhin, P. Extremely efficient exciton fission and fusion and its dominant contribution to the photoluminescence yield in rubrene single crystals. *Appl. Phys. Lett.* **103**, 263301 (2013).

[217] McGhie, A. R., Garito, A. F. & Heeger, A. J. A gradient sublimer for purification and crystal growth of organic donor and acceptor molecules. *J. Cryst. Growth* **22**, 295–297 (1974).

[218] Jurchescu, O. D., Baas, J. & Palstra, T. T. M. Effect of impurities on the mobility of single crystal pentacene. *Appl. Phys. Lett.* **84**, 3061–3063 (2004).

[219] Rao, V. J. *et al.* AFM-IR and IR-SNOM for the characterization of small molecule organic semiconductors. *J. Phys. Chem. C* **124**, 5331–5344 (2020).

[220] Ashiotis, G. *et al.* The fast azimuthal integration Python library: pyFAI. *J. Appl. Crystallogr.* **48**, 510–519 (2015).

[221] Jiang, Z. GIXSGUI: a MATLAB toolbox for grazing-incidence X-ray scattering data visualization and reduction, and indexing of buried three-dimensional periodic nanostructured films. *J. Appl. Crystallogr.* **48**, 917–926 (2015).

[222] Albert-Seifried, S. & Friend, R. H. Measurement of thermal modulation of optical absorption in pump-probe spectroscopy of semiconducting polymers. *Appl. Phys. Lett.* **98**, 223304 (2011).

[223] Rao, A., Wilson, M. W. B., Albert-Seifried, S., Di Pietro, R. & Friend, R. H. Photophysics of pentacene thin films: The role of exciton fission and heating effects. *Phys. Rev. B* **84**, 195411 (2011).

[224] Berera, R., van Grondelle, R. & Kennis, J. T. M. Ultrafast transient absorption spectroscopy: principles and application to photosynthetic systems. *Photosynth. Res.* **101**, 105–118 (2009).

[225] Jaumot, J., Gargallo, R., de Juan, A. & Tauler, R. A graphical user-friendly interface for MCR-ALS: a new tool for multivariate curve resolution in MATLAB. *Chemom. Intell. Lab. Syst.* **76**, 101–110 (2005).

[226] Jaumot, J., de Juan, A. & Tauler, R. MCR-ALS GUI 2.0: New features and applications. *Chemom. Intell. Lab. Syst.* **140**, 1–12 (2015).

[227] Bossanyi, D. G. *et al.* Emissive spin-0 triplet-pairs are a direct product of triplet–triplet annihilation in pentacene single crystals and anthradithiophene films. *Nat. Chem.* **13**, 163–171 (2021).

[228] Frankevich, E., Lesin, V. & Pristupa, A. Rate constants of singlet exciton fission in a tetracene crystal determined from the RYDMR spectral linewidth. *Chem. Phys. Lett.* **58**, 127–131 (1978).

[229] Burdett, J. J., Gosztola, D. & Bardeen, C. J. The dependence of singlet exciton relaxation on excitation density and temperature in polycrystalline tetracene thin films: Kinetic evidence for a dark intermediate state and implications for singlet fission. *J. Chem. Phys.* **135**, 214508 (2011).

[230] Busby, E. *et al.* A design strategy for intramolecular singlet fission mediated by charge-transfer states in donor–acceptor organic materials. *Nat. Mater.* **14**, 426–433 (2015).

[231] Schrauben, J. N., Ryerson, J. L., Michl, J. & Johnson, J. C. Mechanism of singlet fission in thin films of 1,3-diphenylisobenzofuran. *J. Am. Chem. Soc.* **136**, 7363–7373 (2014).

[232] Margulies, E. A. *et al.* Direct observation of a charge-transfer state preceding high-yield singlet fission in terrylenediimide thin films. *J. Am. Chem. Soc.* **139**, 663–671 (2017).

[233] Liu, H. *et al.* Synthesis and photophysical properties of a "face-to-face" stacked tetracene dimer. *Phys. Chem. Chem. Phys.* **17**, 6523–6531 (2015).

[234] Korovina, N. V. *et al.* Singlet fission in a covalently linked cofacial alkynyltetracene dimer. *J. Am. Chem. Soc.* **138**, 617–627 (2016).

[235] Kim, C.-H. *et al.* Decoupling the effects of self-assembled monolayers on gold, silver, and copper organic transistor contacts. *Adv. Mater. Interfaces* **2**, 1400384 (2015).

[236] Paudel, K., Giesbers, G., Van Schenck, J., Anthony, J. & Ostroverkhova, O. Molecular packing-dependent photoconductivity in functionalized anthradithiophene crystals. *Org. Electron.* **67**, 311–319 (2019).

[237] Campbell, R. B., Robertson, J. M. & Trotter, J. The crystal structure of hexacene, and a revision of the crystallographic data for tetracene and pentacene. *Acta Crystallogr.* **15**, 289–290 (1962).

[238] Wilson, M. W. B., Rao, A., Ehrler, B. & Friend, R. H. Singlet exciton fission in polycrystalline pentacene: From photophysics toward devices. *Acc. Chem. Res.* **46**, 1330–1338 (2013).

[239] Poletayev, A. D. *et al.* Triplet dynamics in pentacene crystals: Applications to fission-sensitized photovoltaics. *Adv. Mater.* **26**, 919–924 (2014).

[240] Wallikewitz, B. H., Kabra, D., Gélinas, S. & Friend, R. H. Triplet dynamics in fluorescent polymer light-emitting diodes. *Phys. Rev. B* **85**, 045209 (2012).

[241] Trinh, M. T. *et al.* Distinct properties of the triplet pair state from singlet fission. *Sci. Adv.* **3**, e1700241 (2017).

[242] Piland, G. B. & Bardeen, C. J. How morphology affects singlet fission in crystalline tetracene. *J. Phys. Chem. Lett.* **6**, 1841–1846 (2015).

[243] Ye, C., Gray, V., Mårtensson, J. & Börjesson, K. Annihilation versus excimer formation by the triplet pair in triplet–triplet annihilation photon upconversion. *J. Am. Chem. Soc.* **141**, 9578–9584 (2019).

[244] Aoki-Matsumoto, T. *et al.* Excitonic photoluminescence in pentacene single crystal. *Int. J. Mod. Phys. B* **15**, 3753–3756 (2001).

[245] He, R., Chi, X., Pinczuk, A., Lang, D. V. & Ramirez, A. P. Extrinsic optical recombination in pentacene single crystals: Evidence of gap states. *Appl. Phys. Lett.* **87**, 211117 (2005).

[246] Anger, F. *et al.* Photoluminescence spectroscopy of pure pentacene, perfluoropentacene, and mixed thin films. *J. Chem. Phys.* **136**, 054701 (2012).

[247] He, R. *et al.* Resonant Raman scattering in nanoscale pentacene films. *Appl. Phys. Lett.* **84**, 987–989 (2004).

[248] Walker, B. J., Musser, A. J., Beljonne, D. & Friend, R. H. Singlet exciton fission in solution. *Nat. Chem.* **5**, 1019–1024 (2013).

[249] Della Valle, R. G. *et al.* Intramolecular and low-frequency intermolecular vibrations of pentacene polymorphs as a function of temperature. *J. Phys. Chem. B* **108**, 1822–1826 (2004).

[250] Della Valle, R. G. *et al.* Exploring the polymorphism of crystalline pentacene. *Org. Electron.* **5**, 1–6 (2004).

[251] Brillante, A. *et al.* Raman phonon spectra of pentacene polymorphs. *Chem. Phys. Lett.* **357**, 32–36 (2002).

[252] Mizuno, K., Matsui, A. & J. Sloan, G. Intermediate exciton-phonon coupling in tetracene. *J. Phys. Soc. Japan* **53**, 2799–2806 (1984).

[253] Nishimura, H., Yamaoka, T., Matsui, A., Mizuno, K. & J. Sloan, G. Exciton self-trapping in tetracene crystals: A case of shallow self-trap depth. *J. Phys. Soc. Japan* **54**, 1627–1633 (1985).

[254] Matsui, A. The polarized absorption edge and the Davydov splitting of anthracene. *J. Phys. Soc. Japan* **21**, 2212–2222 (1966).

[255] Mizuno, K.-i. & Matsui, A. Frenkel exciton dynamics in anthracene under high pressure and quasi-free exciton state. *J. Phys. Soc. Japan* **55**, 2427–2435 (1986).

[256] Mizuno, K.-i., Matsui, A. & Sloan, G. J. Exciton-phonon interaction in tetracene single crystals under pressure. *Chem. Phys.* **131**, 423–433 (1989).

[257] Kobayashi, M., Mizuno, K.-i. & Matsui, A. High-pressure study of free excitons and self-trapped excitons in anthracene crystals at 1.5K. *J. Phys. Soc. Japan* **58**, 809–812 (1989).

[258] Urbach, F. The long-wavelength edge of photographic sensitivity and of the electronic absorption of solids. *Phys. Rev.* **92**, 1324–1324 (1953).

[259] Coropceanu, V., Chen, X.-K., Wang, T., Zheng, Z. & Brédas, J.-L. Charge-transfer electronic states in organic solar cells. *Nat. Rev. Mater.* **4**, 689–707 (2019).

[260] Schweicher, G. *et al.* Molecular semiconductors for logic operations: Dead-end or bright future? *Adv. Mater.* **32**, 1905909 (2020).

[261] Raimondo, L., Silvestri, L., Borghesi, A. & Tavazzi, S. Exciton–lattice phonon coupling in organic semiconductor crystals beyond the static disorder. *J. Phys. Chem. C* **117**, 26248–26254 (2013).

[262] Salleo, A. Electronic traps in organic semiconductors. In Cicoira, F. & Santato, C. (eds.) *Organic Electronics: Emerging Concepts and Technologies*, chap. 14, 341–380 (WILEY-VCH, 2013).

[263] Schreiber, M. & Toyozawa, Y. Numerical experiments on the absorption lineshape of the exciton under lattice vibrations. III. The Urbach rule. *J. Phys. Soc. Japan* **51**, 1544–1550 (1982).

[264] Turlet, J. & Philpott, M. R. Surface and bulk exciton transitions in the reflection spectrum of tetracene crystals. *J. Chem. Phys.* **62**, 4260–4265 (1975).

[265] Vukmirović, N., Bruder, C. & Stojanović, V. M. Electron-phonon coupling in crystalline organic semiconductors: Microscopic evidence for nonpolaronic charge carriers. *Phys. Rev. Lett.* **109**, 126407 (2012).

[266] Sánchez-Carrera, R. S., Paramonov, P., Day, G. M., Coropceanu, V. & Brédas, J.-L. Interaction of charge carriers with lattice vibrations in oligoacene crystals from naphthalene to pentacene. *J. Am. Chem. Soc.* **132**, 14437–14446 (2010).

[267] Coropceanu, V. *et al.* Hole- and electron-vibrational couplings in oligoacene crystals: Intramolecular contributions. *Phys. Rev. Lett.* **89**, 275503 (2002).

[268] Kurik, M. V. & Tsikora, L. I. Exciton–phonon interaction in crystals of linear polyacenes. *Phys. status solidi* **66**, 695–702 (1974).

[269] Klafter, J. & Jortner, J. Urbach rule in the optical spectra of crystalline and amorphous organic-solids. *Chem. Phys.* **26**, 421–430 (1977).

[270] Hall, J. L., Jennings, D. A. & McClintock, R. M. Study of anthracene fluorescence excited by the ruby giant-pulse laser. *Phys. Rev. Lett.* **11**, 364–366 (1963).

[271] Pope, M. & Swenberg, C. E. *Electronic Processes in Organic Crystals and Polymers*. Monographs on the physics and chemistry of materials (Oxford University Press, 1999).

[272] Ryasnyanskiy, A. & Biaggio, I. Triplet exciton dynamics in rubrene single crystals. *Phys. Rev. B* **84**, 193203 (2011).

[273] Köhler, A. & Bässler, H. What controls triplet exciton transfer in organic semiconductors? *J. Mater. Chem.* **21**, 4003–4011 (2011).

[274] Ostroverkhova, O. *et al.* Ultrafast carrier dynamics in pentacene, functionalized pentacene, tetracene, and rubrene single crystals. *Appl. Phys. Lett.* **88**, 162101 (2006).

[275] Minari, T., Nemoto, T. & Isoda, S. Temperature and electric-field dependence of the mobility of a single-grain pentacene field-effect transistor. *J. Appl. Phys.* **99**, 34506 (2006).

[276] Herkstroeter, W. G. & Merkel, P. B. The triplet state energies of rubrene and diphenylisobenzofuran. *J. Photochem.* **16**, 331–342 (1981).

[277] Lewitzka, F. & Löhmannsröben, H.-G. Investigation of triplet tetracene and triplet rubrene in solution. *Zeitschrift für Phys. Chemie* **150**, 69–86 (1986).

[278] Löhmannsröben, H. G. Photophysical properties and laser performance of rubrene. *Appl. Phys. B* **47**, 195–199 (1988).

[279] Jurchescu, O. D., Meetsma, A. & Palstra, T. T. M. Low-temperature structure of rubrene single crystals grown by vapor transport. *Acta Crystallogr. Sect. B Struct. Sci.* **62**, 330–334 (2006).

[280] Qian, Y. *et al.* Herzberg–Teller effect on the vibrationally resolved absorption spectra of single-crystalline pentacene at finite temperatures. *J. Phys. Chem. A* **124**, 9156–9165 (2020).

[281] Qian, Y. *et al.* Symmetry-breaking enhanced Herzberg–Teller effect with brominated polyacenes. *J. Phys. Chem. A* acs.jpca.1c01293 (2021).

[282] Chen, Y., Lee, B., Fu, D. & Podzorov, V. The origin of a 650 nm photoluminescence band in rubrene. *Adv. Mater.* **23**, 5370–5375 (2011).

[283] Ma, L. *et al.* Two-photon-induced singlet fission in rubrene single crystal. *J. Chem. Phys.* **138**, 184508 (2013).

[284] Tavazzi, S. *et al.* Optical response and emission waveguiding in rubrene crystals. *Phys. Rev. B* **75**, 245416 (2007).

[285] Wen, X., Yu, P., Yuan, C.-T., Ma, X. & Tang, J. Singlet and triplet carrier dynamics in rubrene single crystal. *J. Phys. Chem. C* **117**, 17741–17747 (2013).

[286] Mitrofanov, O. *et al.* Oxygen-related band gap state in single crystal rubrene. *Phys. Rev. Lett.* **97**, 166601 (2006).

[287] Stöhr, R. J. *et al.* Enhanced photoluminescence from self-organized rubrene single crystal surface structures. *Appl. Phys. Lett.* **96**, 231902 (2010).

[288] Ishibashi, Y., Inoue, Y. & Asahi, T. The excitation intensity dependence of singlet fission dynamics of a rubrene microcrystal studied by femtosecond transient microspectroscopy. *Photochem. Photobiol. Sci.* **15**, 1304–1309 (2016).

[289] Finton, D. M., Wolf, E. A., Zoutenbier, V. S., Ward, K. A. & Biaggio, I. Routes to singlet exciton fission in rubrene crystals and amorphous films. *AIP Adv.* **9**, 95027 (2019).

[290] Zhu, T., Wan, Y., Guo, Z., Johnson, J. & Huang, L. Two birds with one stone: Tailoring singlet fission for both triplet yield and exciton diffusion length. *Adv. Mater.* **28**, 7539–7547 (2016).

[291] Tao, S. *et al.* Optical pump-probe spectroscopy of photocarriers in rubrene single crystals. *Phys. Rev. B* **83**, 75204 (2011).

[292] Jankus, V. *et al.* Competition between polaron pair formation and singlet fission observed in amorphous rubrene films. *Phys. Rev. B* **87**, 224202 (2013).

[293] Brown, E. J., Pastirk, I. & Dantus, M. Ultrafast rotational anisotropy measurements: Unidirectional detection. *J. Phys. Chem. A* **103**, 2912–2916 (1999).

[294] Bossanyi, D. G. *et al.* Spin statistics for triplet–triplet annihilation upconversion: Exchange coupling, intermolecular orientation, and reverse intersystem crossing. *JACS Au* **1**, 2188–2201 (2021).

[295] Kondakov, D. Y. Triplet–triplet annihilation in highly efficient fluorescent organic light-emitting diodes: Current state and future outlook. *Philos. Trans. R. Soc. A Math. Phys. Eng. Sci.* **373**, 20140321 (2015).

[296] Yang, Z. *et al.* Recent advances in organic thermally activated delayed fluorescence materials. *Chem. Soc. Rev.* **46**, 915–1016 (2017).

[297] Wang, W. *et al.* Efficient triplet–triplet annihilation-based upconversion for nanoparticle phototargeting. *Nano Lett.* **15**, 6332–6338 (2015).

[298] Kon, H. Parmagnetic resonance of molecular oxygen in condensed phases. *J. Am. Chem. Soc.* **95**, 1045–1049 (1973).

[299] Kitaura, R. *et al.* Formation of a one-dimensional array of oxygen in a microporous metal-organic solid. *Science* **298**, 2358 LP – 2361 (2002).

[300] Hagiwara, M. *et al.* Haldane state formed by oxygen molecules encapsulated in single-walled carbon nanotubes. *J. Phys. Soc. Japan* **83**, 113706 (2014).

[301] Futagoishi, T. *et al.* A stable, soluble, and crystalline supramolecular system with a triplet ground state. *Angew. Chemie Int. Ed.* **56**, 4261–4265 (2017).

[302] Teichen, P. E. & Eaves, J. D. Collective aspects of singlet fission in molecular crystals. *J. Chem. Phys.* **143**, 44118 (2015).

[303] Smyser, K. E. & Eaves, J. D. Singlet fission for quantum information and quantum computing: the parallel JDE model. *Sci. Rep.* **10**, 18480 (2020).

[304] Matsuda, S., Oyama, S. & Kobori, Y. Electron spin polarization generated by transport of singlet and quintet multiexcitons to spin-correlated triplet pairs during singlet fissions. *Chem. Sci.* **11**, 2934–2942 (2020).

[305] Atkins, P. & Evans, G. Magnetic field effects on chemiluminescent fluid solutions. *Mol. Phys.* **29**, 921–935 (1975).

[306] Tang, X., Pan, R., Zhao, X., Zhu, H. & Xiong, Z. Achievement of high-level reverse intersystem crossing in rubrene-doped organic light-emitting diodes. *J. Phys. Chem. Lett.* **11**, 2804–2811 (2020).

[307] Ieuji, R., Goushi, K. & Adachi, C. Triplet–triplet upconversion enhanced by spin–orbit coupling in organic light-emitting diodes. *Nat. Commun.* **10**, 5283 (2019).

[308] Mezyk, J., Tubino, R., Monguzzi, A., Mech, A. & Meinardi, F. Effect of an external magnetic field on the up-conversion photoluminescence of organic films: The role of disorder in triplet-triplet annihilation. *Phys. Rev. Lett.* **102**, 087404 (2009).

[309] Schmidt, T. W. & Castellano, F. N. Photochemical upconversion: The primacy of kinetics. *J. Phys. Chem. Lett.* **5**, 4062–4072 (2014).

[310] Reindl, S. & Penzkofer, A. Higher excited-state triplet-singlet intersystem crossing of some organic dyes. *Chem. Phys.* **211**, 431–439 (1996).

[311] Xu, Y. *et al.* Highly efficient blue fluorescent OLEDs based on upper level triplet–singlet intersystem crossing. *Adv. Mater.* **31**, 1807388 (2019).

[312] Iwasaki, Y., Maeda, K. & Murai, H. Time-domain observation of external magnetic field effects on the delayed fluorescence of N,N,N′,N′-Tetramethyl-1,4-phenylenediamine in alcoholic solution. *J. Phys. Chem. A* **105**, 2961–2966 (2001).

[313] Mani, T. & Vinogradov, S. A. Magnetic field effects on triplet–triplet annihilation in solutions: Modulation of visible/NIR luminescence. *J. Phys. Chem. Lett.* **4**, 2799–2804 (2013).

[314] Gao, C. *et al.* Intramolecular versus intermolecular triplet fusion in multichromophoric photochemical upconversion. *J. Phys. Chem. C* **123**, 20181–20187 (2019).

[315] Gholizadeh, E. M. *et al.* Photochemical upconversion of near-infrared light from below the silicon bandgap. *Nat. Photonics* **14**, 585–590 (2020).

[316] Song, L. & Fayer, M. Temperature dependent intersystem crossing and triplet-triplet absorption of rubrene in solid solution. *J. Lumin.* **50**, 75–81 (1991).

[317] Aggarwal, N. & Patnaik, A. Unusual nonemissive behavior of rubrene J-aggregates: A rare violation. *J. Phys. Chem. B* **121**, 3190–3201 (2017).

[318] Nijegorodov, N., Ramachandran, V. & Winkoun, D. P. The dependence of the absorption and fluorescence parameters, the intersystem crossing and internal conversion rate constants on the number of rings in polyacene molecules. *Spectrochim. Acta Part A Mol. Biomol. Spectrosc.* **53**, 1813–1824 (1997).

[319] Wang, F., Dukovic, G., Brus, L. E. & Heinz, T. F. Time-resolved fluorescence of carbon nanotubes and its implication for radiative lifetimes. *Phys. Rev. Lett.* **92**, 177401 (2004).

[320] Cruz, C. D., Choi, H. H., Podzorov, V., Chronister, E. L. & Bardeen, C. J. Photon upconversion in crystalline rubrene: Resonant enhancement by an interband state. *J. Phys. Chem. C* **122**, 17632–17642 (2018).

[321] Beimborn, J. C., Zagorec-Marks, W. & Weber, J. M. Spectroscopy of resonant intermediate states for triplet–triplet annihilation upconversion in crystalline rubrene: Radical ions as sensitizers. *J. Phys. Chem. Lett.* **11**, 7212–7217 (2020).

[322] Darmanyan, A. P. Laser photolysis study of the mechanism of rubrene quenching by molecular oxygen. *Chem. Phys. Lett.* **86**, 405–410 (1982).

[323] Kondakov, D. Y., Pawlik, T. D., Hatwar, T. K. & Spindler, J. P. Triplet annihilation exceeding spin statistical limit in highly efficient fluorescent organic light-emitting diodes. *J. Appl. Phys.* **106**, 124510 (2009).

[324] Liu, W. *et al.* Nondoped blue fluorescent organic light-emitting diodes based on benzonitrile-anthracene derivative with 10.06% external quantum efficiency and low efficiency roll-off. *J. Mater. Chem. C* **7**, 1014–1021 (2019).

[325] Lampert, R. A. & Phillips, D. Photophysics of meso-substituted anthracenes. Part 2.—Temperature effects in the solution and vapour phases. *J. Chem. Soc. Faraday Trans. 2 Mol. Chem. Phys.* **81**, 383–393 (1985).

[326] Gibson, J., Monkman, A. P. & Penfold, T. J. The importance of vibronic coupling for efficient reverse intersystem crossing in thermally activated delayed fluorescence molecules. *ChemPhysChem* **17**, 2956–2961 (2016).

[327] Wang, R. *et al.* Magnetic dipolar interaction between correlated triplets created by singlet fission in tetracene crystals. *Nat. Commun.* **6**, 8602 (2015).

[328] Imperiale, C. J., Green, P. B., Miller, E. G., Damrauer, N. H. & Wilson, M. W. B. Triplet-fusion upconversion using a rigid tetracene homodimer. *J. Phys. Chem. Lett.* **10**, 7463–7469 (2019).

[329] Adams, J. M. & Ramdas, S. The crystal structure of solution-grown 9,10-diphenylanthracene. A combined computational and X-ray study. *Acta Crystallogr. Sect. B* **35**, 679–683 (1979).

[330] Monguzzi, A. *et al.* High efficiency up-converting single phase elastomers for photon managing applications. *Adv. Energy Mater.* **3**, 680–686 (2013).

[331] Khnayzer, R. S. *et al.* Upconversion-powered photoelectrochemistry. *Chem. Commun.* **48**, 209–211 (2012).

[332] MacQueen, R. W., Cheng, Y. Y., Danos, A. N., Lips, K. & Schmidt, T. W. Action spectrum experiment for the measurement of incoherent photon upconversion efficiency under sun-like excitation. *RSC Adv.* **4**, 52749–52756 (2014).

[333] Yanai, N. *et al.* Absolute method to certify quantum yields of photon upconversion via triplet–triplet annihilation. *J. Phys. Chem. A* **123**, 10197–10203 (2019).

[334] Olesund, A., Gray, V., Mårtensson, J. & Albinsson, B. Diphenylanthracene dimers for triplet–triplet annihilation photon upconversion: Mechanistic insights for intramolecular pathways and the importance of molecular geometry. *J. Am. Chem. Soc.* **143**, 5745–5754 (2021).

[335] Monguzzi, A., Tubino, R., Hoseinkhani, S., Campione, M. & Meinardi, F. Low power, non-coherent sensitized photon up-conversion: modelling and perspectives. *Phys. Chem. Chem. Phys.* **14**, 4322 (2012).

[336] Bossanyi, D. G. *et al.* In optimized rubrene-based nanoparticle blends for photon upconversion, singlet energy collection outcompetes triplet-pair separation, not singlet fission. *J. Mater. Chem. C* (2022).

[337] Nienhaus, L. *et al.* Speed limit for triplet-exciton transfer in solid-state PbS nanocrystal-sensitized photon upconversion. *ACS Nano* **11**, 7848–7857 (2017).

[338] Ekins-Daukes, N. J. & Schmidt, T. W. A molecular approach to the intermediate band solar cell: The symmetric case. *Appl. Phys. Lett.* **93**, 63507 (2008).

[339] McKenna, B. & Evans, R. C. Towards efficient spectral converters through materials design for luminescent solar devices. *Adv. Mater.* **29**, 1606491 (2017).

[340] Mahboub, M., Huang, Z. & Tang, M. L. Efficient infrared-to-visible upconversion with subsolar irradiance. *Nano Lett.* **16**, 7169–7175 (2016).

[341] Abulikemu, A. *et al.* Solid-state, near-infrared to visible photon upconversion via triplet–triplet annihilation of a binary system fabricated by solution casting. *ACS Appl. Mater. Interfaces* **11**, 20812–20819 (2019).

[342] Nagata, R., Nakanotani, H., Potscavage Jr., W. J. & Adachi, C. Exploiting singlet fission in organic light-emitting diodes. *Adv. Mater.* **30**, 1801484 (2018).

[343] Radiunas, E. *et al.* NIR-to-vis photon upconversion in rubrenes with increasing structural complexity. *J. Mater. Chem. C* **9**, 4359–4366 (2021).

[344] Wolf, E. A. & Biaggio, I. Geminate exciton fusion fluorescence as a probe of triplet exciton transport after singlet fission. *Phys. Rev. B* **103**, L201201 (2021).

[345] Seki, K., Yoshida, T., Yago, T., Wakasa, M. & Katoh, R. Geminate delayed fluorescence by anisotropic diffusion-mediated reversible singlet fission and triplet fusion. *J. Phys. Chem. C* **125**, 3295–3304 (2021).

[346] Irkhin, P., Biaggio, I., Zimmerling, T., Döbeli, M. & Batlogg, B. Defect density dependent photoluminescence yield and triplet diffusion length in rubrene. *Appl. Phys. Lett.* **108**, 63302 (2016).

[347] Chen, C.-H. *et al.* Thickness-dependent exciton dynamics in thermally evaporated rubrene thin films. *J. Phys. Chem. C* **124**, 25729–25737 (2020).

[348] Takahashi, S., Watanabe, K. & Matsumoto, Y. Singlet fission of amorphous rubrene modulated by polariton formation. *J. Chem. Phys.* **151**, 074703 (2019).

[349] Griffith, O. L. & Forrest, S. R. Exciton management in organic photovoltaic multidonor energy cascades. *Nano Lett.* **14**, 2353–2358 (2014).

[350] Yee, W. A., Kuzmin, V. A., Kliger, D. S., Hammond, G. S. & Twarowski, A. J. Quenching of the fluorescent state of rubrene directly to the ground state. *J. Am. Chem. Soc.* **101**, 5104–5106 (1979).

[351] Shushin, A. I. Manifestation of T-exciton migration in the kinetics of singlet fission in organic semiconductors. *Chem. Phys. Lett.* **678**, 283–288 (2017).

[352] Zeis, R. *et al.* Field effect studies on rubrene and impurities of rubrene. *Chem. Mater.* **18**, 244–248 (2006).

[353] Sher, P.-H. *et al.* Distinct routes of singlet fission and triplet fusion: A fluorescence kinetic study of rubrene. *J. Phys. Chem. C* **123**, 3279–3284 (2019).

[354] Yeh, T.-S., Chu, C.-S. & Lo, Y.-L. Highly sensitive optical fiber oxygen sensor using Pt(II) complex embedded in sol–gel matrices. *Sensors Actuators B Chem.* **119**, 701–707 (2006).

[355] Arnold, S., Whitten, W. B. & Damask, A. C. Triplet exciton trapping by dislocations in anthracene. *J. Chem. Phys.* **53**, 2878–2884 (1970).

[356] Giebink, N. C., Sun, Y. & Forrest, S. R. Transient analysis of triplet exciton dynamics in amorphous organic semiconductor thin films. *Org. Electron.* **7**, 375–386 (2006).

[357] Chen, L. *et al.* Optical and transport properties of single crystal rubrene: A theoretical study. *Chem. Phys.* **481**, 198–205 (2016).

[358] Petrenko, T., Krylova, O., Neese, F. & Sokolowski, M. Optical absorption and emission properties of rubrene: Insight from a combined experimental and theoretical study. *New J. Phys.* **11**, 15001 (2009).

[359] Paraskar, A. S. *et al.* Rubrenes: Planar and twisted. *Chem. – A Eur. J.* **14**, 10639–10647 (2008).

[360] Sakai, H. *et al.* Multiexciton dynamics depending on intramolecular orientations in pentacene dimers: Recombination and dissociation of correlated triplet pairs. *J. Phys. Chem. Lett.* **9**, 3354–3360 (2018).

[361] Sakuma, T. *et al.* Long-lived triplet excited states of bent-shaped pentacene dimers by intramolecular singlet fission. *J. Phys. Chem. A* **120**, 1867–1875 (2016).

[362] Pun, A. B., Sanders, S. N., Sfeir, M. Y., Campos, L. M. & Congreve, D. N. Annihilator dimers enhance triplet fusion upconversion. *Chem. Sci.* **10**, 3969–3975 (2019).

[363] Ogawa, T. *et al.* Donor–acceptor–collector ternary crystalline films for efficient solid-state photon upconversion. *J. Am. Chem. Soc.* **140**, 8788–8796 (2018).

[364] Mongin, C., Garakyaraghi, S., Razgoniaeva, N., Zamkov, M. & Castellano, F. N. Direct observation of triplet energy transfer from semiconductor nanocrystals. *Science* **351**, 369–372 (2016).

[365] Jortner, J., Choi, S.-i., Katz, J. L. & Rice, S. A. Triplet energy transfer and triplet-triplet interaction in aromatic crystals. *Phys. Rev. Lett.* **11**, 323–326 (1963).

[366] Wang, X., Garcia, T., Monaco, S., Schatschneider, B. & Marom, N. Effect of crystal packing on the excitonic properties of rubrene polymorphs. *CrystEngComm* **18**, 7353–7362 (2016).